Final Report

Improving UXO Detection and Discrimination in Magnetic Environments

SERDP Project MM-1414

MAY 2010

Yaoguo Li, Richard Krahenbuhl, Todd Meglich
Center for Gravity, Electrical, & Magnetic Studies
Department of Geophysics
Colorado School of Mines

Doug Oldenburg, Len Pasion
UBC – Geophysical Inversion Facility
University of British Columbia

Steve Billings
Sky Research, Inc.

Remke van Dam
Michigan State University

Bruce Harrison
New Mexico Institute of Technology

SERDP

Strategic Environmental Research and Development Program

Report Documentation Page	*Form Approved* *OMB No. 0704-0188*

1. REPORT DATE **MAY 2010**	2. REPORT TYPE	3. DATES COVERED **00-00-2010 to 00-00-2010**

4. TITLE AND SUBTITLE **Improving UXO Detection and Discrimination in Magnetic Environments**	5a. CONTRACT NUMBER 5b. GRANT NUMBER 5c. PROGRAM ELEMENT NUMBER
6. AUTHOR(S)	5d. PROJECT NUMBER 5e. TASK NUMBER 5f. WORK UNIT NUMBER
7. PERFORMING ORGANIZATION NAME(S) AND ADDRESS(ES) **Colorado School of Mines,Department of Geophysics,Center for Gravity, Electrical, & Magnetic Studies,Golden,CO,80401**	8. PERFORMING ORGANIZATION REPORT NUMBER
9. SPONSORING/MONITORING AGENCY NAME(S) AND ADDRESS(ES)	10. SPONSOR/MONITOR’S ACRONYM(S) 11. SPONSOR/MONITOR’S REPORT NUMBER(S)

12. DISTRIBUTION/AVAILABILITY STATEMENT
Approved for public release; distribution unlimited

13. SUPPLEMENTARY NOTES

14. ABSTRACT

15. SUBJECT TERMS

16. SECURITY CLASSIFICATION OF:			17. LIMITATION OF ABSTRACT	18. NUMBER OF PAGES	19a. NAME OF RESPONSIBLE PERSON
a. REPORT **unclassified**	b. ABSTRACT **unclassified**	c. THIS PAGE **unclassified**	**Same as Report (SAR)**	**280**	

Standard Form 298 (Rev. 8-98)
Prescribed by ANSI Std Z39-18

SERDP Project MM-1414

Improving UXO Detection and Discrimination in Magnetic Environments

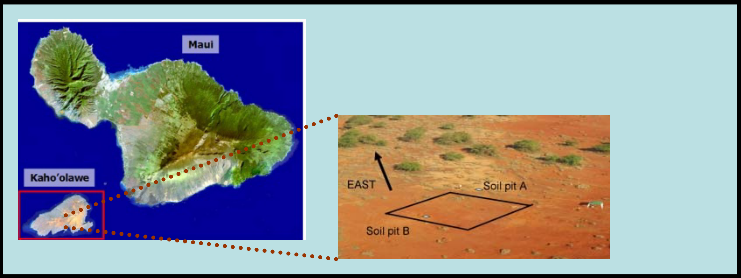

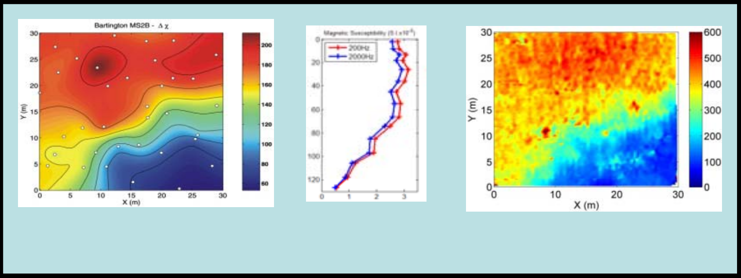

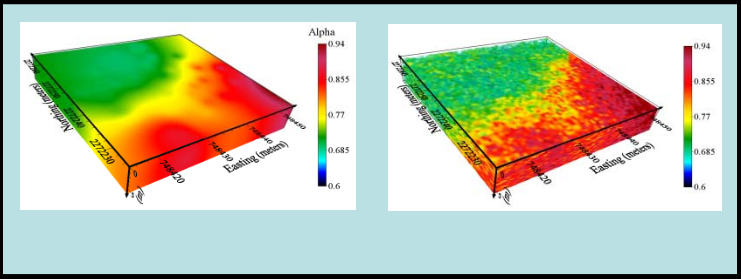

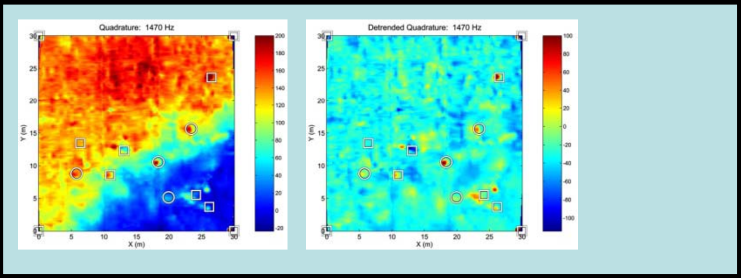

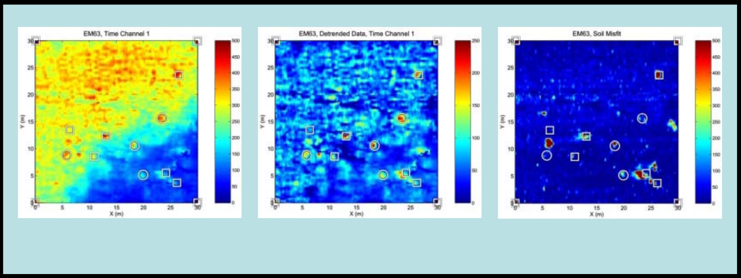

Final Report

Yaoguo Li, Richard Krahenbuhl, Todd Meglich
Center for Gravity, Electrical, & Magnetic Studies
Department of Geophysics
Colorado School of Mines

Doug Oldenburg, Len Pasion
UBC – Geophysical Inversion Facility
University of British Columbia

Steve Billings
Sky Research, Inc.

Remke van Dam
Michigan State University

Bruce Harrison
New Mexico Institute of Technology

May 2010

SERDP
Strategic Environmental Research and Development Program

Approved for public release; distribution is unlimited

Executive Summary

This is the final report for the SERDP project MM-1414 and it covers the research results accomplished since the projects inception in 2005. The basic premise of the project is the theoretical understanding achieved through SERDP SEED project UX-1285, which predicted that spatially variable frequency-dependent susceptibility in soils hosting UXO can produce strong background response in both electromagnetic and magnetic data. Such responses can mask UXO signatures or produce false alarms. Improving UXO detection and discrimination in such strongly magnetic environments requires the characterization and removal of these responses. The overall objective of the current project has therefore been to understand and characterize the spatial variation and frequency dependence of soil magnetic susceptibility so that effective means can be developed for characterizing and removing soil responses.

The research performed over the 4-year life span of this project progressed satisfactorily with all major research tasks completed according to the project plan. To start, five major field sessions were conducted at four sites: Kaho'olawe Island and Big Island, HI; Chevalier Ranch, MT; and Sentinel Plains, AZ. Through laboratory analyses of soil samples and interpretation of geophysical data collected at these sites, we have developed a significant improvement in understanding the origins, composition and spatial distribution of magnetic soils in varying magnetic environments. For example, we have confirmed observationally the frequency-dependent magnetic susceptibility of soils originating from well-weathered volcanics and volcanic ashes. Strong correlation between the strength of frequency-dependent susceptibility and measured background responses confirms the effect of such soil on magnetic and electromagnetic sensor data. Thus, we have observed the viscous remanent magnetization in the field. Through our laboratory and field observations, we have also developed a 3D soil distribution model and 3D geostatistical model of frequency dependent magnetic susceptibility for improved modeling of geophysical data in these environments. Lastly, through our field work we have discovered that sites previously thought to be benign may exhibit weak viscous remanent magnetization. Thus the field activities from this project have broad implications for ongoing and future remediation efforts in similar environments within the continental US.

On another research front, we have utilized the information gathered from our field and laboratories activities to develop robust forward modeling algorithms and material on filter analysis of TDEM data in the presence of magnetic geologic noise. For example, we present a method for simulating the background response of strong magnetic environments on EM data using correlated random numbers. We show how these simulated responses may prove viable for discrimination of UXO in these magnetic terrains.

Finally, we demonstrate new sets of procedures for improved target detection and decreased false positives in strongly magnetic environments based on the magnetic method. This includes development and implementation of iterative Wiener and wavelet based filter approaches for separating the response of magnetic geology from those of UXO. In addition, we demonstrate successful implementation of a high-pass Butterworth filter originally applied during decorrugation of unleveled magnetic data for the same purpose.

Table of Contents

1. Introduction 7
1.1 Background 8
1.2 Research approach and strategy 9
1.3 Summary of Accomplishments 9
2. Field Sites and Data Collection 11
2.1 Hawaii 12
2.1.1 Background and site geology 12
2.1.2 Field work 18
2.1.3 Geophysical data collections 22
2.1.4 Summary 29
2.2 Montana – Chevallier Ranch 31
2.2.1 Background and site geology 31
2.2.2 Field work 34
2.2.3 Geophysical data collections 44
2.2.4. Summary 52
2.3 Sentinel Plains 53
2.3.1 Background and site geology 53
2.3.2 Field work 55
2.3.3 Geophysical data collections 59
2.3.4 Summary 70
3. Field Component, UXO Remediation Sites 71
3.1 Introduction 71
3.2. Methods and Materials 73
3.2.1 Sampling strategy and field measurements 74
3.2.2 Laboratory techniques – magnetic measurements 78
3.2.3. Laboratory techniques – mineralogy 81
3.3. Results 83
3.3.1 Hawaii 83
3.3.2 Montana – Chevallier Ranch 104
3.3.3 Sentinel Plains 111

3.4 Discussion 117
3.5. Conclusions 118
4. Soil Characterization 129
4.1 Introduction 129
4.2. 3D soil distribution model 130
4.2.1 Cole-Cole model for parameter estimation 132
4.2.2 3-D soil model 134
4.3. 3D statistical simulation of soil model 136
4.4. Summary 138
5. Magnetic Data Analysis 140
5.1 Introduction 140
5.2 Magnetic data processing 140
5.2.1 Iterative Wiener filter 142
5.2.2 Wavelet filter 156
5.2.3. Leveling / decorrugation filter 161
5.3 Target selection 165
5.3.1. Extended Euler method 166
5.3.2. Workflow details for automatic anomaly detection 167
5.3.3. Results 169
5.3.4. Discussion 176
5.4. Summary 176
6. Electromagnetic Data Analysis 177
6.1 Introduction 177
6.2 Electromagnetic response of a viscous remnant magnetic halfspace 179
6.3 Effect of height variations on sensor response 183
6.3.1 Simulation of VRM geologic background response due to height variations 184
6.3.2 Height errors and data variances 187
6.3.3 Sensor height and orientation on VRM response 188
6.4 Additivity of background and target responses 191
6.5 Estimating response of background geology 192
6.6 Testing EMI processing methods using simulated TEM data 195
6.6.1 Simulated noise 197

6.6.2 Baseline noise ... 198
6.6.3 Sensor position uncertainty ... 200
6.6.4 Simulating the magnetic background signal ... 200
6.6.5 Examples of simulated data sets ... 201
6.7 Picking targets in highly magnetic soils ... 203
6.7.1 Single channel of data ... 205
6.7.2 Misfit to a soil model ... 209
6.8 Accuracy of filtering when estimating background response ... 214
6.9 Effect of VRM noise on recovered model parameters ... 216
6.10 Processing of data collected on Kaho'olawe Island, Hawaii ... 221
6.10.1 Geonics EM63 TEM data ... 223
6.10.2 Geophex GEM3 FEM data ... 230
6.10.3 Target picking by calculating probability of false alarm ... 234
6.10.4 Target picking from log-misfit image ... 237
6.11 Simulating data response using correlated random numbers ... 240
6.11.1 Radial power spectra ... 241
6.11.2 2D power spectra ... 242
6.11.3 Recovery of power spectrum models ... 244
6.11.4 Multiple correlated random numbers ... 245
6.11.5 Averaging functions ... 246
6.11.6 Example using MCRN ... 247
6.11.7 Discrimination using MCRN at field site ... 251
6.11.8. Summary ... 259
6.12 Discussion ... 259
7. Discussion ... 261
8. References ... 269
9. Appendices ... 276
9.1 Articles or papers published in peer-reviewed journals ... 276
9.2 Technical reports ... 276
9.3. Conference/symposium proceedings and/or papers scientifically recognized and referenced ... 276
9.4 Published technical abstracts ... 277

1. Introduction

This project addresses one of the Department of Defense's (DOD) most pressing environmental problems; that is, the efficient and reliable identification of unexploded ordnance (UXO) without the need to excavate large numbers of non-UXO. The task of discriminating UXO from non-UXO items is more difficult when sensor data are contaminated with geological noise originating from magnetic soils. In regions of highly magnetic soil, magnetic and electromagnetic sensors often detect large anomalies that are of geologic, rather than metallic, origin. This study therefore focuses on four primary research tasks which we completed and report on in this document. These objectives include understanding the geologic origins and physics of soil magnetization, characterizing the spatial variation magnetic susceptibilities at UXO remediation sites, developing methods and procedures for removing the effects of magnetic soils from magnetic data, and developing methods and procedures for preprocessing of electromagnetic data in highly magnetic environments. The research is focused on four UXO remediation sites that have different magnetic soil properties.

In 2005 this project first began addressing the origins of magnetic soils by conducting field research at three different sites. We built upon this work in 2006 by completing field activities at a fourth and final field site. Additional work was also conducted on understanding the origins of the magnetic soils using chemical analysis as well as the impact that physical properties, such as viscous remanent magnetization, have on the collected data. In 2007 and 2008, we built upon the previous years by developing algorithms and techniques for simulating the response of magnetic geology in geophysical data in an attempt to separate these responses from magnetic and electromagnetic data.

In this Final Report, we bring together all of the research results generated throughout the life of SERDP Project MM-1414. This includes our current understanding of the origins of magnetic soils and their influences on geophysical sensors, methods developed for simulating the signatures of magnetic soils in geophysical data, and the foundational developments of techniques and algorithms for separating these environmental anomalies from those of UXO for improved remediation efforts in magnetic environments.

1.1 Background

The two most effective geophysical techniques for UXO investigations are magnetic and electromagnetic (time or frequency domain) surveys. These have a well-documented ability to locate UXO but are prone to excessive false alarms, which significantly increases the cost of clean up. For instance, at some sites up to 99% of excavated items are non-UXO (Defense Science Board, 2003). The key to reducing these false alarms is the development of algorithms that can discriminate between an intact UXO and other items such as scrap metal or geological features.

Recent developments have enabled the recovery of dipole or ellipsoidal parameters through inversion of magnetic data. Additionally, frequency and time-domain electromagnetic measurements can be inverted to recover parameters in reduced modeling formulations. These recovered parameters can be used to discriminate between UXO and other items. For example, the recovered parameters in a two-dipole model for time-domain electromagnetics can be used to determine whether the object is magnetic (possibly UXO) or not, and whether the object is platelike (non-UXO) or rod-like (UXO). The above inversion methodologies have been developed with the underlying assumption that the collected data result from objects buried in a very resistive and non-magnetic background. In practice this is not always the case. At many sites (e.g. former Fort Ord; the former Naval range at Kaho'olawe, and Helena Valley, Montana) the soils are known to be magnetic. That soil background significantly modifies the measured magnetic or electromagnetic responses and thus adversely affects the performance of the existing inversion algorithms. This reduces our ability to discriminate and results in false alarms. For instance, approximately 60,000 anomalies were dug at the Kaho'olawe site where approximately 70% of the false anomalies were caused by non-hazardous metal objects and 27% were caused by geology. Therefore, it is important that we understand the effect of magnetic soil on these two widely used techniques in UXO detection and discrimination and develop approaches to mitigate such effect in order to improve the detection and discrimination capabilities.

The emphases on research for this project are twofold. The first is to develop an understanding of the geologic origins and physics of soil magnetization and characterizing the magnetic susceptibilities at various UXO remediation sites, with emphasis on fieldwork to quantify the spatial variability and frequency dependence of soil magnetic susceptibility. The second component involves developing methods and procedures for removing the effects of magnetic soils from magnetic and electromagnetic data.

1.2 Research approach and strategy

The long term goal of this project has been to address four practical aspects at UXO remediation sites with different geologic histories, and therefore different soil magnetization properties and distributions:

(1) Identification of the geologic origins and physics of soil magnetization at remediation sites;

(2) Development of protocols and practical procedures for characterizing site magnetization;

(3) Development of methods and procedures for removing the effects of soil responses from magnetic and electromagnetic data.

(4) Development of methods and procedures for preprocessing of electromagnetic data in highly magnetic environments.

In order to address the topics described above, this project focuses on four UXO remediation sites that have different magnetic soil properties:

(1) Kaho'olawe, HI

(2) Waikoloa and Waimea, Big Island, HI

(3) Chevalier Ranch, MT

(4) Barry M. Goldwater Bombing Range at the Sentinel Plains, southwest Arizona

1.3 Summary of Accomplishments

In this report, we summarize the major research accomplishments of the SERDP MM-1414 project with focus on the four field sites. In short, we have achieved our long term research goals set out at the start of the project. Chapter 2 starts by presenting a summary of the field activities from the project's field sites, and it includes geologic descriptions of the four sites, grid details, geophysical data collected, and soil sample locations. In Chapter 3, we present detailed results from soil experiments in the lab, and our current understanding of the physics and distributions of soil magnetization acquired through this research project. Chapter 4 provides a methodology for simulating 3-D soil distribution and geostatistical models based on field and laboratory measurements of frequency dependent magnetic susceptibility at the Kaho'olawe remediation site in Hawaii.

Chapter 5 demonstrates a new series of procedures for improved target detection and decreased false positives in strongly magnetic environments based on the magnetic method. This includes the development and/or application of several filtering techniques for removing the geologic noise, and foundation work on a detection algorithm for identifying potential UXO in these environments. In Chapter 6, we present our understanding of the frequency- and time-domain electromagnetic responses of geophysical sensors in magnetic terrain. In addition to presenting methods for simulating the background response of strong magnetic environments on EM data, we also demonstrate how these simulated responses may prove viable for discrimination of UXO in these magnetic terrains. Finally, we conclude this report in Chapters 7 and 9 with a discussion of the projects results, recommendations, and publications/presentations generated throughout the lifespan of SERDP Project MM-1414.

2. Field Sites and Data Collection

There are four major tasks addressed by SERDP Project MM-1414. Each of these task have been developed to provide information necessary to properly understand, model, and ultimately remove the soil response from geophysical data for improved remediation efforts in difficult magnetic environments. These complementary tasks include:

> Building an understanding – through field and laboratory analysis of soil samples and geophysical data – of the geologic origins and physics of soil magnetization.
>
> Developing a practical means for identifying and modeling the spatially variable frequency-dependent magnetic susceptibility in soils hosting UXO.
>
> Developing methods and procedures for removing the effects of soil response from magnetic measurements for improved UXO detection and discrimination in magnetic environments.
>
> Developing methods and procedures for removing the effects of soil response from electromagnetic measurements for improved UXO detection and discrimination in magnetic environments.

The research presented in this opening chapter focuses on the major field efforts at four UXO remediation sites that have different magnetic soil properties. These field activities are the foundation of SERDP Project MM-1414, providing all subsequent soil samples for laboratory study and geophysical data in magnetic environments to achieve the long term project goals. These sites include:

(1) Kaho'olawe, HI
(2) Waikoloa and Waimea, Big Island, HI
(3) Chevalier Ranch, MT
(4) Barry M. Goldwater Bombing Range at the Sentinel Plains, southwest Arizona

We present here the field work and background information on site geology, geomorphology, soil descriptions, data grids, geophysical methods employed, and data collection results for the four sites. In Chapter 3, we then discuss our understanding of the geologic origins and physics of soil magnetization (task 1) based on field site data introduced here.

2.1 Hawaii

The first major field activities presented are those associated with the Hawaiian Islands sites. Those are the Navy QA range on the island of Kaho'olawe, and the maneuver areas of Waimea and Waikoloa on Hawaii, also referred to as Hawaii Island or Big Island throughout the report.

2.1.1 Background and site geology

The islands and the seamounts of the Hawaiian Ridge and Emperor Seamounts include more than 107 individual volcanoes. The chain is age progressive, ranging from 70 to 80 million year old submerged volcanoes in the northwest, to still-active volcanoes at the southeastern end (Clague and Dalrymple, 1989). Commonly accepted theory on the formation of the Emperor Seamount is that the chain of islands formed through a steady movement of the Pacific lithospheric plate over a Hawaiian Hot Spot ('plume theory'), in which the magma source produces volcanoes on the sea floor. It is worth mentioning, however, that recent geologic and geophysical studies (Hamilton, 2003) argue that common plume theory is derived largely from conjecture, and claim that integrated data better support island formation from a propagating rift (crackspot) due to perpetuation of regional stresses, rather than from a single hotspot. The Hawaiian ridge on the southeastern end of the chain comprises the eight major Hawaiian Islands, Figure 2.1. We have studied the islands of Kaho'olawe (lower left), which has an age of approximately 1 million years, and Hawaii (lower right), which is the youngest, with still-active volcanoes.

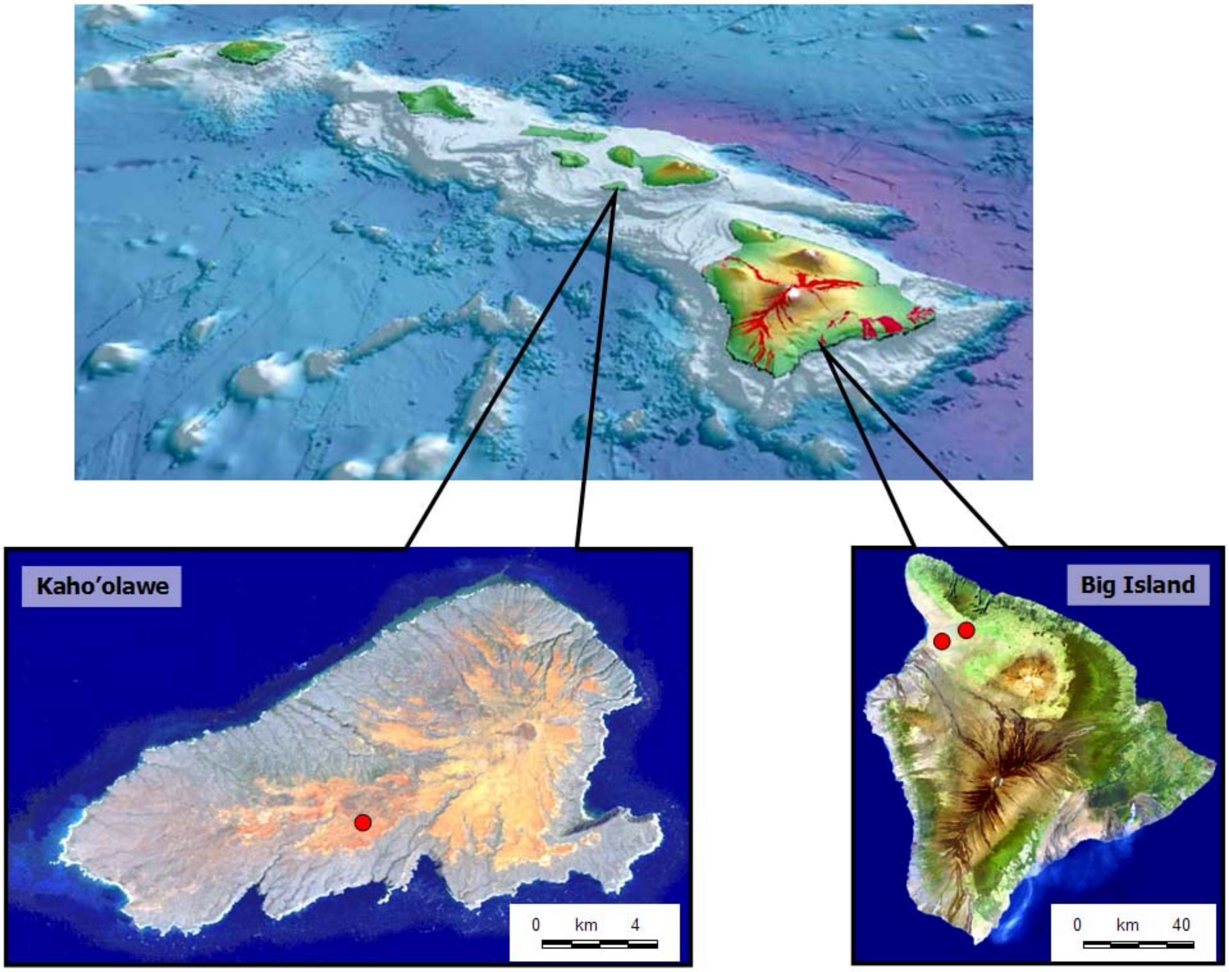

Figure 2.1: Hawaiian Islands (top), Island of Kaho'olawe (lower-left) and Big Island of Hawaii (lower right). The three Hawaiian UXO study sites are identified with red dots. Landsat images and GIS data files available at the Hawaii Statewide GIS Program website: http://www.state.hi.us/dbedt/gis/download.htm.

An idealized Hawaiian volcano evolves through a sequence of four eruptive stages (preshield, shield, postshield, and rejuvenated), distinguished by lava composition, eruptive rate and style, and stage of development (Wolfe and Morris, 1996). Preshield volcanics, formed below sea level, are the oldest parts of a volcano. Shield-stage lavas comprise 95-98% of the volume of the Hawaiian volcanoes and are dominated by tholeiitic basalt. Tholeiitic basalt is relatively rich in silica and poor in alkalic minerals, such as sodium and potassium. On most islands, including the older volcanoes (Mauna Kea, Kohala) on the Island of Hawaii, tholeiitic shield-stage lavas have been capped by postshield lavas (Clague and Dalrymple, 1989). Alkalic postshield basalts are relatively poor in silica and rich in alkalic minerals. The rejuvenated stage, in which small amounts of silica-poor lava erupt, occurs after up to a few million years of dormancy. The primary lithogenic iron oxides in Hawaiian rocks are titanomagnetite ($Fe_{3-x}Ti_xO_4$) and ilmenite or titanohematite ($FeTiO_3$). The composition of titanomagnetites varies from x=0 (magnetite) to x=0.8. The end member ulvospinel, with x=1, is rare. The average (titano)magnetite content of the tholeiitic olivine basalts and alkalic basalts, characteristic for Kaho'olawe and Hawaii, is 3.7-4.6% and 3.3-7.4%, respectively. Ilmenite content ranges from 2.5-5.0% and 1.2-6.2% for tholeiitic and alkalic basalts, respectively (Cornell and Schwertmann, 2003; Wedepohl, 1969).

In general, the soils on the Islands of Hawaii contain significant amounts of hematite (α-Fe_2O_3), and magnetite (Fe_3O_4), or maghemite (γ-Fe_2O_3). The source of iron oxides in these soils are the basaltic rocks that contain significant amounts of magnetite and other iron-containing minerals (Wright and Clague, 1989). However, even in soils developed on the relatively uniform parent material of Hawaii the magnetic susceptibility varies significantly over relatively short distances (Van Dam *et al.*, 2004).

2.1.1.1 Navy QA range, Kaho'olawe Island, HI

Setting and Geology – Kaho'olawe is the smallest of the eight major islands in the state of Hawaii and lies approximately 10 km southwest of Maui, as seen in Figure 2.2. It is one of the smallest single-shield volcanoes of the Hawaiian Islands and is 1-2 million years old (Wood and Kienle, 1990). Kaho'olawe has not erupted in historic time and is considered to be extinct. Kaho'olawe is a Koolau-type volcano, characterized by the near-absence of alkalic postshield basalts (Wright and Clague, 1989; p.220). Alkalic flows are present only locally atop the tholeiitic sequence (Macdonald *et al.*, 1983). Potassium-argon dates of postshield alkalic basalts suggest that the island is around 1 million years old (Naughton *et al.*, 1980). The average magnetite and ilmenite content of the tholeiitic and alkali olivine basalts, characteristic for Kaho'olawe, lies between 37-46 and 24-50 g/kg (Wedepohl, 1969).

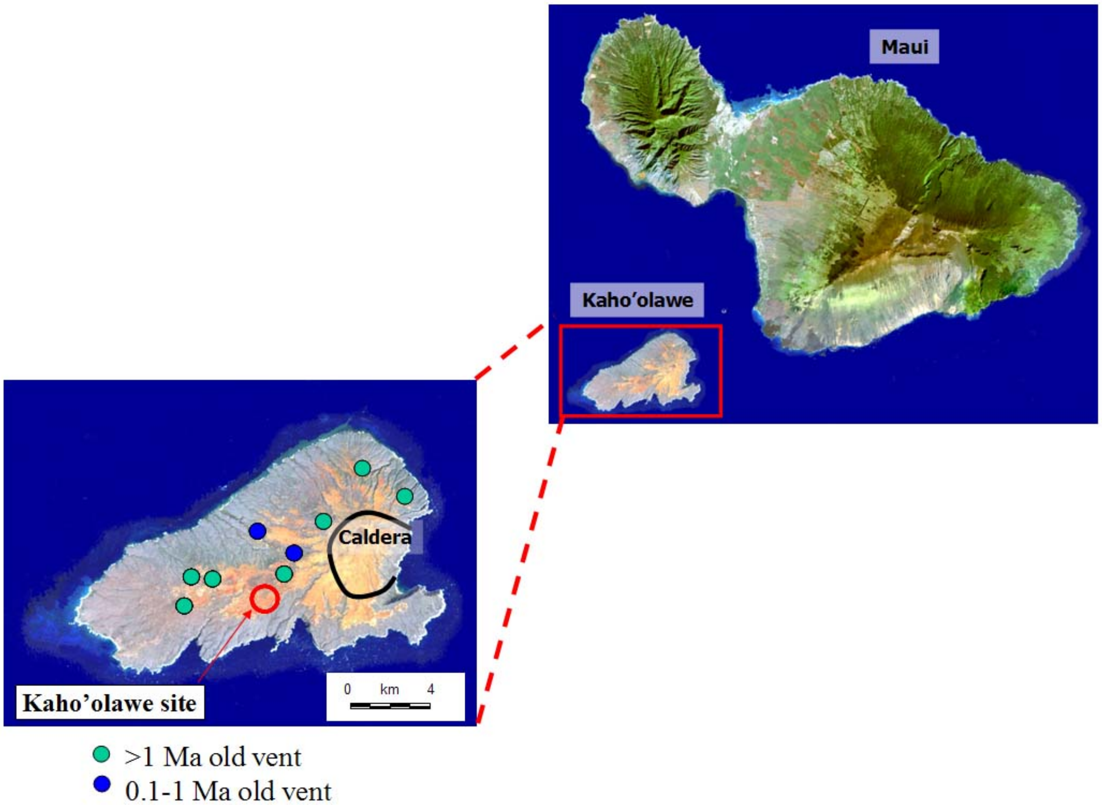

Figure 2.2: Landsat image for islands of Maui and Kaho'olawe (top-right). Landsat image of Kaho'olawe (lower-left). The UXO study site on Kaho'olawe is identified with the red circle. Landsat images and GIS data files available at the Hawaii Statewide GIS Program website: http://www.state.hi.us/dbedt/gis/download.htm.

Geomorphology and Soils – Due to its position on the leeward side of Haleakala Volcano on Maui and its limited elevation (maximum 450 meters), Kaho'olawe receives very little rainfall throughout the year. The annual rainfall is estimated to range from 250 to 650 millimeters (Macdonald *et al.*, 1983; Nakamura and Smith, 1995). Overgrazing by cattle that were first introduced in 1864 has caused large areas of the island to be stripped of vegetation. The bare surface and the strong trade winds from the east have led to severe soil erosion. The amount of erosion averages 1.5 meters and is locally as much as 2.5 meters (Macdonald *et al.*, 1983). The sparse vegetation of the central plateau consists of piligrass and kiawe trees.

The Navy QA Grid that was selected for our research lies in the Kunaka/Na'alapa province and is dominated by soils of the Kaneloa Series and Puu Moiwi Series (Nakamura and Smith, 1995).

The parent material of these soils is strongly weathered volcanic ash over strongly weathered basic igneous rock. The Kaneloa soils reach saprolite (weathered bedrock) within 40 to 75 centimeters from the surface, while the Puu Moiwi soils have a deeper soil cover. New measurement of the magnetic properties and mineralogical composition conducted in this study indicate that the two soil series could be classified as one soil type (Van Dam *et al.*, 2008).

2.1.1.2 Big Island Sites: Waimea and Waikoloa Maneuver Areas, Hawaii, HI

Hawaii is the youngest and largest of the eight major islands in the state of Hawaii and it consists of five subaerial volcanos and one that is (still) submerged, as shown in Figure 2.3. The ages of the volcanoes range from 0.43 million years for Kohala Volcano in the north to active in the south. Potassium-argon dates of shield-stage tholeiitic basalts indicate an age of 0.375 million years for Mauna Kea (Clague and Dalrymple, 1989). This age should be treated with caution as the lava flows at the surface show a wide range of ages (Wolfe and Morris, 1996).

Both the Waimea Geophysical Prove-out (GPO) near the town of Waimea and the Geophysical Prove-out at Waikaloa Village lie on the northwestern flanks of Mauna Kea Volcano in lava flows of the Hamakua Volcanics. Lava flows originated from vents widely distributed over the flanks of Mauna Kea and have both alkalic and tholeiitic characteristics. The rocks contain variable amounts of olivine, plagioglase and clinopyroxene phenocrysts (Wolfe and Morris, 1996). Rocks of the Hamakua Volcanics have been Potassium-argon dated between 250 and 65 thousand years (Pleistocene).

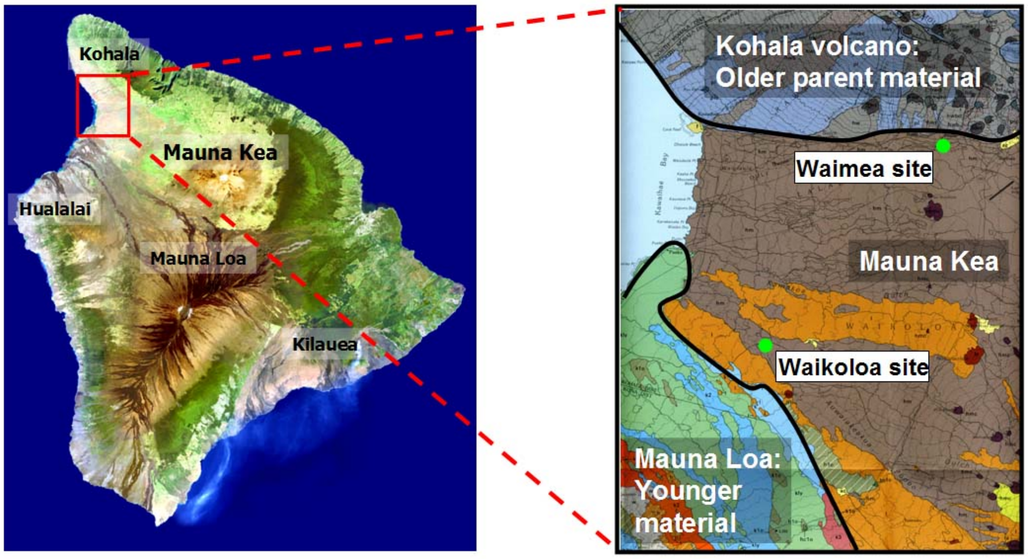

Figure 2.3: Landsat image of Big Island of Hawaii, HI (left). Surface geology map (right) identifying surface lava flows around the UXO study sites of Waimea and Waikoloa. The two sites, identified with green circles are on Mauna Kea surface flows of the similar age. Landsat images and GIS data files available at the Hawaii Statewide GIS Program website: http://www.state.hi.us/dbedt/gis/download.htm; GIS data for surface geology map available at the USGS Hawaiian Volcano Observatory website: http://hvo.wr.usgs.gov/products.

Geomorphology and soils – The parent material of the soils at both sites is basalt, covered by local tephra falls and eolian deposits of variable thickness. Mean annual rainfall ranges from to 150 to 500mm near Waikaloa Village to 1500mm near Waimea. As a result, the soils at the Waimea Geophysical Prove-out are stronger developed than those at the Geophysical Prove-out at Waikaloa Village, where soils are mostly stony and are characterized by surface rock outcroppings and eolian deposit. The Waimea soils are characterized by a shallow organic-rich soil over shallow bedrock. Rocks are common at the surface at both locations.

Magnetic minerals – The primary lithogenic iron oxides in magmatic rocks are Magnetite, Fe_3O_4, Titanomagnetite, $Fe_{3-x}Ti_xO_4$, and Ilmenite, $FeTiO_3$. FeO content for Mauna Kea alkalic basalts ranges from 11.1 to 13.2% (Wright & Clague, 1989).

2.1.2 Field work

The field work occurred from September 20, 2004 to October 1, 2004 in conjunction with two other projects. The first project is SERDP UX-1355: UXO target detection and discrimination using EM differential illumination. The second is the magnetic soil research project at Engineering & Research Development Center (ERDC). Three sites in Hawaii were visited: Navy QA grid on Kaho'olawe, and Waimea and Waikoloa on the Big Island. At each site, we collected both regular soil samples for magnetic susceptibility measurements and oriented samples for measuring remanent magnetization. In addition, magnetic and electromagnetic geophysical data were acquired in the field as part of the effort for the two collaborative projects. The details of the fieldwork are described below.

2.1.2.1 Island of Kaho'olawe

On Kaho'olawe, the soil sampling centered around one of the 30x30 m grids in the Navy QA grid. TEM data collected over Grid 2E showed a strong gradient across the grid (more than 500 mV in Channel 1 data collected with the Geonics EM61-MK2). At this site, samples were collected from the surface as well as from four soil pits, Figure 2.4.

For the surface sampling, a stratified random approach was used. The 30x30 m grid was subdivided into thirty-six 5x5 m smaller grids. In each sub-grid, one sampling location was selected using a random number generator. Locations of all 36 sampling points were surveyed in using a Differential Global Positioning System (DGPS). Four soil pits were dug, and soil samples were collected at different depths. Each pit was excavated with a backhoe and reached bedrock (approximately 1 meter depth). A total of 49 samples were collected from the soil pits (Soil Pit A – 7 samples, Soil Pit B – 15, Soil Pit C – 15 samples, and Soil Pit D – 12 samples)

In addition, 21 oriented soil samples were collected at the Kaho'olawe site. Nine samples were collected from the surface and 12 from the four soil pits. Five of these surface samples were collected from the 30x30 m grid at or near where the surface soil samples were collected.

Magnetic data using the Geometrics G858 in a horizontal gradient mode and TEM data using the Geonics EM61-MK2 and EM63 were collected over the QA grid. In addition, the Geonics EM38 was used to measure ground conductivity and magnetic susceptibilities. Magnetic susceptibilities were also measured at the surface and along the walls of the soil pits with the Bartington MS2 field instrument using the MS2D and MS2F sensors.

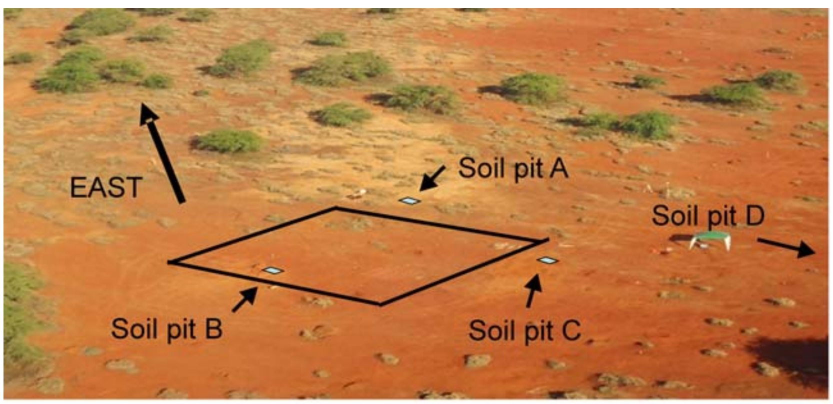

Figure 2.4: Kaho'olawe field site. The top picture shows the location of the soil pits with respect to the 30x30 m grid (outlined in black). Note that soil pit D is located just off the picture. The bottom picture is a panoramic view from the southern corner of the grid.

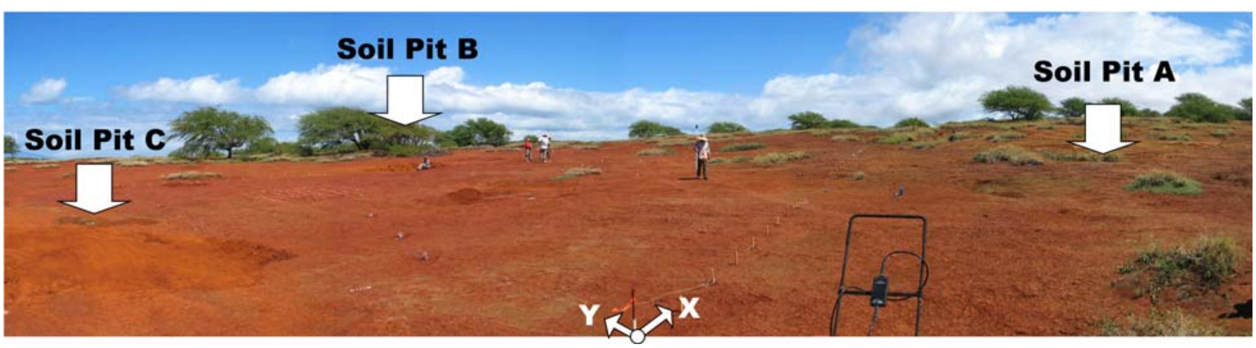

2.1.2.2 The Big Island

Due to safety restrictions soil samples were only obtained from the surface and from the unseeded grid at both the Waimea (Figure 2.5) and Waikoloa (Figure 2.6) sites. The Waimea and Waikoloa GPO areas were similar in grid construction. At each site, a 90x30 m grid had been established. These large grids were then broken down into three 30x30 m sub-grids.

At Waimea, thirty-six soil samples were collected from the surface of the unseeded 30x30 m grid. This grid was then divided into 36 smaller grids (5x5 m) and samples taken using the same approach as on Kaho'olawe. Ten oriented samples were collected at locations coincident with ten of the surface soil sample locations. In addition, six core samples were obtained from two rock outcrops.

Time Domain EM data were collected over the seeded and unseeded grids using the EM61-MK2 and EM63. Horizontal gradient magnetic data were collected over the seeded and unseeded grid at Waimea.

Figure 2.5.: Waimea field site

The soil sampling procedures at the Waikoloa GPO were identical to those used at Waimea. Six oriented samples were collected at this site. Sample locations were coincident with the regular soil samples. Six core samples were also obtained from two rock outcrops at this site.

Figure 2.6.: Waikoloa field site

Total field magnetic data were collected in the same manner as the other Hawaii sites over the unseeded grid. Due to time constraints, a complete geophysical survey was not conducted at this site. Instead, EM63 measurements were taken at each of the 36 soil sample locations.

In total, 156 soil samples were collected for susceptibility measurements, and 37 oriented samples were collected for remanent-magnetization measurements. Accompanying geophysical data were also acquired to supplement those already existing from previous SERDP-funded projects. We now have the basic materials for moving forward to the next phase of research, which will concentrate on analyses of mineralogy of the soil samples, measurement of susceptibility and remanent magnetization of soil samples, and characterize the frequency and spatial dependence of the magnetic properties at these sites.

2.1.3 Geophysical data collections

Numerous geophysical data sets were collected at each site in Hawaii. Total field magnetic data were collected with the Geometrics G858 cesium vapor magnetometer, and magnetic susceptibility measurements collected with the Bartington were made at all three sites. EM61 and EM63 data were collected at Kaho'olawe and Waimea. Due to time constraints only EM63 soundings were collected at Waikoloa. Soundings were taken at each of the soil sample locations.

All magnetic data were collected using a Differential Global Positioning System (DGPS) for data positioning and collected in a horizontal gradient mode. The sensors were spaced a half a meter apart and a 1-meter line spacing was used. Magnetic data were collected using the shoulder strap assembly and were at height of 20-30 cm above the ground. EM data (EM61 and EM63) were collected using a Robotic Total Station (RTS) for data positioning and collected at 1 meter line spacing with a sensor height of 40cm.

The following figures are presented to give a visual indication of the problems faced by remediation efforts in these environments. Figure 2.7 shows data from the EM61-MK2 over grid 2E on Kaho'olawe. Note the large gradient in the data from top to bottom (> 500mV).

Figure 2.8 shows the difference in the magnetic susceptibilities at two frequencies as measured with the Lake Shore Cryotronics, Inc. AC Susceptometer (LACS). Comparison of this figure with Figure 2.7 shows that areas with the largest variation in susceptibility are producing the largest response in the EM data. Soil sample locations were placed on the figure for reference, and soil study results will be discussed in greater detail in the next chapter.

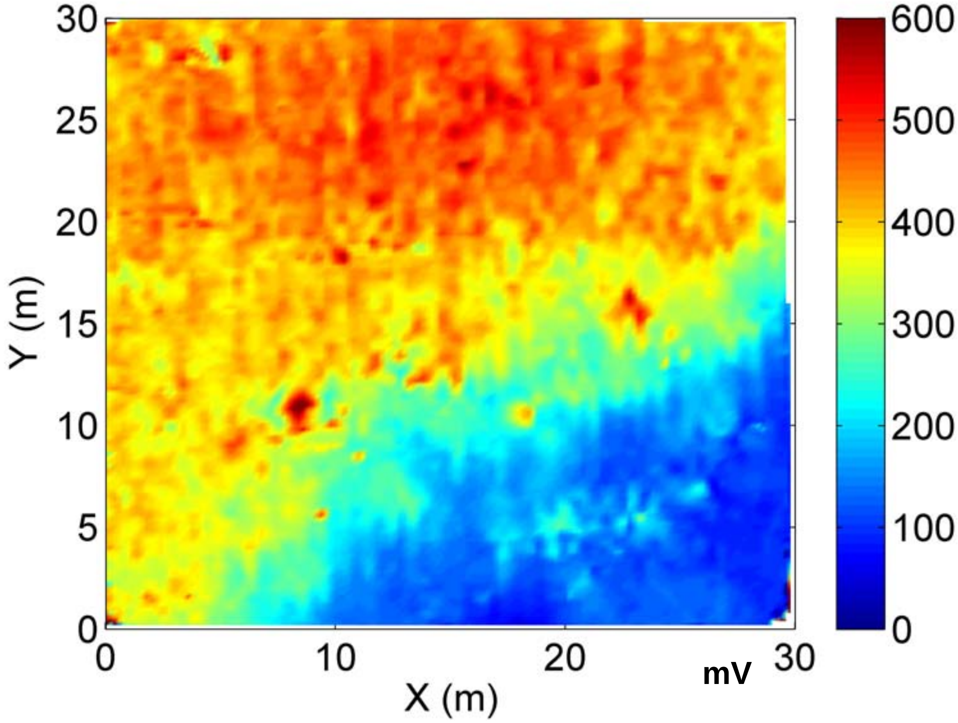

Figure 2.7: EM61 data (Channel 1) collected over grid 2E at Kaho'olawe.

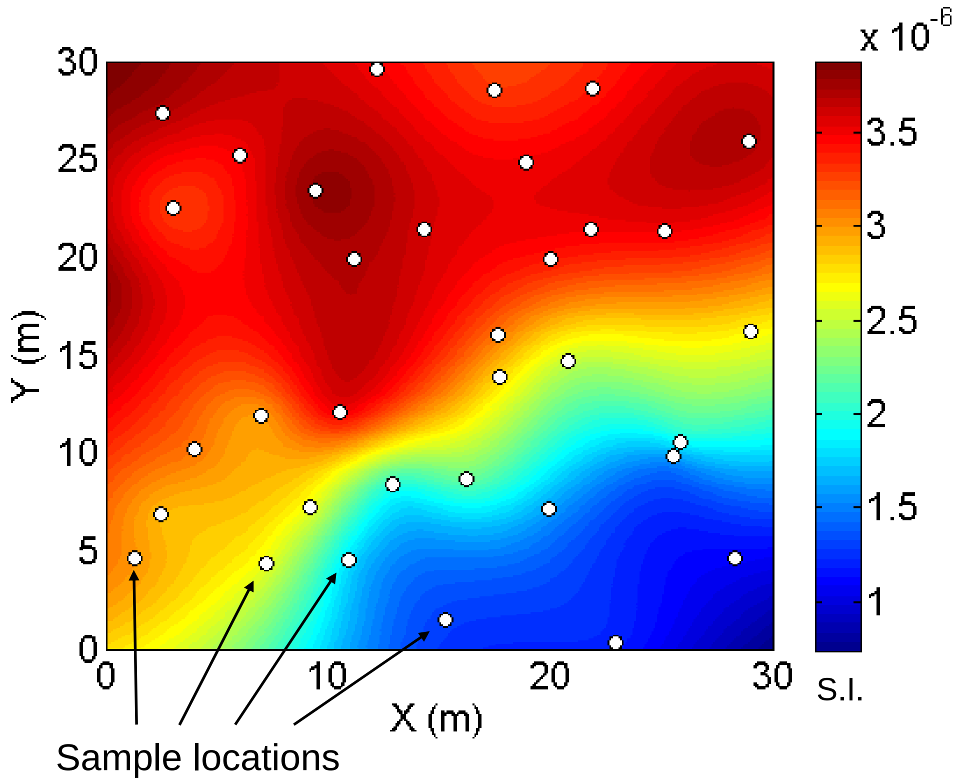

Figure 2.8: Difference in magnetic susceptibility measurements from surface samples collected at grid 2E on Kaho'olawe (LACS 75Hz – 4000Hz).

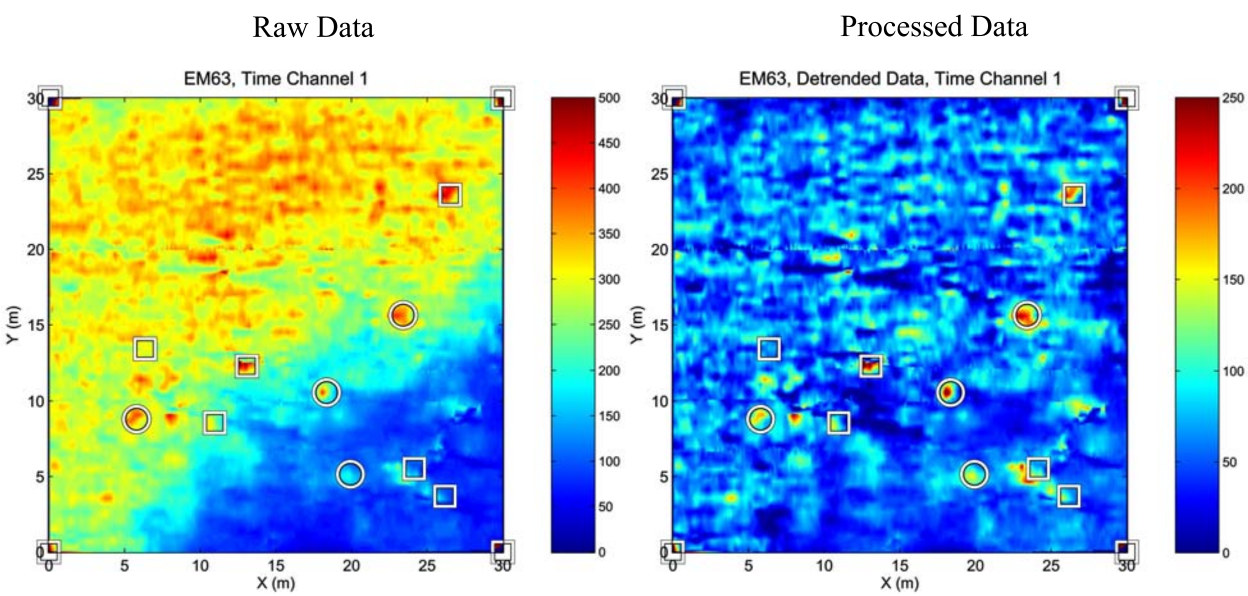

Figure 2.9: EM63 data from grid 2E (circles are ordnance items, squares are metal scrap).

Figure 2.9 shows EM63 data collected by Parsons at grid 2E. This data shows the same gradient as in the EM61 data shown previously (Figure 2.7). Viscous remnant magnetic (VRM) soil model fitting combined with a low-pass spatial filter was used to remove the long spatial wavelength VRM soil response in the processed data.

Figure 2.10 shows the total field magnetic data collected over grid 2E on Kaho'olawe. There is more than 1000nT variation across the grid.

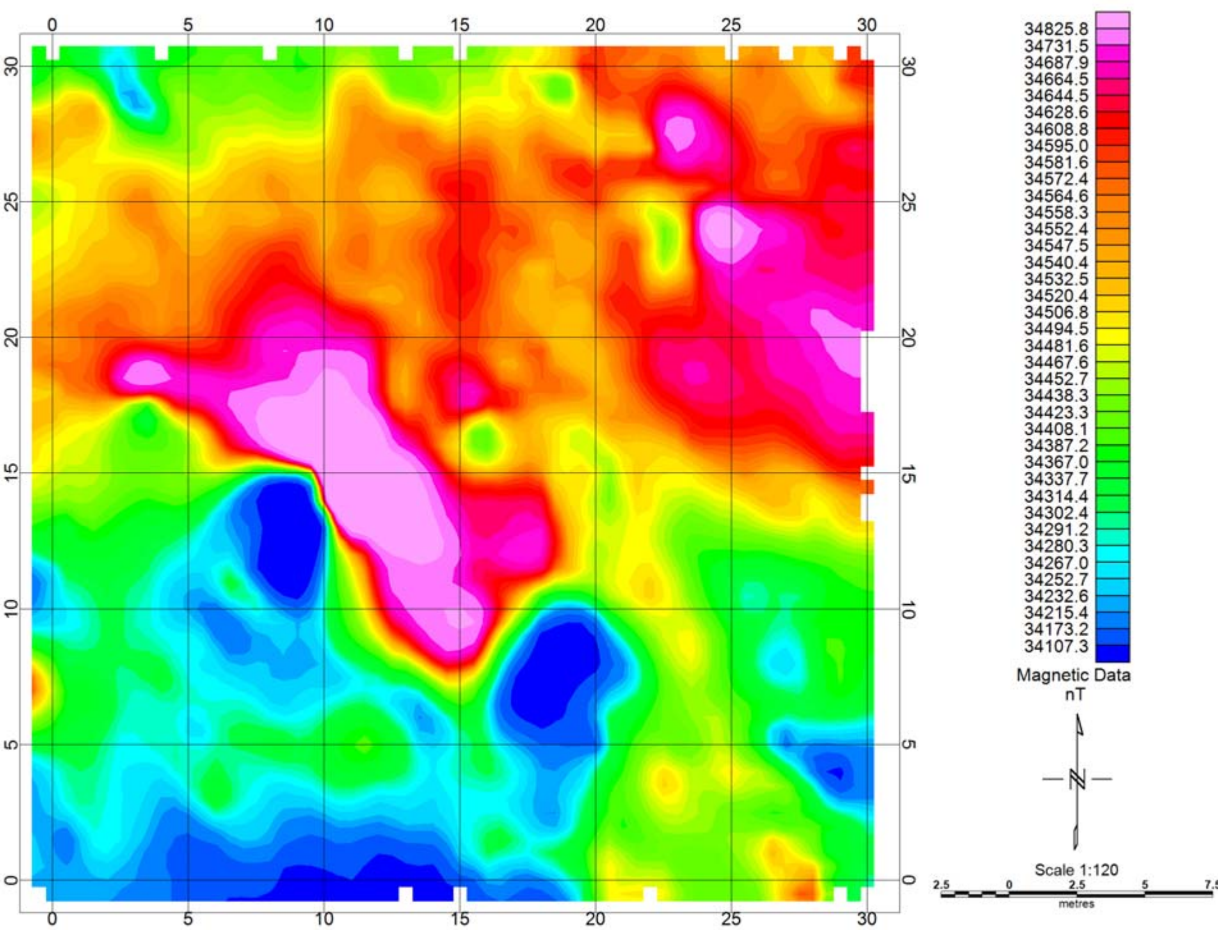

Figure 2.10: The total field magnetic data from Kaho'olawe.

Figure 2.11 shows the total field magnetic data collected at Waimea. Data from Waimea and Waikoloa have been left in UTM Zone 5N coordinates. These data show a > 500nT variation across the grid. Soil sample locations are shown for reference.

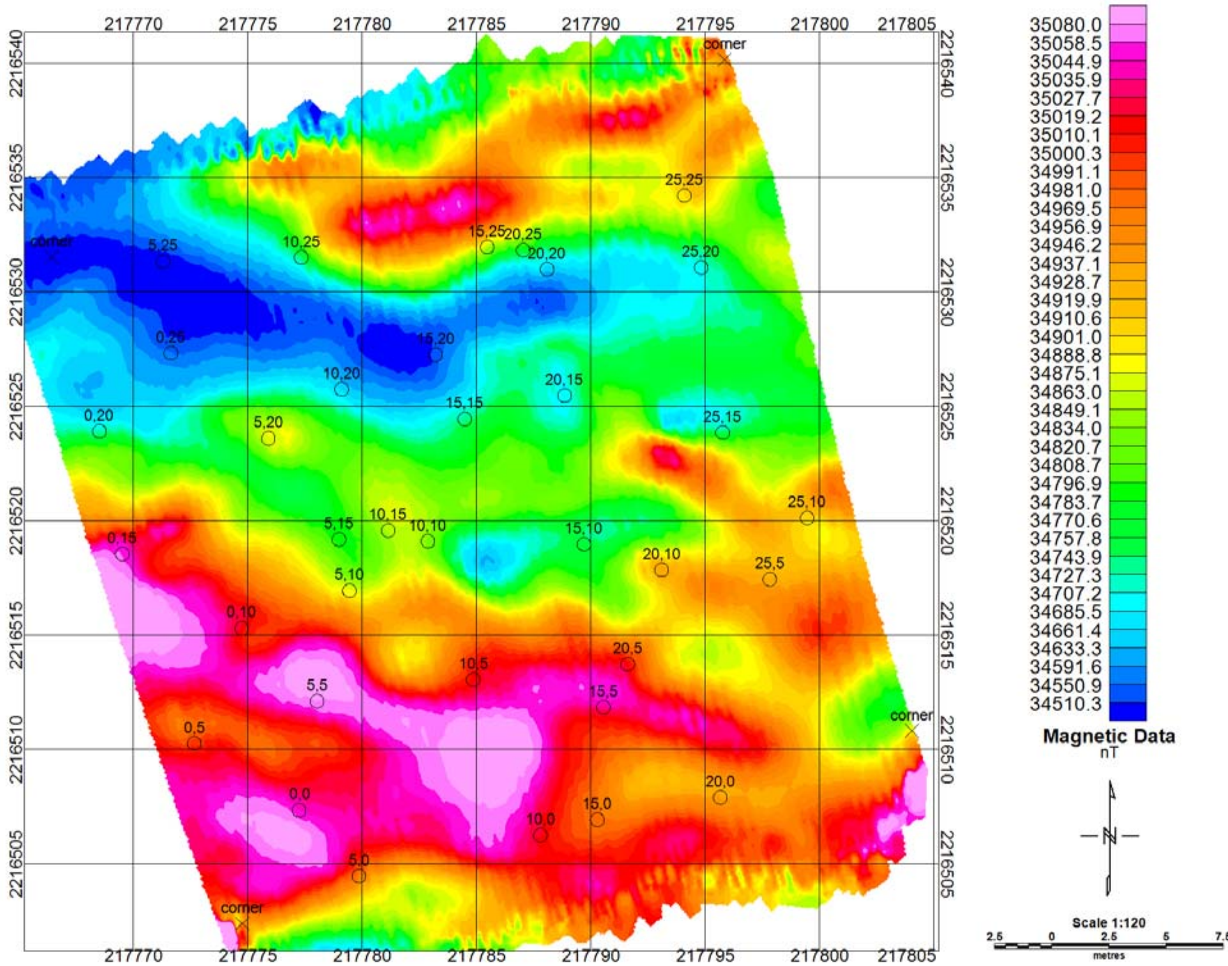

Figure 2.11: Total field magnetic data collected over the unseeded grid at Waimea. Surface soil sample locations are identified with circles and the corresponding sub-grid number.

Total field magnetic data collected at Waikoloa is shown in Figure 2.11. These data show a much larger variation than data at Waimea. The local topography may account for some of this variation as the grid was cut with several small gulleys. Soil sample locations have plotted for reference.

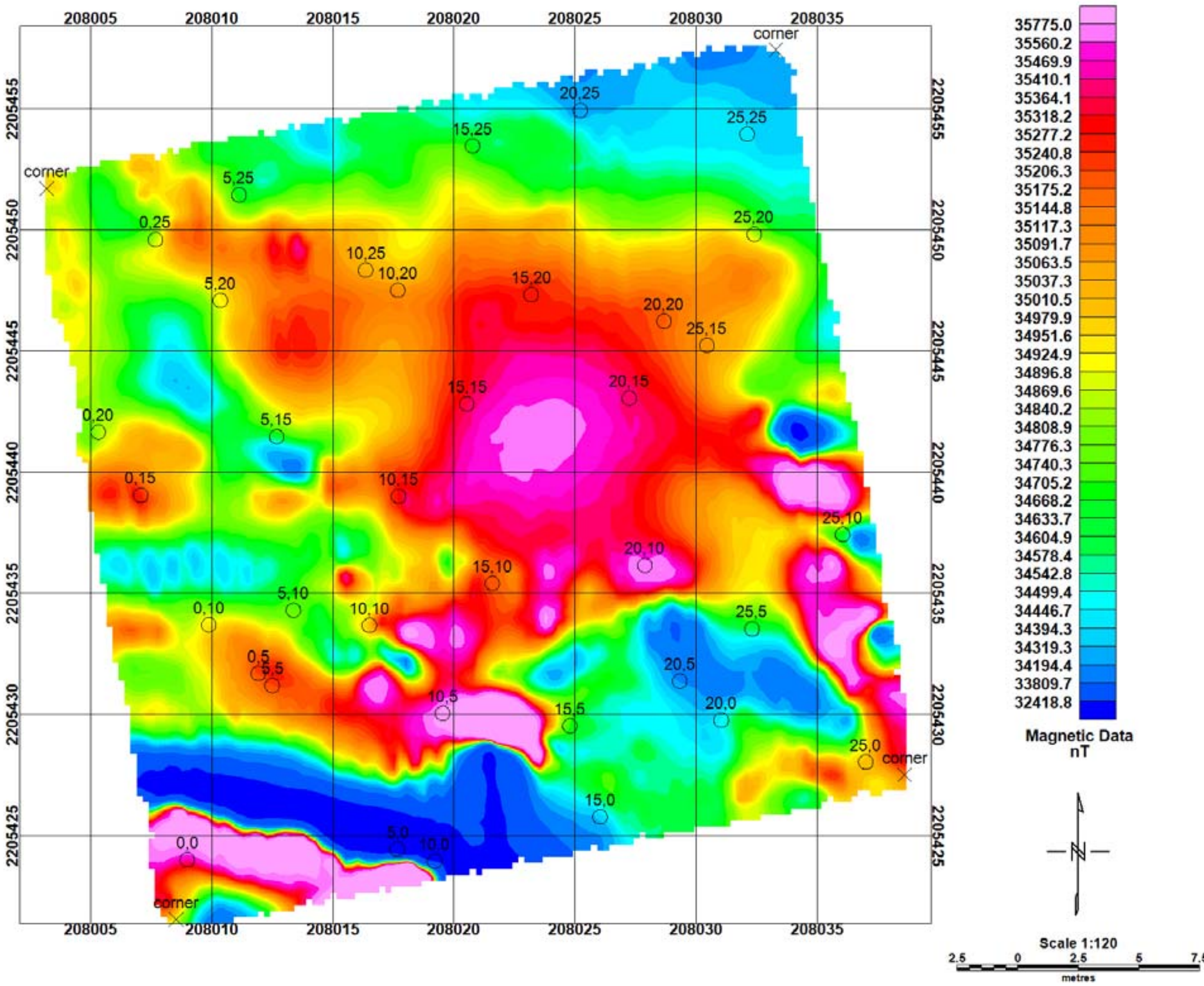

Figure 2.12: Total field magnetic data collected over the unseeded grid at Waikoloa. Surface soil sample locations are identified with circles and the corresponding sub-grid number.

Figure 2.13 shows the EM61 data (Channel 1) collected over the unseeded grid at Waimea. Although there is geologic noise present the total response is much less than recorded at Kaho'olawe.

Figure 2.14 shows the difference in the magnetic susceptibilities at two frequencies as measured with the Bartington MS2F and MS2D. Comparison of this figure with Figure 2.11 shows that there are some similarities between the EM data and susceptibility measurements but not as noticeable as data from Kaho'olawe (Figures 2.7 and 2.8).

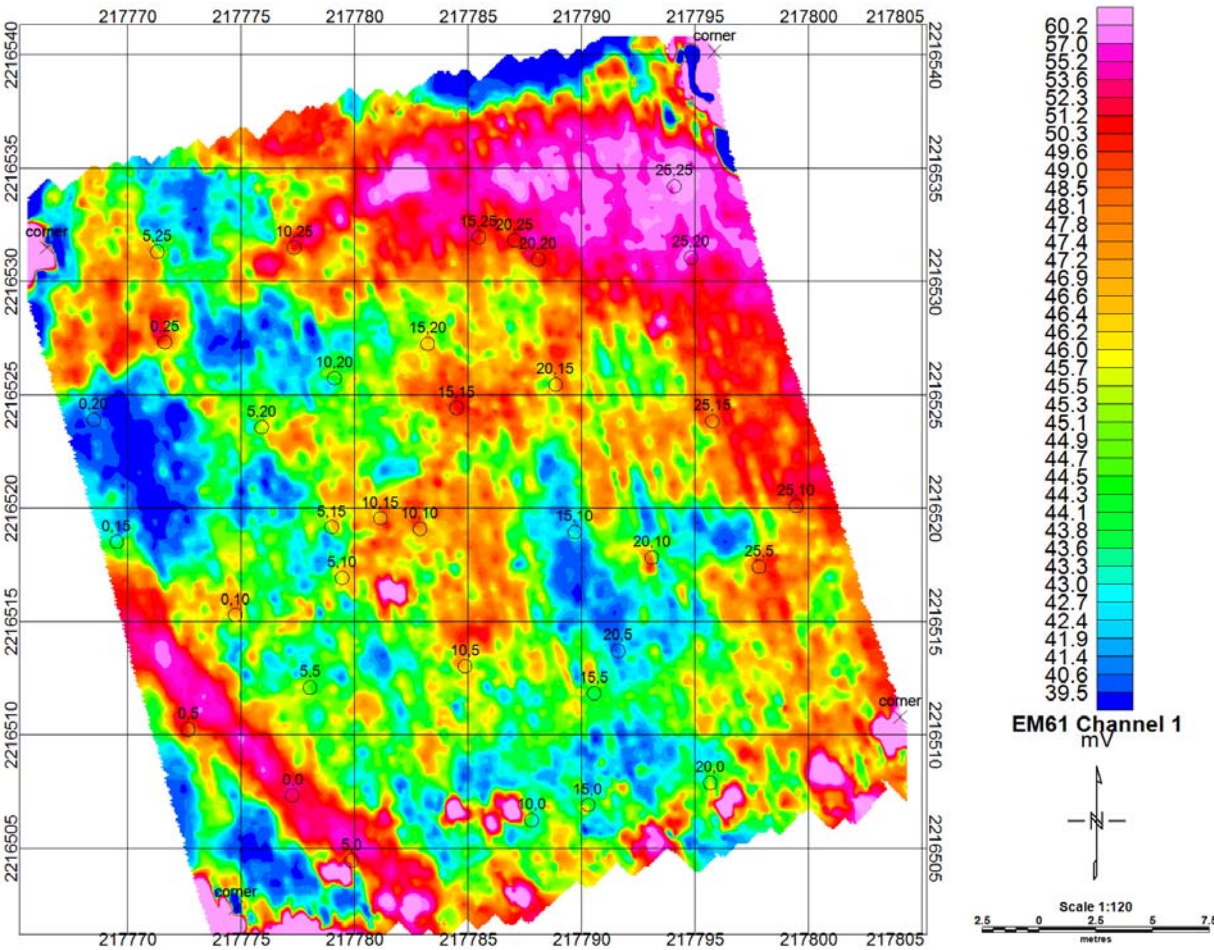

Figure 2.13: EM61 data (Channel 1) collected over the unseeded grid at Waimea. This is the raw data that has only been corrected for position.

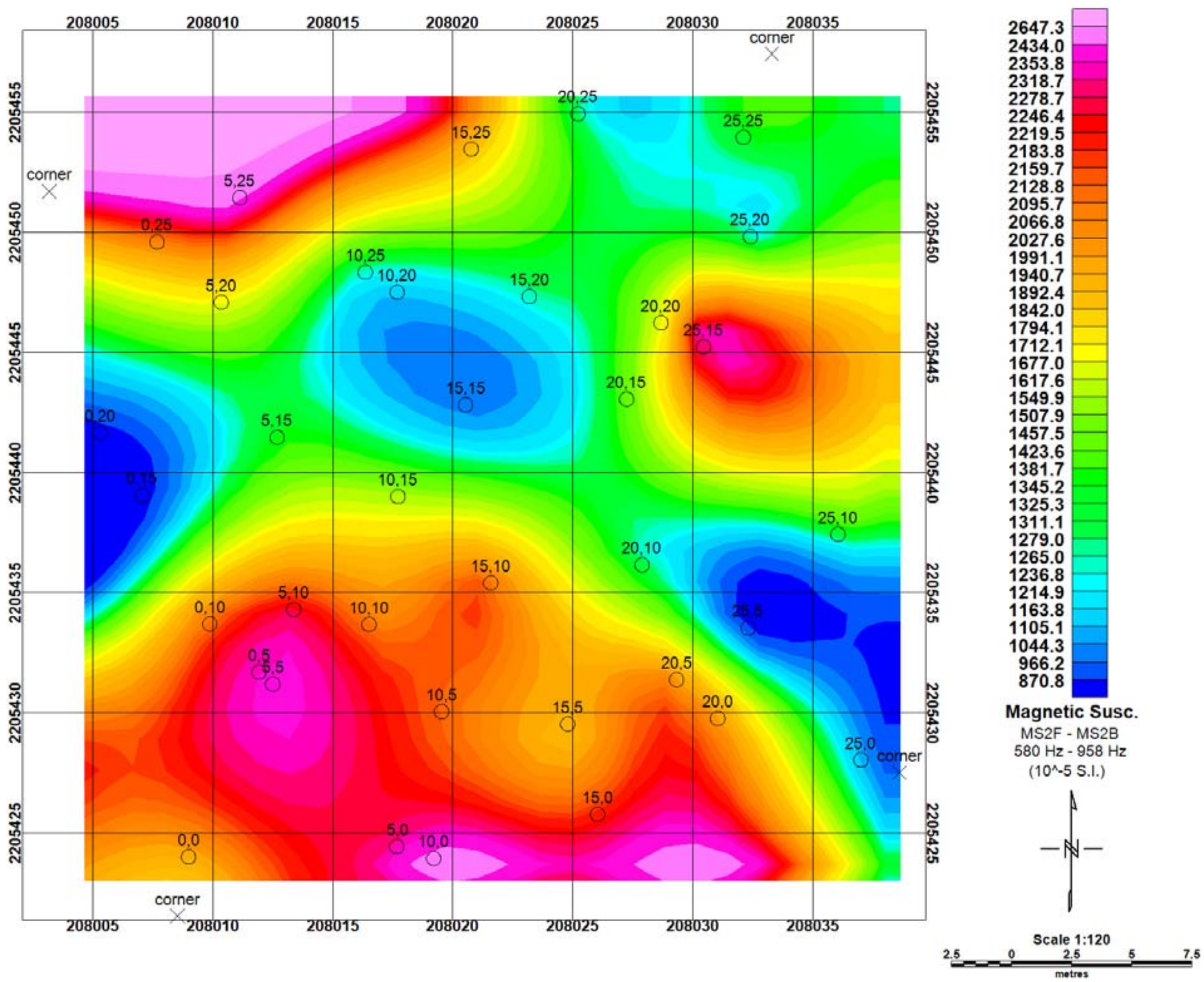

Figure 2.14: Difference in the field measurements (Bartington MS2F and MS2D) of the magnetic susceptibilities at Waikoloa.

2.1.4 Summary

Both sites in Hawaii have soils derived from volcanics and they contain an abundance of magnetic minerals. As a result, the soils are highly magnetic. These sites are among the first where interference of soil response in UXO clearance was encountered. Thus, these sites provide ideal settings for studying the effect of soil magnetism and how to improve UXO detection and discrimination in such environments.

At these two sites, we collected a total of 155 regular soil samples for determining the frequency dependence and spatial variability of soil magnetic susceptibilities. Samples were gathered both from the surface and from soil pits at Kaho'olawe QA2E grid, whereas they were collected only from the surface on the Big Island (Waimea and Waikoloa). 37 oriented samples were collected to study the remanent magnetization of soils at these sites. Both magnetic and electromagnetic data were also acquired at the sites. In addition, field measurements of susceptibility were made using a Bartington susceptibility meter and EM38 ground conductivity/susceptibility meter.

Major effort was expended on laboratory analyses of the soil samples. As expected, all samples show strong magnetic susceptibilities and they are frequency dependent and complex. Specifically, the frequency dependence is consistent with that arising from the presence of a broad range of relaxation times. Within the frequency range of EMI instruments, the real part of the complex susceptibility is a linearly decreasing function with logarithmic frequency and the imaginary part is proportional to the slope of the real part. This is consistent with the theoretical susceptibility model from SEED project UX-1285 that predicted the inverse time decay of measured voltage in time-domain EMI methods.

Mineralogically, high susceptibility values and coinciding strong frequency dependence are correlated with the maturity of soil development. This is typified by the contrast between soil Pit-A and Pit-B near QA2E grid on Kaho'olawe. Less developed soil in Pit-A have weaker susceptibility and frequency dependence, whereas the soil in Pit-B is much more mature as indicated by the coloration and texture. The strong frequency dependence arises from the presence of fine particles derived from weathering. Further supporting this observation is the fact that the susceptibility and its frequency dependence increase towards the ground surface, where the strongest weathering occurs.

The correspondence between the presence of complex susceptibility and strong background EMI responses is typified by the data from the QA2E grid. Within this grid, the frequency dependence of susceptibility increases towards the northwest corner, and so does the EMI response. Thus, the research has confirmed the specific susceptibility model and its presence as the cause for the observed EMI responses that mask the UXO signatures.

Based on these basic understandings and the soil susceptibility model, we have also been able to develop data processing techniques to characterize and remove the soil response. Specifically, fitting the measured EMI data to a theoretic soil response at each station enables us to identify the spatial variation of the data produced by magnetic soil. A low-pass filter based on the spatial variability can be constructed to separate the soil and UXO responses. Although further work is required in the subsequent stages of this project, this approach has already yielded promising result in anomaly detection.

2.2 Montana – Chevallier Ranch

2.2.1 Background and site geology

In May of 2005 geophysical fieldwork and soil sampling were performed at the Chevalier Ranch UXO sites near Helena, Montana. The Chevallier Ranch UXO site, Figure 2.15, has three distinctly different parent materials that vary over short distances. The primary parent material of the Chevallier Ranch UXO site is Precambrian-age Spokane Shale. A 60 to 55 million year old (Paleocene) volcanic intrusion is found in the northwestern area of the Chevallier Ranch UXO survey site. The intrusion is characterized by a large abundance of Fe-Mg minerals (hornblende, pyroxene, olivine, and possibly magnetite). Several narrow (tens of meters) volcanic dikes, characterized by similar material as in the plug, are radiating from the plug. Several of these dikes are found under the survey area. Coarse gravel and cobbles deposited in ephemeral streams that dissect the site form the third type of parent material. The lithology of the deposited material is mostly shale, but occasionally volcanic rock is found as well. All three types of parent material have been found in the study area covering 200 by 200 m^2. The site is located 6 km north of the Scatch Gravel Hills, which is the northernmost part of the Boulder Batholith. Figure 2.16 illustrates a simplified geologic map of the region, along with total field magnetic data collected over the same area. Magnetic data verify the presence of these volcanic intrusives.

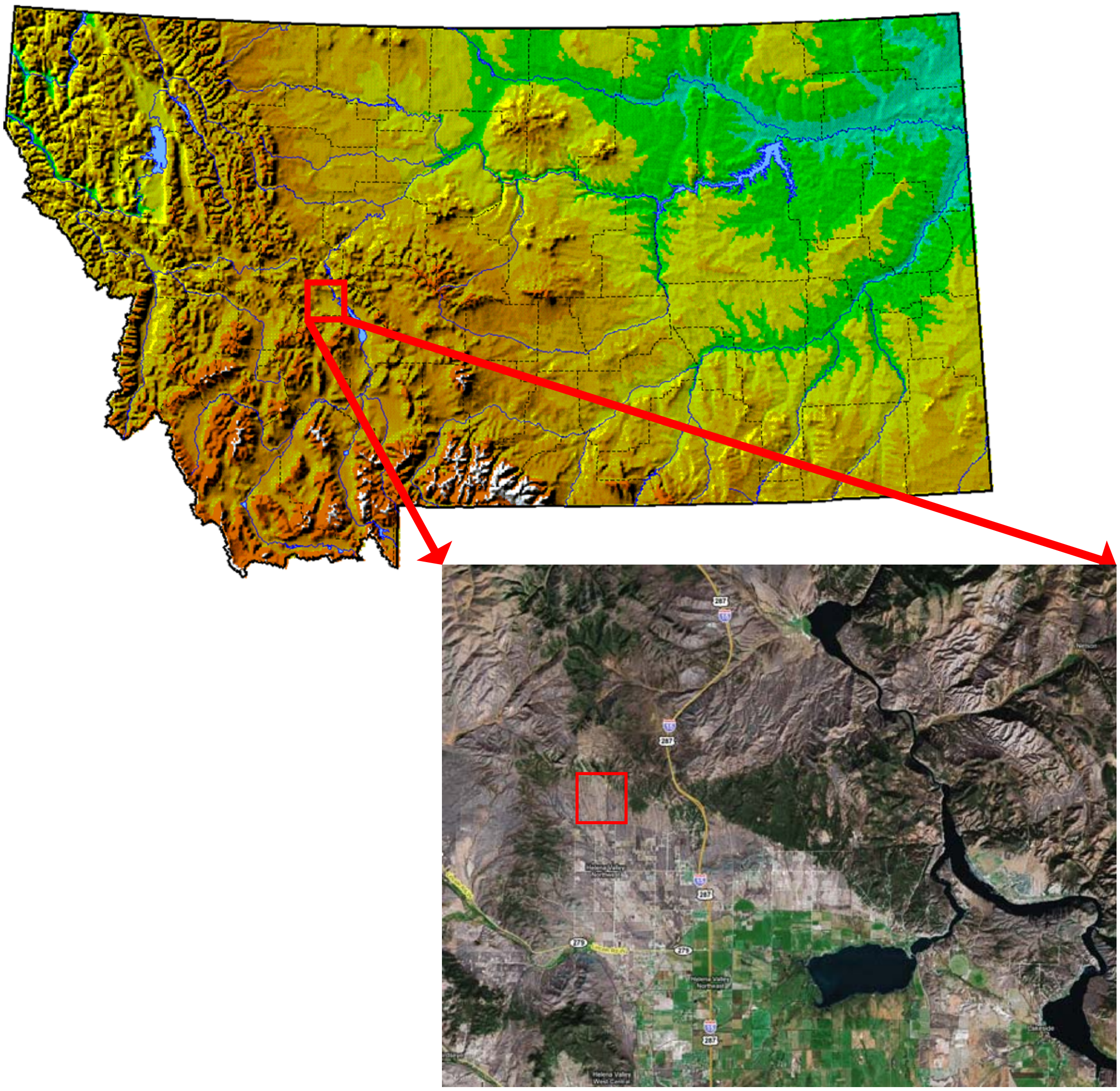

Figure 2.15: The Chevalier Ranch field site in Helena Montana (top image retrieved from www.geology.com, bottom image from www.maps.google.com)

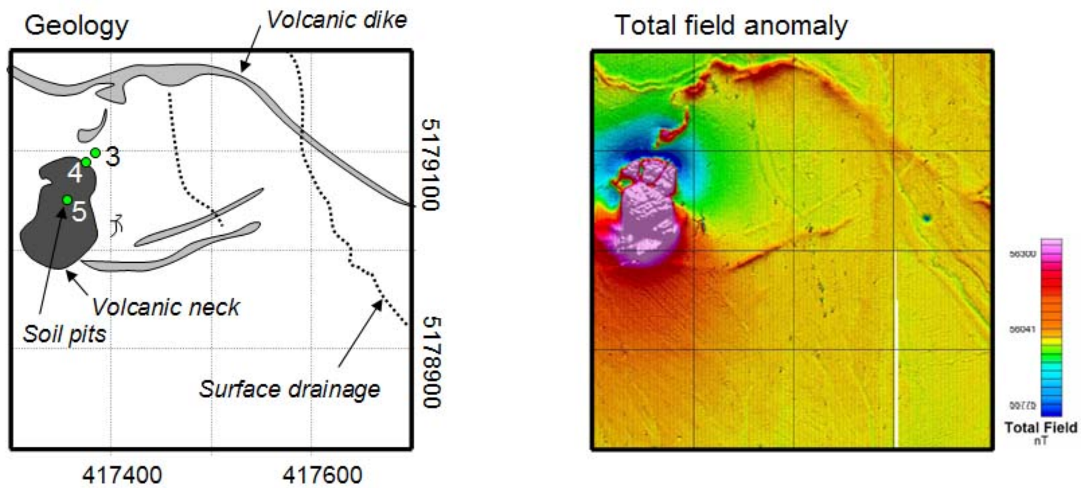

Figure 2.16: Simplified geologic map of the Chevalier Ranch survey site (left). Total field magnetic data (right) show volcanic neck and subsurface dikes with difference in total field strength.

Geomorphology and soils – The survey area is a broad open plain that ranges in elevation from 1270 to 1340 m and gently slopes off toward the south to south-southeast. Several ephemeral streams dissect the area. These streams may be collection areas for heavy minerals such as magnetite, as evidenced by the small black-sand lag (or placer) deposits in the drainage channels. Alternatively, channel erosion may lead to a smaller depth to bedrock, which in the case of a volcanic dike may cause a higher magnetic background signal. The vegetation at the site is predominantly sage brush, grass, and some pine trees. Most of the gridded site has a 3-4 degree slope towards the southeast. Outcrops of shale are found in several locations, especially along streams and on a small hill at the NW of the study site (parking location).

Magnetic minerals – The magnetite source is most likely the Paleocene basalt intrusion and associated dikes, northwest of and below the survey area, respectively. This intrusive material is rich in Fe and Mg minerals (hornblende, pyroxene, and olivine). The distribution of ferrimagnetic grains is related to the type of parent material, the depth to bedrock, and redistribution of weathered material by surfacial processes.

2.2.2 Field work

The 200x200m area of the Chevalier Ranch site that has been cleared of UXO was selected for detailed geophysical surveying and soil characterization work. This area was selected because it contained a suite of geologic responses that have been identified as problematic for the magnetic surveying performed during the clearance activities at Chevalier Ranch. The geologic responses can be broken into four classes: 1) area of intense magnetic response (>2000nT anomaly) associated with a 100x100m basalt intrusive, 2) extensive linear monopolar anomalies (>50m strike length, ~100 nT anomaly) likely associated with deeper mafic dykes, 3) linear dipolar anomalies which are spatially compact (< 5m strike length, ~100-200nT anomaly) with a character that could be interpreted as a UXO response, and 4) linearly extensive weak magnetic responses associated with drainage features (< 20nT anomaly). Each of these responses has the potential to mask or distort the response of a UXO.

We have excavated 7 soil pits and 2 trenches that cover most of the relevant magnetic geology. This includes the magnetic plug and dikes, on the Spokane Shale, in the ephemeral streams, and on topographic highs and in topographic lows. The soils are highly variable over short distances and reflect their parent material and relative position in the landscape. The mostly young soils are generally weakly developed, reflecting the slow soil-forming conditions. Most soils have a thin organic horizon and are characterized by carbonate precipitation in the B and C horizons, typical for desert-like conditions. In most soils clay content is low and gravel content, which increases with depth, is up to 40%.

We have collected 43 samples from the 7 soil pits at the test site. Sampling depths have been selected based on soil horizonation. In two small trenches, which cross small linear dipolar anomalies, we have collected 2x15 samples in a grid-type layout. Over a 15x175m section of the study site that has been used for detailed geophysical measurements, we have collected 142 surface samples. The samples were collected at 5 meters distance along four north-south trending lines. Soil composition on the surface and in the pits (loose and gravelly) prevented the acquisition of oriented soil samples.

The magnetic susceptibility of all soil samples has been measured at two frequencies using a Bartington MS2B sensor in the laboratory. Preliminary magnetic susceptibility measurements show that soils at the Chevalier Ranch have much lower susceptibilities than those from Kaho'olawe. The soil material is characterized by a low frequency dependence, regardless of the parent material and soil horizon. The low-frequency magnetic susceptibility (or induced magnetization) is strongly correlated with the parent material.

In addition, in-phase component data were collected in the field with the Geonics EM38 coupled with Differential Global Positioning Satellites (DGPS) in a meandering path over the four features described at the start of Section 2.2.2. Small variations in the recorded field values were noted in the field, most notably across feature-2.

The Montana Air National Guard emplaced 20 76mm projectiles within the various geologic areas of interest. Full coverage (0.5 line spacing) magnetic data was collected over each area. The features that obscured the UXO the most were the basalt plug (due to sheer amplitude of response) and the compact dipolar anomalies (similar character as a UXO). Areas in which magnetics had difficulty were selected for surveying with EMI instruments. EM61 data was collected over areas containing features-1, 3 and 4 described above. GEM-3 data was collected over the most problematic area of the basalt intrusive. In each case the EMI instruments were able to detect the emplaced rounds. The magnetic geology (basalt intrusive) appears to have some effect on the EMI instruments, though not enough to mask the UXO response.

A summary of the data collection carried out at Chevalier Ranch in May 2005 is presented in Figure 2.17. The gridded image is the total field magnetics data collected during clearance operations in 2002 by G-Tek. The black polygons represent four areas (labeled A, B, C and D) selected for geophysical surveying. The cyan squares represent the location of emplaced ordnance (all 76mm projectiles). The white circles represent the location of soil pits. The pits are labeled CR1-CR9. Two pits (CR6 and CR7) were located to the south of area A and are not shown on the summary map. Surface soil samples were collected over area A on a grid with 5m sample spacing. All data are plotted in NAD83 UTM Zone 12.

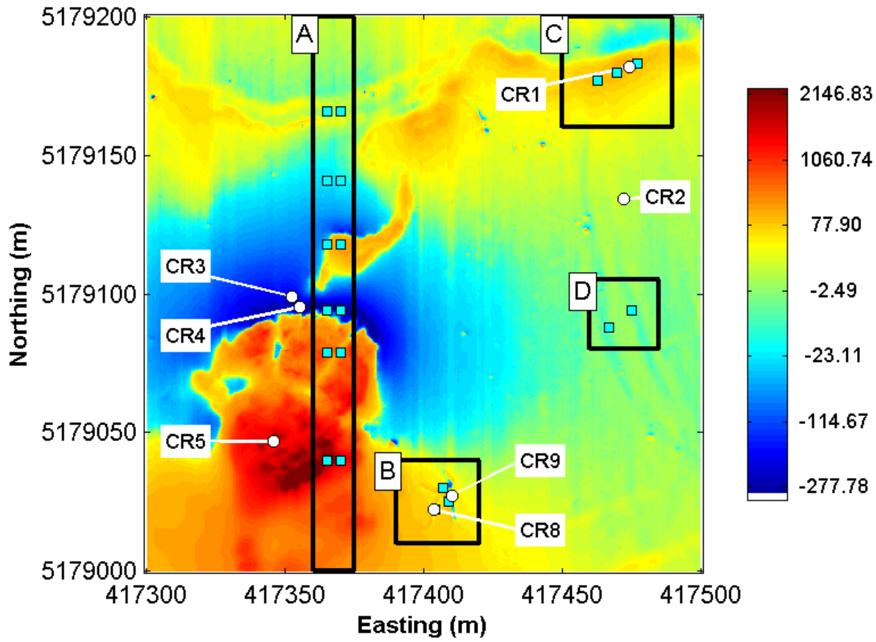

Figure 2.17: Summary of data collection at Chevalier Ranch. Gridded total field magnetics data is in nanoTeslas. The four black polygons are areas selected for geophysical surveys. The cyan squares are the locations of emplaced UXO. The white circles represent the locations of soil pits.

2.2.2.1 Geophysical Surveys Performed

The geophysical data collection at Chevalier Ranch consisted of total field magnetic, time domain electromagnetic (EM) and frequency domain EM surveys.

2.2.2.1.1 Total Field Magnetics

Total field magnetic surveys utilized the Sky Research man portable magnetometer array consisting of four Geometrics G-823 optically pumped cesium vapor magnetometers for survey data acquisition (Figure 2.18), and a G-856AX1 proton precession magnetometer for base station measurements. The G-823 measures the intensity of the Earth's magnetic field in nanoTeslas (nT). At Chevalier Ranch, the magnetic intensity is approximately 55,700 nT. The G-823 sensor separation was 0.5 m covering a 2.0 m data swath. The G-823 system was configured to stream data at ten samples per channel per second (10 Hz). At a nominal traverse rate of 0.76 m per second, this equates to approximately one sample per 0.07 - 0.1 m of forward advance. A Trimble 5800 RTK GPS system was deployed for sensor positioning. All of the magnetic data were collected and managed using the propriety Sky Logger Data Acquisition System (DAS). Areas A, B, C and D were all surveyed using the Sky Research magnetometer array.

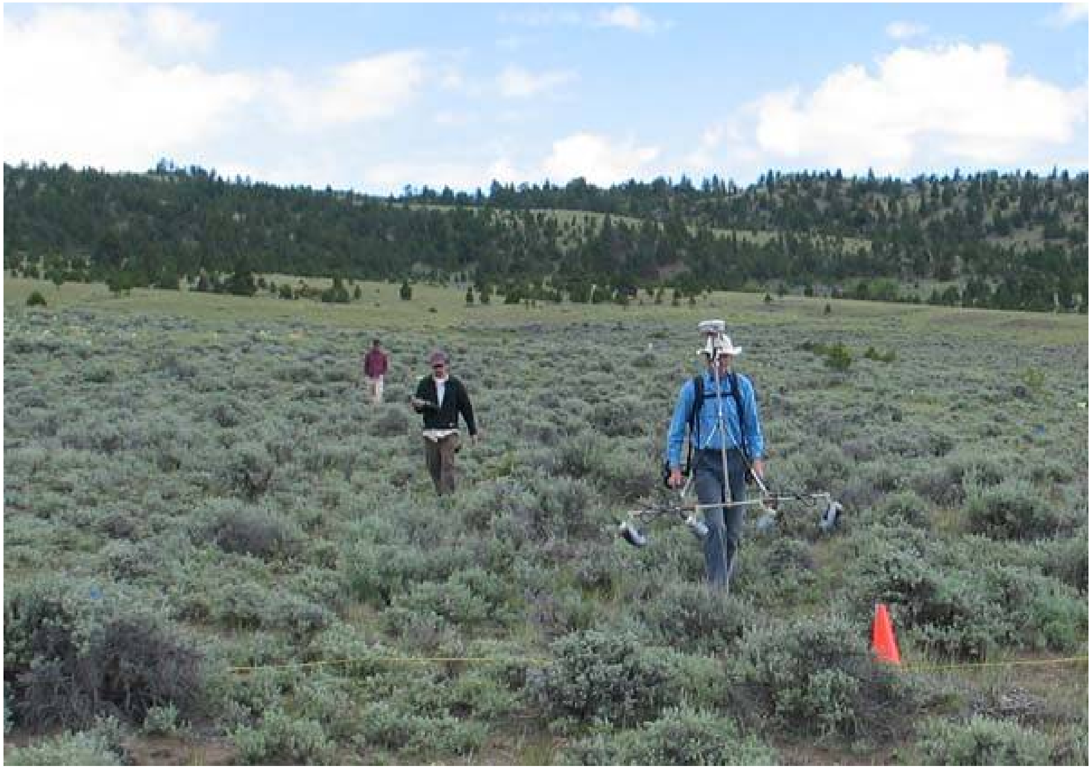

Figure 2.18: Magnetics data collection using the Sky Research magnetometer array at Chevalier Ranch, Montana.

As part of the magnetics surveying a set of calibration tests were performed. These tests included a lag test and an octant test. The lag test was performed along a North trending line approximately 6 m in length. A board with a thin steel wire was placed at the mid-point of the segment and the magnetometer array was walked forward and then backward along the 6 m line. The lag test is used to calculate the time slew value to precisely merge the magnetometer sensor data with the positional information from the GPS. The magnetometer profiles for the data collected in the two different directions will only line up when the time slew is adjusted to its correct value. The octant test is performed in order to quantify the effect of the orientation of the various sensors in relation to the console electronics and the operator. A total of eight lines of magnetic data are collected, passing over the same central point where a target is located. The lines are oriented S-N, N-S, SE-NW, NW-SE, E-W, W-E, NE-SW, SW-NE. The difference in the response over the central point documents heading effects and is used to calculate a heading correction.

2.2.2.1.2 Time Domain EM

Time domain EM surveys were carried out using the Geonics EM61-MK2. Due to the variable terrain and vegetation on the Chevalier Ranch site, it was only possible to survey one 50x15m section of Area A using the wheeled cart mode. For the remainder of the surveys the EM61 was deployed in stretcher mode. A Trimble 5800 RTK GPS system was deployed for sensor positioning. Surveys were conducted using 0.5m line spacing and a nominal measurement height of 40cm. Areas A and C were surveyed with the EM61.

As part of time domain EM surveying, a set of calibration tests were performed. These tests included a static test and a lag test. During the static test a measurement was performed with the EM61 elevated above the ground. The purpose of this measurement is to get a source-free measurement at the beginning and end of the survey in order to estimate and correct for the presence of time dependent instrument drift. It also provides an estimate of the background response that can be removed from the data. The particular EM61 used during this survey appeared to drift more than usual and therefore multiple static measurements were collected throughout surveying to better correct for drift. The lag test was the same as the one performed during magnetics survey except that the object was a copper loop.

2.2.2.1.3 Frequency Domain EM

Frequency domain EM surveys were carried out using the Geophex GEM3. The GEM3 was deployed in hand held mode (Figure 2.19). Due to time constraints only a small (15x15m) section of Area A was surveyed with the GEM3. There was minimal vegetation in the survey area and a nominal sensor height of 25cm was maintained throughout the survey. The line spacing was 0.5m. A Trimble 5800 RTK GPS system was deployed for sensor positioning.

Figure 2.19: GEM3 data collection at Chevalier Ranch.

As part of frequency domain EM surveying a set of calibration tests were performed. These tests included a static test, a ferrite rod calibration and a lag test. During the static test a measurement was performed with the GEM3 elevated above the ground. The purpose of this measurement is to get a source-free measurement at the beginning and end of the survey in order to estimate and correct for the presence of time dependent instrument drift. It also provides an estimate of the background response that can be removed from the data. During the ferrite rod calibration a measurement is made directly over a ferrite rod. The GEM3 response, after the background response is removed, should be a pure susceptibility response. This will consist of zero quadrature and a constant negative inphase at all frequencies. The lag test was the same as the one performed during the magnetics survey except that the object was the ferrite rod.

2.2.2.2 Description of Survey Areas and UXO Emplacement

A description of each of the four areas selected for geophysical surveying is provided below. A table summarizing the details of the emplaced UXO is provided in Table 2.1. Locations of the survey areas are illustrated in Figure 2.17.

<u>*Area A*</u>

This is a 200x15m swath crossing the volcanic plug geologic feature. Six pairs of ordnance were emplaced at various locations along the swath. One of the pair was emplaced at an azimuth of 0 and one at 90 degrees. Each location represents a different magnetic regime. From North to South these regimes are; 1) a weak magnetic anomaly due to drainage (A1-E, A2-E), 2) a non-magnetic background (A3-E, A4-E), 3) a moderately magnetic background due to intrusive geology (A5-E, A6-E), 4) a dipolar low at edge of magnetic plug (A7-E, A8-E), 5) a highly magnetic response within the volcanic plug (A9-E, A10-E), and 6) an extremely high magnetic response within the magnetic plug (A11-E, A12-E).

<u>*Area B*</u>

This is a 30x30m area covering a group of radiating dipolar geologic anomalies. The area was selected because this type of anomaly is common in the Chevalier data and they cause problems when picking targets. Their finite strike length and dipolar nature make it difficult to definitively discount the presence of UXO. By emplacing three UXO within these anomalies we plan to improve our methodology for discriminating between geology and UXO. The UXO are labeled (B1-E, B2-E and B3-E).

Table 2.1: Summary of UXO Emplacement. The round type 76mm APT stands for Armor Piercing Tracer and 76mm TPT stands for Training Practice Tracer. A declination of 0 denotes horizontal, NU denotes nose up and ND denotes nose down. Ordnance marked with * were found at Chevalier Ranch.

Round ID #	Easting	Northing	Orientation	Round Type	Depth	Azimuth	Declination
A1-E	417365	5179040	Parallel to Earth's field	76mm APT*	6 cm	180 deg	8 deg ND
A2-E	417370	5179040	Perpendicular to Earth's field	76mm APT*	13 cm	270 deg	0 deg
A3-E	417365	5179079	Parallel to Earth's field	76 mm APT*	15 cm	0 deg	0 deg
A4-E	417370	5179079	Perpendicular to Earth's field	76 mm APT*	15 cm	270 deg	2 deg ND
A5-E	417365	5179094	Parallel to Earth's field	76mm APT*	18 cm	0 deg	0 deg
A6-E	417370	5179094	Perpendicular to Earth's field	76mm APT*	17 cm	270 deg	15 deg ND
A7-E	417365	5179118	Parallel to Earth's field	76mm APT*	17 cm	0 deg	8 deg ND
A8-E	417370	5179118	Perpendicular to Earth's field	76mm APT*	5 cm	270 deg	8 deg NU
A9-E	417365	5179141	Parallel to Earth's field	76mm APT*	15 cm	180 deg	0 deg
A10-E	417370	5179141	Perpendicular to Earth's field	76mm APT*	19 cm	90 deg	0 deg
A11-E	417365	5179166	Parallel to Earth's field	76mm APT*	17 cm	0 deg	18 deg ND
A12-E	417370	5179166	Perpendicular to Earth's field	76mm APT*	15 cm	270 deg	0 deg
B1-E	417409	5179025	Parallel to Earth's field	76mm TPT	14 cm	0 deg	0 deg
B2-E	417407	5179030	Perpendicular to Earth's field	76 mm APT	10 cm	90 deg	0 deg
B3-E	417404	5179022	Random	76 mm APT	4 cm	30 deg	12 deg NU
C1-E	417463	5179177	Parallel to Earth's field	76 mm APT	11 cm	0 deg T	0 deg

C2-E	417470	5179180	Perpendicular to Earth's field	76 mm TPT	9 cm	90 deg	0 deg
C3-E	417477	5179183	Random	76 mm APT	9 cm	82 deg	8 deg NU
D1-E	417475	5179094	Parallel to Earth's field	76mm TPT	6 cm	0 deg	1 deg NU
D2-E	417467	5179088	Perpendicular to Earth's field	76mm TPT	6 cm	270 deg	0 deg

<u>*Area C*</u>

This area is a 40x40m area covering a magnetic high dyke. We have defined three points along the dyke to emplace UXO. The area was selected to test our ability to detect UXO within large background magnetic fields. The UXO are labeled (C1-E, C2-E and C3-E).

<u>*Area D*</u>

This area is a 25x25m area covering two linear drainage related magnetic anomalies. The area was selected to test our ability to differentiate drainage anomalies from subtle UXO responses. The UXO are labeled (D1-E and D2-E).

2.2.2.3 Soil Descriptions

Soils at the Chevallier Ranch are very hard, dry to slightly moist at depth, with a defined, leached calcic layer at the lower B to upper C horizon, and small shale/argillite chips 0.25 to 0.5 inch in size (derived from the Proterozoic-age Spokane Shale). The mostly young soils are generally weakly developed, reflecting the slow soil-forming conditions (Van Dam *et al.*, 2006). Most soils have a thin organic horizon and are characterized by carbonate precipitation in the B and C horizons, typical for desert-like conditions. In most soils clay content is low and gravel content, which increases with depth, is up to 40%. The soils are highly variable over short distances and reflect their parent material and relative position in the landscape. Soil horizon descriptions are given in the next chapter in more detail.

2.2.3 Geophysical data collections

<u>Area A</u>

Figure 2.20 shows the magnetics and EM61 data over the southern half of Area A (5179000N to 5179100N). The top left panel has been split so that the data can be presented with separate colour scales. This part of area A covers the complex high amplitude magnetic feature associated with volcanic plug. Only one of the UXO can be detected in magnetics data (A7-E, the top-left circle). The response is visible on the edge of the plug. The ordnance next to it (A8-E) is lost in the dipolar low. The other four ordnance are completely overwhelmed by the amplitude of the magnetic response of the volcanic plug. We see from the EM61 data that all six ordnance are easily detected. It also appears that there is some “geologic” response at 5179050N. It is interesting to note that this EMI “geologic” response does not correlate with any obvious feature in the magnetics.

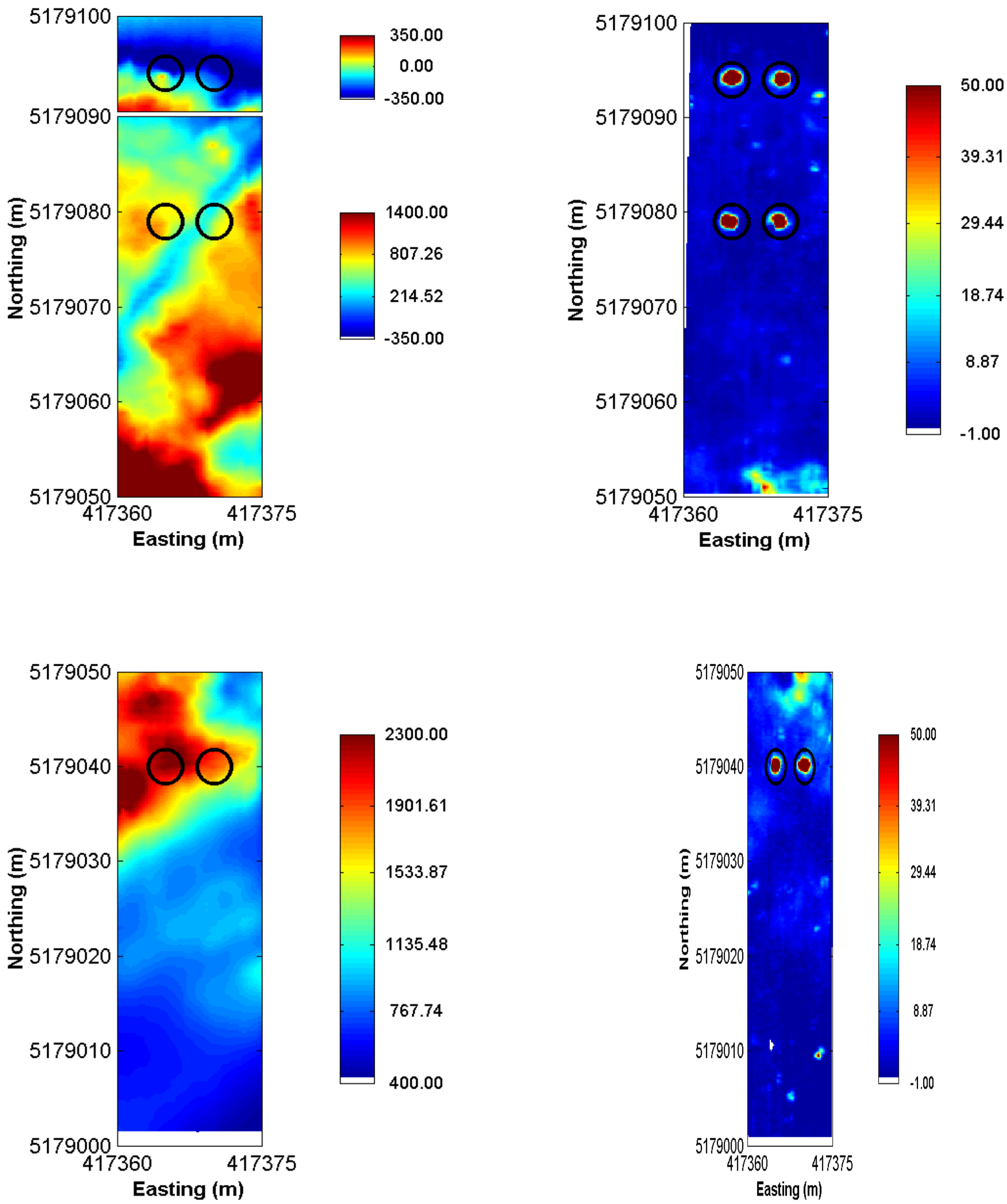

Figure 2.20: Magnetics and EM61 data over the southern half of Area A (5179000N to 5179100N). Left column: total field magnetics data in nanoTeslas. Right column: Channel 1 EM61 data in mV. Top row: surveys from the northern part of the area (5179050N to 5179100N). Bottom row: surveys from the southern part of the area (5179000N to 5179050N). Black circles indicate the location of emplaced ordnance.

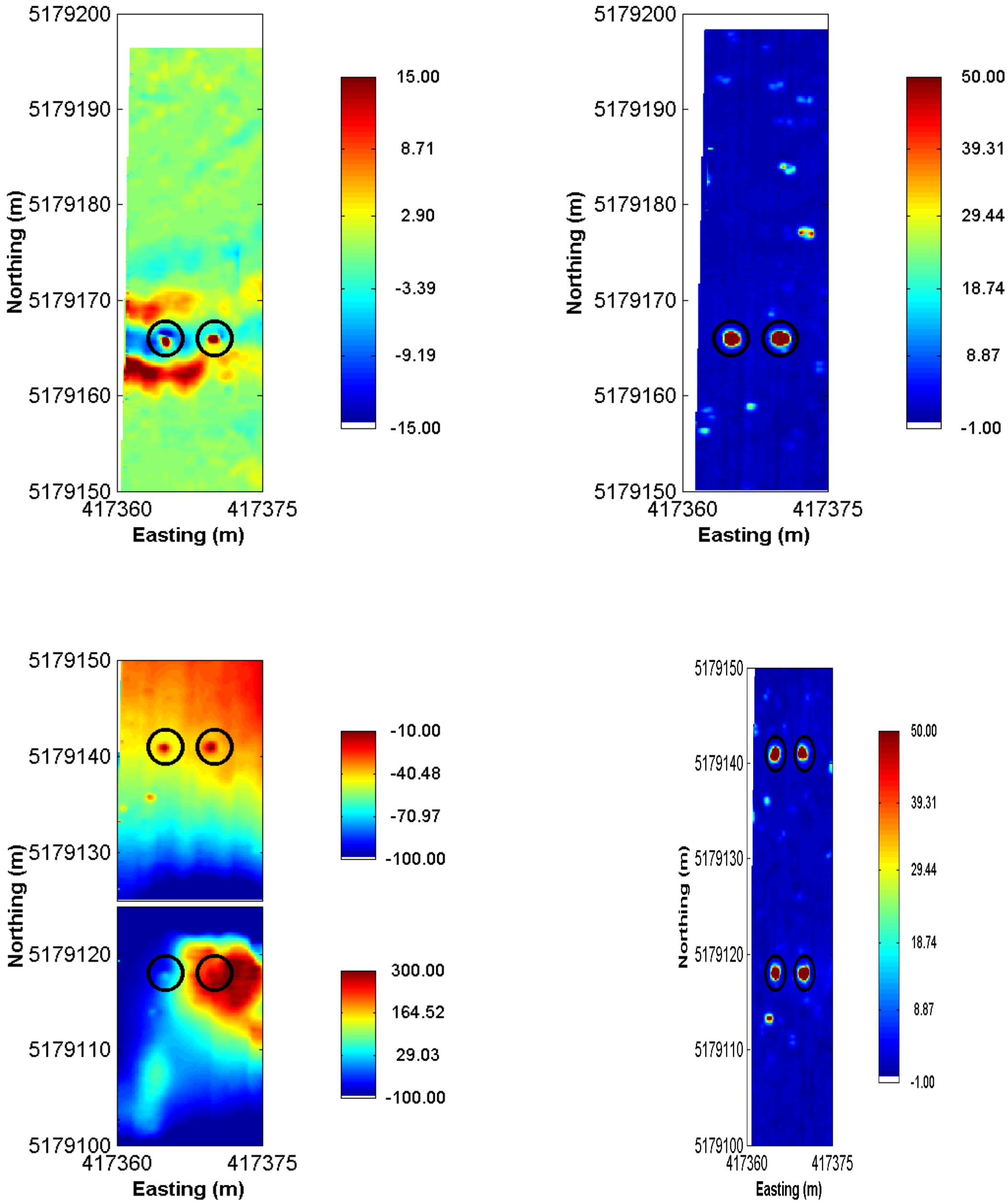

Figure 2.21: Magnetics and EM61 data over the northern half of Area A (5179100N to 5179200N). Left column: total field magnetics data in nanoTeslas. Right column: Channel 1 EM61 data in mV. Top row: surveys from the northern part of the area (5179150N to 5179200N). Bottom row: surveys from the southern part of the area (5179100N to 5179150N). Black circles indicate the location of emplaced ordnance.

Figure 2.21 shows the magnetics and EM61 data over the northern half of Area A (5179100N to 5179200N). The bottom left panel has been split so that the data can be presented with separate colour scales. This part of area A covers the complex high amplitude magnetic feature associated with intrusive geology. All but one of the UXO can be detected in magnetics data (A6-E, the bottom-right circle). The response is obscured by the magnetic geology. The ordnance next to the edge of the intrusive (A5-E) is somewhat hidden but is detectable. The other four ordnance lie in relatively quiet areas and are easily detectable. We see from the EM61 data that all six ordnance are easily detected.

GEM3 data was also collected over part of Area A. Prior to data collection it was not possible to produce the correct ferrite rod response. It was later established that the problem resulted from the use of an incorrect configuration file, however at the time we were not able to fix the problem. With the hope that the data could be post processed to extract some information data collection proceeded. This resulted in data that was uninterpretable.

Besides the frequencies there is detailed information stored in the configuration file about the transmitter and receiver characteristics. By examining the contents of the GEM3 configuration files it is clear that without a detailed knowledge of the design of the GEM3 sensor there is not much hope in using the hardware settings to correct the data. However, the fact that the configuration file contains a set of coefficients and offsets that are applied to the inphase and quadrature data at each frequency is more promising. An approximate conversion factor was calculated by comparing the configuration coefficients of the file that was used and the file that should have been used. Using this correction we were able to salvage the four lowest frequencies. While this data should not be used for modeling or inversion it can provide use with some indications as to the frequency domain EM response of the ordnance.

A gridded image of the 90Hz inphase and quadrature data is shown in Figure 2.22. We see that, similar to the EM61, GEM3 is able to detect the response from UXO A-9E and A-10E. The signature is spatially much smaller than the EM61, however this is not unexpected due to the smaller size of the GEM3 transmitter head.

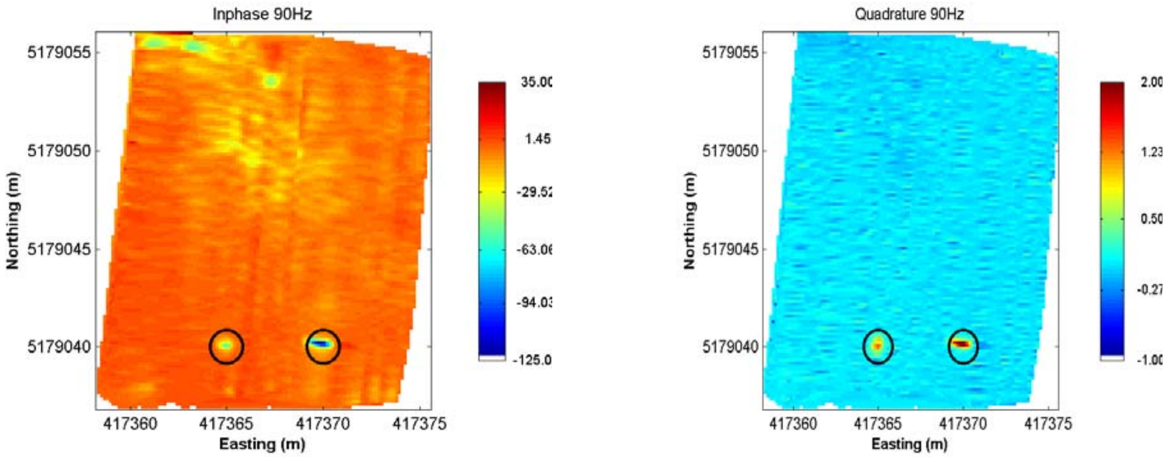

Figure 2.22: GEM3 Data over part of Area A. Left: 90 Hz inphase data in PPM, Right: 90 Hz quadrature data in PPM. Black circles indicate the location of emplaced ordnance.

Area B

The plots in the upper row of Figure 2.23 show magnetic data over area B before and after UXO emplacement. The magnetic response does not appear to have been altered by emplacing the UXO. It is difficult to determine the location of the emplaced UXO in both images. This illustrates the difficulties these dipolar geologic anomalies pose when picking targets. The EM61 Channel 1 data in the bottom row of Figure 2.23 detects all three emplaced ordnance. The data gaps (white areas in the grid) are due to navigating around soil piles from the pits. The amplitude of the southern-most ordnance is decreased due to the data gap.

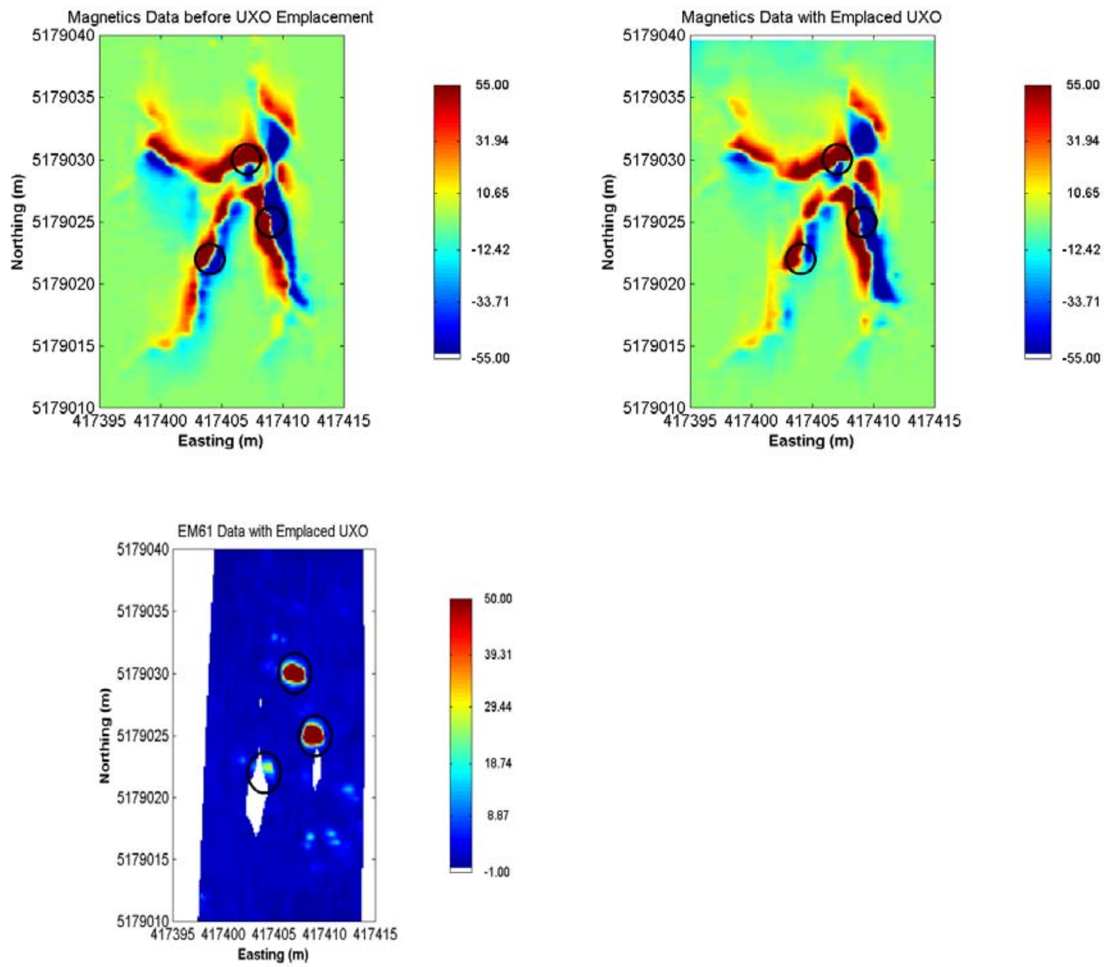

Figure 2.23: Magnetics and EM61 data over area B. Top left: Magnetics data prior to UXO emplacement, top right: Magnetics data after UXO emplacement, and bottom: Channel 1 EM61 data after UXO emplacement. Black circles show the location of emplaced UXO. Magnetics data is in nanoTeslas and EM61 data is in mV.

Area C

Magnetics data from Area C is shown in Figure 2.24. The gridded data show the linear mag high feature associated with a magnetic dyke. This feature appears to partially obscure the emplaced ordnance. However, the profile data show that while the amplitude of the dyke is large the peaks associated with the ordnance are clearly visible (red lines in Figure 2.24).

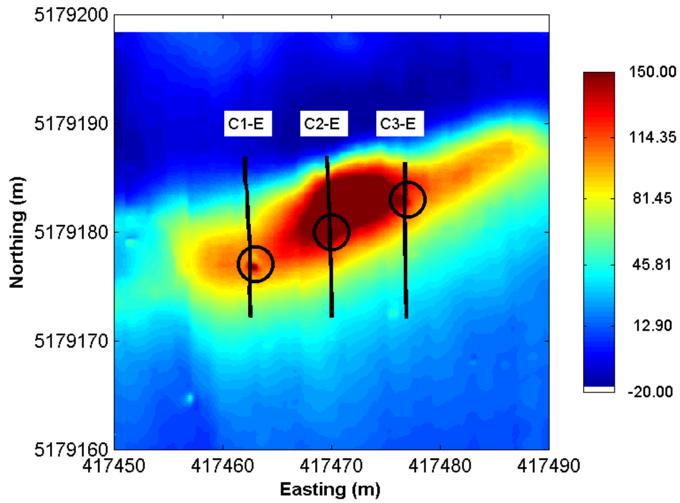

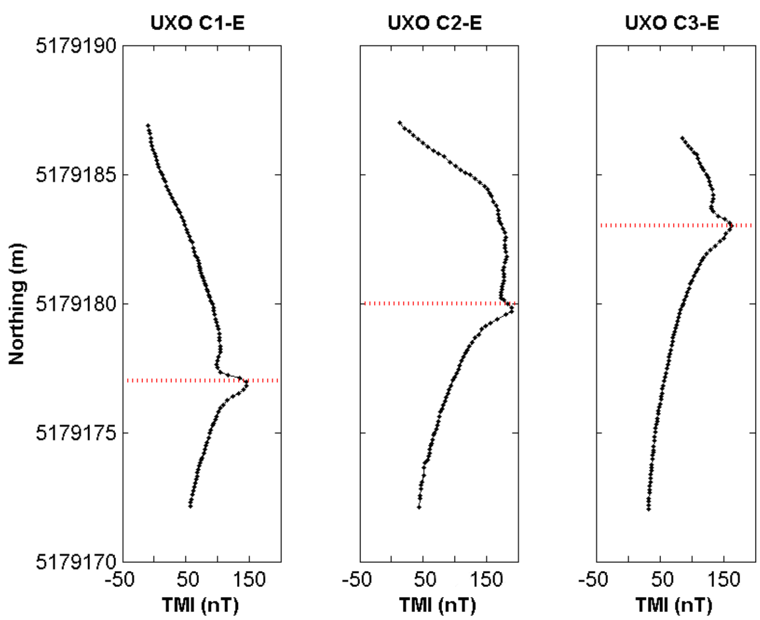

Figure 2.24: These images show data over area C. Top: Gridded image of magnetics data, bottom: profiles from magnetic data over three ordnance. The UXO locations are shown as black circles in the top panel and as dotted red lines in the bottom panel. The magnetic data is in nanoTeslas.

Area D

This magnetics data from Area D is shown in Figure 2.25. Both emplaced UXO are clearly visible within the subtle magnetic response associated with the drainage feature.

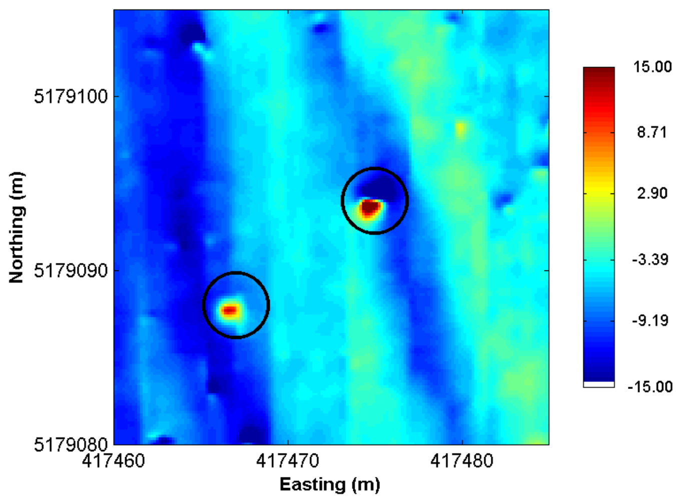

Figure 2.25: Magnetics data over Area D. The UXO locations are shown as black circles. The magnetic data is in nanoTeslas.

2.2.3.1 Summary

Complex, high amplitude responses associated with geology like that found in the area near the volcanic plug and the intrusive can completely obscure the response of emplaced UXO. Due to the complexity of the response, detrend (high pass) filtering will likely not help. Linear, dipolar features such as those found in Area B can entirely hide UXO response. The difference pre and post emplacement are not discernable. The short wavelength of these features makes filtering ineffective. Moderate amplitude, linear magnetic high features like the dyke in Area C can appear to partially obscure the response of emplaced UXO. However, careful inspection of the profiles shows that the response is distinct. The nature of the response makes it a good candidate for enhancement using high pass filtering. Subtle background responses such as those associated with drainage features in Areas A and D do not pose a problem for UXO detection.

2.2.4. Summary

Soils at Chevalier Ranch in Helena, Montana, are derived from Precambrian-age Spokane Shale and they contain minor amounts of magnetic minerals. The primary background magnetic responses arise from a volcanic intrusion (plug) and associated dykes radiating from the plug. A secondary source of background responses is the concentration of weathered materials from the volcanic intrusion in drainage channels. This site represents an entirely different geologic setting from those in Hawaii.

Three areas at Chevalier Ranch were chosen for detailed study. The first area intersects the volcanic plug and the remaining two overlap with different dykes. 20 inert rounds were emplaced for the study based on existing magnetic data acquired prior to this study. A total of 185 soil samples were collected from surface and soil pits. Total-field magnetic, EM38, EM61, and GEM3 data were acquired over each grid.

Laboratory analyses show that the magnetic susceptibilities from all Chevalier samples are 1 to 3 orders of magnitude smaller than those of samples collected in Hawaii. The frequency dependence of susceptibility is highly variable. Several samples exhibit no frequency dependence while others show frequency dependence consistent with those observed in Hawaii, albeit the susceptibility is much smaller. As a result, EMI data experience relatively little influence from the soil susceptibility whereas the magnetic data are strongly affected. Major interference is produced by the volcanic intrusive, but not by the magnetic materials accumulating in drainage channels.

Preliminary analyses indicate that the spatial scales of the background magnetic response are quite different from those of emplaced inert UXO anomalies. Visually, the background response appears to mask the UXO signature and direct detection of these UXO targets based on magnetic data is not always possible. The data sets lend themselves well to research on developing different filtering approaches to remove the background responses. This work is currently on-going.

2.3 Sentinel Plains

In November and December of 2006, the research team conducted the final field investigation for project MM-1414. This work finished a task that was started three years earlier with the first field trip to Hawaii. The research group has collected numerous geophysical data sets at four different field sites through out the U.S. This section provides an overview of the work conducted at the fourth field site, Sentinel Plains, AZ. All figures of geophysical data should be considered raw and unprocessed unless otherwise stated. The research team was granted access to Sentinel Plains due to production field work being conducted by Sky Research, Inc. Project field work was conducted in conjunction with the Sky Research field crew.

2.3.1 Background and site geology

The Sentinel Plain volcanic field located on the Luke Air Force Base Bombing Range is a 225 square mile volcanic field consisting of basalt flows up to 30 meters thick. Figure 2.26 shows the location of the field area approximately 30 miles west-southwest of Gila Bend, AZ. The basalt lava flows developed from at least twelve eruptive centers between 3.3 million and 1.3 million years ago (Oxford and Bender, 1973). The lava flows are partially covered by young deposits of eolian sand. Currently, the Sentinel Plains are predominantly flat-to-moderate in grade with small amounts of steeper topography. In addition to frequent basaltic outcrops, the regolith is often shallow. The land is largely open with sparse to moderate vegetation typical of the desert southwest (Van Devender and Dimmitt, 2006).

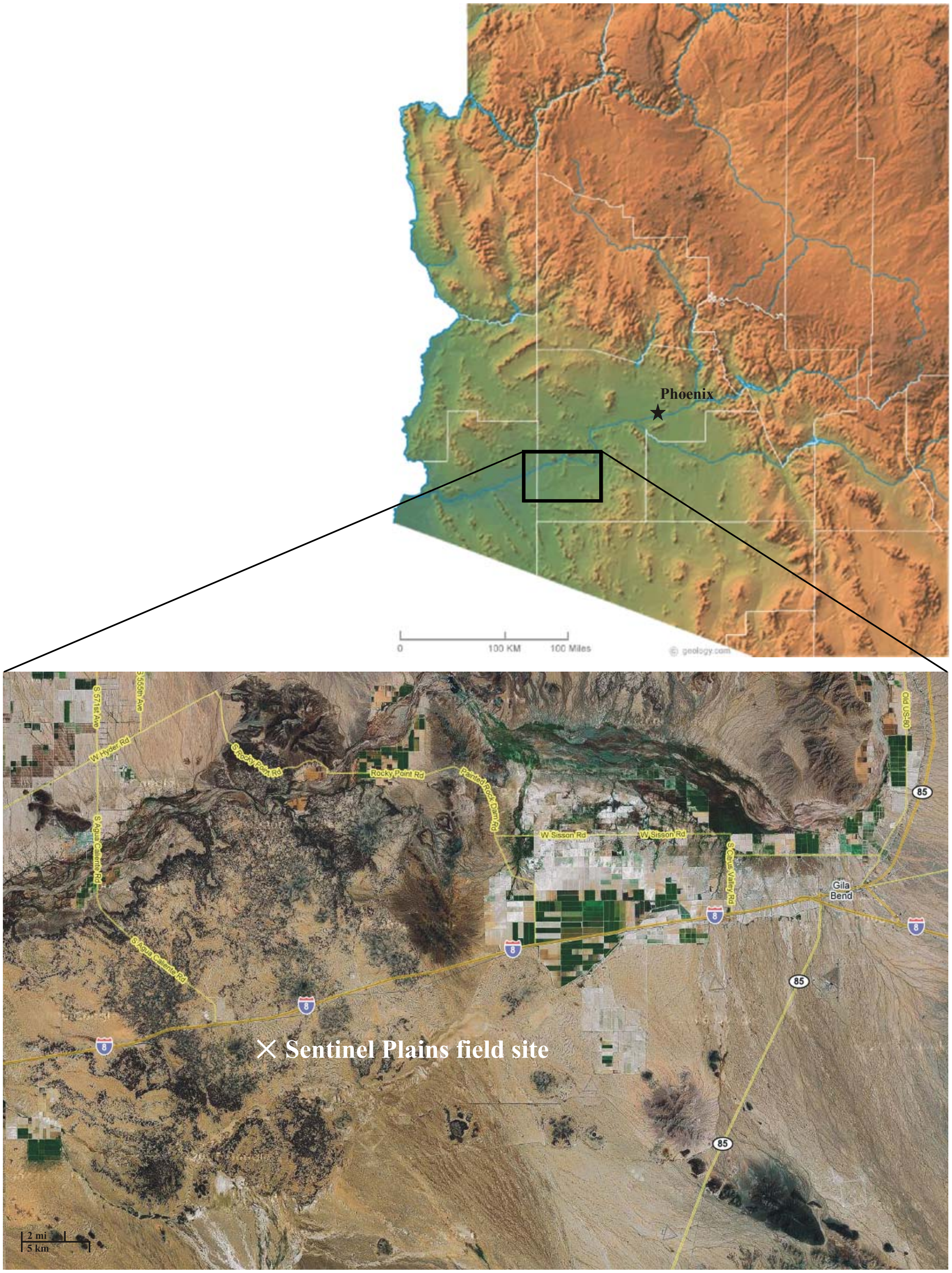

Figure 2.26: The Sentinel Plains field site outside Gila Bend, AZ (top image retrieved from www.geology.com, bottom image from www.maps.google.com)

2.3.2 Field work

Figure 2.27 shows the locations of the soil pits with relation to where geophysical data were collected at Sentinel Plains. Details on the site geology and in-field soil analysis are presented next followed by an overview of the geophysical data acquisition.

2.3.2.1 Soil descriptions

Soils at the Sentinel Plains study area have been formed in two distinctly different parent materials that vary over short distances. The older parent material is magnetite-bearing basalt. Fine sand and silt deposited by eolian processes form the second type of parent material.

The northern two-third of the grid is characterized by sandy surface material and little vegetation. The southern part of the grid is characterized by an outcropping of basalt (identified on Figure 2.27 as basalt field), and an absence of vegetation. The two areas are separated by a narrow (~5m) zone with shrub vegetation. We have excavated three soil pits to study the soil forming conditions and to take samples for characterization of texture, mineralogy, and magnetic susceptibility. In addition, we have measured surface soil magnetic susceptibility in a 10x10m grid using a Bartingon MS2D sensor. We have collected 35 soil samples from three soil pits and 33 samples from surface measurement locations.

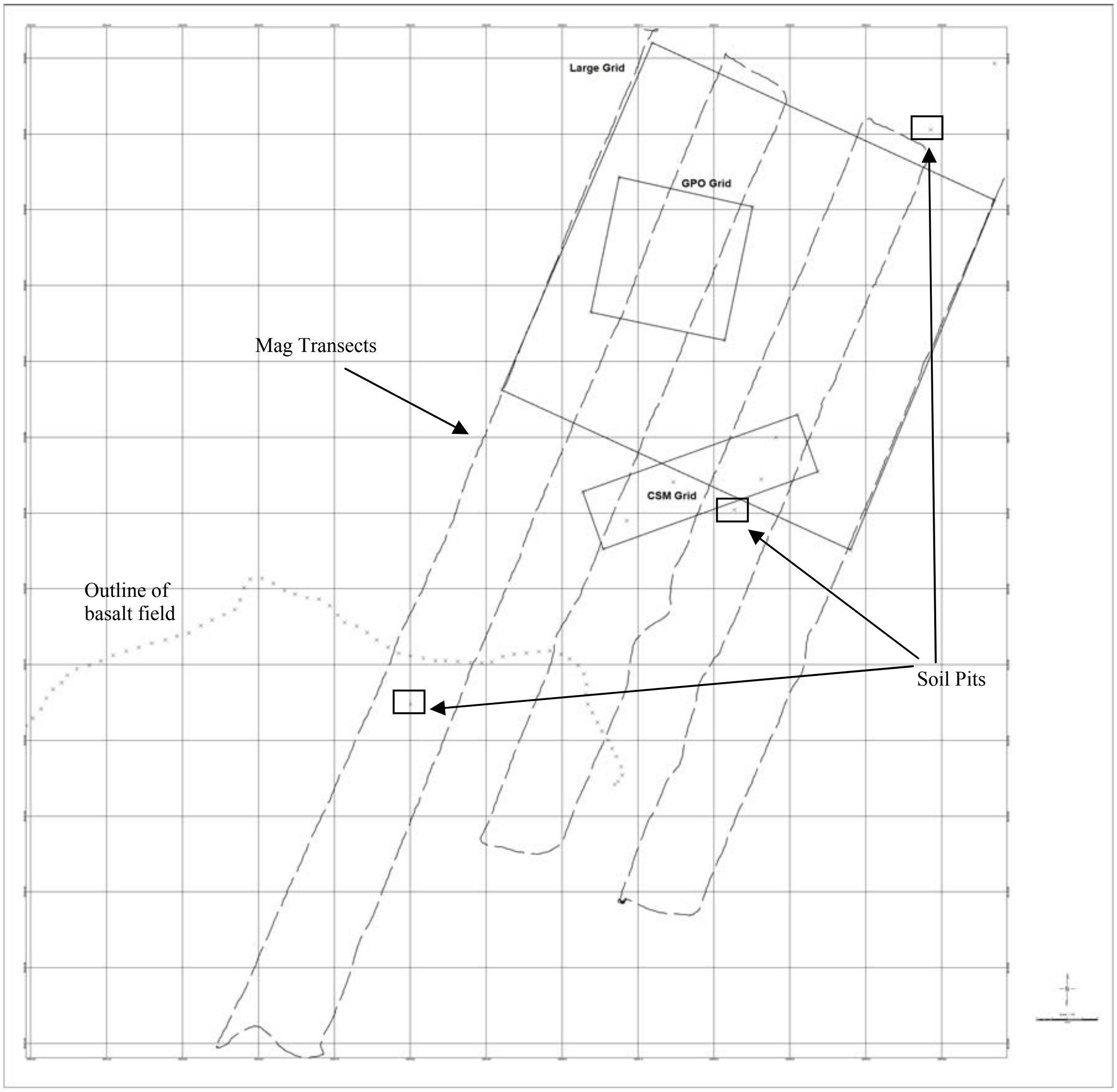

Figure 2.27: Plan map showing spatial relationship of survey grids, soil pits, and transects.

Figure 2.28 shows pictures of the three soil pits, the surrounding landscape and a close-up image of the surface conditions. Soil 1 is characterized by ~50cm of very loose sand and silts over a hard calcic horizon on top of the basaltic bedrock, which is found at 1m depth. The basaltic bedrock has thick coatings of calcic material on its surface. Soil 2 is considerably deeper and denser than soil 1. Using a hand auger, soil samples were collected to a depth of 1.76m, after which no further progress could be made. Calcic material was largely absent in the upper meter, but increased with further depth. The maximum depth of the borehole was likely in close proximity to the bedrock. Soil 3 is very shallow, and consists of a thin layer of windblown sand

and some calcic nodules over the basaltic bedrock. Numerous unweathered basaltic rocks and remnants of thick calcic coatings of these rocks are found spread over the surface.

All soils are characterized by a vesicular top horizon, characterized by tiny pores or vesicles, which form as a result of trapped or expanded air from rainwater in the soil. Based on detailed profile descriptions we recognize three phases in the soil development of the site. The thick calcic coatings on the basaltic (bed)rock at depth in soil pit 1 and 2 indicate that a significant period of soil formation has taken place during some period in the past. The second soil-development phase has consisted of a period of intense erosion. This phase can be identified from the calcic coatings on nearly unweathered basalt rocks, which are found at the surface of the lava flow outcropping of Soil 3. Finally, during a third development phase, topographic lows have been covered with eolian deposits.

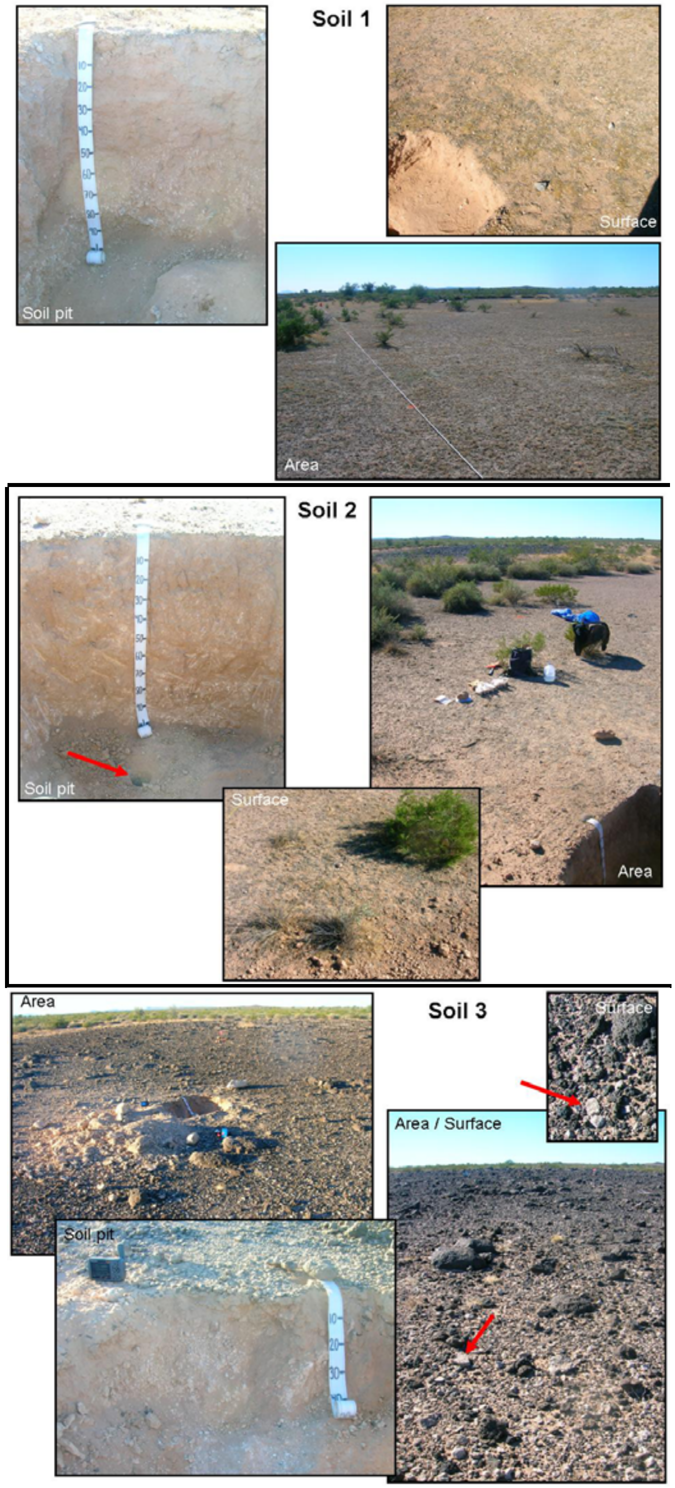

Figure 2.28: Sentinel Plains soil pits (see Fig. 2.27 for locations). Top left: Soil pit 1; area picture taken in a Southwestern direction. Top right: Soil pit 2; red arrow points to location of drill hole in bottom of soil pit. Area picture was taken in a western direction. Note the narrow zone of shrubs separating the sandy surface area form the basalt outcropping. Bottom: Soil pit 3; red arrows indicate erosional remnants of calcic crusts. Area picture taken in western direction.

Field magnetic susceptibility readings show a baseline value of 125-150 10^{-5} SI (Figure 2.29). Over the basaltic outcropping, the susceptibility readings increase slightly, but due to the irregular surface the readings must be interpreted with caution. As a next step we plan to measure the frequency dependent magnetic properties of the soil samples collected at the site using a Bartington MS2B sensor. Based on the observed variability we will select a group of samples for detailed characterization of the mineralogy using XRF diffraction and chemical extractions.

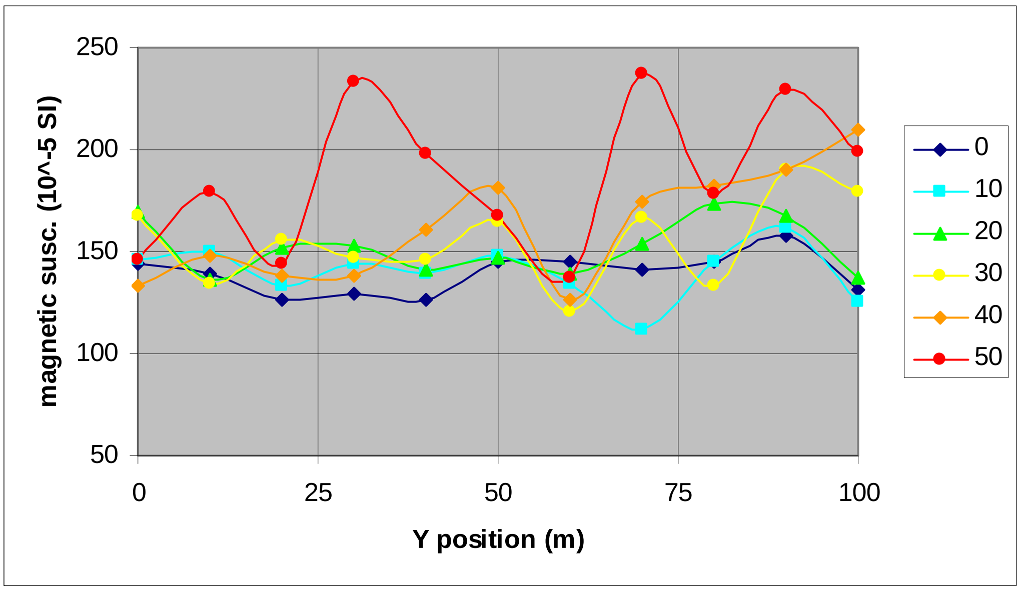

Figure 2.29: Magnetic susceptibility along six 100m long lines covering the study area. The individual lines are separated by 10 meters. All lines run North to South with Line 0 at the eastern end of the grid and Line 50 at the western end.

2.3.3 Geophysical data collections

Geophysical data were collected over three grids as well as along transects. Data acquisition was conducted using the Geonics EM63, EM61-MK2, and EM38 and the Geometrics G-858 magnetometer. The following text describes the different grids along with what geophysical data were collected.

Sky Research established a 50m x 50m grid to collect EM61-MK2 data over. This larger grid, referred to as the 'Large Grid', was used to identify a smaller area (18m x 18m) used to construct Sky's geophysical prove-out (GPO) grid in. This smaller area will be identified as the 'GPO'. A second grid was constructed to the south in an area that had more variation in the total-field magnetic data. This second grid measured 8m x 30m and will be referred to as the 'CSM Grid'.

Twenty-three UXO items and simulants were placed in the GPO grid following the background data collection. Four UXO items were buried in the CSM grid. Figure 2.30 shows an emplacement map used for the GPO grid.

2.3.3.1 Pre-Seed Data:

- Large Grid – due to time constraints and problems with the EM63 data logger only magnetic data and EM38 data were collected over the Large Grid. EM38 data were collected at 1-m line spacing and coupled with DGPS. The magnetic data were collected in a horizontal gradient mode with a 0.5m sensor separation and 1m line spacing.

- CSM Grid – background EM63 and magnetic data were collected. EM63 data were collected at a 0.5-m line spacing and the magnetic data were collected in a horizontal gradient mode with a 0.25-m sensor separation and .5-m line spacing. EM38 data were not collected prior to seeding over this grid.

- GPO – Members of the SERDP project did not collect any background data over this grid. Sky personnel collected EM61-MK2 data over this grid. Data were collected at a 0.5- and 1-m line spacing in both a N-S and E-W direction.

2.3.3.2 Post-Seed Data:

- Large Grid – UXO items were only seeded in the CSM Grid and GPO.

- CSM Grid – EM63 data were collected at a 0.5m line spacing and the magnetic data were collected in a horizontal gradient mode with a 0.25m sensor separation and 0.5m line spacing. EM38 were collected at a 0.5m line spacing. Four UXO items were emplaced in this grid.

- GPO – EM63 data were collected at a 0.5m line spacing and the magnetic data were collected in a horizontal gradient mode with a 0.25m sensor separation and .5m line spacing. EM38 were collected at a 0.5m line spacing.

2.3.3.3 Additional data:

Transects – 5 transects of magnetic data were collected. Each transect measured ~100-150 meters. Two these five transects were partially repeated with the EM63.

The following figures show the different data collected at Sentinel Plains. The data has only been corrected for latency, no other processing has been performed. The superimposed grid is on 10 meter intervals for all figures.

Frag TBA	100 lb Bomb Simulant	1000 lb Fuze @ 0.30 m	500 lb Fuze @ 0.30 m	100 lb Fuze @ 0.30 m	100 lb Bomb @ 0.75 m Nose Down
100 lb Bomb Simulant	Undisturbed	1000 lb Fuze @ 0.15 m	500 lb Fuze @ 0.15 m	100 lb Fuze @ 0.15 m	10" barbed wire @ 0.15 m
Frag TBA	Fuze TBA	Frag @ 0.30 m	Flare body just below surface	0.50 caliber cart. Casing just below surface	Frag @ 0.15 m
Frag TBA	Frag TBA	37mm @ 0.30 m	37mm @ 0.15 m	Frag @ 0.60 m	Frag @ 1 m
Native rocks in cross-hatch pattern					

Figure 2.30: Emplacement map for the GPO grid at Sentinel Plains.

2.3.3.4 Magnetic Data

Figures 2.31 to 2.34 show the pre- and post-seed data collected over the various grids at Sentinel Plains.

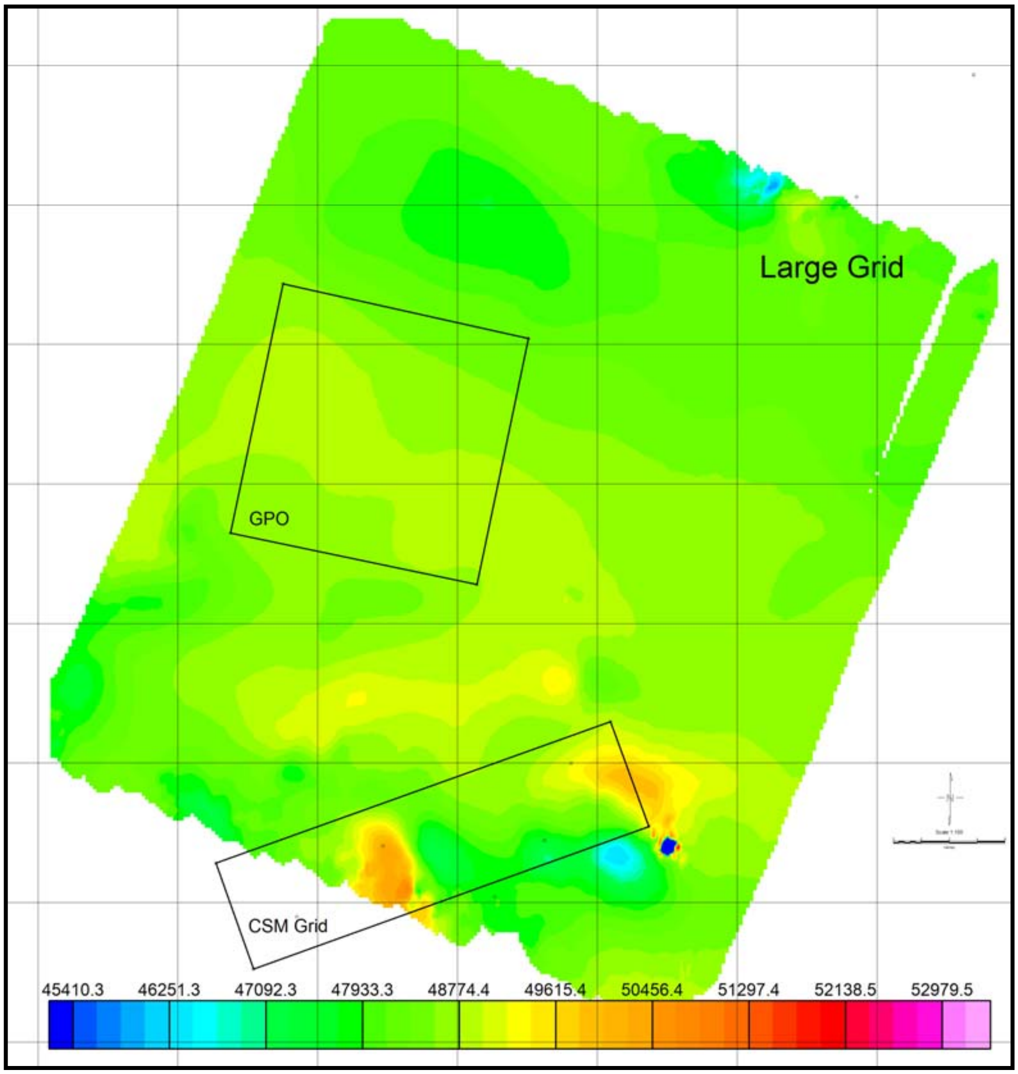

Figure 2.31: Pre-seed magnetic data over the Large Grid. The GPO and CSM Grid have been outlined for reference

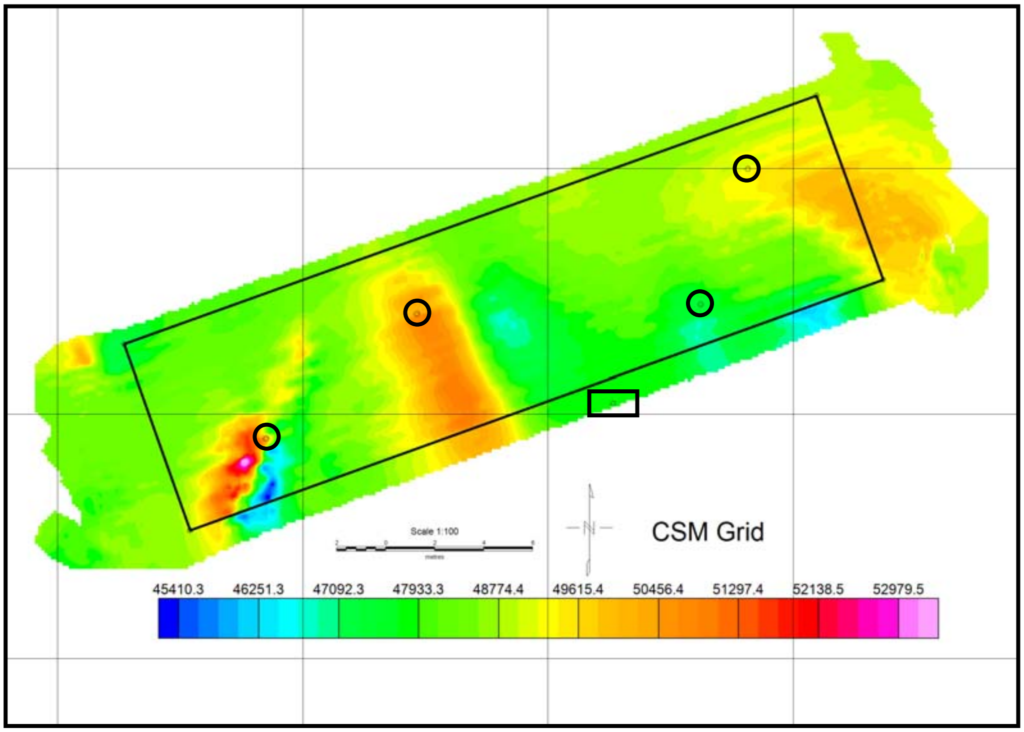

Figure 2.32: Pre-seed magnetic data over the CSM Grid. The data are presented using the same color scale as the large grid above. The four circles in the grid denote where UXO were buried. The black rectangle outside the grid denotes where a soil pit was dug.

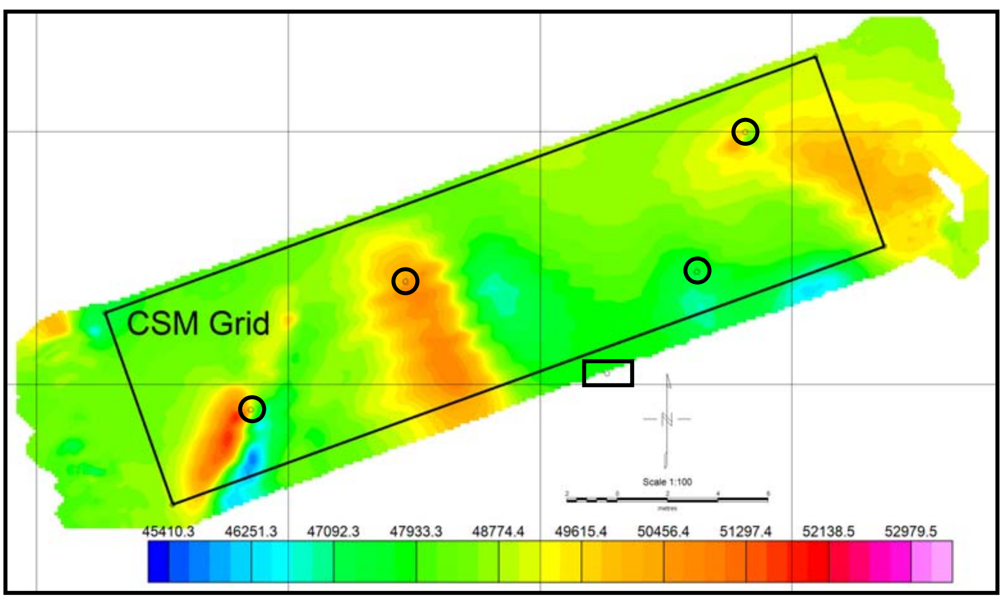

Figure2.33: Post-seed magnetic data over the CSM Grid. The data are presented using the same color scale as the large grid above. The four circles in the grid denote where UXO were buried. The black rectangle outside the grid denotes where a soil pit was dug.

Post-seed magnetic data collected over the GPO Grid: The color scale was decreased to better show the anomalies in the data. The cross hatch pattern is evident.

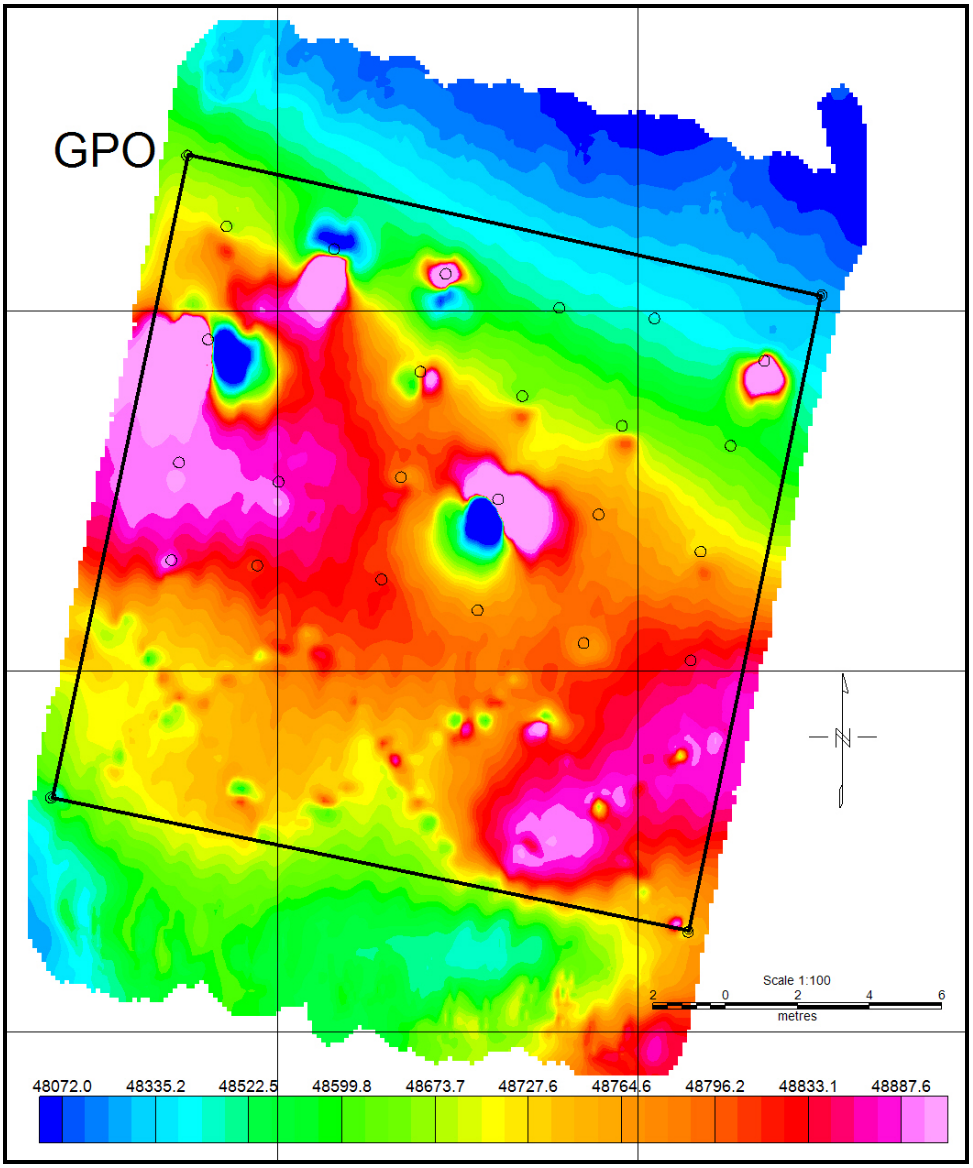

Figure 2.34: Post-seed magnetic data over the GPO Grid.

2.3.3.5 EM63 Data

Channel 1 from the pre-seed EM63 data collected over the CSM Grid is shown in Figure 2.35. Data were collected at 0.5 meter line spacing (black lines on figure) over the grid. Data collection started at the northeastern corner. Note the variation in the recorded data values from the northern most lines to the southern most lines. This unprocessed data shows the large drift present in the EM63 instrument. This drift is visible in all the data presented here.

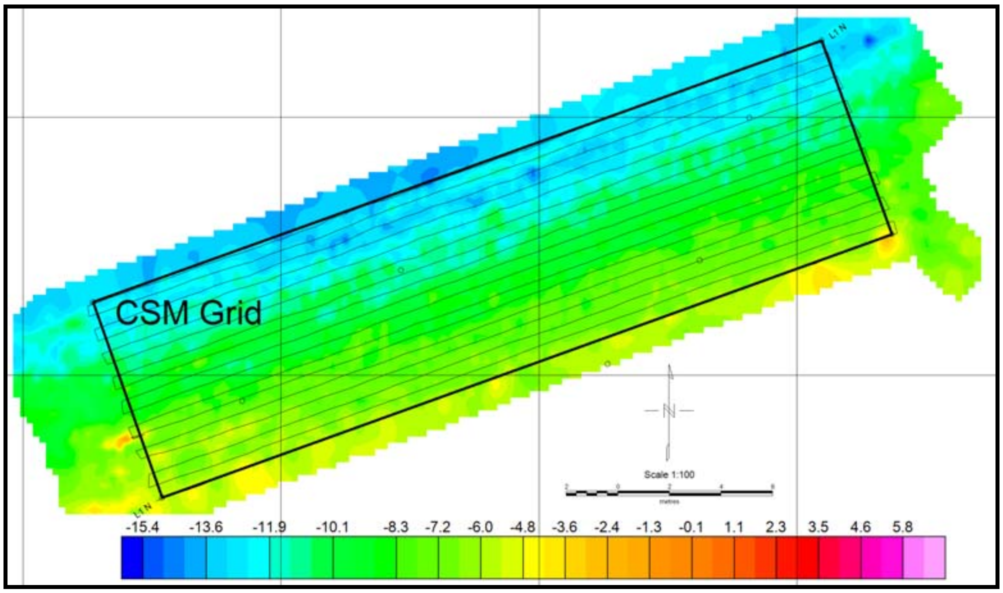

Figure 2.35: Pre-seed EM63 data over the CSM Grid: Channel 1 from the EM63 data collected at .5 meter line spacing (black line on figure) over the grid. Data collection started at the northeastern corner.

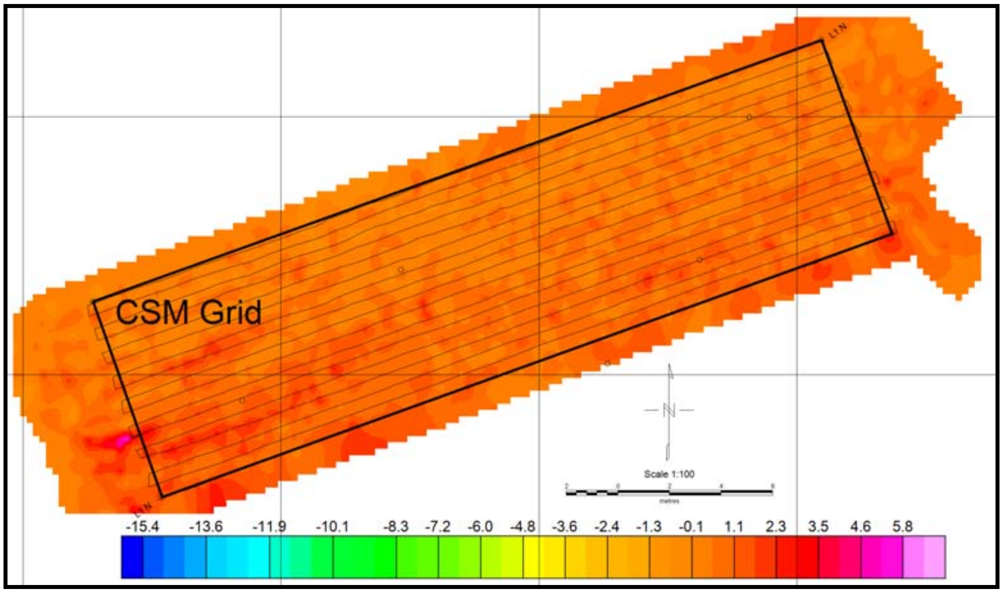

Figure 2.36: Pre-seed EM63 data over the CSM Grid: Channel 5 from the EM63 data.

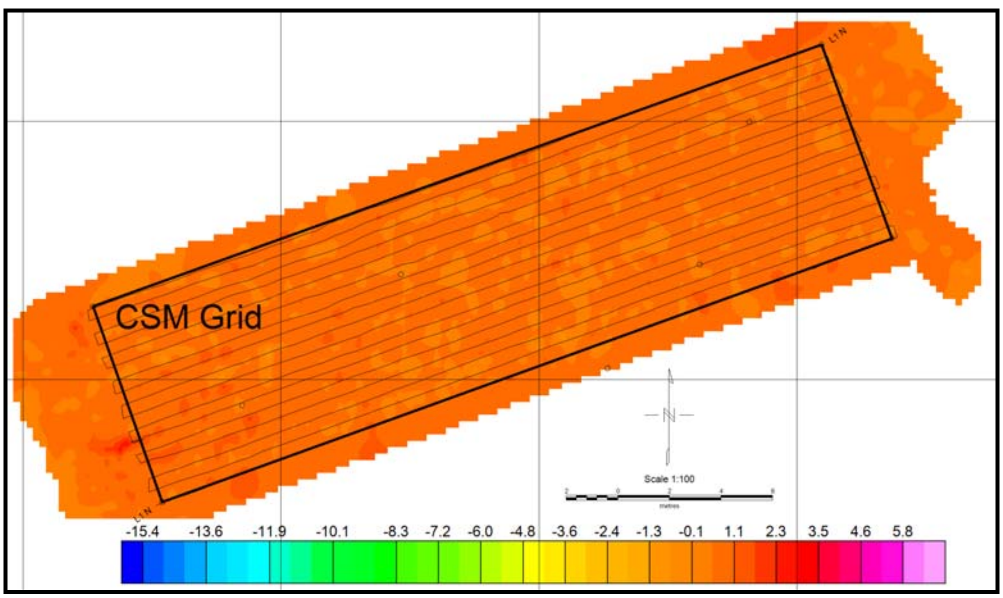

Figure 2.37: Pre-seed EM63 data over the CSM Grid: Channel 10 from the EM63 data

Figure 2.36 and 2.37 show later time gates from the same pre-seed data set, channels 5 and 10, respectively. These data do not show the same drift associated with the first channel (Figure 2.35) and show little variation over all.

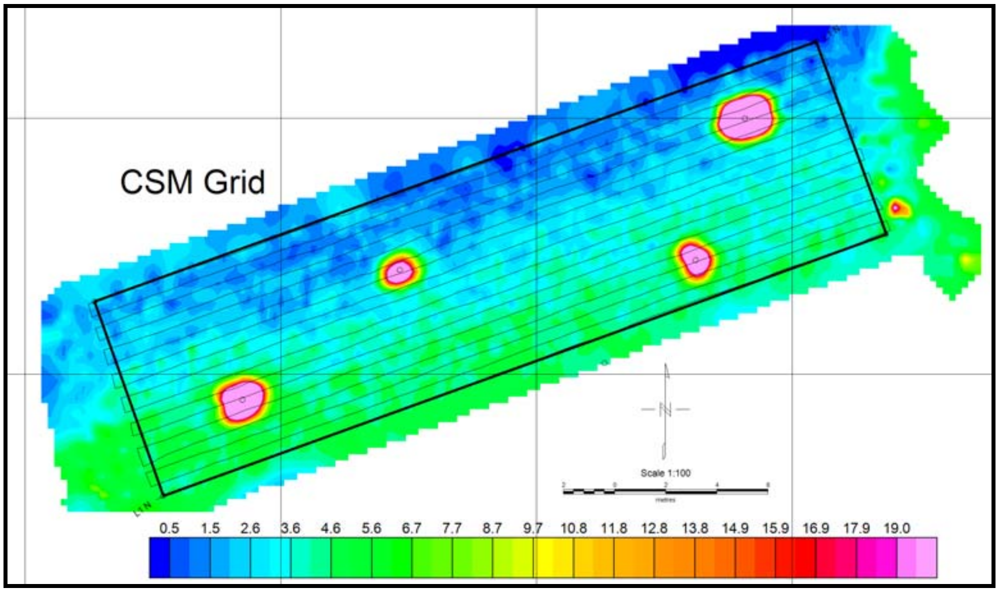

Figure 2.38: Post-seed EM63 data over the CSM Grid: Channel 1 from the EM63 data collected at 0.5 meter line spacing (black line on figure) over the grid.

Figure 2.38 shows channel 1 of the EM63 post-seed data collected over the CSM Grid. The data exhibit regional change consistent with pre-seed data illustrated in Figure 2.35. This data drift does not hinder detection of buried targets within the grid. The four UXO are clearly visible in the post-seed EM63 data at this site.

Figure 2.39 shows the data collected over the GPO grid. The data collection started in the southwest corner. This map shows the same increasing trend in Channel 1 visible in the data from the CSM grid. Note the negative values around the two anomalies in the north-west corner of the grid. These are a result of the minimum curvature routine and the large response of those two buried UXO.

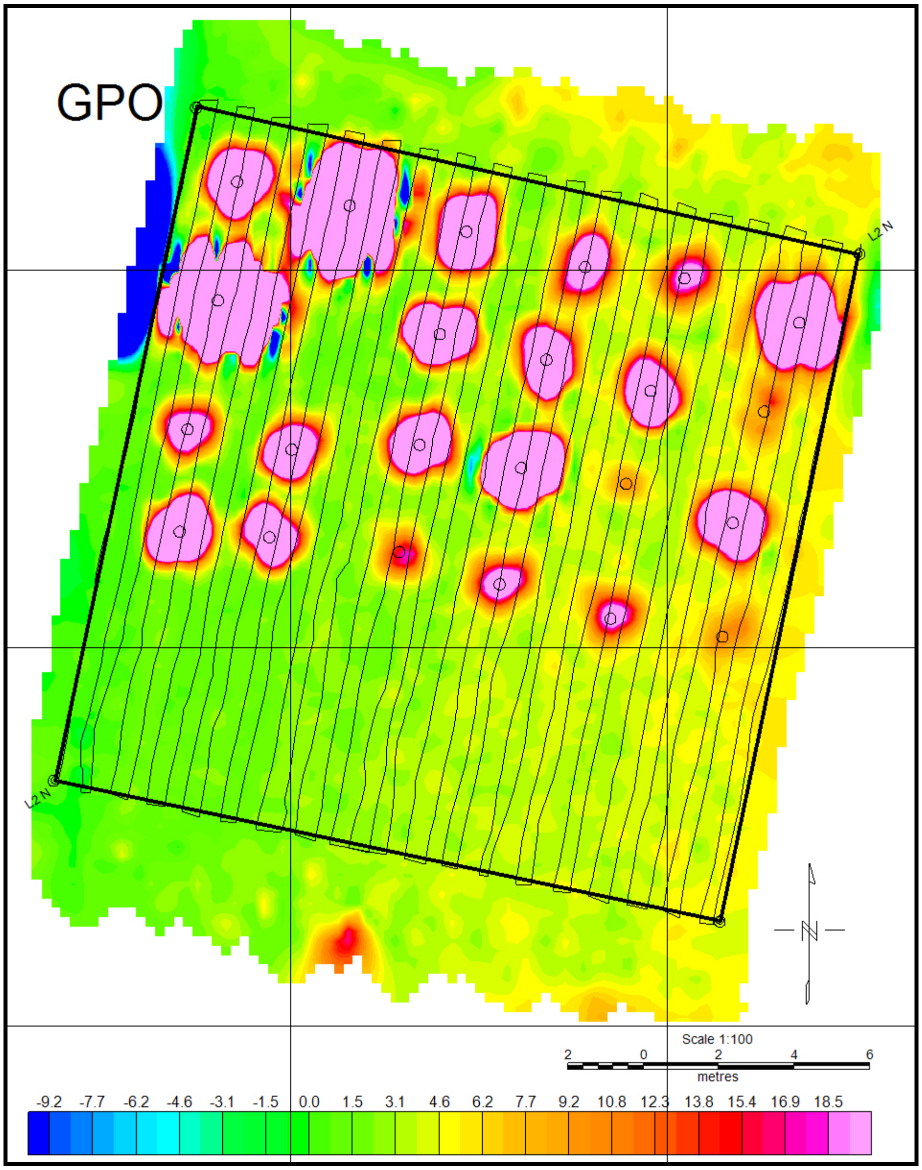

Figure 2.39: Post-seed data from the GPO grid: Channel 1 from the EM63 data collected at 0.5 meter line spacing (black line on figure) over the grid.

2.3.4 Summary

The data presented here gives an indication of the problems associated with production surveys conducted in this area. While the TDEM data seem to be unaffected, the total-field magnetic data is severely contaminated. Analysis indicates that TDEM surveys will produce clean data but will require additional man-power due to required collection procedures. The vegetation and ground cover present will prevent standard acquisition techniques involving wheeled EM61/63 carts. Evolution of processing methods for total-field magnetic data may help to reduce the required manpower and overall costs associated with future remediation efforts at Sentinel Plains.

3. Field Component, UXO Remediation Sites

The first major objective addressed by SERDP Project MM-1414 is to:

> Build an understanding – through field and laboratory analysis of soil samples and geophysical data – of the geologic origins and physics of soil magnetization.

Its motivation stems from the fact that at many UXO remediation sites, the task of discriminating UXO from non-UXO items is more difficult when sensor data are contaminated with geological noise originating from magnetic soils. This is because in regions of highly magnetic soil, magnetic and electromagnetic sensors often detect large anomalies that are of geologic, rather than metallic, origin. Improving UXO detection and discrimination in such strongly magnetic environments requires, first and foremost, an understanding of the geologic origins and physics of soil magnetization – such that one can properly characterize and remove these responses.

In this chapter, we follow the field activities presented in the previous chapter by demonstrating our current understanding of the geologic origins and physics of soil magnetization, which is the first major goal of Project MM-1414. The results which we present here summarize the field and laboratory measurements of both surface and soil-pit samples collected during field activities at the four sites. In the next chapter (Chapter 4), we then expand upon results presented here by demonstrating an effective means of modeling the spatially variable frequency-dependent magnetic susceptibility in soils hosting UXO, which is the second major task of Project MM-1414.

3.1 Introduction

The magnetic properties of soils result from the presence of iron oxides in different forms and quantities. Paramagnetic and antiferromagnetic iron oxides such as goethite and hematite are the most abundant iron oxide minerals in soils but play a minor role in determining the magnetic character of a soil. Ferrimagnetic minerals such as magnetite, maghemite, and pyrrothite are the most magnetic of the iron oxides, and are of primary importance in their effects on geophysical sensors. Iron oxide minerals can be both pedogenic (i.e., a product of soil formation) and lithogenic (i.e., unweathered minerals from the parent material) in origin. Two types of magnetic behavior associated with magnetic soil minerals can have a significant impact on the magnetic and electromagnetic characteristics of the subsurface. Both magnetic susceptibility and viscous remanent magnetization (VRM) can have a negative effect on the performance of geophysical sensors (Billings *et al.*, 2003).

The presence of iron oxides is the predominant cause for the magnetic behavior of soils (Mullins, 1977). Iron oxide minerals can be both lithogenic (i.e., unweathered minerals from the parent material) and pedogenic (i.e., a product of soil formation) in origin. Iron-containing minerals can be found in igneous rock such as basalt, gabbro, and granite, but also in metamorphic and sedimentary rocks. Weathering of rock material leads to the release of Fe into surface environments, where it will form pedogenic iron oxides (Singer and Fine, 1989). However, the concentration and type of iron oxides in soils is not only affected by the mineralogy of the parent material, but also by soil age, soil forming processes, biological activity, and soil temperature (Fabris *et al.*, 1998; Hendrickx *et al.*, 2005; Singer *et al.*, 1996; Van Dam *et al.*, 2005). Due to the complex processes that control soil mineralogy, the knowledge of spatial distribution and temporal evolution of soil magnetic properties in most soils is limited (Das *et al.*, 2002).

Many books and review papers have addressed the physical background of magnetic minerals in general (Lindsley, 1991; Thompson and Oldfield, 1986) and magnetic mineralogy of soils in particular (Cornell and Schwertmann, 2003; Mullins, 1977; Stucki *et al.*, 1988). Three types of magnetization are commonly used to describe the magnetic behavior of a material. The first is remanent magnetization, which occurs within ferromagnetic and ferrimagnetic minerals and exists in the absence of an applied field. The second is magnetic susceptibility. When a low-intensity magnetic field is applied to a material, the net magnetic moment (magnetization, M) is proportional to the applied field strength (H). Therefore, the low-field magnetic susceptibility, which is defined as M/H and expressed per unit volume (κ) or per unit mass (χ), is a material-specific property. The magnetic susceptibility affects the performance of both electromagnetic and magnetic sensors (Billings *et al.*, 2003). The third is viscous remanent magnetization (VRM), which refers to the effect where the secondary magnetic field is delayed relative to the primary magnetic field, and has been linked to the presence of superparamagnetic (SP) grains (Dearing, 1994). VRM causes frequency dependence in magnetic susceptibility, which has important implications for time- and frequency-domain electromagnetic sensors (Billings *et al.*, 2003). The formation of SP grains is generally considered to be associated with processes occurring under normal pedogenic oxidation-reduction cycles (Mullins, 1977; Thompson and Oldfield, 1986), but the exact processes leading to recrystallization of these SP grains are poorly understood.

Table 3.1 (pg. 120) shows the magnetic class and magnetic susceptibilities for several iron- and iron-titanium-oxides, iron-sulfides and other soil constituents. Water and quartz are diamagnetic and have a small negative magnetic susceptibility. Hydrated iron oxides like goethite (which is the most abundant iron oxide in soils around the world), ferrihydrite, and lepidocrocite play a minor role in determining the magnetic character of soils. Likewise, hematite (which is the most abundant iron oxide in tropical soils), pyrite, and ilmenite hardly affect the magnetic soil characteristics. As follows from Table 3.1 (page 120), the magnetic character of a soil is dominated by the combined amount of lithogenic and pedogenic ferrimagnetic magnetite (Fe_3O_4) and maghemite (γ-Fe_2O_3) minerals in a soil (Ward, 1990).

3.2. Methods and Materials

One of the goals of the research program was to understand the geologic origins of soil magnetization for sites in three states:

1. **Hawaii**
    a. The Navy QA range on the Former Navy Bombing Range on Kaho'olawe Island
    b. Geophysical Prove-out at Waikaloa Village in the Former Waikaloa Maneuver Area
    c. Waimea Geophysical Prove-out on the Former Waikaloa Maneuver Area

2. **Montana**
    a. Limestone Hills UXO sites near Helena

b. Chevallier Ranch UXO sites near Helena

3. **Arizona, Sentinel Plains**

This section first describes, by site, the sampling strategies and measurements performed in the field. This is followed by a general description of the laboratory techniques used to identify magnetic properties and mineralogical characteristics of the different field sites.

3.2.1 Sampling strategy and field measurements

Navy QA range, Kaho'olawe Island, Hawaii – Four soil pits that represent the variation in magnetic properties of the site were excavated in and around test plot 2E (Fig. 3.1). Soil pit A was located in the area with the lowest magnetic background, just outside the 2E Grid, while soil pit B was dug in the area with the highest magnetic background readings. Soil pit C was dug in an area with intermediate magnetic readings. Soil pit D was dug at a distance of approximately 75 meters south of the Grid 2E in a topographic low. For all pits the soil profiles were divided in separate horizons. After description of the horizon characteristics in the field, samples were collected for laboratory analyses of soil texture and mineralogy and frequency dependent magnetic properties. A total number of 50 soil and 2 rock samples were collected from the soil pits. The magnetic susceptibility was measured in vertical increments of 5 centimeters using a Bartington MS2 system at frequencies of 0.958 kHz (D-sensor) and 0.58 kHz (F-sensor).

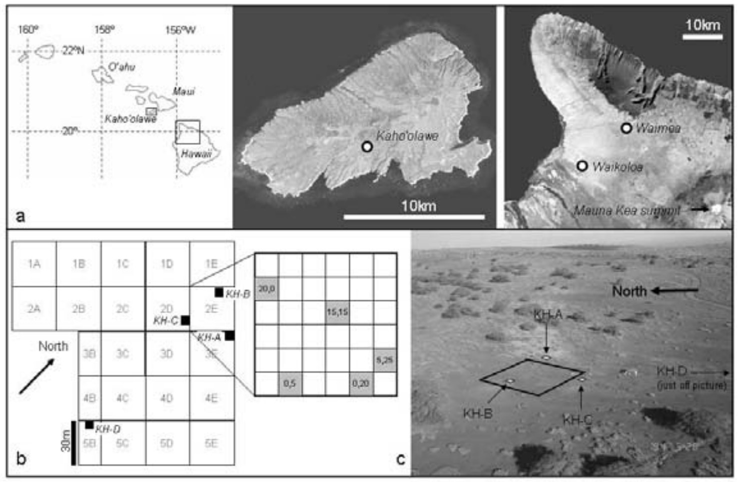

Figure 3.1. Location and setting of the field areas in Hawaii. a) The eight main Hawaiian islands and detailed satellite images (Landsat) of Kaho'olawe and the northern part of the Big Island of Hawaii with the approximate locations of the field sites given by the circles. b) Outline of the Navy QA Grid on Kaho'olawe and locations of the four soil pits. The gray squares in the inset show the locations of the 5 surface samples studied in detail; the same stratified random sampling strategy was used for the two sites in the Former Waikoloa Maneuver area. c) Aerial photograph of the field site with the locations of test grid 2E and the soil pits.

Former Waikaloa Maneuver Area, Hawaii – The former Waikoloa Maneuver Area field sites are designed as geophysical test locations. Both sites consisted of three 30x30 m grids, similar to the grids at the Navy QA range on Kaho'olawe Island. Due to security restrictions our samples were collected from unseeded grids. We had no permission to dig soil pits and were restricted to surface sampling of both the Waikoloa and Waimea sites. The format of the surface soil sampling was similar as that on Kaho'olawe (see Fig. 3.1b). At both sites a 5x5 m grid was laid out inside the unseeded grid. From each 5x5 m grid one random sample was taken (using the same stratified random sampling strategy as on Kaho'olawe Island). Thirty-six samples have been collected from both sites. In addition, two samples of unweathered basalt were collected from a road cut from Kohala Volcano on the Big Island of Hawaii.

Chevallier Ranch, Helena Valley, Montana – The 200x200m area of the Chevallier Ranch site that has been cleared of UXO was selected for detailed geophysical surveying and soil characterization work. This area was selected because it contained a suite of geologic responses that have been identified as problematic for the magnetic surveying performed during the clearance activities at Chevallier Ranch. The geologic responses can be broken into four classes: 1) area of intense magnetic response (>2000nT anomaly) associated with a 100x100m basalt intrusive, 2) extensive linear monopolar anomalies (>50m strike length, ~100 nT anomaly) likely associated with deeper mafic dykes, 3) linear dipolar anomalies which are spatially compact (< 5m strike length, ~100-200nT anomaly) with a character that could be interpreted as a UXO response, and 4) linearly extensive weak magnetic responses associated with drainage features (< 20nT anomaly). Each of these responses has the potential to mask or distort the response of a UXO.

Soil and rock samples were collected from soil pits and from a surface grid. We excavated seven soil pits and two trenches on the magnetic plug and dikes, on the Spokane Shale, in the ephemeral streams, and on topographic highs and in topographic lows. (Fig. 3.2) We collected 43 samples from these seven soil pits; sampling depths have been chosen based on soil horizonation. In the two small trenches, which cross small linear dipolar anomalies, we collected thirty samples in a grid-type layout (2 x 15). Over a 15- x 175-m section of the study site that was used for detailed geophysical measurements, we collected 142 surface samples. The samples were collected at a 5 meter distance along four north-south trending lines. Basaltic rock samples were collected from the south wall of soil pit 4 (Sample CR4a = weathered basalt, 0.25m depth and Sample CR4b = unweathered basalt, 0.0m depth). Shale samples were collected from horizon Ck in soil pit 5 (1 red and one green-colored Spokane shale sample).

The magnetic susceptibility of all samples was measured at two frequencies using a Bartington MS2B sensor in the laboratory. Soil composition on the surface and in the pits (loose and gravelly) prevented the acquisition of oriented soil samples.

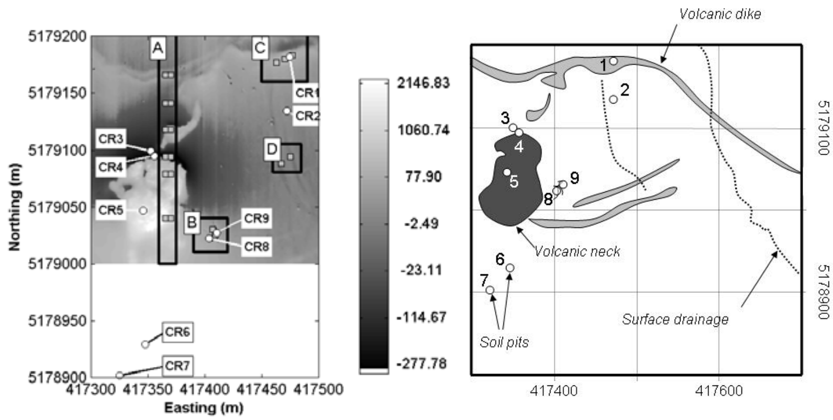

Figure 3.2. Total field magnetic anomaly (nT) map of the Chevallier Ranch field site (obtained by the Montana Army National Guard) after removal of the background, with locations of the detailed geophysical test plots (rectangles) and 9 soil pits (left). Surface samples were collected from rectangle A in a 5x5m grid. Interpretation of major geological and topographical features at the site (right).

Sentinel Plains, Arizona – Within the Sentinel Plain volcanic field located on the Luke Air Force Base Bombing Range we selected an area of 100 by 50 meters for detailed study of the soil conditions and magnetic susceptibility (Fig. 3.3). The northern two-thirds of the grid is characterized by sandy eolian surface material and little vegetation. The southern part of the grid is characterized by an outcropping of basalt, and an absence of vegetation. The two areas are separated by a narrow (~5m) zone with shrub vegetation. We excavated three soil pits to study the soil forming conditions and to take samples for characterization of texture, mineralogy, and magnetic susceptibility. In addition, we measured surface soil magnetic susceptibility in a 10x10m grid using a Bartingon MS2D sensor. We collected ~35 soil samples from three soil pits and 33 samples from surface measurement locations.

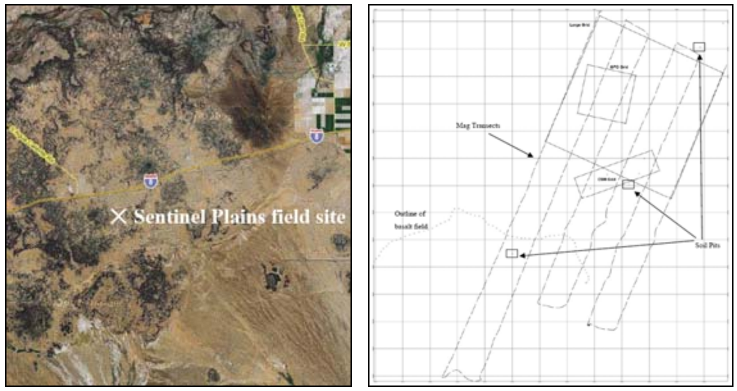

Figure 3.3. Aerial photograph of the Sentinel Plains field site (left, from Google Earth) and site map showing locations of the geophysical measurements and excavated soil pits (rectangles; pit 1 in the north, pit 3 in the south). Surface samples were collected along the magnetic transects in a 5x5m grid.

3.2.2 Laboratory techniques – magnetic measurements

Low-field-strength magnetic susceptibility – For all samples collected during this project magnetic susceptibility (κ) was measured using a Bartington MS2B dual-frequency sensor, which is a standard instrument in environmental geophysics research. First, $10cm^3$ pots were filled, dried, and weighed on an A&D GR-120 balance with 0.1mg accuracy. Next, the volume specific magnetic susceptibility (κ) was measured at two frequencies (0.46 and 4.6 kHz). Measurements were conducted at the "1.0" or "0.1" sensitivity setting, depending on the magnetic character of the sample material. Each sample was measured three times with an air reading before and after each series for correction of drift. The mass-specific susceptibility (χ) was calculated from the volume-specific susceptibility using $\chi = 10\kappa / m$, where m is the sample mass in grams (Dearing, 1994). The (percent) difference between readings at the two frequencies can be used to estimate the viscous remanent magnetization of the samples. The frequency dependent susceptibility was calculated using $\chi fd\% = ((\chi_{lf} - \chi_{hf}) / \chi_{lf}) \times 100$, where χ_{lf} is the mass-specific susceptibility measured at a frequency of 0.46kHz and χ_{hf} is the mass-specific susceptibility measured at 4.6 kHz.

Frequency-dependent complex magnetic susceptibility – Complex magnetic susceptibility measurements were made at the University of Minnesota's Institute for Rock Magnetism (IRM) using a Lake Shore Cryotronics, Inc. AC Susceptometer (LACS). The LACS is capable of measuring the magnetic susceptibility across a broad frequency spectrum (10-10000 Hz) and temperature range (15-300 K). For this study measurements were made at room temperature (~17 °C or 290 K) and across the full frequency spectrum at 32 separate frequencies.

Temperature-dependent magnetic susceptibility (high temperatures) – Despite very large electronic exchange forces in ferrimagnetic materials, thermal energy, if high enough, overcomes these forces and produces a randomizing effect. This occurs at a particular temperature called the Curie temperature (T_C). Below T_C, the ferrimagnet is ordered and above it, disordered. Above T_C the material is also paramagnetic and thus the net magnetic moment is not zero. T_C is an intrinsic property and is a diagnostic parameter for mineral identification. However, different magnetic minerals can have the same Curie temperature, potentially complicating interpretation.

At the University of Minnesota's Institute for Rock Magnetism, a Kappabridge Furnace was used to determine T_C for select samples. The Kappabridge measures magnetic susceptibility over a temperature range of 300-975 K, at a fixed frequency of 920 Hz and fixed AC field with strength of 300 A/m RMS. The sensitivity of the instrument is 4E-8 SI.

Temperature-dependent magnetic susceptibility (low temperatures) – Low-temperature magnetic susceptibility measurements can be used to characterize magnetic domain size distributions, and to identify the presence of ultrafine-grained superparamagnetic (SP) grains. When the instrument is used in a frequency-sweep mode, certain reductions in the in-phase component of susceptibility with increasing frequency indicate the likely presence of SP material, which causes frequency dependence. Similarly, a non-zero out-of-phase component indicates grains near the boundary of SP and single-domains (SD). When the temperature-sweep mode is used, spikes (e.g., *Verwey* transition in magnetite, near 120 K) or steps (e.g., *Morin* transition in hematite, near 263 K) in the susceptibility curves indicate mineral and magnetic transitions. Cold Curie temperatures can also be determined, because the susceptibility drops to zero above the Curie point.

A Lake Shore *MPMS* instrument at the University of Minnesota's Institute for Rock Magnetism was used to measure select samples at 3 different frequencies (1, 9.99, and 99.94 Hz) and with a range of temperatures from ~0-300 K.

Magnetic hysteresis loop – Ferrimagnets can retain a memory of an applied field once it is removed. This behavior is called hysteresis and a plot of the variation of magnetization with magnetic field is called a hysteresis loop. In such a hysteresis loop (Fig. 3.4) several charactistic features can be recognized. The *saturation magnetization* (M_s) is measured by applying a magnetic field of 1-2 Tesla. This field strength is usually sufficient to saturate most magnetic minerals. Upon reducing the field to zero, the magnetization does not go to zero but persists as a *saturation remanence* (M_{rs}). Increasing the field in the negative direction, a point is reached where the induced magnetization becomes zero. The field at this point is called the *coercivity* ($-B_c$). Increasing the field further in the negative direction results in negative saturation. The *coercivity of remanence* (B_{cr}) is the reverse field which, when applied and then removed, reduces the saturation remanence to zero. It is always larger than the coercive force. The *initial susceptibility* (χ_0) is the magnetization observed at low field strengths (as is measured using the Bartington equipment).

A Vibrating Sample Magnetometer (VSM) instrument at the University of Minnesota's Institute for Rock Magnetism was used to measure select samples.

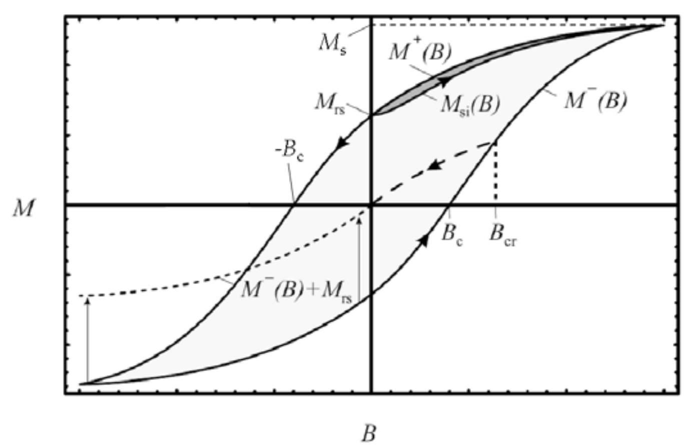

Figure 3.4: Schematic depiction of a (extended) hysteresis loop (after Fabian, 2003). Indicated are the definitions of, amongst others, M_s, M_{rs}, B_c, and B_{cr}.

3.2.3. Laboratory techniques – mineralogy

Chemical dissolution techniques – The content and composition of pedogenic iron oxides was determined by selective chemical dissolution techniques. The total amount of secondary iron oxyhydroxides (Fe_d) was determined using the concentrated citrate-dithionite method (Holmgren, 1967). Poorly crystalline and amorphous iron oxyhydroxides (Fe_o), such as ferrihydrite, were extracted using the hydroxylamine procedure (Chao and Zhou, 1983). Iron content was measured using an Instrumentation Laboratory video 12 flame atomic absorption spectrometer. An increase in Fe_d and Fe_o are both indicative for weathering of mafic minerals from ferrous (Fe^{2+}) to ferric (Fe^{3+}). Amorphous iron oxides (Fe_o) are considered unstable under most conditions and are expected to be present only during initial soil formation, or when the presence of silicate and organics impede formation of crystalline iron oxides (Cornell and Schwertmann, 2003).

X-Ray techniques – X-ray techniques were used to perform chemical, mineralogical, and crystallographic analyses of fine-powdered soil material. X-ray diffraction (XRD) allows for the identification of polymorphic iron oxides (for example α-Fe_2O_3, hematite, and γ-Fe_2O_3, maghemite). However, because of overlapping peaks in the resulting spectrum it is very difficult to make the distinction between lithogenic magnetite (Fe_3O_4) and pedogenic maghemite (γ-Fe_2O_3). Also, XRD cannot be used to identify poorly crystalline minerals such as ferrihydrite ($Fe_5HO_8{\bullet}4H_2O$). We used a Rigaku D/MAX II X-ray diffractometer with a Cu anode to scan over a 2θ range of 2-70° with a step width of 0.03° and a count time of 0.5 seconds per step. The Cu Kα2 peak was removed using JADE software before peak search with the ICDD database and its minerals subset.

X-ray fluorescence spectroscopy (XRF) was used to quantitatively analyze the chemical composition of selected samples. To insure homogeneity, mixtures of 1 gram of finely ground soil material, 9 grams of lithium tetraborate (flux), and 0.25 grams of ammonium nitrate (oxidizer), were fused at 1000° C in a platinum crucible in an oxidizing flame for at least 30 minutes, and then poured into platinum molds to produce glass disks. These disks were used for all analyses using a Bruker AXS S-4 Pioneer, a 4 kW, wavelength dispersive instrument. XRF element analyses were determined by reducing the X-ray intensities using SPECTRAplus software (copyright Bruker AXS), which uses alpha factors to determine the fundamental parameters. Twelve well-known standards were used for calibration. Accuracy was checked by analyzing two known standards.

Thermal analysis – Thermal analysis refers to the study of the behavior of materials as a function of temperature change and gives information on sample composition, thermal characteristics of the sample, and on the products formed during heating (Speyer, 1994; Van Dam *et al.*, 2002). While thermogravimetric analysis (TGA) shows the change in weight with time or temperature, differential thermal analysis (DTA) shows whether specific events are endothermic or exothermic. Several factors such as the heating rate, amount of sample, and particle size, play a role in the shape of the curves and the magnitude of events (Speyer, 1994). We used a Linseis Thermal Balance L81/1550, which is sensitive to the nearest microgram for approximately 250 mg starting weight. The instrument has a temperature range of 20-1550ºC and a variable heating rate of 0.01-50°C/minute.

Changes in magnetic susceptibility as a result of chemical transformations that occur due to temperature variations can be measured with a furnace and susceptibility meter combination. The effect of temperature on magnetic susceptibility ($\chi(T)$) was measured with a CS-2 furnace and a Kappabridge KLY-2 AC susceptibility bridge using a 300 A/m induced magnetic field at a single frequency of 920 Hz in an argon (reducing) atmosphere. A small glass test tube is used to hold approximately 0.5 cm^3 of sample material during the susceptibility measurements. The mass is measured to normalize the recorded susceptibility values to the sample density. The test tube is then placed into a water-cooled jacket integrated in the Kappabridge. A thermo-couple device attached to the furnace rests directly on the sample. Susceptibility measurements began at room temperature and were taken approximately every 18 seconds while the temperature increased at about 10 degrees per minute. Susceptibility was recorded in µSI units, and normalized to mass-specific susceptibility.

3.3. Results

3.3.1 Hawaii

3.3.1.1 Geology and Geomorphology

The islands and the seamounts of the Hawaiian Ridge and Emperor Seamounts include more than 107 individual volcanoes. The chain is age progressive, ranging from 70 to 80 million year old submerged volcanoes in the northwest, to still-active volcanoes at the southeastern end (Clague and Dalrymple, 1989). Commonly accepted theory on the formation of the Emperor Seamount is that the chain of islands formed through a steady movement of the Pacific lithospheric plate over a Hawaiian Hot Spot (‘plume theory’), in which the magma source produces volcanoes on the sea floor. It is worth mentioning, however, that recent geologic and geophysical studies (Hamilton, 2003) argue that common plume theory is derived largely from conjecture, and claim that integrated data better support island formation from a propagating rift (crackspot) due to perpetuation of regional stresses, rather than from a single hotspot. The Hawaiian ridge on the southeastern end of the chain comprises the eight major Hawaiian Islands shown in Figure 3.5. We have studied the islands of Kaho’olawe (lower left), which has an age of approximately 1 million years, and Hawaii (lower right), which is the youngest, with still-active volcanoes.

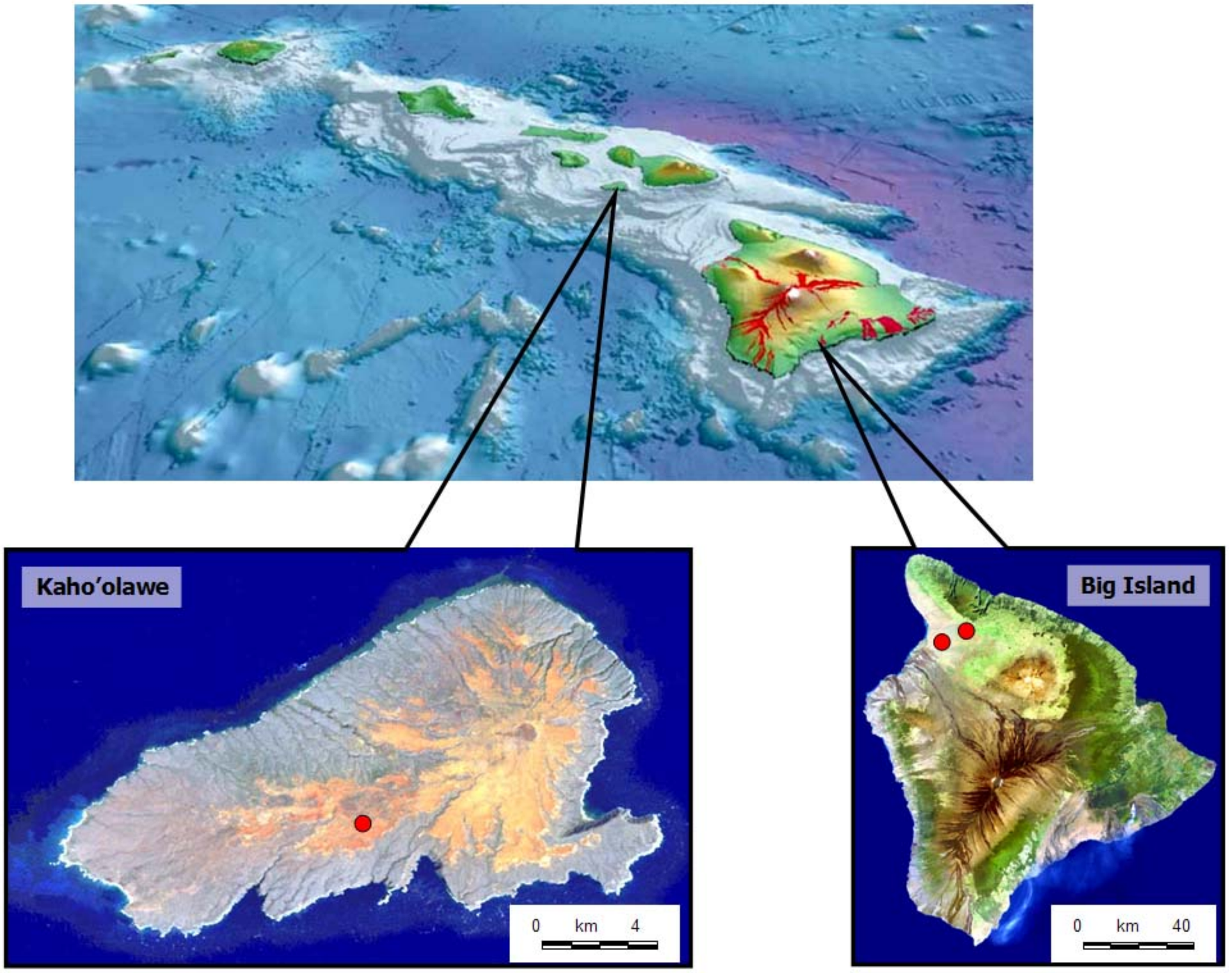

Figure 3.5: Hawaiian Islands (top), Island of Kaho'olawe (lower-left) and Big Island of Hawaii (lower right). The three Hawaiian UXO study sites are identified with red dots. Landsat images and GIS data files available at the Hawaii Statewide GIS Program website: http://www.state.hi.us/dbedt/gis/download.htm.

An idealized Hawaiian volcano evolves through a sequence of four eruptive stages (preshield, shield, postshield, and rejuvenated), distinguished by lava composition, eruptive rate and style, and stage of development (Wolfe and Morris, 1996). Preshield volcanics, formed below sea level, are the oldest parts of a volcano. Shield-stage lavas comprise 95-98% of the volume of the Hawaiian volcanoes and are dominated by tholeiitic basalt. Tholeiitic basalt is relatively rich in silica and poor in alkalic minerals, such as sodium and potassium. On most islands, including the older volcanoes (Mauna Kea, Kohala) on the Island of Hawaii, tholeiitic shield-stage lavas have been capped by postshield lavas (Clague and Dalrymple, 1989). Alkalic postshield basalts are relatively poor in silica and rich in alkalic minerals. The rejuvenated stage, in which small amounts of silica-poor lava erupt, occurs after up to a few million years of dormancy. The primary lithogenic iron oxides in Hawaii rocks are titanomagnetite ($Fe_{3-x}Ti_xO_4$) and ilmenite or titanohematite ($FeTiO_3$). The composition of titanomagnetites varies from x=0 (magnetite) to x=0.8. The end member ulvospinel, with x=1, is rare. The average (titano)magnetite content of the tholeiitic olivine basalts and alkalic basalts, characteristic for Kaho'olawe and Hawaii, is 3.7-4.6% and 3.3-7.4%, respectively. Ilmenite content ranges from 2.5-5.0% and 1.2-6.2% for tholeiitic and alkalic basalts, respectively (Cornell and Schwertmann, 2003; Wedepohl, 1969).

In general, the soils on the Islands of Hawaii contain significant amounts of hematite (α-Fe_2O_3), and magnetite (Fe_3O_4), or maghemite (γ-Fe_2O_3). The source of iron oxides in these soils are the basaltic rocks that contain significant amounts of magnetite and other iron-containing minerals (Wright and Clague, 1989). However, even in soils developed on the relatively uniform parent material of Hawaii the magnetic susceptibility may vary significantly over relatively short distances (Van Dam *et al.*, 2004).

Navy QA range, Kaho'olawe Island, Hawaii – Kaho'olawe is the smallest of the eight major islands in the state of Hawaii and lies approximately 10 km southwest of Maui, as seen in Figure 3.6. It is one of the smallest single-shield volcanoes of the Hawaiian Islands and is 1-2 million years old (Wood and Kienle, 1990). Kaho'olawe has not erupted in historic time and is considered to be extinct. Kaho'olawe is a Koolau-type volcano, characterized by the near-absence of alkalic postshield basalts (Wright and Clague, 1989; p.220). Alkalic flows are present only locally atop the tholeiitic sequence (Macdonald *et al.*, 1983). Potassium-argon dates of postshield alkalic basalts suggest that the island is around 1 million years old (Naughton *et al.*, 1980). The average magnetite and ilmenite content of the tholeiitic and alkali olivine basalts, characteristic for Kaho'olawe lies between 37-46 and 24-50 g/kg (Wedepohl, 1969).

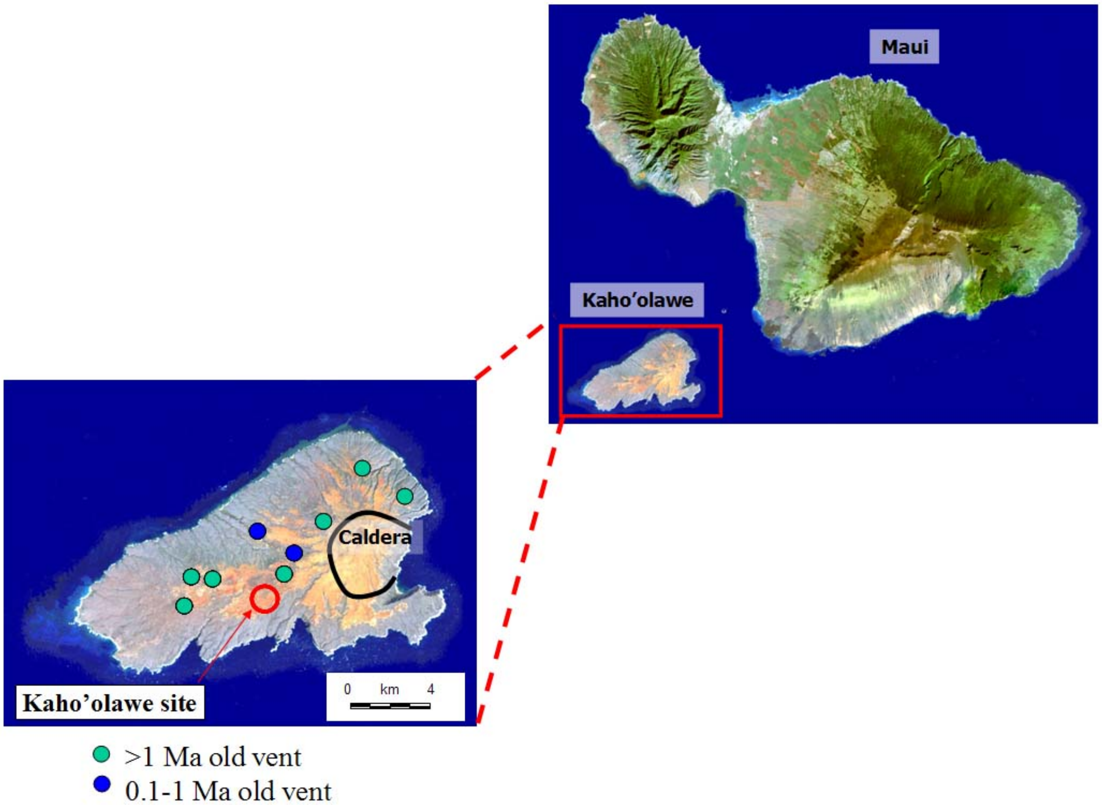

Figure 3.6: Landsat image for islands of Maui and Kaho’olawe (top-right). Landsat image of Kaho’olawe (lower-left). The UXO study site on Kaho’olawe is identified with the red circle. Landsat images and GIS data files available at the Hawaii Statewide GIS Program website: http://www.state.hi.us/dbedt/gis/download.htm.

Due to its position on the leeward side of Haleakala Volcano on Maui and its limited elevation (maximum 450 meters), Kaho’olawe receives very little rainfall throughout the year. The annual rainfall is estimated to range from 250 to 650 millimeters (Macdonald *et al.*, 1983; Nakamura and Smith, 1995). Overgrazing by cattle that were first introduced in 1864 has caused large areas of the island to be stripped of vegetation. The bare surface and the strong trade winds from the east have led to severe soil erosion. The amount of erosion averages 1.5 meters and is locally as much as 2.5 meters (Macdonald *et al.*, 1983). The sparse vegetation of the central plateau consists of piligrass and kiawe trees.

The Navy QA Grid that was selected for our research lies in the Kunaka/Na'alapa province and is dominated by soils of the Kaneloa Series and Puu Moiwi Series (Nakamura and Smith, 1995). The parent material of these soils is strongly weathered volcanic ash over strongly weathered basic igneous rock. The Kaneloa soils reach saprolite (weathered bedrock) within 40 to 75 centimeters from the surface, while the Puu Moiwi soils have a deeper soil cover. New measurement of the magnetic properties and mineralogical composition conducted in this study indicate that the two soils series could be classified as one soil type (Van Dam *et al.*, 2008).

Former Waikaloa Maneuver Area, Hawaii – Hawaii is the youngest and largest of the eight major islands in the state of Hawaii and it consists of five subaerial volcanos and one that is (still) submerged, as shown in Figure 3.7. The ages of the volcanoes range from 0.43 million years for Kohala Volcano in the north to currently active in the south. Potassium-argon dates of shield-stage tholeiitic basalts indicate an age of 0.375 million years for Mauna Kea (Clague and Dalrymple, 1989). This age should be treated with caution as the lava flows at the surface show a wide range of ages (Wolfe and Morris, 1996).

Both the Waimea Geophysical Prove-out (GPO) near the town of Waimea and the Geophysical Prove-out at Waikaloa Village lie on the northwestern flanks of Mauna Kea Volcano in lava flows of the Hamakua Volcanics. Lava flows originated from vents widely distributed over the flanks of Mauna Kea and have both alkalic and tholeiitic characteristics. The rocks contain variable amounts of olivine, plagioglase and clinopyroxene phenocrysts (Wolfe and Morris, 1996). Rocks of the Hamakua Volcanics have been Potassium-argon dated between 250 and 65 thousand years (Pleistocene).

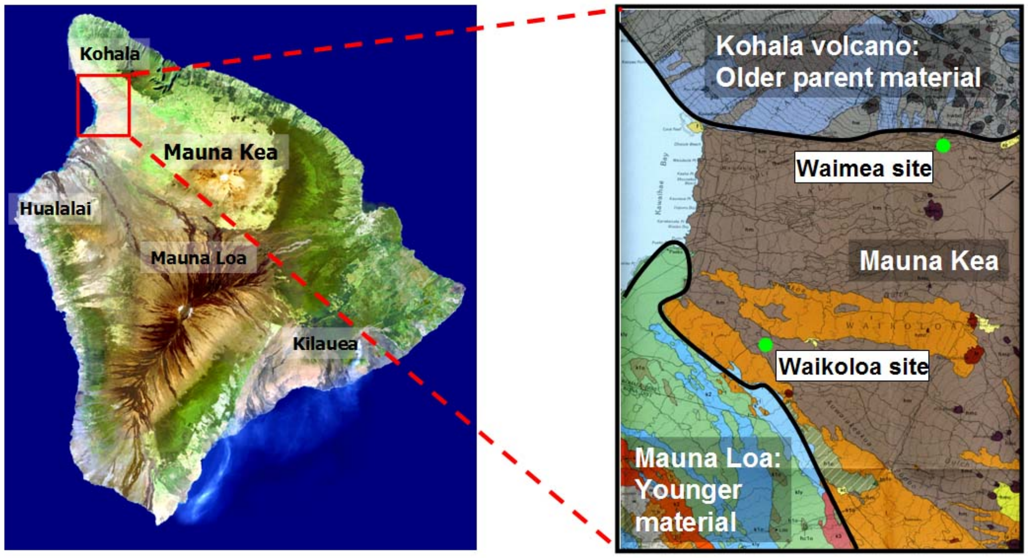

Figure 3.7: Landsat image of Big Island of Hawaii, HI (left). Surface geology map (right) identifying surface lava flows around the UXO study sites of Waimea and Waikoloa. The two sites, identified with green circles are on Mauna Kea surface flows of the similar age. Landsat images and GIS data files available at the Hawaii Statewide GIS Program website: http://www.state.hi.us/dbedt/gis/download.htm; GIS data for surface geology map available at the USGS Hawaiian Volcano Observatory website: http://hvo.wr.usgs.gov/products.

The parent material of the soils at both sites is basalt, covered by local tephra falls and eolian deposits of variable thickness. Mean annual rainfall ranges from to 150 to 500mm near Waikaloa Village to 1500mm near Waimea. As a result, the soils at the Waimea Geophysical Prove-out are stronger developed than those at the Geophysical Prove-out at Waikaloa Village, where soils are mostly stony and are characterized by surface rock outcroppings and eolian deposit. The Waimea soils are characterized by a shallow organic-rich soil over shallow bedrock. Rocks are common at the surface at both locations.

3.3.1.2 Soil Descriptions

The soil in pit A (KH-A) is located in an area of low magnetic background (Walker *et al.*, 2005) and magnetic susceptibility readings. The area has been significantly eroded. Weathered bedrock is found within 40 cm of the surface (Fig. 3.8). A very thin remnant of a lower B horizon lies directly over the Cox horizon. The surface color at this site is yellowish to dark grey to green, similar to what is seen at depth in the bedrock. The entire soil profile is dominated by partly weathered basalt or saprolite. The Cox1 and Cox2 horizons below the Bw/Cox horizon are characterized by increasing amounts of saprolite. This soil, at the highest elevation of the four soil pits, has been subject to more severe erosion than the other soils. Before the erosion started, the Bw/Cox horizon exposed at the surface here, was located below A and B horizons in the profile.

Soil profile B (KH-B), the only one located within the 2E Grid, has the highest magnetic background readings of any site (Walker *et al.*, 2005). In appearance, the soil is very similar to KH-C and KH-D, although the upper horizon appears more purple, perhaps indicating a higher hematite content. Six horizons were identified, all of them showing significant weathering (Fig. 3.8b). There is no strong indication of clay translocation in the soil. Originally, these horizons may have been formed under an A horizon, characterized by the accumulation of organic matter, as found in most of the other soil types on Kaho'olawe (Nakamura and Smith, 1995). Its absence demonstrates the erosive history of the soil. Starting from a depth of around 0.4 meters the soil color gradually changes from red (10R) to yellowish red (5YR). Below 1.1 meters, the amount of unweathered parent material in the soil increases, and the physical properties start to resemble the material in soil KH-A.

The profiles and horizon characteristics of soil KH-C and soil KH-D are very similar to that of soil KH-B and are not discussed in detail in the remainder of the paper. One notable difference of soil KH-D with the other soils is the 20-cm thick layer of eolian or fluvially deposited material on top of the original profile. This soil is in a topographic low and has accumulated eroded material from the soils upslope.

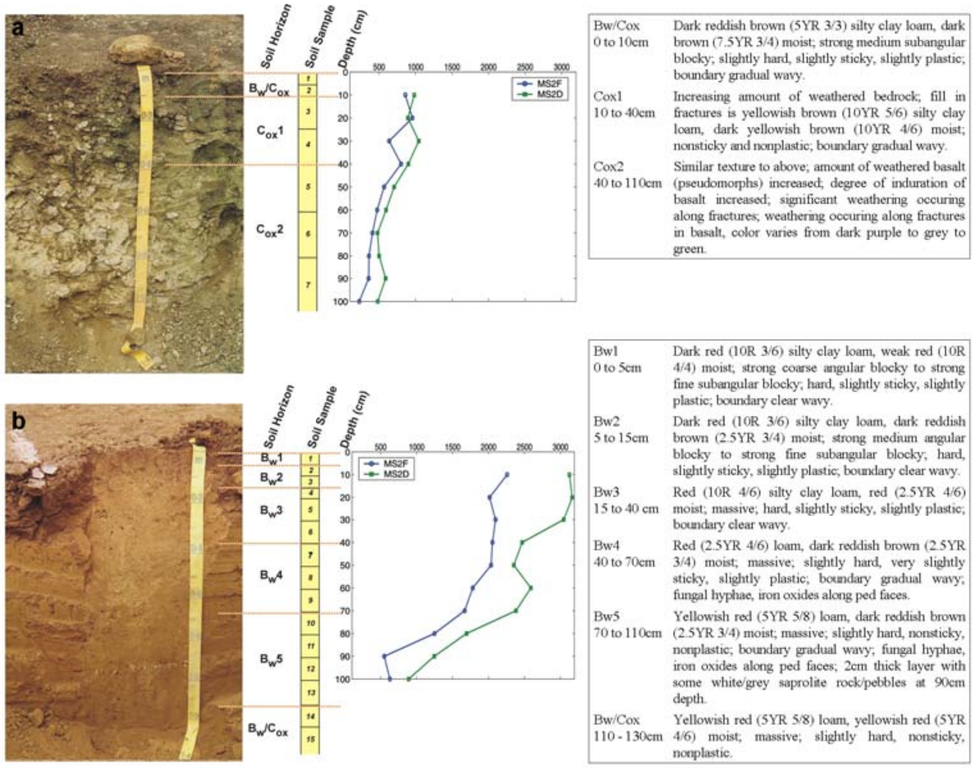

Figure 3.8. Pictures and description of a) soil KH-A and b) soil KH-B on Kaho'olawe Hawaii. Field measurements of magnetic susceptibility using Bartington MS2D and F sensors are included (values given in 10^{-5} SI); see **Fig. 3.1** for the location of these soil pits.

3.3.1.3 Magnetic Measurements

Low-field-strength magnetic susceptibility – The MS2 and MS2B were used to measure the magnetic susceptibility and its frequency dependence of soil samples collected in the field. We measured 35 surface samples from QA 2E grid on Kaho'olawe Island, and 49 samples from soil pits. One of the surface samples from Kaho'olawe was lost during transportation bringing the total surface samples to 34.

A contour plot of the surface susceptibility readings for Kaho'olawe indicates a change from high values in the west and north of the grid to lower values in the east to southeast (Fig. 3.9a). The region of large susceptibility corresponds to the area with a high TEM signal strength (Walker *et al.*, 2005). The values are comparatively much higher than on Waimea and Waikoloa (Fig. 3.9b,c). At the Waimea site the ground surface was covered by grass and a shallow litter layer. The low bulk density and the high organic matter content reduce the susceptibility readings.

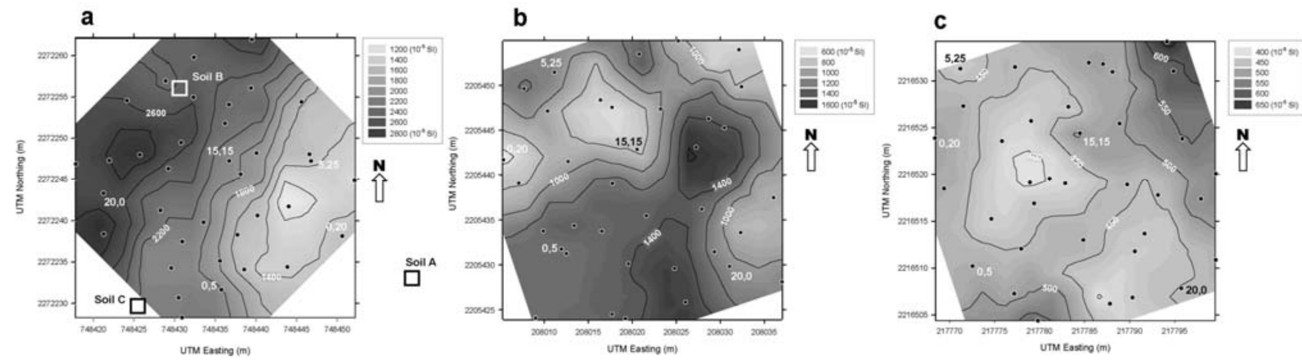

Figure 3.9: a) Surface soil magnetic susceptibilities (corrected for air drift) measured in the field using a Bartington MS2 sensor with D-loop at a frequency of 0.958 kHz at a) Kaho'olawe, b) Waikoloa, and c) Waimea field sites. The "●" symbols indicate the exact locations of the measurements, distributed according to a stratified random sampling scheme in the 30x30m grids. Sample material from the numbered locations (0,5; 0,20; 5,25; 15,15; 20,0) has been used for additional analysis. The open squares give locations of the soil pits.

The laboratory Bartington measurements with the MS2B sensor system indicate a very large magnetic susceptibility in the top horizons of soils KH-B and KH-C (Fig. 3.10). Below a depth of 0.7 meters the magnetic susceptibility decreases significantly to similar values as found in soil KH-A. The high magnetic susceptibility values in the Bw1-Bw4 horizons (Fig. 3.8) are probably associated with the increase in concentration of iron oxides, which are the most stable end product for low-pH soils in this climate. In soil KH-A the magnetic susceptibility values are much lower than those in soil KH-B, and similar to values found for unweathered, fresh basalt from the Big Island of Hawaii (Fig. 3.10). The magnetic susceptibility values (measured with the MS2D sensor) for the top horizons (Bw) in Pits KH-A and KH-B (1000 and $3000 \cdot 10^{-5}$ SI, respectively) are consistent with those observed in the surface measurements (Fig. 3.9).

Dual frequency measurements (Bartington MS2B) show that the frequency dependence is lowest in soil KH-A. In the soils KH-B and KH-C the frequency dependence is higher (Fig. 3.10c,d). From these numbers it follows that in soil KH-A superparamagnetic minerals are mostly absent.

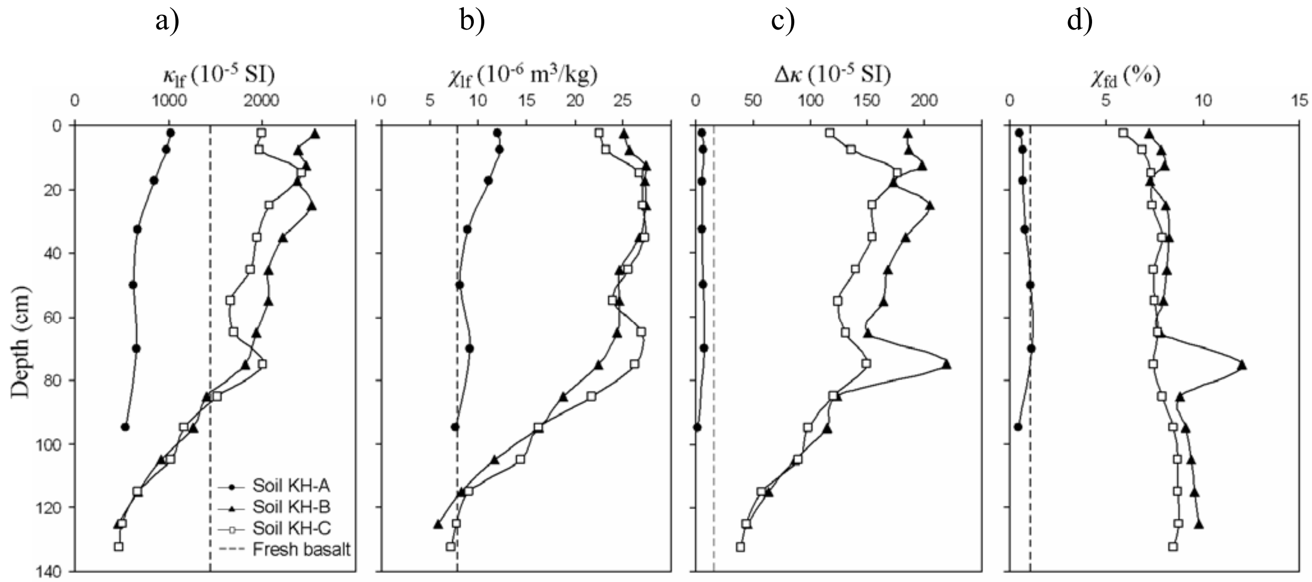

Figure 3.10: Results of magnetic susceptibility measurements for soils A, B, and C, measured using the Bartington MS2 system with B sensor. a) Low-frequency (0.46 kHz) volume-specific susceptibility (κ_{lf}), b) low-frequency mass-specific susceptibility (χ_{lf}), c) difference between volume-specific susceptibility measured at 0.46 and 4.6 kHz, which is a good measure for amount of viscous remanent magnetization and d) percent frequency dependence, measured at 0.46 and 4.6 kHz, which is a measure amount of neo-formed ultra-fine ferrimagnetic minerals.

Frequency-dependent complex magnetic susceptibility – Complex magnetic susceptibility measurements were made at the University of Minnesota's Institute for Rock Magnetism (IRM) using the LACS. A total of 76 samples have been measured from Hawaii. The samples are as follows:

(1) 62 samples from Kaho'olawe with magnetic susceptibilities that range from 8.6 x 10^{-7} to 3.46 x 10^{-5} m3/kg S.I. (35 from the surface and 27 from the soil pits)

(2) 7 surface samples from Waimea with magnetic susceptibilities that range from 3.48 x 10^{-7} to 1.15 x 10^{-5} m3/kg S.I.

(3) 7 surface samples from Waikoloa soils have magnetic susceptibilities that range from 5.3 x 10^{-7} to 2.56 x 10^{-5} m3/kg S.I.

Results from the LACS measurements exhibit varying degrees of frequency dependence, as illustrated in Figures 3.11 and 3.12. The susceptibilities of samples showing a frequency dependence are characterized by real components that decrease linearly with increasing logarithmic frequency and imaginary components that are near several orders of magnitude smaller than the corresponding real component and remain constant with frequency.

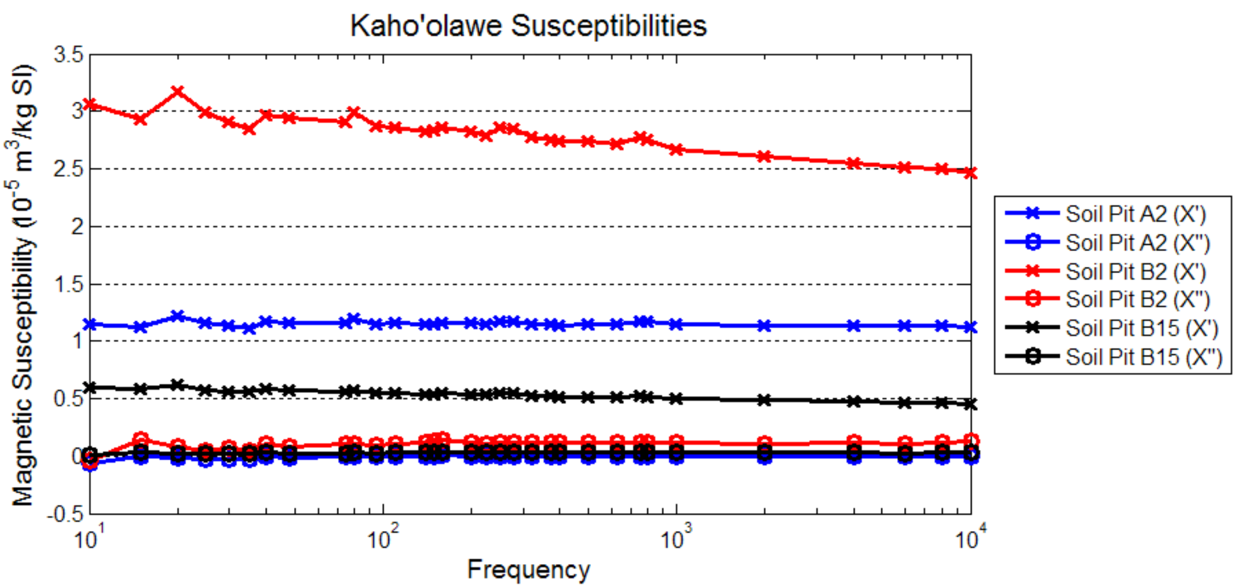

Figure 3.11: Frequency dependent magnetic susceptibility measurements with the LACS for soil samples from Pits A and B at Kaho'olawe. Lines with circles represent the imaginary components and lines with x-marks are the real components.

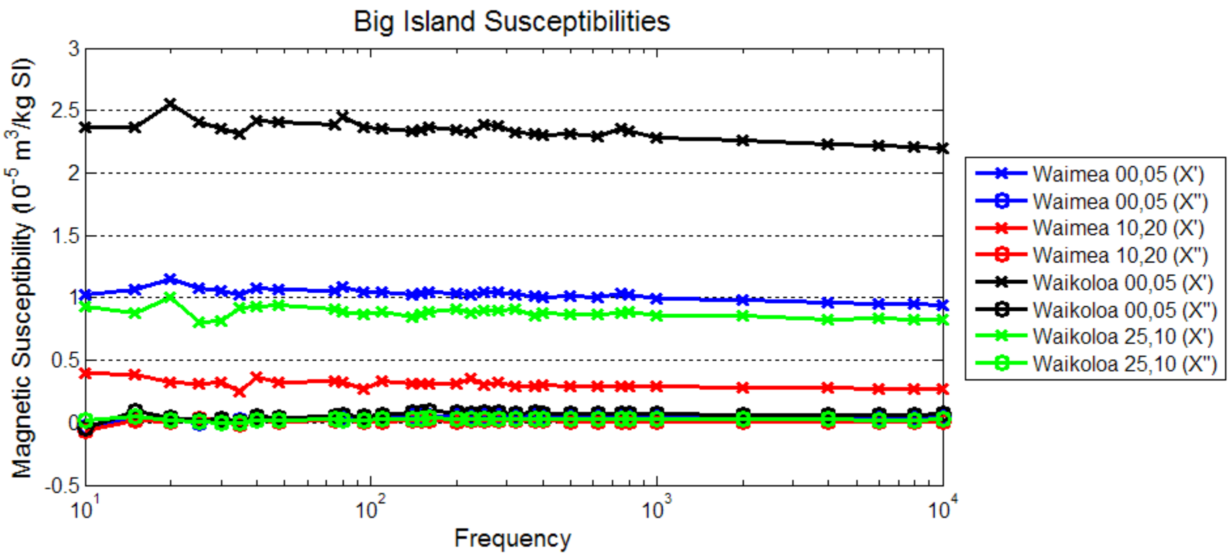

Figure 3.12: Frequency dependent magnetic susceptibility measurements with the LACS for surface samples at Waimea and Waikoloa. Lines with circles represent the imaginary components and lines with x-marks are the real components.

This is the first observational confirmation of the major conclusion drawn from theoretical work during the SEED UX-1285: i.e., if soil is comprised of magnetic domains having a wide range of relaxation times, its complex susceptibility will exhibit a strongly frequency-dependent real component and a much smaller and nearly constant imaginary component. This form of complex susceptibility leads to the strong 1/t decay of TEM data that masks UXO responses. This is a significant finding. It both confirms an earlier result that formed one of the cornerstones of the current project, and provides us with solid laboratory and observational data to make significant progress in the next stages.

The soil pits at Kaho'olawe allowed the mapping of the magnetic susceptibility as a function of depth. Soil samples were collected at different horizons in each pit. LACS measurements were conducted on all soil samples from pits A and B. Figures 3.13 and 3.14 show the variation in the magnetic susceptibility at two frequencies as a function of depth in soil pits A and B at Kaho'olawe.

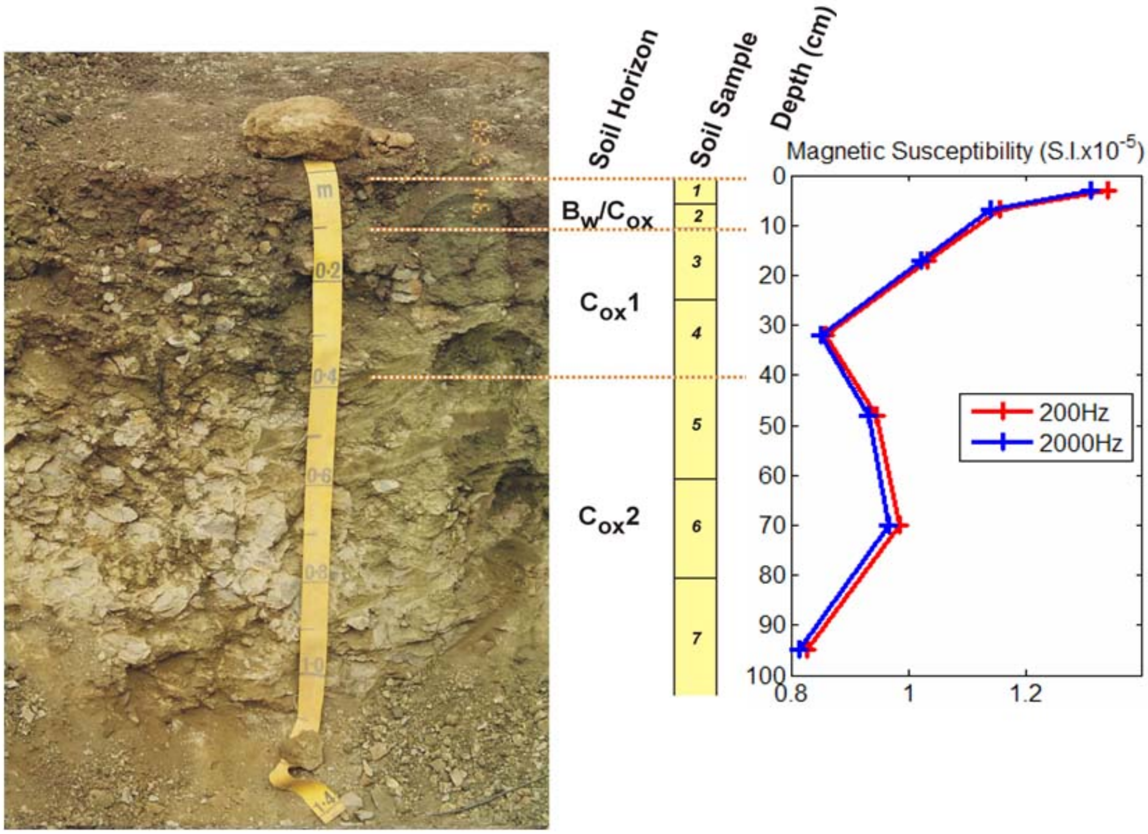

Figure 3.13: Magnetic susceptibility as a function of depth for Soil Pit A at Kaho'olawe.

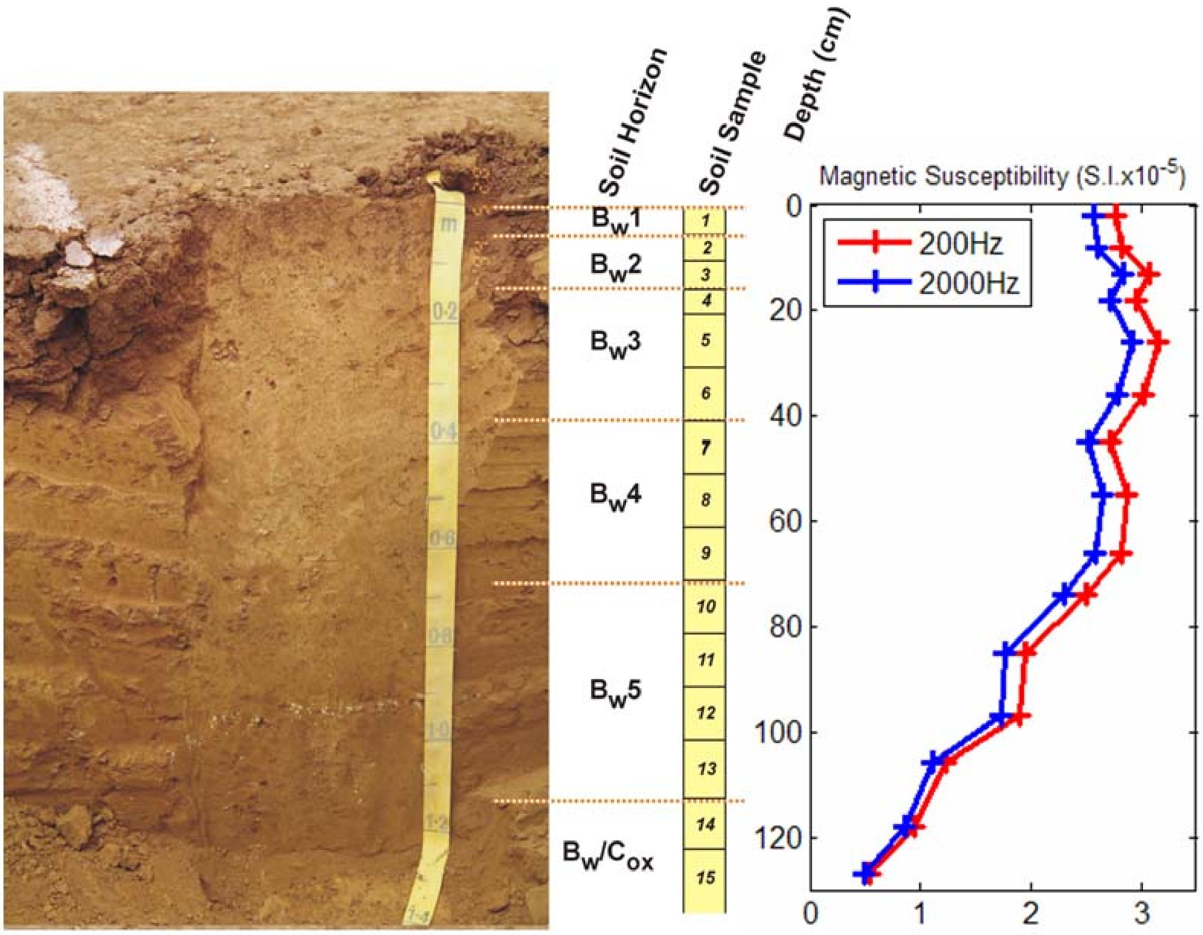

Figure 3.14: Magnetic susceptibility as a function of depth for Soil Pit B at Kaho'olawe.

Temperature-dependent magnetic susceptibility (high temperatures) – Using a Kappabridge KLY-2 AC susceptibility bridge and CS-2 furnace the magnetic susceptibility was measured over a broad temperature range of 30 to 650°C for a total of 8 samples from soils KH-A and KH-B and 3 surface samples from the three field locations. The susceptibilities at the start of the measurements (indicated by a closed symbol, Fig. 3.15) agree reasonably well with the values found with the MS2 system (Fig. 3.10). Differences may be explained by inter-sample variations in mineralogy and by equipment effects (magnetic field strength and frequency). The large discrepancy between starting susceptibility and that measured with the MS2 system for sample KH-B15 is not understood at this point.

The results reveal the presence of several key processes. The first is the general increase in susceptibility as the temperature increases from room temperature to around 300°C. This is possibly the result of the production of small amounts of magnetite or maghemite under the influence of organic matter (Tite and Linington, 1975). Another process is the broad peak in the susceptibility around 300°C, which is most likely associated with the dehydroxylation of goethite, which was also observed in TGA and DTA analyses (Van Dam *et al.*, 2008). Between around 450 and 520°C, the susceptibility rapidly decreases and then completely disappears. This effect is the result of the transformation of maghemite to hematite; a process that, under reducing conditions, is absent in magnetite (Cornell and Schwertmann, 2003). This result shows that no lithogenic or pedogenic magnetite exists in any of the samples; lithogenic magnetite would retain its high susceptibility over the entire temperature range.

A number of differences were observed between the curves from soil KH-A and KH-B (Figures. 3.13 and 3.14, respectively). The decrease in susceptibility associated with the transformation of maghemite to hematite starts at a lower temperature for the samples from soil KH-B than those from soil KH-A. The different return curves differ markedly between samples from soil KH-A and KH-B; samples from soil KH-A show a gradual increase in χ with cooling, while sample KH-B5 is characterized by a rapid increase, followed by a decrease in χ. The observed differences in $\chi_{(T)}$ curves between samples from soils KH-A and KH-B may be used as an estimate for the amount of hyperfine maghemite present, which would be an important new way to characterize the presence of superparamagnetic minerals. However, because the processes and rates of thermal interconversions between maghemite and hematite are dependent on crystal size (Cornell and Schwertmann, 2003), more research is required to make quantitative estimates of the proposed relationship between $\chi_{(T)}$ and hyperfine maghemite.

Temperature-dependent magnetic susceptibility (low temperatures) – Four samples from Kaho’olawe (KH-A1, KH-A9, KH-B1, and KH-B15) were selected for analysis using the low-temperature *MPMS* equipment (Fig. 3.16). The result of these measurements is that samples KH-B1 and KH-B15 show a distinct paramagnetic signature, while the two KH-A samples do not (IRM, *personal communication*). The measurements performed on the two KH-A samples also indicate the presence of illmenite and magnetite. The presence of illmenite is an indication for the relatively low weathering state of soil KH-A, which is consistent with XRD measurements (Table 3.3, page 122).

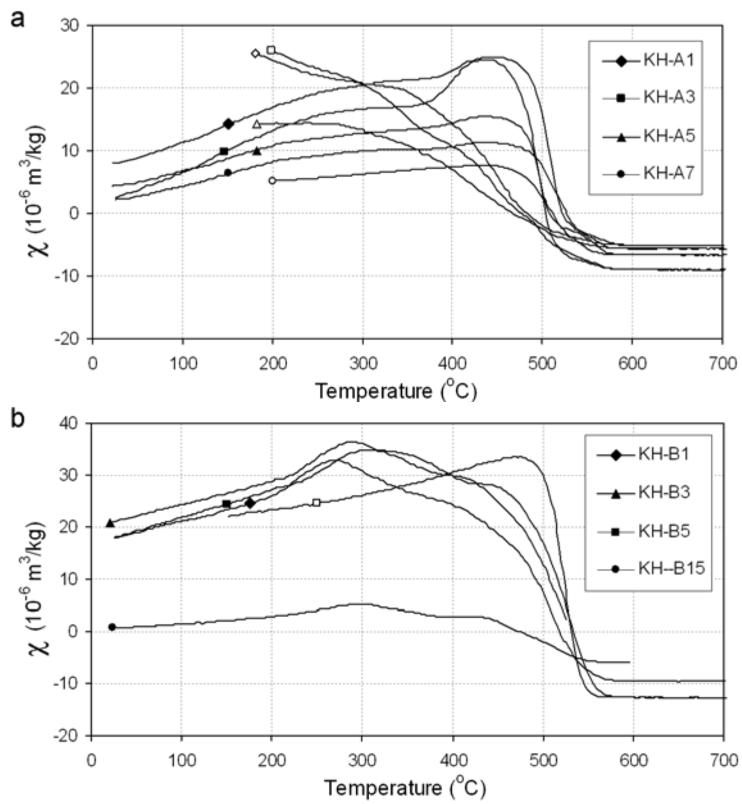

Figure 3.15. Plots of magnetic susceptibility versus temperature for samples from a) Kaho'olawe soil A, and b) Kaho'olawe soil B. Sample codes refer to those in Table 3.4 (page 123). The start of each curve is marked with a closed symbol. The return curves that show the change in magnetic susceptibility for decreasing temperatures are, where present, marked with an open symbol.

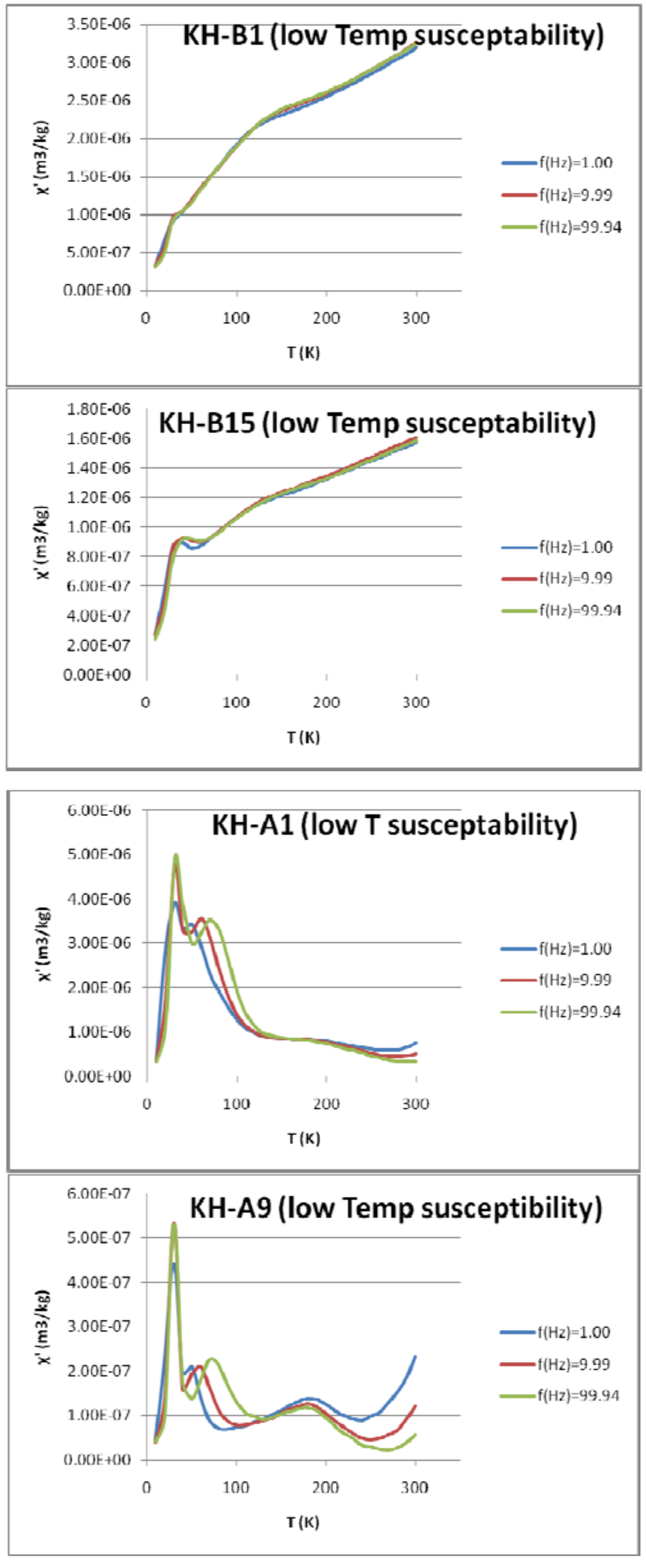

Figure 3.16: Results for low-temperature *MPMS* measurements at three frequencies.

Magnetic hysteresis loop – The various hysteresis parameters are not solely intrinsic properties but are dependent on grain size, domain state, stresses, and temperature (Cornell and Schwertmann, 2003). Results of the VSM measurements are given in Table 3.2 (page 121). In Fig. 3.17 the data have been plotted as the ratio of saturation remanence and saturation magnetization versus the ratio of remanence coercivity and coercivity (see Fig. 3.4 for reference). These data suggest that the ferrimagnetic phases in the Kaho’olawe soils are of pseudo-single domain type (PSD). However, these are difficult to interpret definitively as all analyzed samples are heterogeneous mixtures of different minerals.

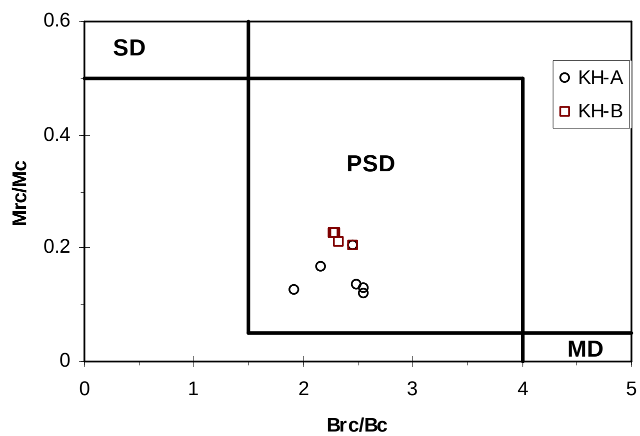

Figure 3.17. Ratio of saturation remanence and saturation magnetization versus the ratio of remanence coercivity and coercivity for samples from Kaho’olawe (Table 3.2, page 121). The fields for single domain (SD), pseudo-single domain (PSD), and multi domain particles (MD) are given for magnetite.

3.3.1.4 Mineralogy

X-Ray Diffraction (XRD) – Four soil samples from different depths in the soil pits A and B have been analyzed using XRD (Table 3.3, page 122). Soil A is characterized by the abundance of numerous minerals at all depths in the profile. Kaolinite is only present in the top 2 samples. Soil B is dominated by iron oxide minerals goethite, hematite, and magnetite in the top three samples. The lowermost sample has several characteristics of the material in soil A: both gibbsite and muscovite are present and only an indication of the presence of hematite and magnetite is found. The presence of illmenite in Soil A is consistent with low-temperature magnetic data.

X-Ray Fluorescence spectroscopy (XRF) – XRF analysis was performed on 5 surface samples from the Kaho'olawe, Waimea, and Waikoloa field sites, as well as two samples of unweathered basalt from Kohala Volcano on the Big Island of Hawaii (Table 3.4, page 123). The samples can be grouped according to weathering stage. High calcium and silica contents show that the Big Island basalt samples are the least weathered (Fig. 3.18a, b), followed by the material from Waikoloa and Waimea. The Kaho'olawe soil samples are most intensely weathered, but the surface samples show that the mineralogy varies widely, depending on the location in the grid. The degree of weathering increases from the saprolite in soil KH-A (A9 in Fig. 3.18b), through the lower weathered horizons (Bw/Cox horizon in soil KH-B; B15 in Fig. 3.18d), to the material in the B horizon of soil KH-B (sample B5 in Fig. 3.18c).

Analysis of the XRF results indicates that initial weathering of the basaltic rocks causes calcium to disappear (Fig. 3.18a) and silica contents to decrease (Fig. 3.18b), leading to a relative enrichment of aluminum and iron. Continued weathering leaches out aluminum and increases iron content (Fig. 3.18c). Iron content is linearly correlated ($R^2 = 0.97$) to titanium (Fig. 3.18d), which is considered to be very stable and least subject to transformations and phase changes. The titanium to iron ratio agrees well with values reported in literature for basic extrusive rocks (Piper, 1987).

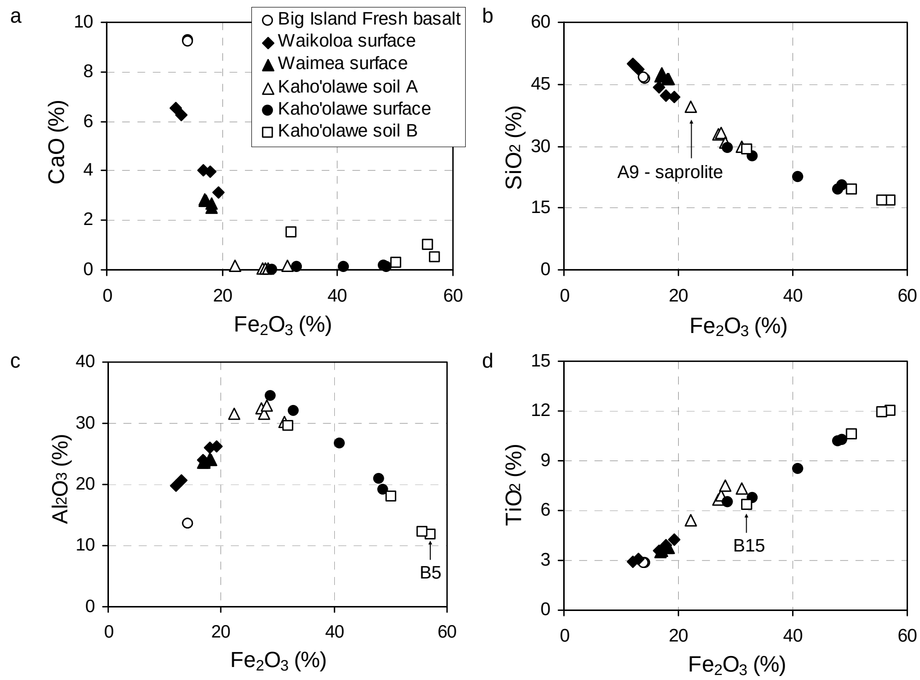

Figure 3.18: Results of XRF measurements for different datasets from Kaho'olawe and Big Island of Hawaii (see also Table 3.4, pg. 123). All values have been adjusted for loss on ignition. Samples "A9", "B5", and "B15", which are discussed in the text, are identified for clarity.

Thermogravimetry – Thermal analysis has been used to analyze one sample from each soil; KH-A3 from a depth of 0.1 to 0.25m in soil A, and KH-B5 from a depth of 0.2 to 0.3m in soil B. The TGA curves (see Van Dam *et al.*, 2008 for graphs and additional details) show a number of clear weight loss events that can be recognized for both samples, around 100, 300, 450-500, and 1400-1450°C. The DTA curves show events at similar temperatures, but indicate the presence of two extra events at around 80°C in sample KH-B5 and at 900°C in sample KH-A3. In the DTA curves negative peaks denote endothermic reactions (i.e., consuming heat) while positive peaks indicate exothermic reactions (i.e., giving off heat).

In Table 3.5 (page 124), the observed events are correlated with literature data on thermal behavior of soil material. The strong weight loss between the start of the measurements and 120°C is caused by the evaporation of free water from the pores. The exothermic reaction at 80°C in sample KH-B5 is possibly due to the presence of a small amount of organic material in the sample. The endothermic effect at around 280°C occurs in both samples and is probably at least partly due to the dehydroxilation of goethite and other minerals with "$\cdot H_2O$" groups. The weight loss event at around 500°C is possibly caused by loss of structural water from kaolin and/or mica type clay minerals. Between about 600 and 1400°C the TGA weight loss is negligible. Nevertheless, the DTA curves indicate an exothermic effect in sample KH-A3 at 900°C, which is most probably caused by a chemical or structural change in the clay mineral kaolinite or muscovite. The drop in the DTA curves around 1380°C is the result of the melting of hematite. The drop is largest in sample KH-B5, which is expected to have the largest amount of hematite.

Chemical Extractions – The content and composition of pedogenic iron oxides on Kaho'olawe was determined by citrate-dithionite and hydroxylamine selective dissolution methods. Soil KH-A has lower values of Fe_d% and Fe_o% than the other three soils (Fig. 3.19), demonstrating the relatively low level of weathering in soil KH-A. Amorphous secondary iron oxyhydroxides (Fe_o) are considered unstable in tropical climates and are expected to form only during initial soil formation. For all soil profiles, the amount of Fe_d is larger than the content of Fe_o. In addition, the Fe_o/Fe_d ratios are very small, which is indicative of the general maturity of the soils.

An important difference between the measured values for Fe_d% and Fe_o% is the observed change in pattern below 100 cm depth for soils B and C. While the Fe_o% values remain relatively constant below 100 cm depth (Fig. 3.19a), the values for Fe_d% show a clear decline. This pattern is also observed in the measurements for frequency dependent susceptibility and χ_{lf} (Fig. 3.10). It appears that the amount of frequency dependency, and thus, the amount of superparamagnetic minerals, can be estimated using the hydroxylamine extraction of amorphous iron oxyhydroxides.

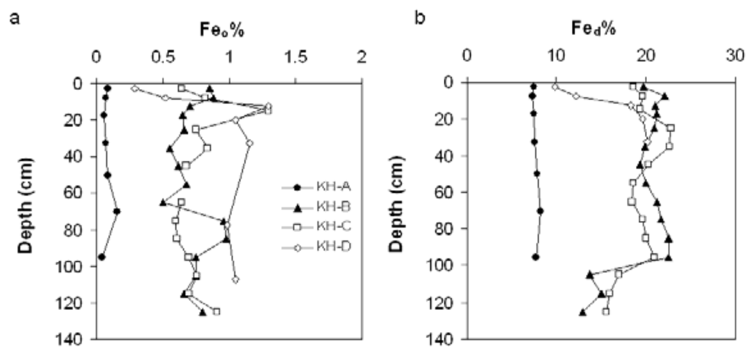

Figure 3.19: Results of selective chemical dissolution of pedogenic iron oxides using an Instrumentation Laboratory video 12 flame atomic absorption spectrometer for soils A, B, C, and D. a) Total amount of secondary iron oxyhydroxides (Fe_d). b) Poorly crystalline and amorphous iron oxyhydroxides (Fe_o).

3.3.2 Montana – Chevallier Ranch

3.3.2.1 Geology and Geomorphology

The Chevallier Ranch UXO site, Figure 3.20, has three distinctly different parent materials that vary over short distances. The primary parent material of the Chevallier Ranch UXO site is Precambrian-age Spokane Shale. A 60 to 55 million year old (Paleocene) volcanic intrusion is found in the northwestern area of the Chevallier Ranch UXO survey site. The intrusion is characterized by a large abundance of Fe-Mg minerals (hornblende, pyroxene, olivine, and possibly magnetite). Several narrow (tens of meters) volcanic dikes, characterized by similar material as in the plug, are radiating from the plug. Several of these dikes are found under the survey area. Coarse gravel and cobbles deposited in ephemeral streams that dissect the site form the third type of parent material. The lithology of the deposited material is mostly shale, but occasionally volcanic rock is found as well. All three types of parent material have been found in the study area covering 200 by 200 m^2. The site is located 6 km north of the Scatch Gravel Hills, which is the northernmost part of the Boulder Batholith.

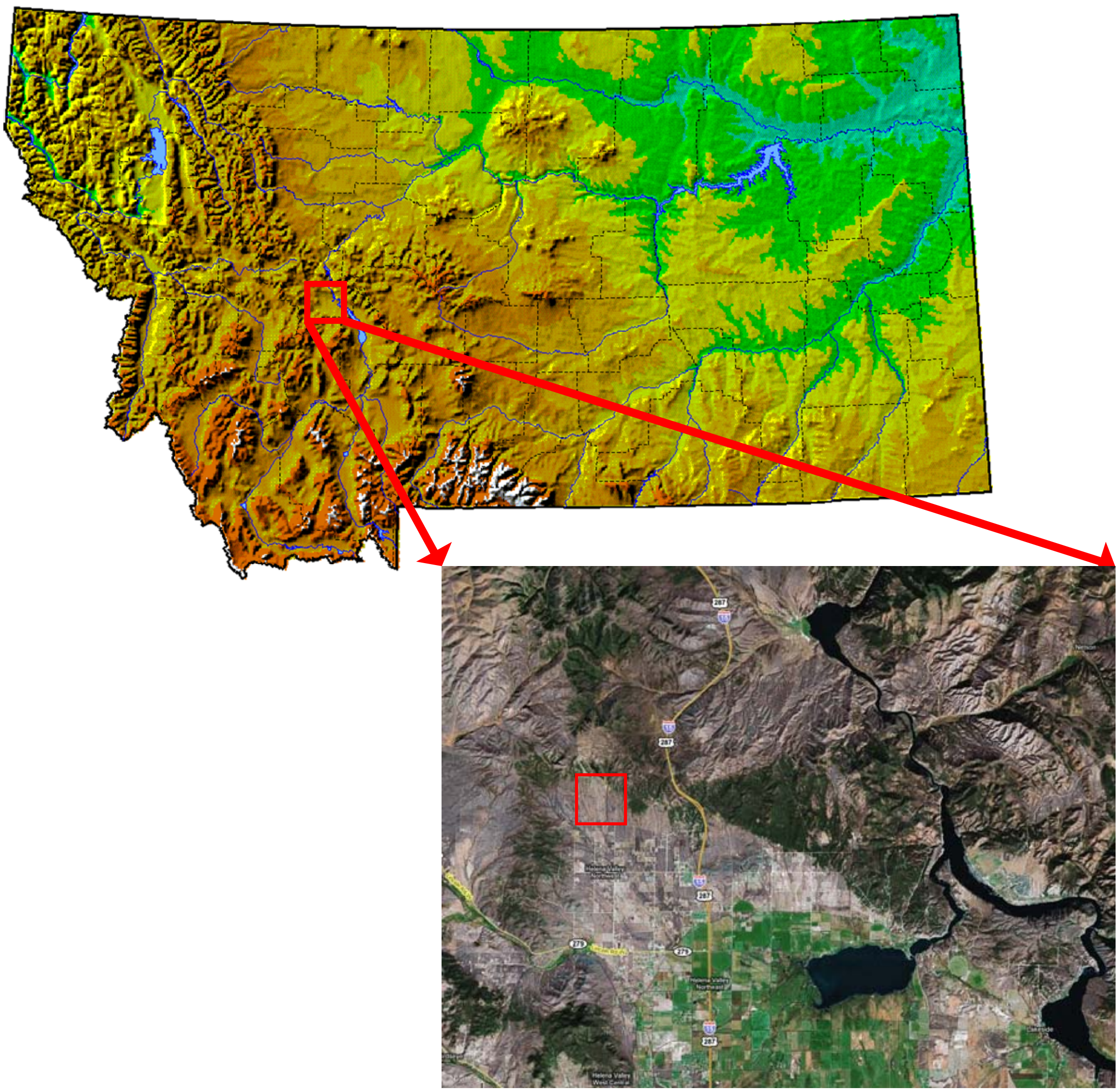

Figure 3.20: The Chevalier Ranch field site in Helena Montana (top image retrieved from www.geology.com, bottom image from www.maps.google.com)

The survey area is a broad open plain that ranges in elevation from 1270 to 1340 m and gently slopes off toward the south to south-southeast. Several ephemeral streams dissect the area. These streams may be collection areas for heavy minerals such as magnetite, as evidenced by the small black-sand lag (or placer) deposits in the drainage channels. Alternatively, channel erosion may lead to a smaller depth to bedrock, which in the case of a volcanic dike may cause a higher magnetic background signal. The vegetation at the site is predominantly sage brush, grass, and some pine trees. Most of the gridded site has a 3-4 degree slope towards the southeast. Outcrops of shale are found in several locations, especially along streams and on a small hill at the NW of the study site (parking location).

3.3.2.2 Soil Descriptions

Soils at the Chevallier Ranch are very hard, dry to slightly moist at depth, with a defined, leached calcic layer at the lower B to upper C horizon, and small shale/argillite chips 0.25 to 0.5 inch in size (derived from the Proterozoic-age Spokane Shale). The mostly young soils are generally weakly developed, reflecting the slow soil-forming conditions (Van Dam *et al.*, 2006). Most soils have a thin organic horizon and are characterized by carbonate precipitation in the B and C horizons, typical for desert-like conditions. In most soils clay content is low and gravel content, which increases with depth, is up to 40%. The soils are highly variable over short distances and reflect their parent material and relative position in the landscape. Soil horizon descriptions are given in Table 3.6 (page 125).

3.3.2.3 Magnetic Measurements

Field and laboratory measurement of magnetic susceptibility show that soils at the Chevallier Ranch have much lower values than those from Kaho'olawe (Fig. 3.21, 3.22, 3.23). The soil material is characterized by a low frequency dependence, regardless of the parent material and soil horizon. However, the magnetic susceptibility is correlated with the parent material, as is apparent from the magnetic measurements of surface grab samples (summarized in Fig. 3.23). The results of the variation in magnetic properties with depth measured with the Bartington MS2B for the samples from nine soil pits are shown in Fig. 3.20. The top four plots show the results for the five soils that have a relatively low magnetic signal, while the lower four plots are for the four soils with a (partially) higher magnetic signal. The magnetic characteristic for soil CR1, which is located directly above one of the feeder dikes (Fig. 3.2), is similar to that of soils away from the volcanic neck. Thus, the depth to the top of the feeder dike is larger than the depth of the soil pit.

Figure 3.21 shows the magnetic susceptibility as a function of frequency as measured with the LACS. Measurements below 25Hz were removed for the plot. Frequency dependence of the susceptibility is still evident but not to the extent seen in Hawaii. Chevalier Ranch soils have magnetic susceptibilities that range from 2.28×10^{-8} to 1.76×10^{-5} m^3/kg S.I. (13 samples measured).

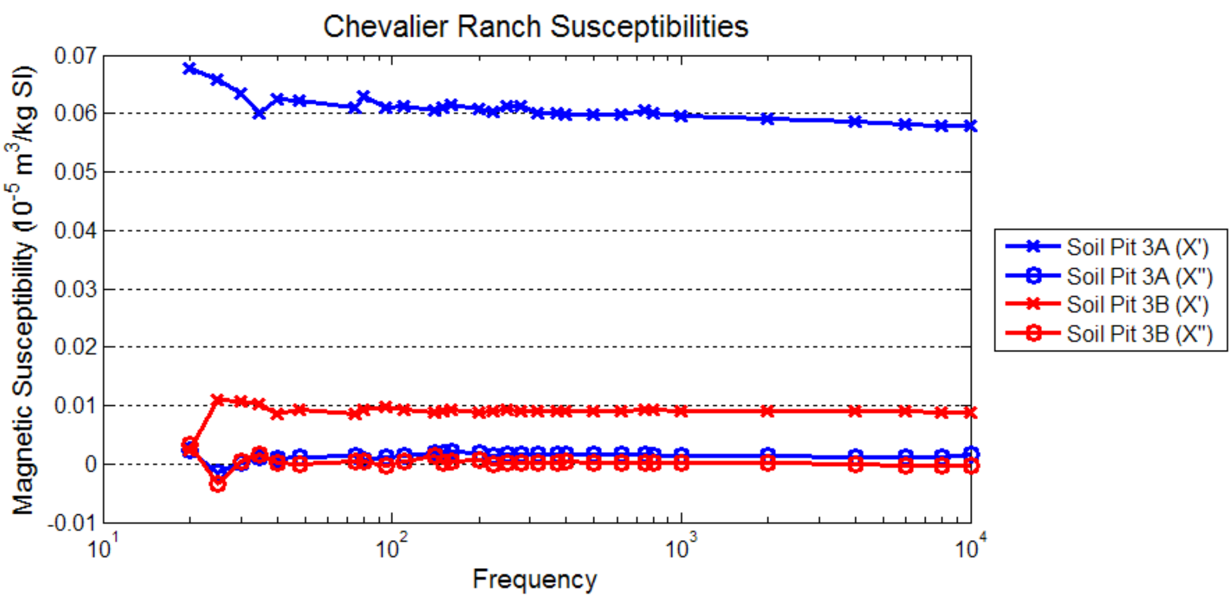

Figure 3.21: Frequency dependent magnetic susceptibility measurements with the LACS on soil pit samples from Chevalier Ranch.

The two soils located directly above and on the edge of the volcanic neck (CR5 and CR4, respectively), have magnetic susceptibilities mostly similar to the other soils. However, both these soil pits reached the weathered top of the basaltic neck near the bottom of the pit; the lowermost sample in each of these two soil pits was collected from the basaltic material. All measures of magnetic susceptibility, except the percent frequency dependence, increase sharply for this bottom sample (Fig. 3.22). The frequency dependence remains low because there are no neo-formed superparamagnetic ferrimagnetic minerals associated with the parent material (the spike in FD% for the 80cm deep sample in CR4 is unexplained). The magnetic measurements in soil pits CR4 and CR5 suggest relatively little mixing between the basalt and the overlying soil material. The dominant soil material is unweathered and angular Spokane Shale fragments, similar to that in the other soils. These findings are a strong indication for the recent sedimentary origin of the material at this site. We believe the material may have been deposited during the Quaternary in glacio-fluvial outwash plains.

Soil pits CR8 and CR9 were excavated over an area with high-frequency anomalies present in the magnetic field data (Fig. 3.2). The narrow shape of these anomalies suggests that they are associated with near surface features. To maximize identification, the two soil pits were excavated as small trenches perpendicular to “arms” of the anomalous feature. Three vertical profiles, each one meter apart, were sampled in both soil pits. The results showed very little difference between the different profiles and have been averaged (Fig. 3.22). The actual origin of the high-frequency anomalies could not be established as CR8 and CR9 were pedogenically similar to the other soils at the site.

All soil profiles show, to some extent, an increase in the percent frequency dependence of the magnetic susceptibility for soil horizons closer to the surface. This feature is the result of pedogenesis and can be attributed to the neo-formation of superparamagnetic grains, as is often observed in soils (Singer *et al.*, 1992). The values for the percent frequency dependence are low to moderate, indicating a low degree of weathering for each of the soils at the CR site.

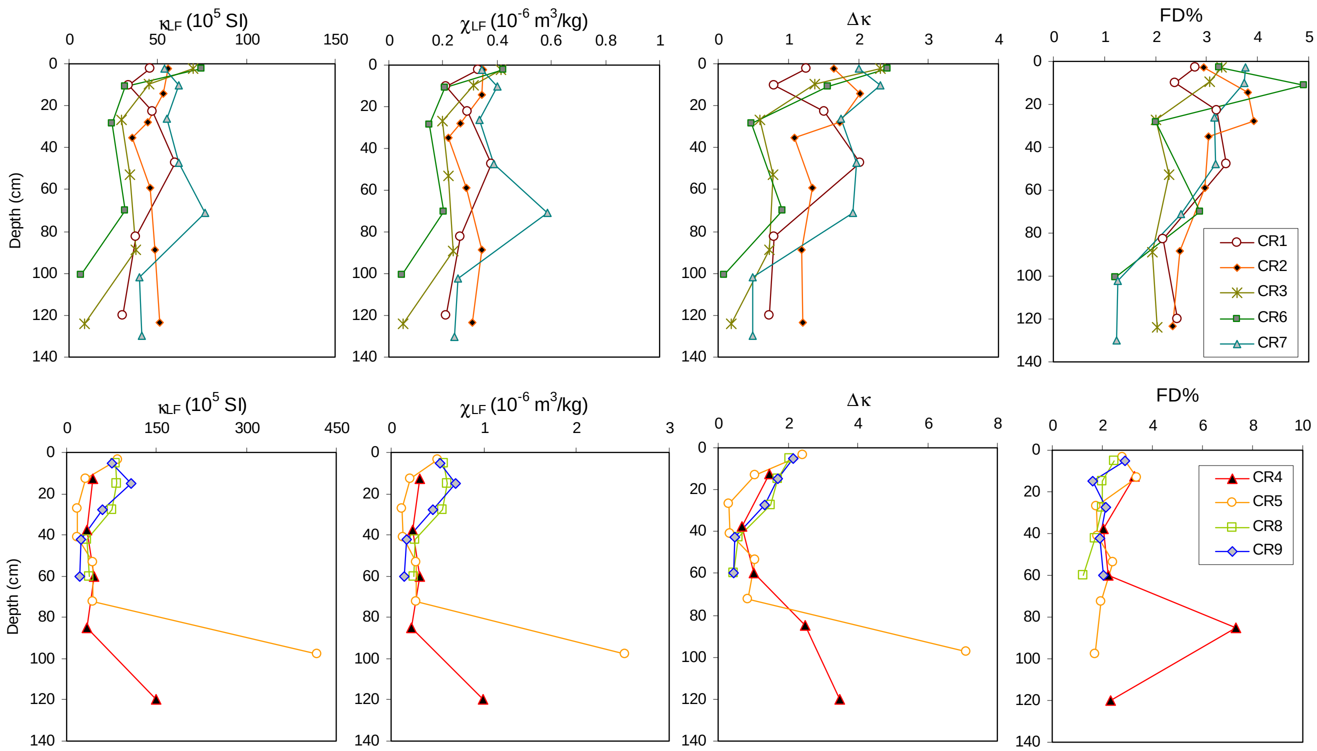

Figure 3.22: Results of magnetic measurements for 9 soil pits at the Chevallier Ranch site, Montana. The depth refers to the center of each soil horizon. Note the different horizontal scales for the plots in the top row and below.

The magnetic properties of Spokane Shale, which is the dominant constituent of the soils, and weathered and unweathered basalt from the volcanic neck are shown in Fig. 3.23. The Spokane Shale is characterized by low susceptibility and low frequency dependence. Both basalt samples (see section 3.2.1 for description) have high susceptibility, but the frequency dependence varies markedly with weathering stage. The weathered basalt has high frequency dependence, while the unweathered basalt has low frequency dependence. The soil material from above the volcanic neck (red triangle in Fig. 3.23a) has the most "basaltic" character of all soil sample groups.

The volume-specific magnetic properties (κ and $\Delta\kappa$) and the mass-specific magnetic susceptibility (χ) of both the surface grab samples and the soil profile averages fall roughly within the bounds set by the parent material (Fig. 3.23). In contrast, the values for the percent frequency dependence (χ_{FD}%) of the soils fall outside the area defined by the parent material

(Fig 3.23b). This clearly shows the effect of neo-formation of superparamagnetic grains on the magnetic signal.

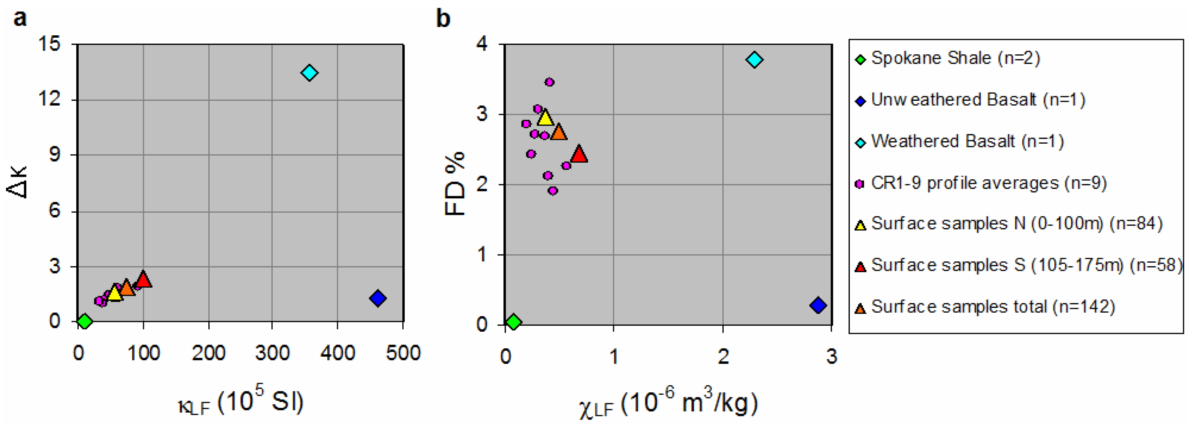

Figure 3.23: Averaged magnetic data for rock samples (diamonds: "♦"), surface grab samples (triangles: "▲"), and soil profiles (circles: "●") from the Chevallier Ranch site. The 142 surface grab samples were collected from a 15x175m regular grid (see Area A in Fig. 3.2 for location). The 58 surface samples from the southern part of rectangle A lie over the basaltic neck, and have been plotted separately from the samples to the north.

3.3.2.4 Mineralogy

X-Ray Fluorescence spectroscopy (XRF) – XRF analysis was performed on 24 samples from soils CR3, CR 4, CR 5 and CR 7 (Table 3.7 on page 126, Fig. 3.24). Of these, soils CR4 and CR5 are located on top of the volcanic dike. The measurements include both regular soil material and the basalt rock samples from near the surface in soil CR4 (see Fig. 3.23 and description in section 3.2.1). The minerals of greatest abundance are silica, aluminum, and calcium. The concentration of iron is small, ranging between 2 and 5%.

No abnormal values were recorded for the sample materials at the bottom of soil pits CR4 and CR5 that are characterized by the strongest magnetic signal (Fig. 3.22). This indicates that the larger magnetic susceptibility for these samples is caused by primary (lithogenic) magnetite. When present in small amounts it can have a significant effect on the bulk magnetic susceptibility (Table 3.1, page 120), without causing in a spike in Fe_2O_3 concentrations.

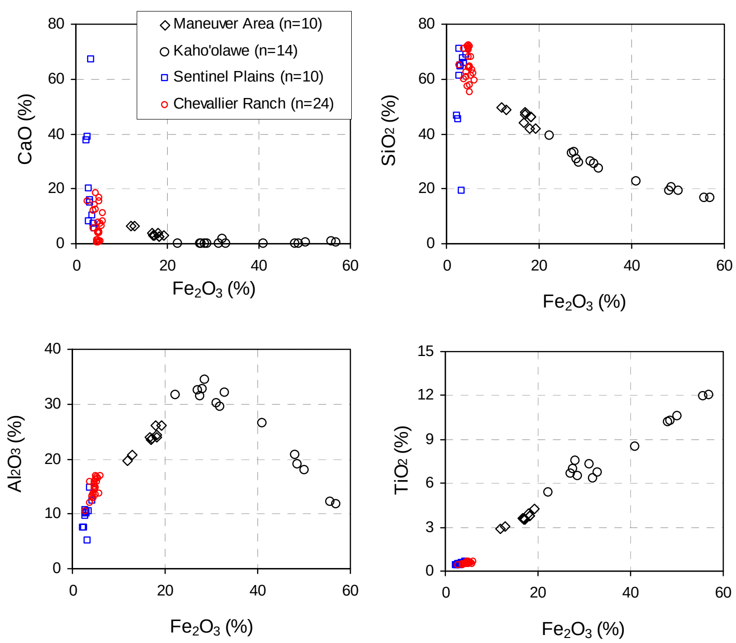

Figure 3.24: Results of XRF measurements for sample sets from the Sentinel Plains and Chevallier Ranch field sites (see also Table 3.7 and Table 3.8 on pages 126 and 127, respectively) added to those from Kaho'olawe and the Big Island of Hawaii (see Fig. 3.18).

3.3.3 Sentinel Plains

3.3.3.1 Geology and Geomorphology

The Sentinel Plain volcanic field located on the Luke Air Force Base Bombing Range is a 225 square mile volcanic field consisting of basalt flows up to 30 meters thick. The basalt lava flows developed from at least twelve eruptive centers between 3.3 million and 1.3 million years ago (Oxford and Bender, 1973). The lava flows are partially covered by young deposits of eolian sand. Currently, the Sentinel Plains are predominantly flat-to-moderate in grade with small amounts of steeper topography. In addition to frequent basaltic outcrops, the regolith is often shallow. The land is largely open with sparse to moderate vegetation typical of the desert southwest (Van Devender and Dimmitt, 2006).

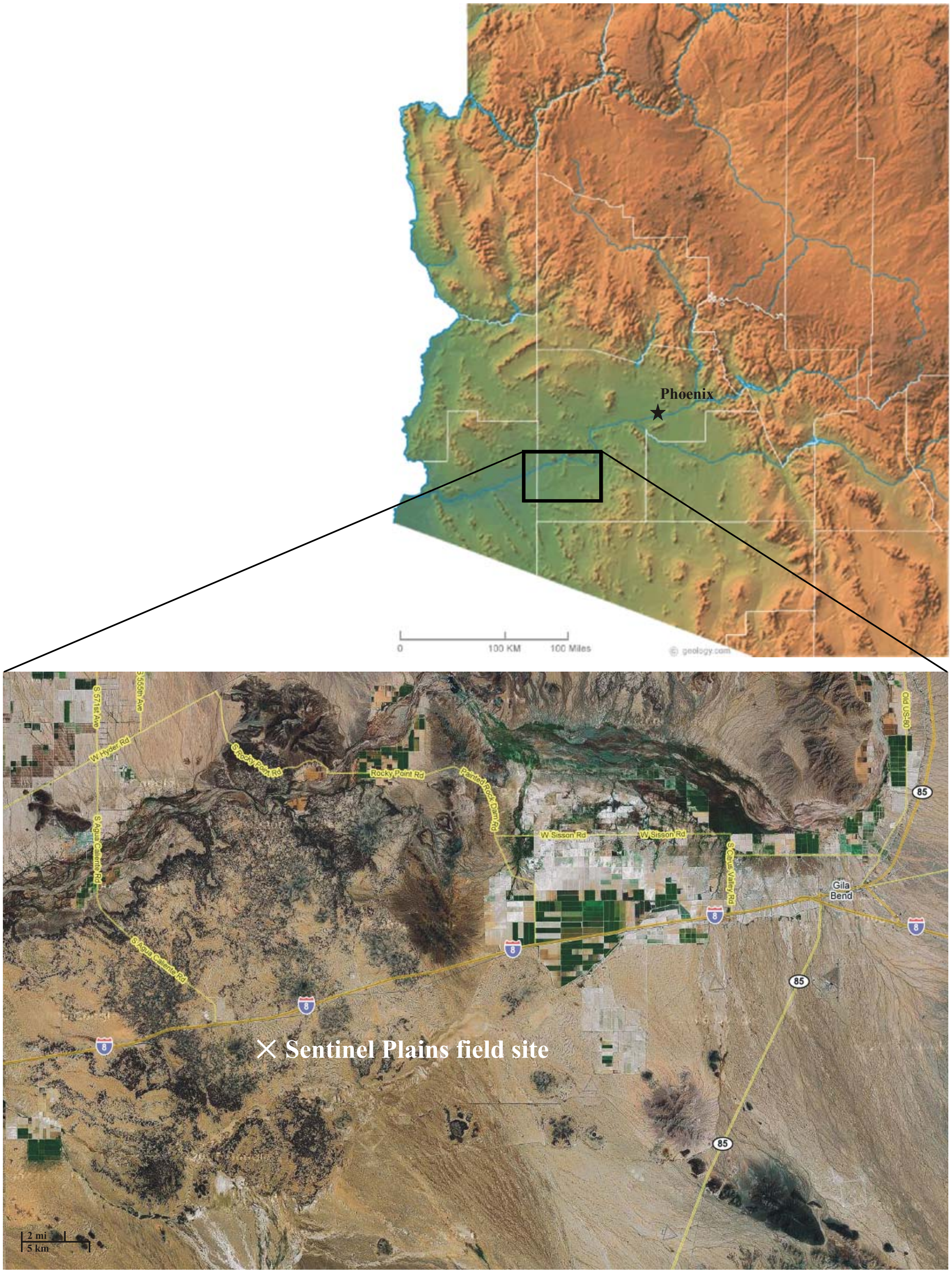

Figure 3.25: The Sentinel Plains field site outside Gila Bend, AZ (top image retrieved from www.geology.com, bottom image from www.maps.google.com)

3.3.3.2 Soil Descriptions

Soils at the Sentinel Plains study area have been formed in two distinctly different parent materials that vary over short distances. The older parent material is magnetite-bearing basalt. Fine sand and silt deposited by eolian processes form the second type of parent material. Figure 3.26 shows pictures of the three soil pits, the surrounding landscape and a close-up image of the surface conditions. Soil 1 is characterized by ~50cm of very loose sand and silts over a hard calcic horizon on top of the basaltic bedrock, which is found at 1m depth. The basaltic bedrock has thick coatings of calcic material on its surface. Soil 2 is considerably deeper and denser than soil 1. Using a hand auger, soil samples were collected from a depth up to 1.76m, after which no further progress could be made. Calcic material was largely absent in the upper meter, but increased with further depth. The maximum depth of the borehole was likely in close proximity to the bedrock. Soil 3 is very shallow, and consists of a thin layer of windblown sand and some calcic nodules over the basaltic bedrock. Numerous unweathered basaltic rocks and remnants of thick calcic coatings of these rocks are found spread over the surface.

All soils are characterized by a vesicular top horizon, characterized by tiny pores or vesicles, which form as a result of trapped or expanded air from rainwater in the soil. Based on detailed profile descriptions we recognize three phases in the soil development of the site. The thick calcic coatings on the basaltic (bed)rock at depth in soil pit 1 and 2 indicate that a significant period of soil formation has taken place during some period in the past. The second soil-development phase has consisted of a period of intense erosion. This phase can be identified from the calcic coatings on nearly unweathered basalt rocks, which are found at the surface of the lava flow outcropping of Soil 3 (Figure 3.3). Finally, during a third development phase, topographic lows have been covered with eolian deposits.

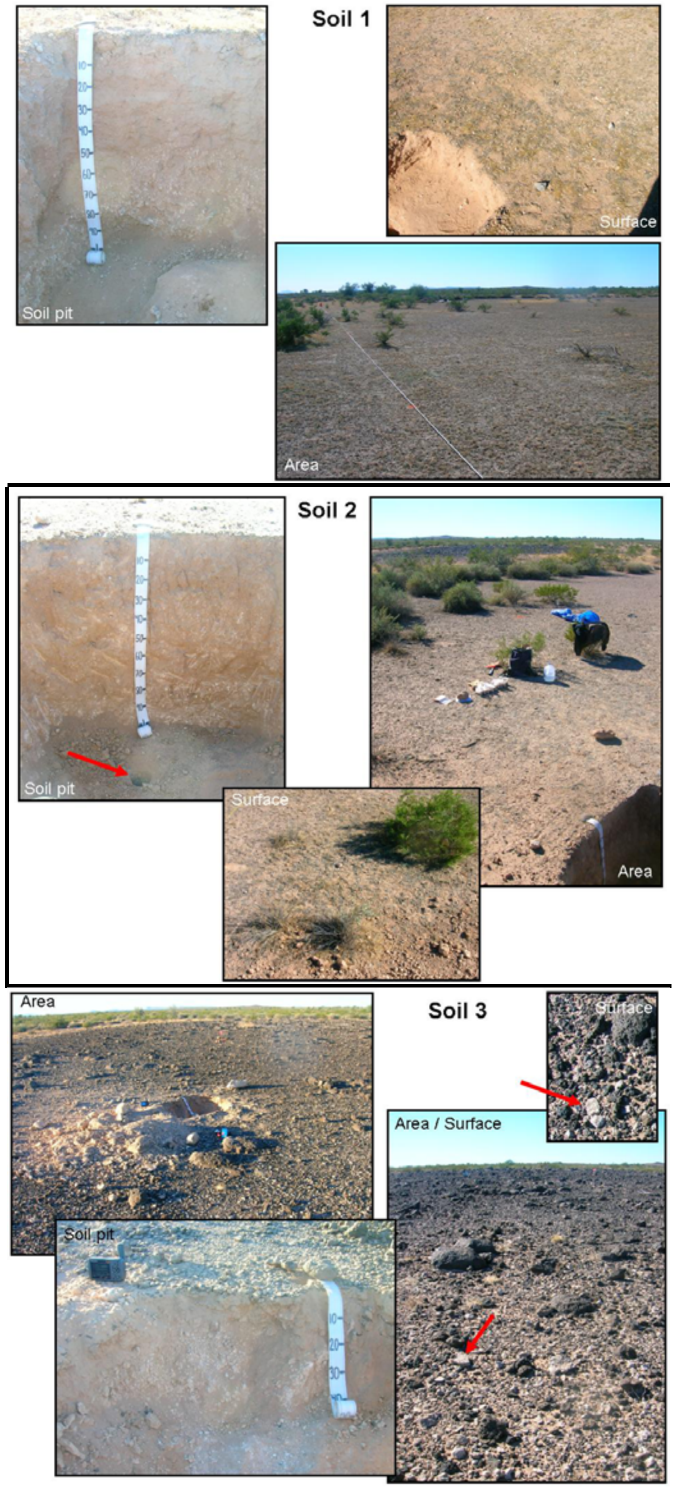

Figure 3.26: Sentinel Plains soil pits (see Fig. 3.3 for locations). Top left: Soil pit 1; area picture taken in a Southwestern direction. Top right: Soil pit 2; red arrow points to location of drill hole in bottom of soil pit. Area picture was taken in a western direction. Note the narrow zone of shrubs separating the sandy surface area form the basalt outcropping. Bottom: Soil pit 3; red arrows indicate erosional remnants of calcic crusts. Area picture taken in western direction.

3.3.3.3 Magnetic Measurements

Field magnetic susceptibility readings using the Bartington MS2D coil on a regular grid 100x50 m grid show values between of 100x and 250x 10^{-5} SI. Over the basaltic outcropping, the susceptibility readings increase slightly, but due to the irregular surface (poor coil-soil contact), the readings must be interpreted with caution. Laboratory analysis using a Bartington MS2B sensor show that the eolian material, which is dominant in areas between the basalt outcrops, has a low susceptibility and negligible frequency dependence (both $\Delta\kappa$ and χ_{fd}%). The data show that there is relatively small variation in magnetic susceptibility between the three soil pits (Fig. 3.27). All soil profiles exhibit enhanced magnetic properties towards the top, as is commonly observed in soils (Singer and Fine, 1989). Soil three (SP3), which was located on top of the basalt outcrop, shows the largest variability, which can be explained by the presence of large amounts of calcic material (low susceptibility) and magnetite bearing basalt material near the surface. Both Soil 1 and Soil 3 show an increase in magnetic susceptibility towards the top of the soil profile.

The material collected from the soil pits has lower magnetic susceptibility (χ and κ) than the surface grab samples (Fig. 3.28), which indicates some form of accumulation of ferrimagnetic material at or near the surface of the soil profiles. Considering the weak soil development in the arid climate at the site, it is unlikely that this increase is due to typical soil forming processes (Singer and Fine, 1989). It is likely that a process of preferential erosion and deposition has caused heavy mineral (e.g., magnetite) concentration at the surface (e.g., Buynevich *et al.*, 2007)

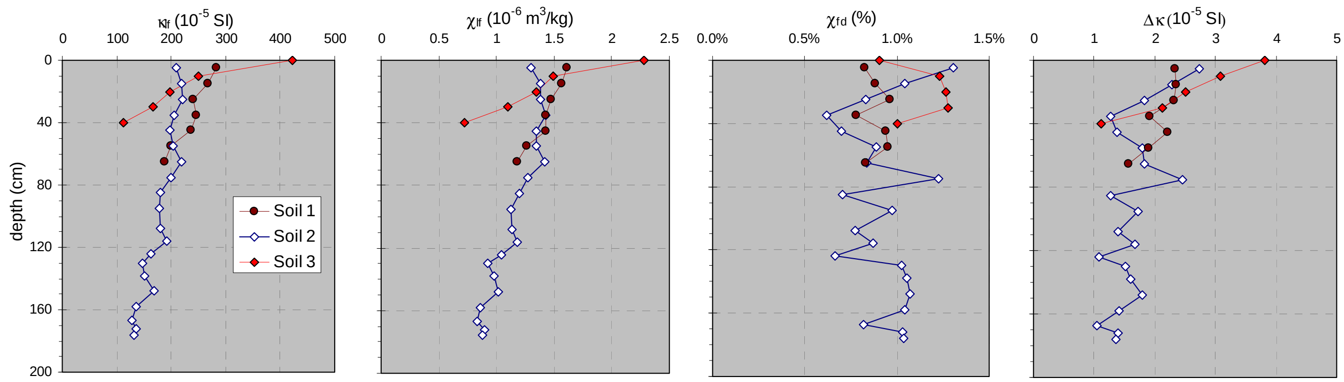

Figure 3.27: Magnetic susceptibility measurements (Bartington MS2B) for Sentinel Plains soil pits.

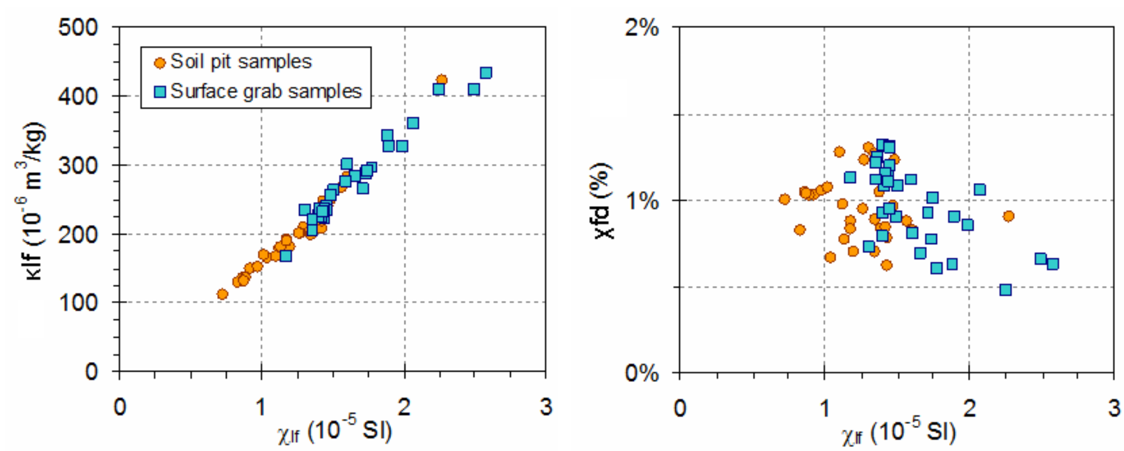

Figure 3.28: Comparison between magnetic properties for surface grab samples and samples from soil pits.

3.3.3.4 Mineralogy

X-Ray Fluorescence spectroscopy (XRF) – Based on the observed variability in magnetic properties XRF analysis was performed on ten samples (three from soil pit 1, five from soil pit 2, and two from soil pit 3). The results are summarized in Table 3.8 (page 127) and in Fig. 3.24. The results show that, except for some variability related to the calcareous concretions and coatings, the material at Sentinel Plains is very comparable with that at the Chevallier Ranch site. There is no direct relationship between the strong total field magnetic anomaly associated with the lava flows at Sentinel Plains and the mineral content of this material. This indicates that similar to Chevallier Ranch, the larger magnetic susceptibility for these samples is caused by small amounts of primary (lithogenic) magnetite in unweathered volcanic bedrock.

3.4 Discussion

An overview of the five sites studied in the SERDP UX1414 project is presented in Table 3.9 (page 128). All sites are characterized by the presence of basaltic parent material, but represent a large range in parent material age, climatic conditions, and magnetic properties. In this section we compare the different measures of mineralogy and magnetic properties for selected samples from the different sites. Not all analyses have been performed for all samples, so this discussion focuses on the samples from Kaho'olawe and the fresh basalt from the Big Island of Hawaii.

The XRF analysis of a range of soils on Kaho'olawe and the Big Island showed that an increase in degree of soil development is accompanied by a gradual increase in the iron content of the soils (Table 3.4 on page 123, Fig. 3.18). For the soil and surface samples from Kaho'olawe, this increase in iron content, in turn, is positively correlated ($R^2 = 0.87$) with the low-frequency mass-specific magnetic susceptibility (χ_{lf}) (Fig. 3.29). The fresh basalt samples and soil material from Waimea, on the Big Island of Hawaii, seem to fit with this general trend (Fig. 3.29b). However, the samples from Waikoloa exhibit anomalously high magnetic susceptibility values, which are unexplained. The mineralogical characteristics as well as the magnetic ones for the soil material from both Chevallier Ranch and Sentinel Plains is significantly different from the Hawaii sample sets (Fig. 3.29c).

Considering the good correlation between mineralogy and magnetic properties, these samples have been studied in more detail. Several strong correlations exist between magnetic susceptibility and concentrations of specific minerals, derived from the thermogravimetric analysis. Also, a strong relationship was found between the frequency dependence (approximate concentration of viscous remanent SP grains) and hydroxylamine-extractable iron. Details of these relationships are given in Figures 12 and 13 of *Van Dam et al.* (2008).

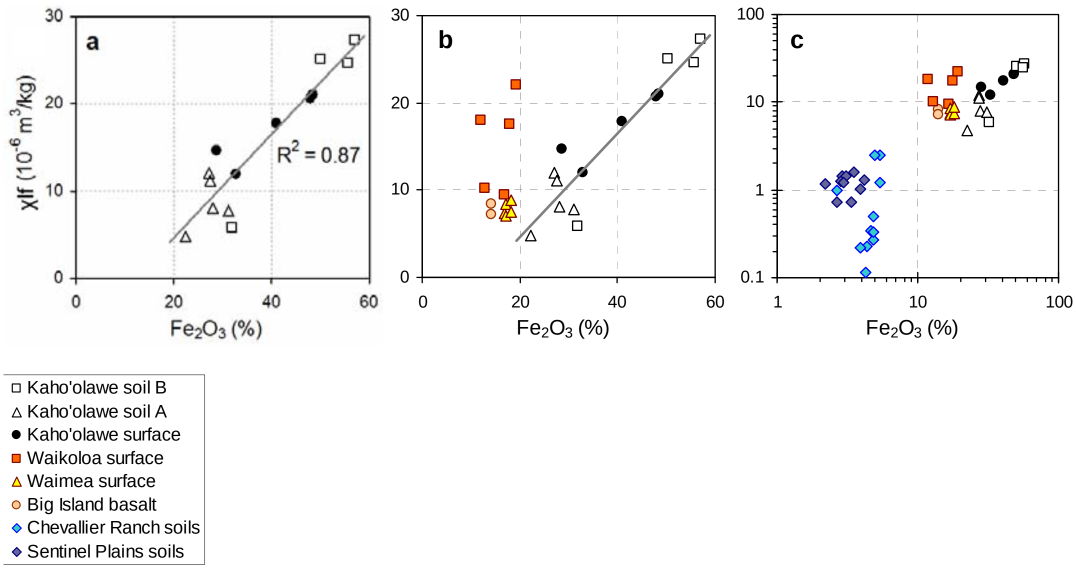

Figure 3.29: Cross plots showing correlations between magnetic susceptibility and XRF iron (Fe_2O_3 %) for a) soil samples from Kaho'olawe, b) the Big Island of Hawaii, and c) Chevallier Ranch and Sentinel Plains. Note the logarithmic axes in c). Discussion is provided in the text.

3.5. Conclusions

The results from this study show the mineralogical and magnetic effects associated with soil development from basaltic parent material. The main conclusions are:

- The analyses show that primary-rock minerals dominate in slow weathering conditions (Chevallier Ranch, Sentinel Plains) and persist in young soils (Kaho'olawe soil A, Big Island of Hawaii) in rapid weathering conditions. In strongly developed soils (e.g., Kaho'olawe soil B), newly formed iron oxides are present in large amounts.

- XRF analysis shows that initial soil development leads to rapid leaching of calcium, and a gradual decrease in silica, which results in a relative enrichment of aluminum and iron. On Kaho'olawe, with a surface age of at least 1 My, the conditions have been favorable for leaching of aluminum and a further development towards an oxisol with large amounts of iron.

- Thermal analysis estimated the relative amounts of goethite and muscovite, both of which vary systematically with position in the soil profile and correlate with the observed variations in magnetic properties.

- The results from the temperature-dependent susceptibility analysis shows that the high magnetic susceptibility and the large viscous remanent magnetization observed in geophysical surveys in Kaho'olawe are entirely due to secondary, or neo-formed minerals.

TABLES

Table 3.1. Magnetic susceptibilities (χ) for several lithogenic and pedogenic iron oxides and soil constituents. Data from Thompson and Oldfield (1986) and Cornell and Schwertmann (2003).

Material	Chemical formula	Magnetic class	χ (10^{-8} m^3 kg^{-1})
Water	H_2O	Diamagnetic	-0.9
Quartz	SiO_2	Diamagnetic	-0.6
Pyrite	FeS_2	Paramagnetic	30
Ferrihydrite	$5Fe_2O_3{\cdot}9H_2O$ †	Paramagnetic	40
Lepidocrocite	γ-FeO·OH	Paramagnetic	70
Ilmenite	$FeTiO_3$	Superparamagnetic	200
Hematite	α-Fe_2O_3	Antiferromagnetic	60
Goethite	α-FeO·OH	Antiferromagnetic	70
Pyrrhotite	$Fe_{7/8/9}S_{8/9/10}$	Ferrimagnetic	~5,000
Maghemite	γ-Fe_2O_3	Ferrimagnetic	40,000
Magnetite	Fe_3O_4	Ferrimagnetic	50,000

† The amount of OH and H_2O is variable (Cornell and Schwertmann, 2003).

Table 3.2. Results of VSM Hysteresis measurements for select Kaho'olawe samples.

Sample name	M_s [Am/kg]	M_{rs} [Am/kg]	B_c [mT]	B_{cr} [mT]	T [K]
KH-A1	1.83709	0.235173	7.81262	19.9503	300
KH-A3	1.57725	0.32325	7.91798	19.4466	300
KH-A6	1.3456	0.181916	7.3894	18.4512	300
KH-A7	1.27525	0.211091	8.84429	19.1462	300
KH-A8	1.457755	0.175522	7.746195	19.77955	297.5
KH-A9	0.928059	0.115653	7.58108	14.56267	295
KH-B1	1.21757	0.255143	8.36836	19.4902	300
KH-B3	1.36672	0.280103	7.91798	19.4466	300
KH-B13	0.561825	0.12658	8.5015	19.4854	300
KH-B15	0.291388	0.066358	9.02731	20.6163	300

Table 3.3. Results of XRD analyses. The symbol "x" denotes a clear presence of the particular mineral, while the symbol "o" denotes an indication of the mineral's presence. In the latter case, a small amount of the mineral-specific peaks does not overlap with the peaks in the X-ray spectrum for the sample.

Sample	Depth (m)	Horizon	Goethite α-FeOOH	Hematite α-Fe_2O_3	Magnetite Fe_3O_4	Ilmenite $FeTiO_3$	Gibbsite $Al(OH)_3$	Muscovite (Mica's)	Kaolinite
KH-A1	0-0.05	Bw/Cox	**x**	**x**	**x**	**x**	**x**	**x**	**x**
KH-A3	0.1-0.25	Cox1	**x**	**o**	**x**	**x**	**o**	**x**	**o**
KH-A5	0.4-0.6	Cox2	**x**	**o**	**x**	**x**	**x**	**x**	
KH-A7	0.8-1.1	Cox2	**x**	**o**	**x**	**x**	**x**	**x**	
KH-B1	0-0.05	Bw1	**x**	**x**	**x**				
KH-B5	0.2-0.3	Bw3	**x**	**x**	**x**				
KH-B8	0.5-0.6	Bw4	**x**	**x**	**x**				
KH-B15	1.2-1.3	Bw/Cox	**x**	**o**	**o**		**x**	**x**	

Table 3.4. Results of XRF measurements for soil pit and surface samples from Kaho'olawe (Kaho) and surface samples from the Waikoloa and Waimea sites on the Big Island of Hawaii. Fresh basalt samples (BI-S3) were collected on Kohala Volcano on the Big Island of Hawaii (Soil 3 in *Van Dam et al.* (2005)). All data have been corrected for loss on ignition.

Location	Sample name	SiO_2 (%)	TiO_2 (%)	Al_2O_3 (%)	Fe_2O_3 (%)	MnO (%)	MgO (%)	CaO (%)	Na_2O (%)	K_2O (%)	P_2O_5 (%)	Rb (ppm)	Sr (ppm)	Zr (ppm)
Waikoloa surface	WKL-20-00	42.1	3.9	26.0	17.9	0.3	3.1	4.0	0.9	1.0	0.8	22	407	506
Waikoloa surface	WKL-15-15	44.2	3.6	23.9	16.7	0.3	3.4	4.0	1.8	1.5	0.6	25	434	449
Waikoloa surface	WKL-05-25	49.8	2.9	19.7	11.9	0.2	3.2	6.6	3.0	1.7	0.9	38	1031	499
Waikoloa surface	WKL-00-20	48.7	3.1	20.7	12.9	0.3	2.9	6.2	2.7	1.5	0.9	38	901	539
Waikoloa surface	WKL-00-05	42.0	4.2	26.1	19.3	0.4	2.7	3.2	0.4	0.7	0.9	14	235	289
Waimea surface	WM-20-00	46.9	3.5	23.5	16.9	0.6	1.7	2.8	1.0	1.5	1.6	54	319	291
Waimea surface	WM-15-15	47.7	3.6	23.5	17.0	0.5	1.4	2.8	1.0	1.5	1.1	52	320	266
Waimea surface	WM-05-25	47.5	3.6	23.7	17.2	0.5	1.4	2.8	0.6	1.5	1.3	52	299	246
Waimea surface	WM-00-20	46.3	3.7	24.3	18.1	0.4	1.3	2.7	0.5	1.4	1.4	39	218	197
Waimea surface	WM-00-05	46.3	3.7	24.0	18.2	0.5	1.4	2.5	0.6	1.3	1.4	36	236	240
Kaho surface	KH2E-20-00	20.4	10.3	19.0	48.6	0.3	0.4	0.1	0.0	0.5	0.4	31	46	546
Kaho surface	KH2E-15-15	19.4	10.2	20.8	48.1	0.1	0.4	0.1	0.0	0.5	0.4	28	54	564
Kaho surface	KH2E-05-25	27.4	6.7	32.0	32.9	0.1	0.2	0.1	0.0	0.3	0.3	17	43	408
Kaho surface	KH2E-00-20	29.5	6.5	34.4	28.7	0.1	0.3	0.0	0.0	0.2	0.2	10	39	435
Kaho surface	KH2E-00-05	22.6	8.5	26.6	41.0	0.1	0.3	0.1	0.0	0.4	0.4	24	42	543
Kaho pit B	KH-B1	19.3	10.6	17.9	50.3	0.1	0.5	0.3	0.0	0.6	0.4	32	87	610
Kaho pit B	KH-B5	16.6	12.0	11.9	57.0	0.1	0.9	0.5	0.0	0.5	0.4	31	141	681
Kaho pit B	KH-B8	16.8	11.9	12.2	55.8	0.3	1.1	1.0	0.0	0.5	0.5	25	136	628
Kaho pit B	KH-B15	29.1	6.3	29.6	32.0	0.0	0.9	1.5	0.0	0.3	0.2	8	98	380
Kaho pit A	KH-A1	32.9	6.7	32.4	27.1	0.1	0.3	0.0	0.0	0.2	0.3	5	52	494
Kaho pit A	KH-A3	33.2	7.0	31.5	27.5	0.1	0.2	0.1	0.0	0.2	0.3	4	36	506
Kaho pit A	KH-A5	30.8	7.5	32.8	28.1	0.1	0.2	0.1	0.0	0.1	0.3	0	35	499
Kaho pit A	KH-A7	29.9	7.3	30.1	31.2	0.1	0.6	0.2	0.0	0.2	0.4	0	32	524
Kaho pit A	KH-A9-saprolite	39.5	5.4	31.6	22.3	0.1	0.4	0.2	0.1	0.2	0.3	5	40	431
Big Island	BI-S3-basalt1	46.4	2.8	13.6	14.2	0.2	10.8	9.3	1.8	0.6	0.3	14	398	196
Big Island	BI-S3-basalt2	46.5	2.9	13.6	14.1	0.2	10.9	9.2	1.7	0.6	0.3	13	401	197

Table 3.5. Comparison of TGA and DTA with events described in literature.

DTA peak temperature (°C)	Reaction type	Sample KH-A3	Sample KH-A5	Probable effect	Temperature (°C)
80	Exothermic		DTA	Organic material	
110	Endothermic	TGA, DTA	TGA, DTA	Loss of free water	~100
280	Endothermic	TGA, DTA	TGA, DTA	Dehydration of Gibbsite and formation of böhmite[1] Dehydroxilation of Gibbsite[2] Dehydroxilation of Goethite[3]	250-330 270-380 280
470	Endothermic		TGA, DTA	Decomposition of böhmite (γ-AlO·OH)[1] Loss of structural water from Kaolin or Micas[1]	
510	Endothermic	TGA, DTA		Decomposition of böhmite (γ-AlO·OH)[1] Loss of structural water from Kaolin or Micas[1]	
900	Exothermic	DTA		Chemical or structural change in Kaolinite or Mica (Muscovite)[1]	
~1380	Endothermic	TGA, DTA	TGA, DTA	Hematite melting[1]	1360-1440

[1] *Blazek* (1973), [2] *Földvari* (1991), [3] *Van Dam et al.* (2002)

Table 3.6. Horizon descriptions for soils at the Chevallier Ranch field site. See Fig. 3.2 for locations.

CR1	CR2	CR3	CR4	CR5	CR6	CR7	CR8	CR9
0-5: Ah	0-5: Ah	0-5: A	0-25: Ah	0-7: Ah	0-5: Ah	0-5: Ah	0-5: Ah	0-5: Ah
5-15: AB	5-24: Bwj	5-14: AB	25-50: Bk1	7-19: Bw1	5-17: Bw1	5-15: Bw1	5-40: Bw1	5-25: Bw1
15-30: Bw(t)1	24-32: 2Ab	14-40: Bk1	50-70: Bk2	19-35: Bwk	17-40: Bk1	15-37: Bw2	40-60: Bk1	25-60: Bk
30-65: 2Bw2	32-38: 2Bw1	40-66: Bk2	70-100: Bk3	35-47: Bk1	40-100: Bk2	37-58: Bw3	60-85: Bk2	60-80: 2C
65-100: 2Bwk	38-80: 3Bw2	66-112: Bk3	100-140: B/C	47-60: Bk2	100+: C	58-84: 2Bk1		
100-140: 2Bk1	80-97: 3Bw3	112-136: Bk4		60-85: Ck		84-120: 3Bk2		
	97-150: 3Bk			85-110: Cn		120-140+: 4C		

Table 3.7. Results of XRF measurements for soil pit and surface samples from Chevallier Ranch (CR). All data have been corrected for loss on ignition.

Location	Sample name	SiO_2 (%)	TiO_2 (%)	Al_2O_3 (%)	Fe_2O_3 (%)	MnO (%)	MgO (%)	CaO (%)	Na_2O (%)	K_2O (%)	P_2O_5 (%)	Rb (ppm)	Sr (ppm)	Zr (ppm)
CR pit 3	CR3-1-27	71.7	0.6	14.7	5.1	0.1	2.2	1.0	0.6	3.7	0.1	140	113	314
CR pit 3	CR3-3-31	57.9	0.6	13.5	5.0	0.1	2.7	16.6	0.4	3.1	0.2	103	176	207
CR pit 3	CR3-6-37	62.1	0.5	13.7	5.8	0.2	1.8	10.9	0.6	4.2	0.1	150	362	216
CR pit 3	CR3-65	70.8	0.6	15.5	4.7	0.1	1.7	1.1	0.7	4.7	0.1	185	210	257
CR pit 4	CR4-63	63.5	0.6	16.4	5.7	0.1	1.0	6.6	3.0	3.0	0.2	63.5	0.6	16.4
CR pit 4	CR4-62	64.5	0.5	16.2	5.2	0.1	3.1	4.3	3.3	2.7	0.2	64.5	0.5	16.2
CR pit 4	CR4-4-45	55.4	0.5	16.3	5.0	0.1	3.1	15.3	1.8	2.2	0.2	55.4	0.5	16.3
CR pit 4	Surface Fresh Basalt	64.3	0.5	15.9	4.8	0.1	3.1	4.4	3.8	2.9	0.2	71	640	141
CR pit 4	Surface Weathered Bas.	64.1	0.5	16.8	5.2	0.1	2.5	3.8	4.0	2.9	0.2	65	679	124
CR pit 4	Bk1 25-50	62.4	0.5	13.3	4.4	0.1	2.8	12.2	1.1	3.2	0.1	107	164	198
CR pit 4	Bk3 70-100	60.1	0.4	15.7	3.9	0.1	1.7	11.8	3.1	3.0	0.2	60	487	110
CR pit 4	B/C 100-140	65.0	0.4	10.4	2.7	0.0	2.1	15.2	1.7	2.3	0.1	67	458	262
CR pit 5	CR5-1-49	72.3	0.6	14.5	4.9	0.1	2.0	1.1	0.9	3.5	0.1	132	118	315
CR pit 5	CR5-3-53	57.1	0.5	12.8	4.5	0.1	2.5	18.3	0.7	3.2	0.2	110	168	204
CR pit 5	CR5-7-61	59.5	0.6	17.0	6.0	0.1	3.2	8.3	2.5	2.7	0.2	84	366	137
CR pit 5	CR5-64	70.9	0.5	12.0	3.8	0.0	3.2	5.5	2.0	2.0	0.1	74	91	271
CR pit 5	Ah 0-07	71.5	0.6	14.4	4.9	0.1	2.7	0.5	1.3	4.0	0.1	134	85	262
CR pit 5	Bwk 19-35	60.7	0.5	13.1	4.2	0.1	2.9	14.2	0.8	3.5	0.1	112	152	204
CR pit 5	Ck 60-85	64.3	0.5	14.2	4.8	0.1	3.6	7.6	1.0	3.8	0.1	131	190	203
CR pit 5	Cn 85-110	61.1	0.5	16.7	5.3	0.1	3.0	7.1	3.2	2.7	0.2	75	405	136
CR pit 7	Ah 0-05	72.1	0.5	13.7	4.7	0.1	2.7	0.3	2.0	3.8	0.1	140	49	265
CR pit 7	Bw2 15-37	71.1	0.6	15.0	4.9	0.1	2.7	0.5	1.3	3.7	0.1	137	72	279
CR pit 7	2Bk1 58-84	68.1	0.7	14.6	4.9	0.1	2.6	4.0	1.8	3.1	0.2	110	154	287
CR pit 7	4C 120-140+	67.9	0.6	15.9	5.4	0.1	2.9	0.9	1.7	4.4	0.1	160	71	235

Table 3.8. Results of XRF measurements for soil pit and surface samples from Sentinel Plains (SP). Data have been corrected for loss on ignition.

Location	Sample name	SiO_2 (%)	TiO_2 (%)	Al_2O_3 (%)	Fe_2O_3 (%)	MnO (%)	MgO (%)	CaO (%)	Na_2O (%)	K_2O (%)	P_2O_5 (%)	Rb (ppm)	Sr (ppm)	Zr (ppm)
SP pit 1	0-10	67.6	0.6	10.6	3.5	0.1	1.7	10.5	2.3	3.1	0.1	74	274	355
SP pit 1	30-40	71.0	0.5	10.8	2.9	0.1	1.4	8.2	2.3	2.8	0.1	74	314	267
SP pit 1	60-70	46.7	0.4	7.6	2.2	0.0	1.7	37.7	1.8	1.9	0.1	39	302	177
SP pit 2	0-10	69.0	0.7	12.5	4.2	0.1	2.4	5.7	2.0	3.3	0.2	96	243	392
SP pit 2	30-40	64.5	0.5	10.1	3.1	0.0	1.6	16.0	1.5	2.5	0.1	65	285	287
SP pit 2	70-80	61.0	0.5	9.7	2.8	0.0	1.6	20.2	1.8	2.3	0.1	58	300	250
SP pit 2	80-90	65.1	0.5	10.2	3.0	0.0	1.7	14.9	2.0	2.4	0.1	64	315	280
SP pit 2	148	66.1	0.5	14.8	3.9	0.1	2.4	7.4	2.1	2.7	0.1	81	297	146
SP pit 3	40 Fine Grained	45.4	0.4	7.6	2.7	0.0	2.4	38.9	1.0	1.6	0.1	36	290	181
SP pit 3	40 Nodule	19.4	0.4	5.2	3.3	0.0	3.2	67.1	0.9	0.4	0.1	4	257	40

Table 3.9. Comparison of field sites in the SERDP UX-1414 project.

Parent material	Hawaii Kaho'olawe	Hawaii Waimea GPO	Hawaii Waikoloa GPO	Montana Chevallier Ranch	Arizona Sentinel Plains
Parent material 1	Basalt	Basalt	Basalt	Shale	Basalt
Parent material 2	-	-	-	Basalt	Windblown sand
Parent material age* (1/2) (My)	1-2	0.065-0.250	0.065-0.250	~550 / ~55	1.3-3.3
Mean annual rainfall (mm)	250-650	1500	150-500	~300	
Median temperature (°C)				6.7	
Altitude (m)	250	800	300	1270 - 1340	220
Soil maturity	large	small	minimal	medium	minimal
κ (10^{-5} SI)	300-3000	350-700	450-1750	5-420	120-440
$\Delta\kappa$ (10^{-5} SI)	2-220	-	-	0-7	1.5-4

* Maximum soil age; soil age / period of soil formation will be considerably less than age of parent material for Chevallier Ranch and Sentinel Plains as the soil age is constrained by the date of deposition.

4. Soil Characterization

4.1 Introduction

Following the research results presented in the previous chapter on origins and physics of soil magnetization, the second major objective of SERDP Project MM-1414 is to:

> Develop a practical means for identifying and modeling the spatially variable frequency-dependent magnetic susceptibility in soils hosting UXO.

In magnetic environments, to illustrate, the host geology will exhibit strong viscous remnant magnetization (VRM) and it will produce strong background response in both electromagnetic and magnetic data that can mask UXO signatures or produce false alarms. Improving UXO detection and discrimination under such condition therefore requires a means of simulating this variable distribution of susceptibility at a site as a foundation for characterizing and removing these soil responses.

For this purpose, we present in this chapter a 3D soil distribution model generated from various project data and representing variable soil distribution at one of the more difficult sites for this project, Kaho'olawe, HI. We use 1-D forward modeling results of the TDEM response to understand the influence of viscous remanent magnetization (VRM) magnitude and layer thickness on field data acquired at Kaho'olawe, HI. As presented throughout the project, VRM is manifested in the form of a complex magnetic susceptibility, and we have directly measured this frequency dependence in soil samples collected from the Kaho'olawe site. The TDEM forward modeling approach has taken current modeling algorithms, and modified them to allow the input of Cole-Cole parameters for this project. These parameters directly incorporate information about the soil's frequency dependent magnetic susceptibility. In this section of the report, we utilize the Cole-Cole model parameter α, distributed over a 3D volume from soil samples collected and cataloged at Kaho'olawe, to generate a 3D soil distribution model exhibiting VRM. By combining this model with field TDEM data, we have likewise performed 3D geostatistical simulations which may be used for future filter technologies based on the 3D spatial distribution of VRM. In this chapter, we present the 3D soil distribution model and the 3D geostatistical simulations.

4.2. 3D soil distribution model

The 3D soil distribution model we present is built directly from soil samples collected at Kaho'olawe Navy QA grid 2E (Figure 4.1). Samples were collected on the surface of the grid as well as at depth from soil pits, and frequency dependent magnetic susceptibilities were subsequently measured for each sample. Results of measured complex susceptibilities for these samples are available in the project's Annual Reports. In Appendix-B of the January 2007 Annual Report, we provide the current parameters generated from the susceptibility values using Cole-Cole model for each sample. The first step in building the 3D soil model of the site was choosing an appropriate parameter which sufficiently describes the frequency dependence of the local soils. This parameter, combined with location information (northing, easting, and depth), was then used to generate a 3D distribution of VRM representative of the local geology.

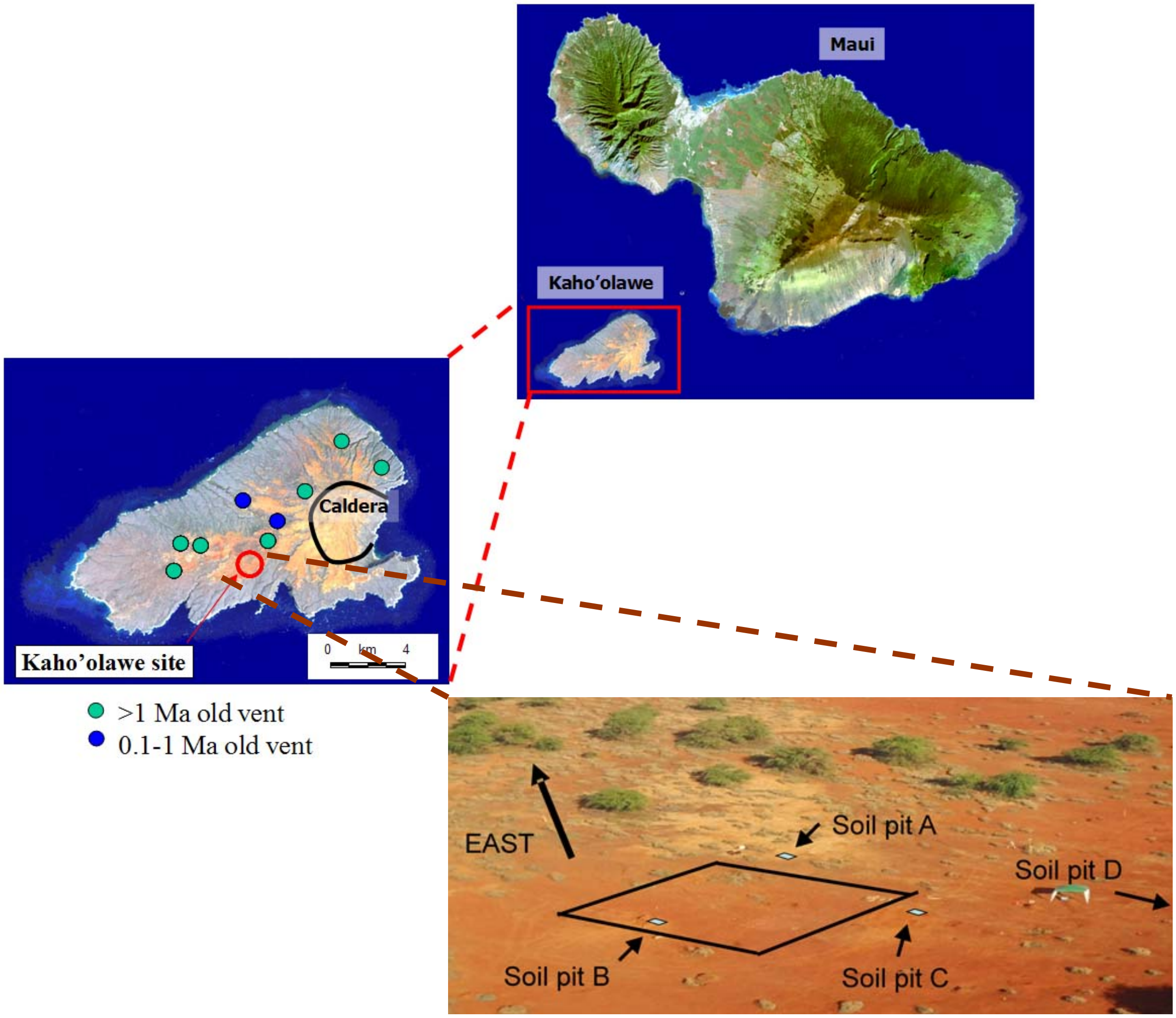

Figure 4.1: Landsat image for islands of Maui and Kaho'olawe (top-right). Landsat image of Kaho'olawe (lower-left). The UXO study site on Kaho'olawe is identified with the red circle. Landsat images and GIS data files available at the Hawaii Statewide GIS Program website: http://www.state.hi.us/dbedt/gis/download.htm. Lower right image is a photograph of the Kaho'olawe field site which shows the location of the soil pits with respect to the 30x30 m grid (outlined in black).

4.2.1 Cole-Cole model for parameter estimation

For the 3D soil model, we have opted to use the parameter, α, estimated from the Cole-Cole model for each soil sample. We start with a brief review of the key components of the Cole-Cole model, as they are relevant to the 3D soil model.

In the case of frequency dependent magnetic susceptibilities, the Cole-Cole model may be written as:

$$\chi = \chi_\infty + \frac{\chi_0 - \chi_\infty}{1 + (i\omega\tau)^{1-\alpha}} \tag{4.1}$$

where χ_∞ and χ_0 are the real magnetic susceptibilities as the frequency approaches infinity ($\omega \rightarrow \infty$) and zero ($\omega \rightarrow 0$), respectively. The τ parameter is the relaxation time constant and the α parameter, which we use to build the 3D soil model, describes the breadth of frequency distribution with limits of $0<\alpha<1$. An $\alpha = 0$ indicates a single Debye relaxation while an $\alpha = 1$ represents an infinitely broad distribution of relaxation times (Olhoeft and Strangway, 1974). It has been assumed that $\chi_\infty = 0$ which allows equation 4.1 to be written as:

$$\chi = \frac{\chi_0}{1 + (i\omega\tau)^{1-\alpha}} \tag{4.2}$$

Using equation 4.2, Figure 4.2 shows the Cole-Cole distributions for different α values with τ = 1. The real (solid lines) and the imaginary (dashed lines) components are shown.

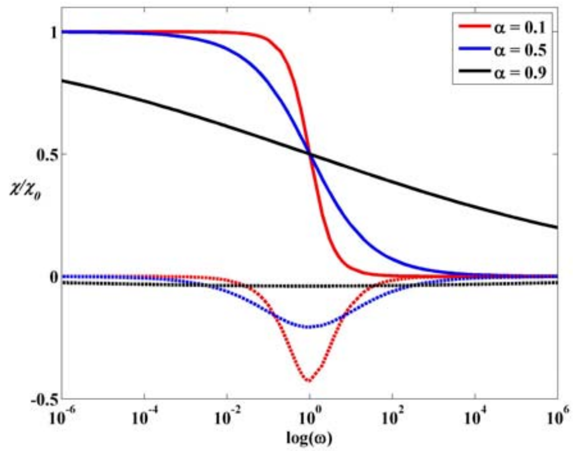

Figure 4.2: The Cole-Cole model plotted for different values of α (0.1, 0.5, and 0.9) and τ = 1.

To determine the values of the Cole-Cole parameters for the 3D soil model, χ_0, τ, and α, we implement a curve fitting approach where the measured magnetic susceptibilities are compared to the calculated values from the Cole-Cole model (Equation 4.2). Figure 4.3 shows an example of the curve fitting routine using the Kaho'olawe surface sample (10,10). For this sample the Cole-Cole parameters are estimated to be α = 0.68 and τ = 10^{-3}.

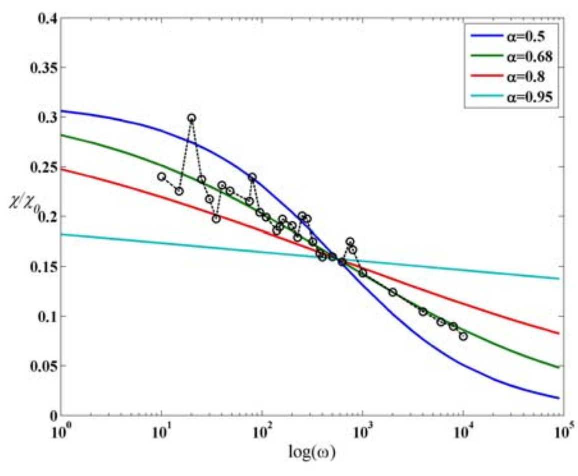

Figure 4.3: Cole-Cole model fit used to derive values for α and τ for one of the soil samples from Kaho'olawe grid 2E.

4.2.2 3-D soil model

The soil model generated from the 3D distribution of Cole-Cole α-parameters is illustrated in Figure 4.4. The model is generated through 3D interpolation of 62 soil samples collected along the surface of the QA test grid, and from three soil pits for depth (pits A, B, and C). To preserve depth information of the discrete weathering layers and soil horizons observed at the site, the Cole-Cole parameters from representative samples within each layer are assumed constant throughout the corresponding soil depth-interval at each pit location. Such parameterization has been incorporated into the 3D interpolation for model construction, and as a result, the Cole-Cole model parameter distribution as a function of spatial position – provided in Appendix-B of the January 2007 Annual Report – contain 116 data-points instead of 62. In brief, individual layers within each soil pit are defined by three samples (top, middle, and bottom depths) which share the same property values.

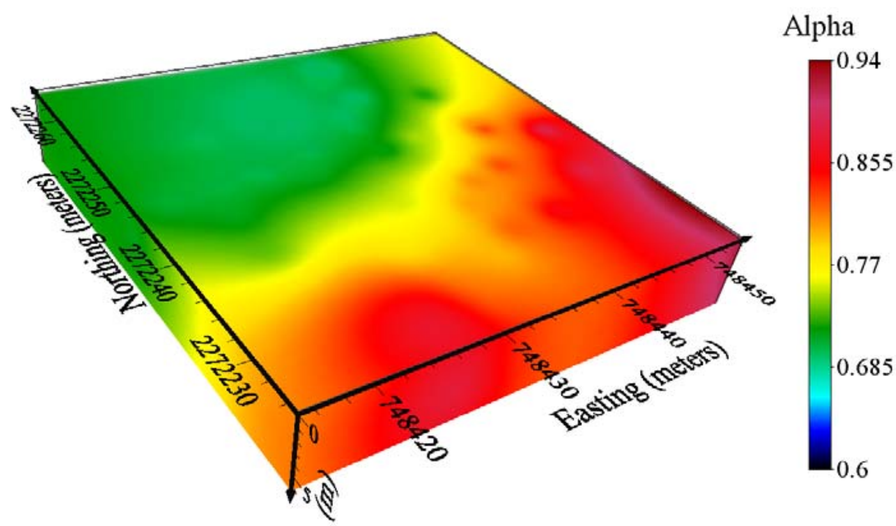

Figure 4.4: 3D soil model of Kaho'olawe Navy QA grid 2E. Property values for the model are the Cole-Cole model parameter α, determined for each soil sample collected at the test site. The α parameter describes the breadth of frequency distribution based on laboratory measurements of frequency dependent magnetic susceptibility, and it has been determined for 62 soil samples.

The gradient observed in the 3D soil model, from $\alpha \cong 0.6$ in the upper-left to $\alpha \cong 1$ in the lower-right, are consistent with observed TDEM data collected at the site. The EM61-MK2 data presented are illustrated in Figure 4.5 to demonstrate this. We see from the model and data that there is an inverse correlation between the Cole-Cole parameter α and the time varying magnetic response of the soils. This is predicted by the Cole-Cole model in Figure 4.3, as well as the theoretical Cole-Cole plots of susceptibility versus frequency. Observing the left portion of Figure 4.3 for example, which best represents the frequency range of the EM61, a small α parameter should directly translate to a higher susceptibility response from an external time varying magnetic field. This increased susceptibility is observed in the higher amplitude response of the EM61 data presented in Figure 4.5. Similarly, the method likewise predicts a smaller susceptibility, and therefore lower magnetic response in EM61 data, for regions with a larger frequency distribution window α.

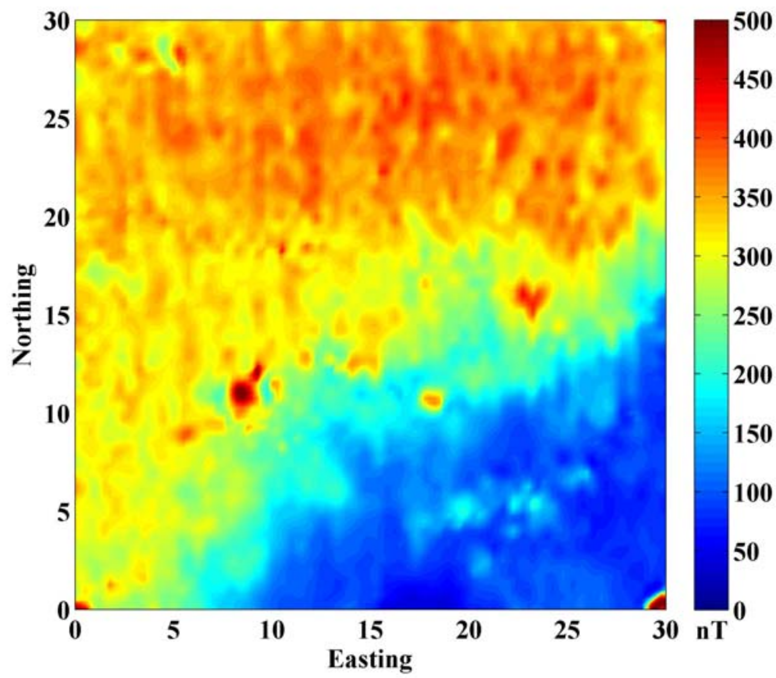

Figure 4.5: EM61 data (Channel 1) collected over grid 2E at Kaho'olawe. The data inversely correlate with the 3D soil model illustrated in Figure 4.4, as predicted by the Cole-Cole model for frequencies consistent with the EM61. The upper-left region of the grid, which is producing the largest magnetic response, is the region with the smallest width of frequency response α.

4.3. 3D statistical simulation of soil model

The soil samples are taken at discrete points separated by distance much greater than the scale of susceptibility variation. These samples are important in providing detailed frequency characteristics of the susceptibility and defining long-wavelength spatial variations. The important question for this project is how to use geophysical data to fill in the gap and provide an indirect characterization of the spatial variability necessary for processing EMI data in UXO detection and discrimination. To this end, establishing a realistic 3D susceptibility model is important. The preceding section describes the direct construction of such a susceptibility volume using the data from soil samples. We now proceed to construction of susceptibility model using statistical simulation based on correlated random process that we developed in the SEED project UX-1285 that precedes the current one.

To simulate a realistic susceptibility distribution, we combine the long-wavelength features defined by soil samples with a spatially random component whose correlation length is defined by time-domain data. The first part is provided by the model described in Section 4.2. The Second part is simulated statistically based on the spectral property of the soil susceptibility derived from EM63 data.

The process consists of two steps. In the first, we estimate the power spectrum of the susceptibility from the spatial amplitude of the TEM data that exhibit the A/t decay due to frequency-dependent soil susceptibility, where A is a constant for each EM63 sounding but varies from location to location. A is obtained by fitting the inverse time decay. The variability of A is then used as a proxy for that of the susceptibility. We then define a power spectrum from A and assume that is the power spectrum of the susceptibility in 3D. Figure 4.6 shows an example of the estimated power spectrum.

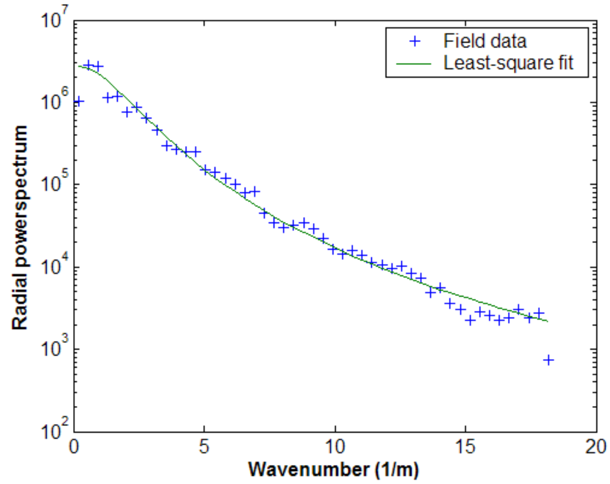

Figure 4.6: Estimated radial power spectrum. The pluses (+) are the radially averaged power spectrum of the EM63 amplitude data, and the solid line is a parametric representation of the radially averaged power spectrum.

In the second step, we generate a random sequence in 3D that has the estimated power spectrum shown in Figure 4.6, but have random phases (e.g., Easley *et al*., 1990; and Shive *et al*., 1990). Assume $\chi(x, y, z)$ is the magnetic susceptibility in the 3D volume of subsurface to be simulated, and $P(\omega_x, \omega_y, \omega_z)$ be its power spectrum, where $(\omega_x, \omega_y, \omega_z)$ are respectively wavenumbers in the x-, y-, and z-directions. Then the 3D Fourier transform of the susceptibility is given by

$$\tilde{\chi}(\omega_x, \omega_y, \omega_z) = \sqrt{P(\omega_x, \omega_y, \omega_z)}e^{-i\phi(\omega_x, \omega_y, \omega_z)}, \tag{4.3}$$

where $\phi(\omega_x, \omega_y, \omega_z)$ is the random phase term. Given a power spectrum, we can simulate different realizations of the random process by assigning different random phases. All realizations would have the same power spectrum, and thus have more or less the same appearance in the space domain. However, the locations of features seen in each realization will be different. The mean and variance of the random process are directly prescribed. This process can be used to simulate the susceptibility or any parameter of a model (such as Cole-Cole or Lee model) that describes the frequency dependence of susceptibility.

To complete the simulation, we treat the statistically simulated part as a perturbation superimposed on the long-wavelength component defined by soil samples. Figure 4.7 is an illustration of one such realization of the parameter α in the Cole-Cole model. We note that this is an unconditioned simulation and it simply combines the two components. Alternatively, a conditioned simulation can be carried out to generate such a susceptibility volume that honors susceptibility (or other parameter) values at all known locations.

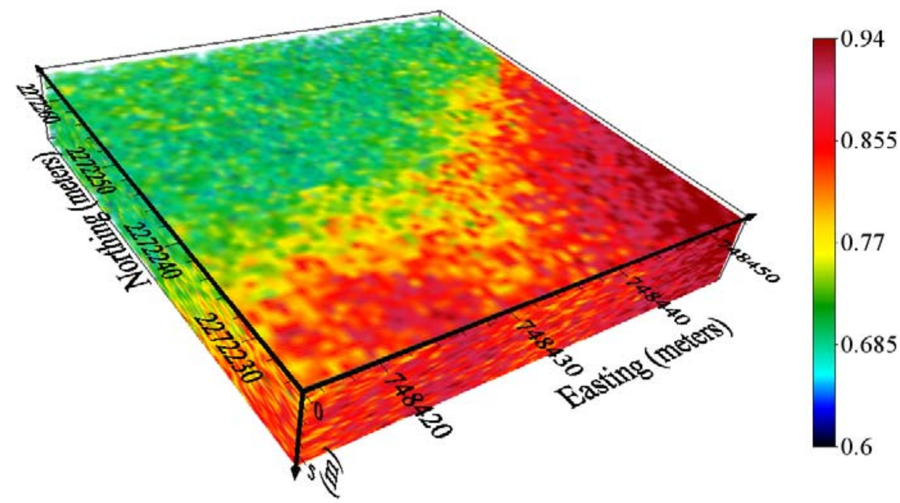

Figure 4.7: 3D soil model simulated for of Kaho'olawe Navy QA grid 2E. Property values for the model are the Cole-Cole model parameter α. The long wavelength features are defined by soil samples (shown in Figure 4.6). The rapidly changing component is simulated statistically.

4.4. Summary

We have developed a method for generating full 3D soil distribution models which incorporate all soil (surface and pit)-sample measurements of frequency dependent magnetic susceptibilities. In this chapter, we have applied the procedure specifically to the Kaho'olawe site utilizing 62 soil samples, which include surface soil samples and samples collected at varying depths throughout soil pits A-B-C-& D. The approach for generating the 3-D soil-distribution models is an essential component of the project, which will allow anyone to better understand the geophysical responses of highly magnetic soils in a fully 3-D geologic setting. To generate the Kaho'olawe model, we have calculated the Cole-Cole model parameter α, distributed over a 3D volume from soil samples collected and cataloged at the site. The net result is a 3D soil model mimicking the 3D distribution of VRM. From this model, we have likewise performed 3D geostatistical simulations which may be used for future development of new filter technologies based on the 3D spatial distribution of magnetic geology.

5. Magnetic Data Analysis

5.1 Introduction

The third major technical objective of SERDP project MM-1414 focuses on the practical aspects of working with static magnetic field data in difficult magnetic environments.

> Develop methods and procedures for removing the effects of soil response from magnetic measurements for improved UXO detection and discrimination in magnetic environments.

In this chapter, we first present several methods for filtering magnetic data in highly magnetic environments using both synthetic and real field data. We then outline a new methodology for robust target selection in magnetic environments based on static magnetic field data, and demonstrate the feasibility of the approach using total-field data collected at the Montana field sites.

5.2 Magnetic data processing

The difficulty of working with static magnetic data in magnetic soil environments occurs at two levels. First, in moderately magnetic environments, the soil magnetic field can distort the dipolar response of UXO items and lead to erroneous recovered dipole parameters from the data. This leads to decreased discrimination capability. Second, in a strong magnetic environment, the soil response can completely mask the UXO signature and render the method ineffective as a detection tool.

The current state of practice for removing geologic noise is to use a median filter. However, its application is limited since a median filter is designed to remove isolated random spikes in the data but the soil response tends to be primarily coherent. For this component of the project, we therefore present three alternative methods which have demonstrated effective for removing the response of magnetic soils from magnetic data based on rigorous signal processing techniques and site-specific information.

The first method is a continuation of research and development of experiments from SERDP SEED project UX-1285 related to the Wiener filter. The Wiener filter (Wiener, 1949) is based on the spectral properties of the UXO and soil responses and can be tuned to data from specific sites. We demonstrated in the SEED project that the successful application of the method depends largely on the knowledge of the power spectra of soil magnetism at a site. Through field and laboratory work associated with this project, such information is now available, and development of an iterative Wiener filter for static magnetic data demonstrates promise in magnetic environments. In the following section of the report, we (1) present current results of the newly developed iterative Wiener filter applied to synthetic and field data, (2) explain our current method for estimating the soil spectral properties for use in Wiener filtering, (3) describe under what conditions we can use this method to detect UXO signatures in magnetic environments, and (4) discuss when we can reliably apply this method to preprocess data for use in advanced discrimination algorithms.

The second method we have researched and implemented here is the use of wavelet transforms for separating the UXO and soil responses. Wavelet transforms decompose different components of a signal into different regions in the space-frequency domain and thereby allow one to separate them or extract a particular feature. Both continuous wavelet transform (CWT) based natural wavelets (e.g., Hornby *et al.*, 1999; Haney and Li, 2002) and discrete wavelet transform (DWT) based on compactly supported orthonormal wavelets (e.g., Ridsdill-Smith and Dentith, 1999; Li and Oldenburg, 2003; Lyrio *et al.*, 2004) have been used successfully in the processing and inversion of magnetic data in exploration geophysics. In the section of the report on filtering using wavelet transforms, we will present current research and results on application of the DWT for separating UXO and soil response in strong magnetic environments. We demonstrate the effectiveness of the approach applied to magnetic data from Chevalier Ranch, MT, and discuss the apparent limitations of the preprocessing technique.

The third method proposed for separating magnetic geology from UXO response is based on the high-pass Butterworth filter, originally implemented during leveling/decorrugation of field data. Iterative Wiener and Wavelet approaches demonstrate successful separation of geologic and UXO response when magnetic soils are present. However, because these tools are designed to mimic longer wavelength response of geology, they do not properly account for magnetic heading errors, if acquired during data collection. The result of not properly filtering these undesired features is increased false targets along acquisition lines. We have identified that in certain magnetic environments, a high-pass Butterworth filter will successfully remove the response of magnetic geology and heading errors in magnetic data while preserving the response of UXO for later detection and discrimination processing.

We next present details on the three methods developed for removing the effects of soil responses from total field data in magnetic environments. We illustrate the effectiveness of each method on field data collected at the Montana test sites.

5.2.1 Iterative Wiener filter

This section focuses on processing of total-field magnetic data collected at Chevalier Ranch in Helena, MT. In geologic settings like Chevalier Ranch, high and variable magnetic susceptibilities may reduce or completely mask the visible identification of buried metallic objects and increase the number of false anomalies that are selected for removal. The Wiener filter assumes that the collected field data is a summation of the desired signal and the background response and that the two components are not correlated. We develop a procedure based on the Wiener filter to separate geologic responses from UXO signals. Application of the Wiener filter involves the estimation of a transfer function defined by the ratio of the signal and data power spectra. We have developed an iterative approach to estimate the transfer function using the power spectra of the data and geologic noise from the measured field data set and limited forward modeling of UXO anomalies. This approach is demonstrated by applying it to synthetic data examples and field data from Chevalier Ranch.

5.2.1.1 Wiener Filter

The Wiener filter was first introduced by Norbert Wiener in 1949 (Wiener, 1949). It operates in the frequency domain and has been used effectively to remove noise from data and images (e.g., Hansen and Pawlowski, 1989). The filter assumes that the data is the sum of the signal (desired information) and noise (undesirable information),

$$d(x) = s(x) + n(x) \tag{5.1}$$

where *d(x)*, *s(x)*, *n(x)* are the spatial representations of the data, signal, and noise, respectively. The Wiener filter uses a transfer function calculated from the power spectra of the data and noise. If the above summation holds true then it can be rewritten in the frequency domain as,

$$d(x) \ = \ s(x) \ + \ n(x) \quad \Leftrightarrow \quad \tilde{d}(\omega) \ = \ \tilde{s}(\omega) \ + \ \tilde{n}(\omega) \tag{5.2}$$

where $\tilde{d}(\omega)$, $\tilde{s}(\omega)$, and $\tilde{n}(w)$ are the Fourier transforms of the data, signal, and noise respectively. Under the assumption that the signal and noise are uncorrelated, the transfer function of a Wiener filter is given by,

$$Y(\omega) = \frac{\left|\tilde{s}(\omega)\right|^2}{\left|\tilde{d}(\omega)\right|^2} = \frac{P_s(\omega)}{P_d(\omega)} = \frac{P_d(\omega) - P_n(\omega)}{P_d(\omega)} \tag{5.3}$$

where $P_d(\omega)$, $P_s(\omega)$, and $P_d(\omega)$ are the power spectra of the data, signal and noise, respectively. Equation 5.3 shows that the transfer function is a simple ratio of the power spectra. Simple multiplication of the transfer function and the Fourier transform of the data is used to produce a filtered data set,

$$Y(\omega) \times \tilde{d}_{obs}(\omega) = \tilde{d}_{filtered}(\omega) \tag{5.4}$$

The effectiveness of the Wiener filter hinges on the ability to estimate or calculate the power spectra of the background noise and data. The power spectrum of the data can be calculated easily, whereas the power spectra of the signal and noise must be estimated. The critical part of applying the Wiener filter is determining a reliable procedure to estimate the signal or noise power spectrum. The power spectra in the following examples were all created using the 2D Fast Fourier Transform.

Material presented here will focus on application of the Wiener filter under different conditions using only the power spectra of the data and the noise (eq. 5.3). We investigate the applicability using the ideal case when the power spectra of the data and the noise are accurately known, as well as the real-world case where estimations of the power spectra must be made.

Synthetic Magnetic Data

A synthetic model was generated to test the applicability of the Wiener filter. The parameters used for the model were derived based on common ordnance items found at Chevalier Ranch (a 76mm projectile) and geographic location (direction of inducing field). The synthetic data in Figure 5.1a was generated using two dipoles modeled at a depth of 0.4 m with a dipole moment of 0.13 Am^2. This dipole moment was estimated using methodology developed by Sanchez *et al.* (2006). The inducing field was modeled using an inclination of 70° and a declination of 14° while the dipoles were modeled using an inclination of 10° and 38° and a declination of -25° and 72°, respectively. The dipole parameters are summarized in Table 5.1.

An estimated background soil response, 'noise', was generated using a correlated random number algorithm developed by Sinex *et al.* (2004). These simulated background noise data are shown in Figure 5.1b. The data presented in Figures 5.1a and 5.1b were added together to obtain the data shown in Figure 5.1c.

The modeled dipoles from Figure 5.1a are now indistinguishable from the background noise shown in Figure 5.1b. The short wavelength of the noise is comparable to the wavelength of the modeled dipole. A high-pass Butterworth filter is first used to try to remove the background geology. Figure 5.2 shows the resulting filtered data using a cutoff wavelength of 2.0 meters. The high-pass Butterworth filter is able to suppress most of the noise introduced into the data from the simulated geology but also eliminates one of the synthetic dipoles from the data (#1). Dipole #2 would be selected from the filtered data using a simple peak picking algorithm.

Table 5.1: Dipole parameters used to create synthetic data shown in Figure 5.1

ID	x (Easting)	y (Northing)	Inclination (degrees)	Declination (degrees)	Depth (m)	Dipole Moment (Am^2)
1	4.25	6.25	10	-25	0.4	0.13
2	10.75	9.0	38	72	0.4	0.13

The Wiener filtered data is shown in Figure 5.3c. The transfer function was generated using the power spectra of the synthetic data (Figure 5.1a) and the geologic noise (Figure 5.1b). This is considered the ideal case where the exact power spectra of both the data and noise may be calculated. The synthetic dipoles are visually identifiable in the filtered data. The Wiener filter is able to suppress the geologic noise, recover the synthetic dipoles and also preserves information about the orientation of the dipoles.

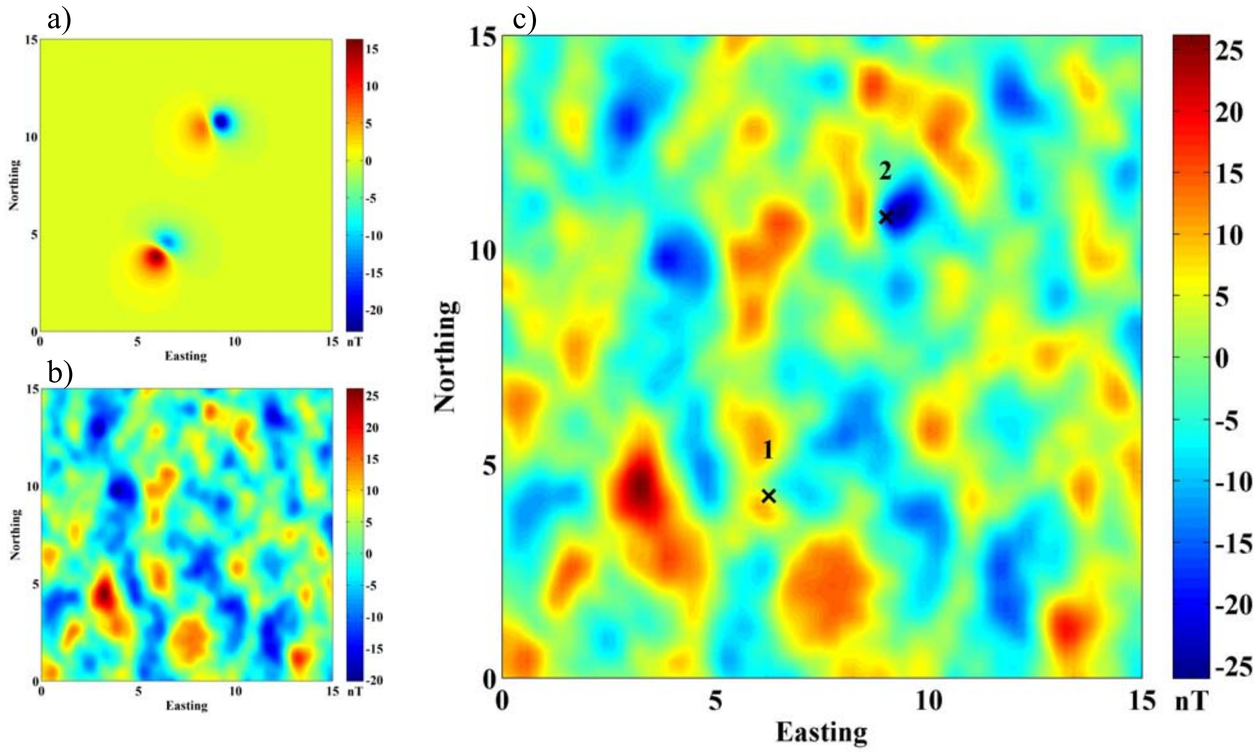

Figure 5.1: Synthetic data used to test the Wiener filter. a) Two synthetic dipoles modeled using the parameters listed in Table 5.1; b) soil simulation generated using random correlated number technique introduced by Sinex *et al.* (2004); c) summation of forward model (Figure 5.1a) and background noise (Figure 5.1b).

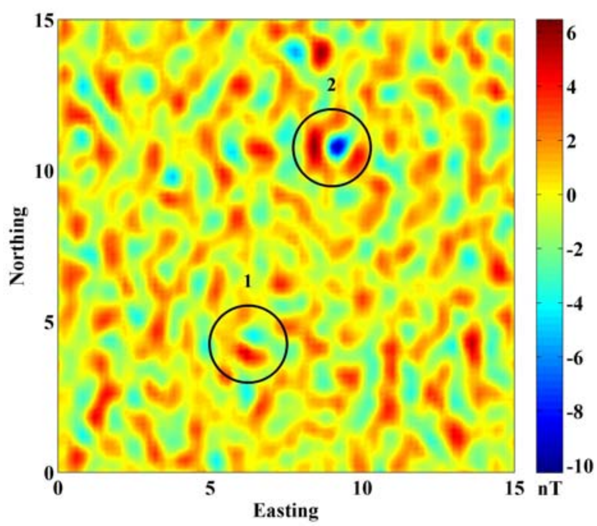

Figure 5.2: Synthetic data after application of a high-pass Butterworth filter with a cutoff wavelength of 2.0 meters.

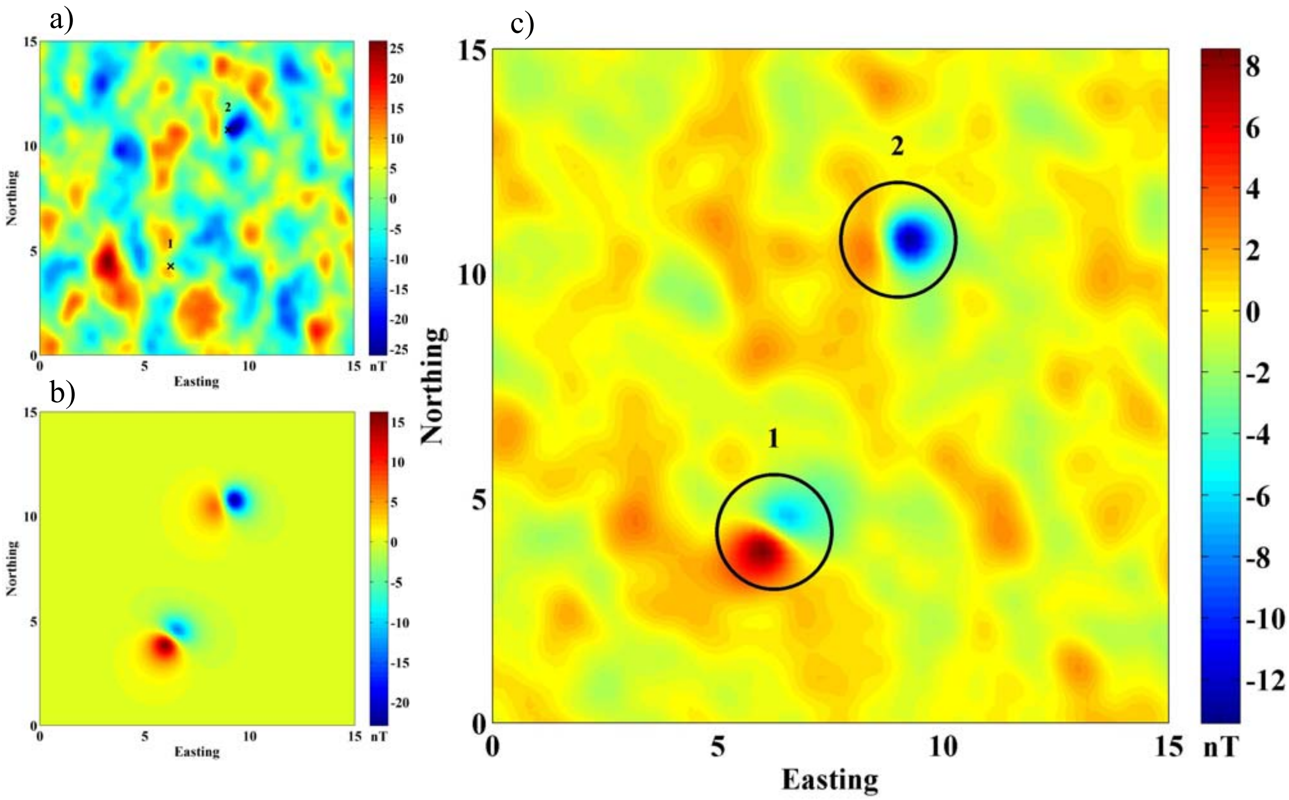

Figure 5.3: a) Summation of the synthetic dipole data and noise data; b) the original synthetic data; c) synthetic data after application of the Weiner filter.

5.2.1.2 Iterative Wiener Filter

The iterative process is carried out by first applying the Wiener filter to the original data using an estimation of the background noise. The first iteration of filtered data is then used in the calculation of the transfer function as the data ($P_d(\omega)$) for the second iteration. Each successive application of the Wiener filter to a particular dataset will produce a filtered dataset where the noise has been suppressed slightly. The same background noise power spectrum is used in each calculation of the transfer function. The iterative process is repeated until the variation between successive filtered datasets is less than 5%. The synthetic data presented in Figure 5.3a will be used to show the convergence of the Wiener filter transfer function.

Figure 5.4a shows the transfer function for the first iteration of the Wiener filter calculated using an estimation of the background noise as $P_n(\omega)$ (Figure 5.4f). The transfer functions calculated for the 5th, 10th, 15th, and 20th iterations are shown in Figure 5.4b-e, respectively. Figure 5.4 shows that there is little variation in the calculated transfer function after the 10th iteration. This indicates that the change in filter data between successive iterations diminishes as the number of iterations increase, and the filtering process converges rapidly.

To simulate realistic processing of field data, the Wiener filter is applied to the contaminated synthetic data (Figure 5.1c) using an estimation of the power spectrum of the geologic noise. This estimation is calculated by dividing the contaminated field data into smaller sub-grids. Within each sub-grid a data value is selected from a random (x,y) location. These random data values are gridded to the same grid size as the original data set to create an estimation of the background noise. The noise power spectrum is calculated from this noise estimation and then used to define the filter transfer function, $Y(\omega)$.

Figure 5.5 shows the results from successive applications of the Wiener filter to the synthetic data. Dipole #2 is evident in the filtered data while dipole #1 is unrecoverable. These results are comparable to the high-pass Butterworth filter shown in Figure 5.2. Dipoles that have a visible expression in the data (i.e. dipole #2 is visible in Figure 5.1c as a dipole feature) are resolved by both the high-pass and Wiener filter. The iterative Wiener filter reduces most of the noise to a level that would minimize the selection of false anomalies originating from geology, but is unable to recover dipole #1. Figure 5.5e shows the noise estimation derived from a 1.5 meter sub-grid.

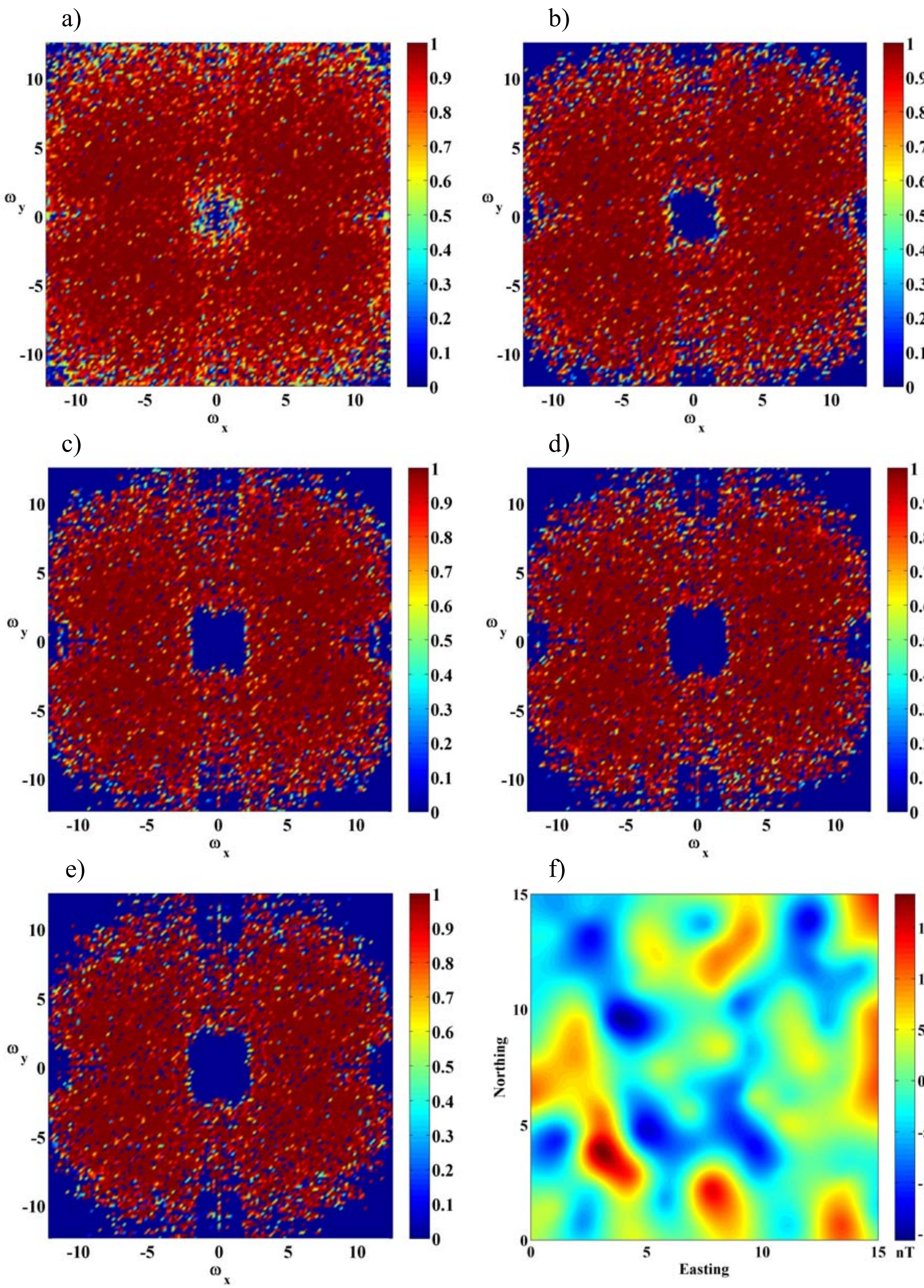

Figure 5.4: Transfer functions associated with iterative Wiener filter: a) 1^{st} iteration; b) 5^{th} iteration; c) 10^{th} iteration; d) 15^{th} iteration; e) 20^{th} iteration; f) noise estimation used in calculation of transfer function.

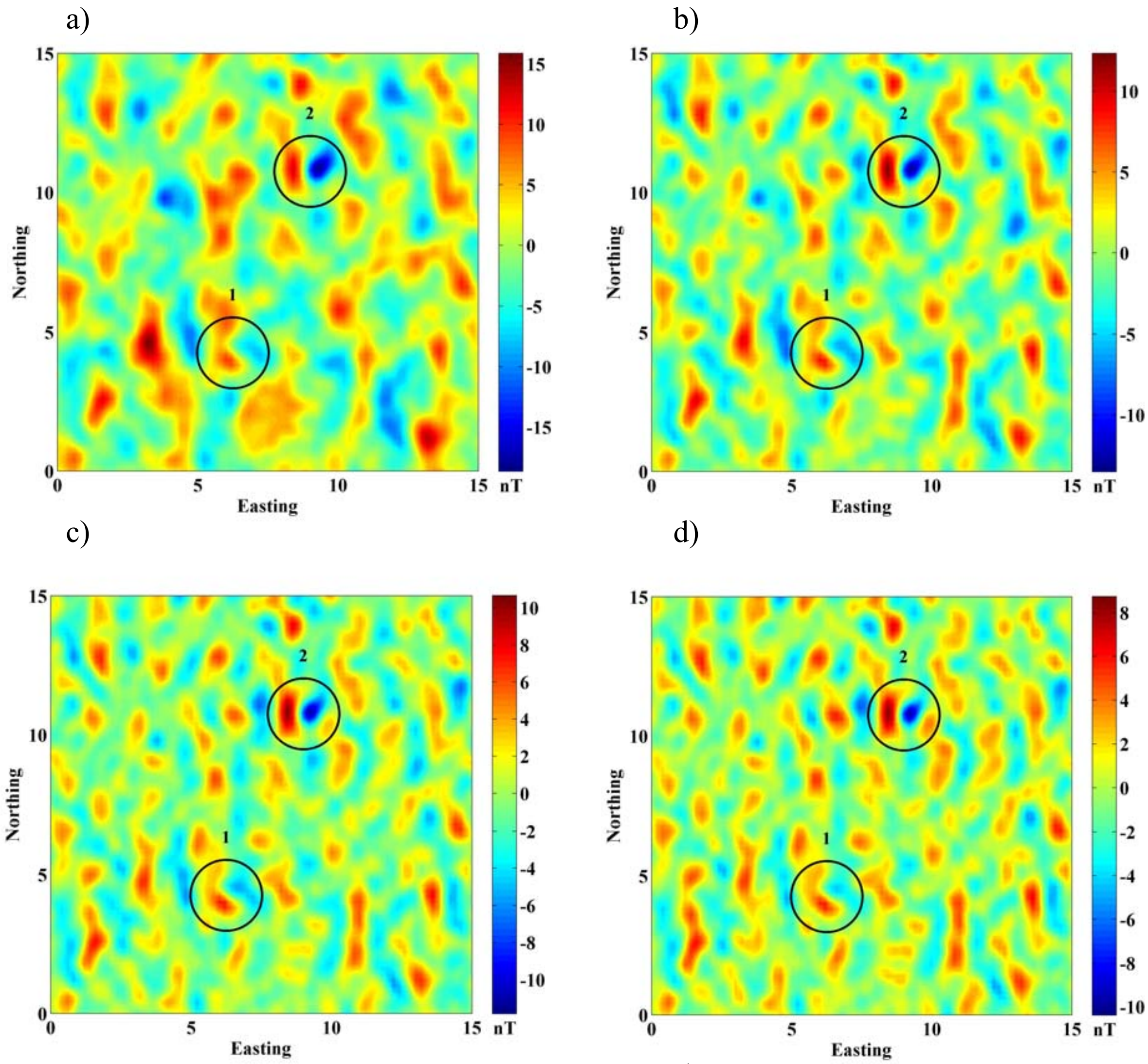

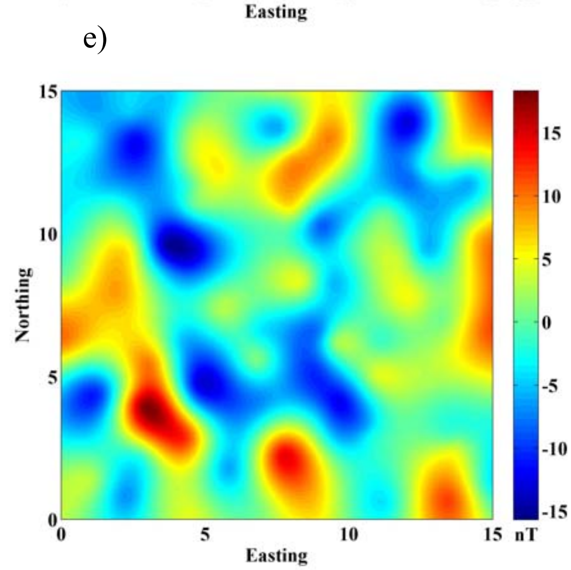

Figure 5.5: Iterative Wiener filter applied to synthetic data. a) 1st iteration; b) 2nd iteration;c) 3rd iteration; d) 4th iteration; e) noise estimation used to generate transfer function.

Chevalier Ranch, Helena, Montana

The Chevalier Ranch area is located approximately 10 miles north-northwest of Helena, Montana. Total field magnetic data were collected at Chevalier Ranch in June, 2005 by the research team. For a more detailed discussion of Chevalier Ranch and field work conducted, the reader is referred to the 2005 SERDP MM-1414 Annual Report. The study area encompassed a 200 x 200 meter area that includes different geologic features. These features have been identified as problematic during the clearance activities conducted at Chevallier Ranch (Billings *et al.*, 2006). This section presents data from two smaller areas within the larger 40,000 m^2 area.

The first area, Figure 5.6a, shows an extensive linear monopolar anomaly (>50m strike length, ~100 nT) likely associated with a deeper mafic dyke. This data set will be referred to as the 'Dyke'. The second area, Figure 5.6b, shows linear dipolar anomalies which are spatially compact (< 5m strike length, ~100-200nT anomaly) with a character that could be interpreted as a UXO response. This data set will be referred to as the 'Anomaly'. In both areas, three 76-mm projectiles have been buried. Table 5.2 shows the depths and orientations of the buried ordnance items. The data presented here has had a base station and heading error correction applied.

Table 5.2: Ordnance locations and orientations buried at Chevallier Ranch

ID	Easting	Northing	Item	Inclination (degrees)	Declination (degrees)	Depth (m)
Dyke						
1	13	17	76 mm APT	0	0	0.11
2	20	20	76 mm TPT	0	90	0.09
3	27	23	76 mm APT	8 (nose up)	82	0.09
Anomaly						
1	24	24	76mm TPT	0	0	0.14
2	22	29	76 mm APT	0	90	0.10
3	19	21	76 mm APT	12 (nose up)	30	0.04

The filtered Dyke and Anomaly data are shown in Figures 5.7 and 5.8, respectively. The Wiener and high-pass Butterworth filter perform equally well on the Dyke data. The three buried ordnance items (identified with circles) are easily distinguished in the filtered data (Figure 5.7b – d). The noise estimation was derived using 2 meter sub-grids (Figure 5.7e). The Dyke structure is simple and easily estimated using the sub-grid method. In addition to the three ordnance items, a peak picking algorithm would probably identify three additional anomalies in the filtered data. These anomalies were not investigated during the field operations to determine if they are geologic or metallic in origin.

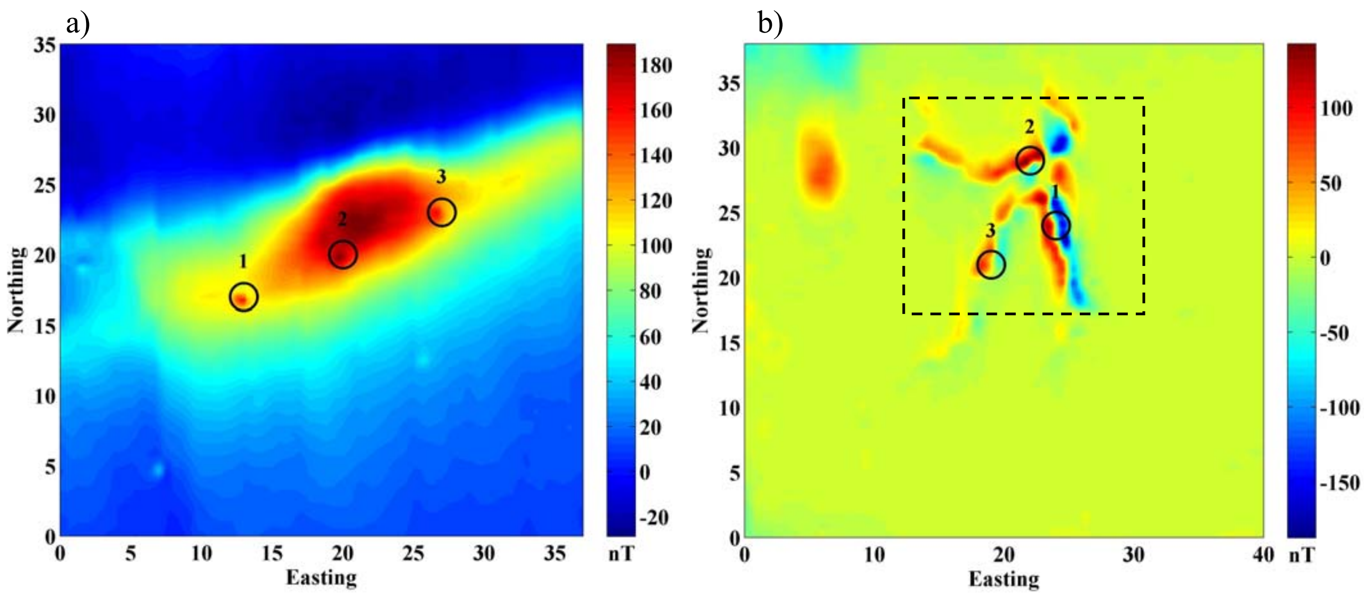

Figure 5.6: a) Magnetic data over the Dyke feature; b) Magnetic data over the Anomaly feature (only the area outlined in black was filtered). The black circles on both figures show the location of the buried ordnance items.

The Anomaly feature data produces poor results in both the Wiener filter and the high-pass Butterworth filter (Figure 5.8). Neither filter technique is able to recover any useful information from the buried ordnance. Although the background geology is suppressed, so is the signal from the ordnance items. It is important to note that none of the three buried ordnance items are visible in the preprocessed data. The anomalous signal is enveloped by the local geology.

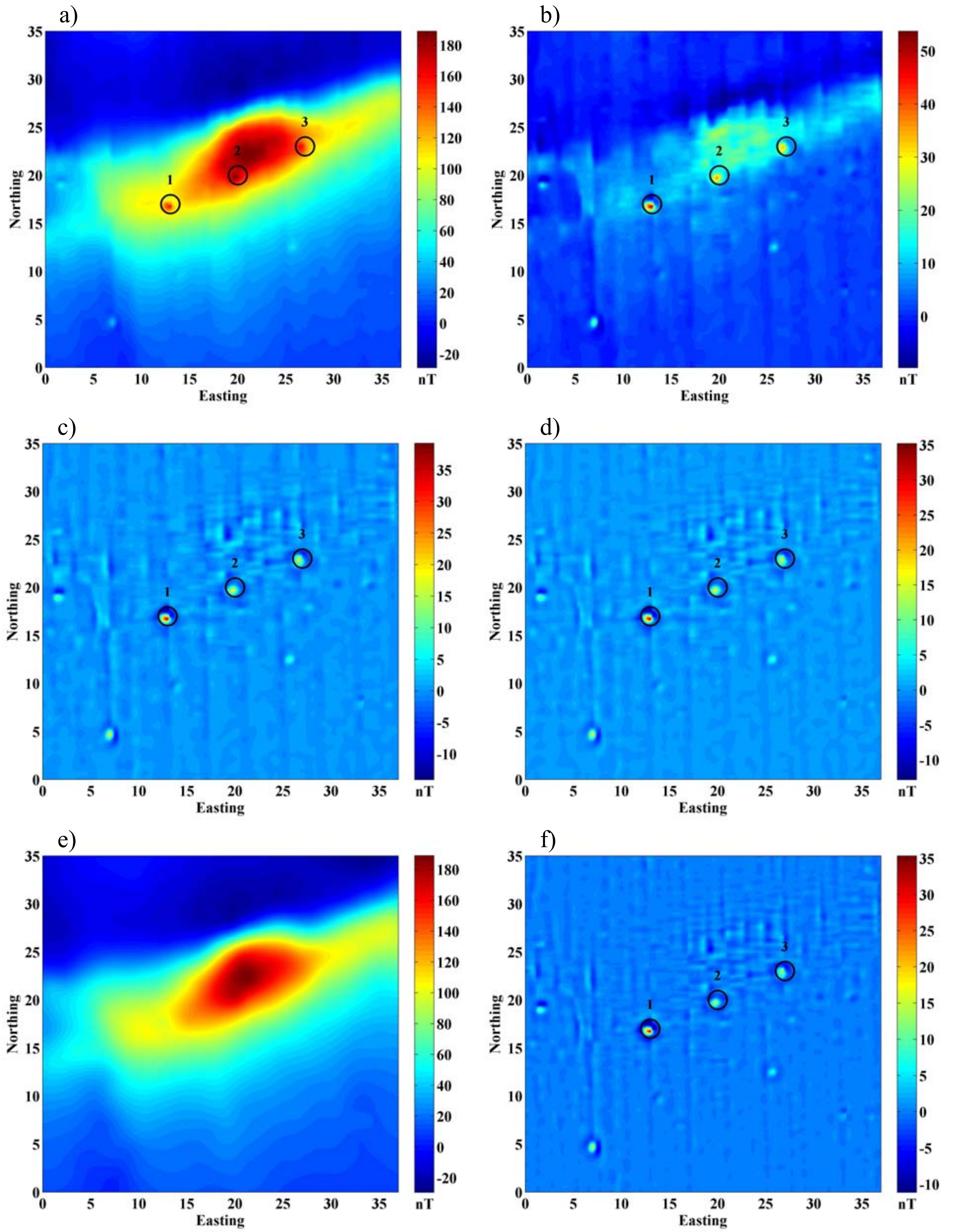

Figure 5.7: Dyke filtered data. a) field data; b, c, and d) 1st, 2nd, and 3rd iteration of the Wiener filter, respectively; e) noise estimation used for Wiener filter using a 2m sub-grid; f) high-pass Butterworth filtered data (2m wavelength cutoff).

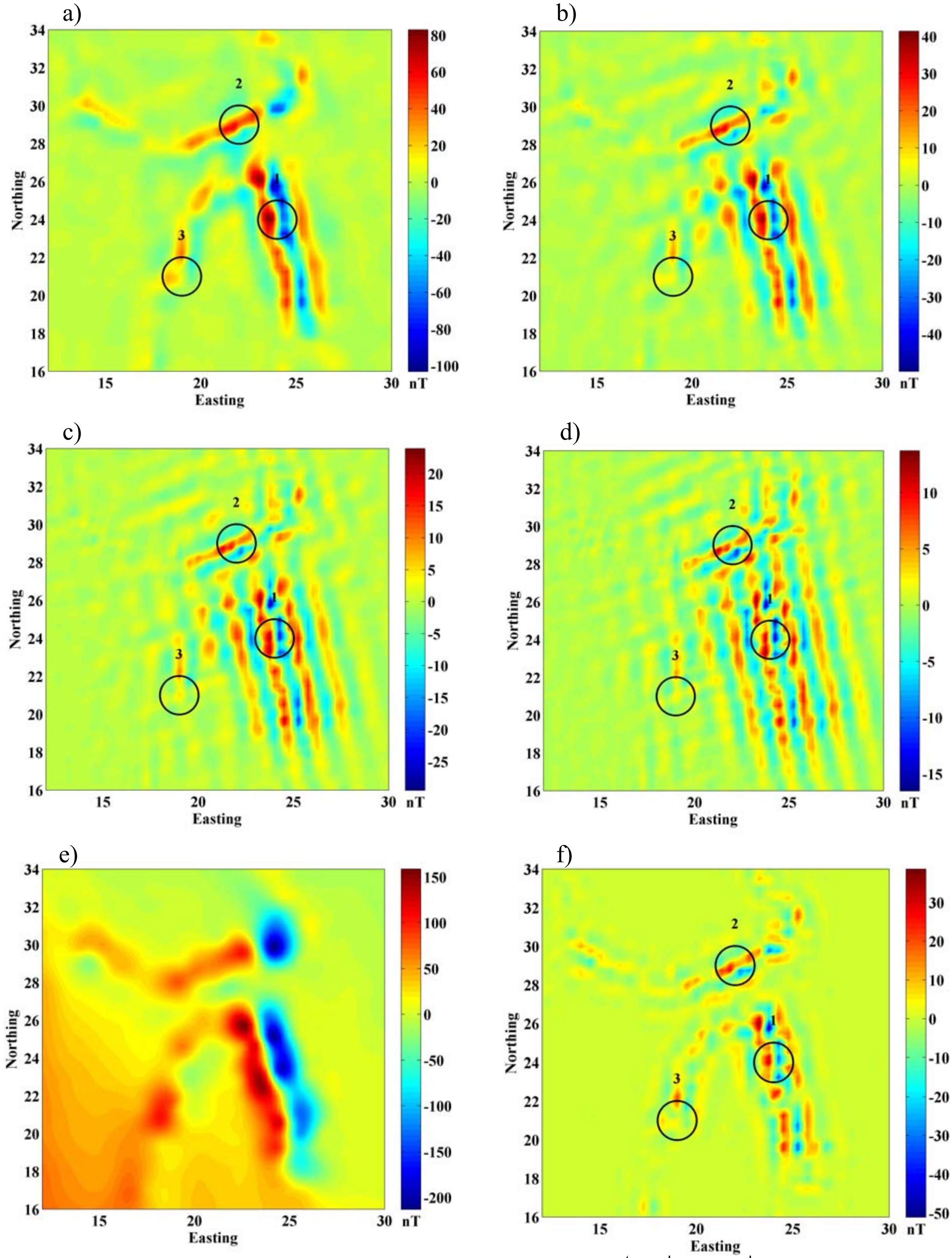

Figure 5.8: Anomaly filtered data. a) field data; b, c, and d) 1^{st}, 2^{nd}, and 3^{rd} iteration of the Wiener filter, respectively; e) noise estimation used for Wiener filter using a 1m sub-grid; f) high-pass Butterworth filtered data (1.25m wavelength cutoff).

Discussion

The iterative Wiener filter is promising in its ability to recover anomalous signal from severely contaminated synthetic total field magnetic data. In the case of the synthetic data, when the power spectrum of the noise is known (ideal scenario) the Wiener filter is capable of anomalous signal recovery. The surrounding geologic response was suppressed and the dipoles were easily identified in the filtered data. Once the background noise is estimated using the sub-grid method from the synthetic data only a single anomaly is visible in the resulting filtered data. The results from the synthetic data indicate that a more accurate estimation of the background noise, as compared to the sub-grid method, would be required to filter contaminated data. When compared to the high-pass Butterworth filter, the Wiener filter produces better results only when using the power spectrum of true background noise rather than an estimation of it. Analysis of the filtered synthetic data suggests that a combination of the Butterworth and Wiener filter may reduce background noise and the number of false anomalies selected for removal.

Two cases involving real field data were presented with different results. The successful filtering results from the Dyke field data come from either the simple shape of the background feature (better noise estimation) or that the ordnance items are visible in the pre-filtered data. In the case of the Anomaly data set none of the three buried ordnance items are visible (with the possible exception of item #1) in the pre-filtered data. The Anomaly feature is more comparable in terms of spatial wavelength to the buried UXO. Pre-processing of the field data using a directional strike filter may reduce some of the geologic noise but may also reduce the response of potential UXO.

The results presented here show that an accurate estimation of the background is needed to recover anomaly information using the Wiener filter. Maximum Entropy Method (MEM) may increase the effectiveness of the Wiener filter by producing a more accurate estimation of the power spectrum. Inverting the data for a magnetic susceptibility distribution may also produce a better estimation of background geologic noise. The methodology presented here should also be directly applicable to TDEM data.

5.2.2 Wavelet filter

In parallel to the iterative Wiener filter, we developed a second approach for separating the response of unexploded ordnance in areas of strong magnetic geology. The method is an adaptation of an automated wavelet filtering technique originally developed at Colorado School of Mines for processing gravity gradiometry data in petroleum exploration (Lyrio *et al.*, 2004). While the iterative Wiener filter from the previous section directly separates UXO-like anomalies from geology - by estimating a transfer function using the power spectra of the data and geology - the wavelet-based method identifies UXO-like anomalies by taking a more roundabout approach. First, localized UXO-type anomalies are treated similar to geologic noise, and as such are separated from the magnetic data using a wavelet transform-based denoising approach. The remaining longer wavelength-component of the magnetic data, assumed to be the response of background geology, is then subtracted from the magnetic dataset. The residual after such a geologic response has been removed is assumed to be the magnetic response of UXO-like targets. Such a preprocessing approach for magnetic data in UXO bears similarities to the regional-residual separation processing techniques of the gravity method in exploration.

The difficulty of the above described approach for separating background from UXO in terrain contaminated with high and variable magnetic geology lies in the frequency content of the data. The magnetic signal of buried UXO and other metallic objects often have frequency content similar to that of the geologic response, such as observed at Chevalier Ranch, MT. Under these conditions, frequency domain filters may not always work well because they tend to remove frequencies globally, causing a generalized smoothing effect that substantially broadens features of interest and decreases their amplitudes. This is one of the main drawbacks of the median filter which is commonly applied to UXO magnetic datasets during preprocessing. Lyrio *et al.* (2004) appropriately describes the differences between these two fundamentally different processing techniques: smoothing versus denoising.

Wavelet transforms have two potential advantages over Fourier transforms for separating the magnetic response of UXO from magnetic soils. The first is multiresolution decomposition, and the second is time/space localization. The wavelet-based approach uses compactly supported orthonormal wavelets and selectively filters out localized high-frequency anomalies, such as those associated with UXO for the proposed approach, while having little effect on other sharp features present in the signal associated with geology. These properties have the potential to allow for a fast and accurate means of separating geology from UXO-like anomalies in magnetic datasets. Details of the methodology, components, and implementation of wavelet transform-based denoising are provided in Appendix-A of the January 2007 Annual Report.

Field Data

We have applied the automated wavelet-transform based de-noising method to two UXO magnetic datasets from Chevalier Ranch in Helena, MT. At our field sites, the magnetic susceptibilities associated with geology are found to either reduce or completely mask the magnetic response of our buried targets. The two test sites for the wavelet filter, referred to as Dyke and Anomaly, are the same locations used for testing the iterative Wiener filter in the previous section. Use of these common data for the two methods of separating geology from UXO-type targets has helped improve our understanding of: (1) the two fundamentally different filtering approaches; and (2) the geologic conditions under which each method may prove valuable, or ineffective.

<u>Dyke Location, Chevalier Ranch, MT</u>

In the first dataset, Figure 5.9(a), the large magnetic anomaly prevalent in the image is the magnetic response of a subsurface volcanic dyke with high magnetic susceptibility. Three 76-mm projectiles were emplaced along the south flank of this geologic anomaly, illustrated by circles in Figure 5.9(a). Table 5.2 provides orientations and depths for the UXO items buried in the Dyke and Anomaly data sets. This site was selected for testing the filtering methods because the response of the magnetic dyke has the undesired effect of obscuring the signal of buried UXO, significantly reducing the dipole response, and hindering current detection and discrimination techniques. In addition, the difference in frequency content, amplitude, and aspect ratio between the magnetic response of UXO and geology at this site provides useful information about the conditions under which wavelet-based separation will and will not be appropriate. This site is a clear example of the need to separate the response of UXO from geology in strong magnetic environments.

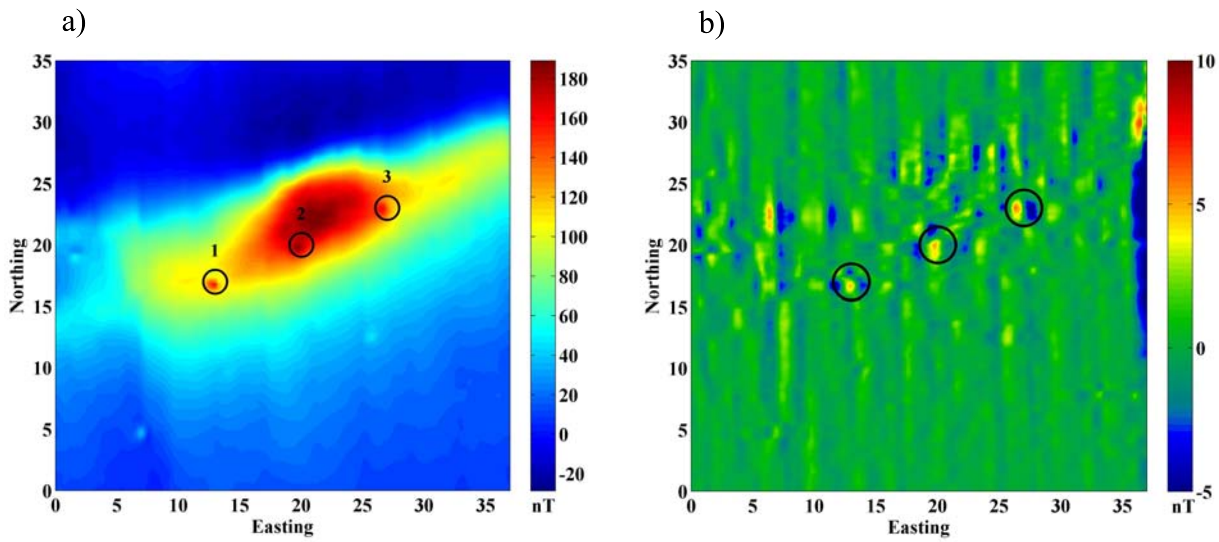

Figure 5.9: Total field magnetic data (a) collected at Dyke site from Chevalier Ranch, MT. Within the data are outlined the locations of the three buried UXO (dark circles) along the south flank of the larger magnetic anomaly associated with the volcanic dyke. The second image (b) is the magnetic data after applying the wavelet filter for separating out the geologic response. UXO responses are clearly visible in the preprocessed magnetic data. North-south trending lines are heading errors from the survey which have been captured along with the UXO anomalies.

Figure 5.9 illustrates the magnetic data collected over the Dyke (a) before wavelet preprocessing, and (b) after separating the geology using a wavelet filter. The wavelet approach for this site, as described previously, treats the UXO anomalies as the residual after removing the higher wavelength monopolar magnetic structure associated with the volcanic dyke. A side result of this approach, is that heading errors present in the data – trending north-south in Figure 5.9(a & b) – are separated along with the three UXO anomalies present along the south flank of the dyke. This effect may be desired for standalone magnetic filters; however, it has the potential to produce negative results for automated target detection algorithms, as these heading errors remain embedded along with the UXO anomalies and can lead to false positives. This effect will be demonstrated in section 5.3 of this chapter during automated target picking.

The wavelet filter has demonstrated similar results, overall, to the iterative Wiener filter for removal of background geology with strong magnetic response at this site. Amplitudes of the UXO anomalies, however, are not preserved as well in this instance of the approach. It is possible that this is due to the wavelet parameters implemented here. For this example, we used the wavelet family of symmlet with 14 coefficients and a resolution of 5. Tuning of these important parameters to the specific site may produce further improvements.

Anomaly Location, Chevalier Ranch, MT

The second magnetic dataset, Figure 5.10(a), is from the Chevalier Ranch location Anomaly. The magnetic data are dominated by linear dipolar anomalies which are spatially compact relative to the previous site. At this location, these strong magnetic anomalies from geology have masked the response of the three buried UXO. The dipole nature from geology in this magnetic dataset is also of interest because target picking algorithms may seek potential UXO targets based on their dipolar field. This site therefore represents a second class of problems for UXO detection/discrimination using magnetic method. However, the much needed outcome from preprocessing is still the same – development of an efficient means for separating the strong magnetic response of background geology from that of UXO.

Figure 5.10 illustrates the magnetic data over the Anomaly location (a) before wavelet preprocessing, (b) after applying the wavelet filter to identify the geologic response, and (c) after using the filtered data to separate the geologic component. In contrast to the previous site, the magnetic response of geology at Anomaly is fairly compact and similar in amplitude to the buried UXO targets. The wavelet filter has performed well in reproducing the geologic response, Figure 5.10(b). However, the result of removing this geologic component is a preprocessed data-set that is highly contaminated with noise and heading errors. Likewise, there are still no discernible UXO dipolar anomalies within the preprocessed data. This result is similar to that of the 3rd iteration Wiener filter (Figure 5.8d).

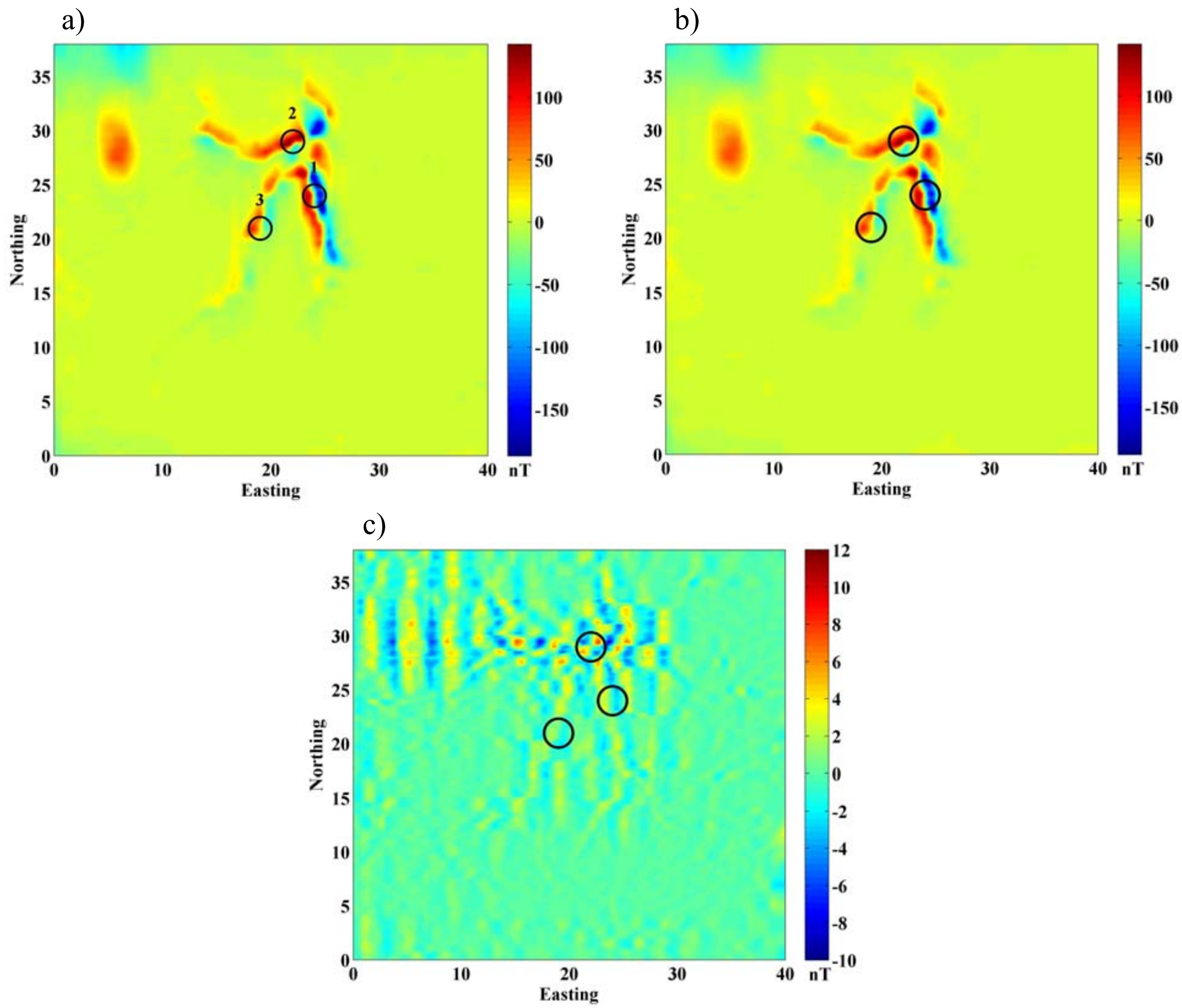

Figure 5.10: Total field magnetic data (a) collected at Anomaly site from Chevalier Ranch, MT. Within the data are outlined the locations of the three buried UXO (dark circles) which are masked by the compact dipolar anomalies from the magnetic geology. The second image (b) is the magnetic response of the geology predicted by the wavelet filter. The third image (c) is the result of applying the wavelet filter for removing the geologic response from the data, i.e. the response of UXO. Results of separating geology with the wavelet filter is not as successful for this site as for the Dyke site presented in the previous example, Figure 5.9.

The current result for separating geology from UXO using wavelet filter, Figure 5.10(c), do not prove as valuable for this site as for the previous one. For this example, we applied the wavelet family of symmlet with 14 coefficients and a resolution of 5. While continued research on the application of wavelet filtering for this site may improve the final result, it is unlikely that alternative wavelet parameters will have a significant impact here due to the similar wavelength of UXO and geologic response. Alternative methods may prove more appropriate for such magnetic environments.

Discussion

Current research demonstrates that using the wavelet filter to separate strong magnetic geology from UXO performs similar to the frequency domain iterative Wiener filter. We believe, however, that the wavelet parameters may be tuned more accurately for magnetic problems similar to that of the Dyke site. For this problem, the geologic signal behaves more as a regional anomaly with different amplitude, frequency content, shape (monopolar versus dipolar) and aspect ratio than the magnetic response of UXO. At sites similar in geologic background to the Anomaly location, we do not predict significant improvements. This is because the magnetic response of background geology is relatively compact and dipolar, which tends to mimic or mask the buried UXO targets.

5.2.3. Leveling / decorrugation filter

The previous sections demonstrated the application of the discrete wavelet filter and iterative Wiener filter for separating the response of magnetic soils from desired UXO targets. In section 5.3 of this chapter, we illustrate that such pre-processing of static magnetic data in magnetic environments is required in order to properly recover and detect the dipole parameters from sought UXO targets. There were two noteworthy observations from the iterative Wiener and wavelet separation approaches. First is that they perform similarly in allowing for the detection of previously masked UXO. The second observation, which we sought to improve upon with this final technique, is that the methods may capture undesired corrugation effects associated with data acquisition, which may likewise increase the number of false positives during detection and discrimination processing.

In many geophysical applications, data are acquired in closely spaced parallel lines, and the results often demonstrate strong corrugation effects associated with: (1) variations in sensor level from line to line, or (2) heading errors inherent to sensor response from changes in orientation/direction of motion. These errors are then illuminated as a series of alternating highs and lows, tracing the survey path when the data are latter gridded and presented as contour or surface plots. A good example of these errors is illustrated in Figure 5.11. When such corrugations are not properly removed from the data through filtering techniques, this may lead to poor interpretations of the data by subsequent processing and inversion.

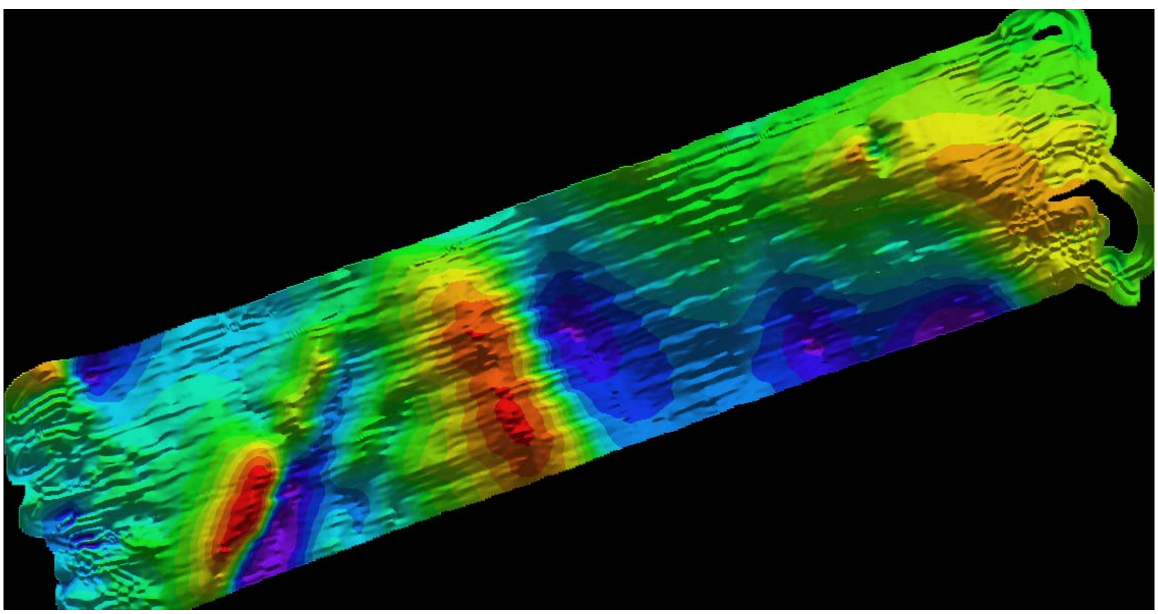

Figure 5.11: Example of corrugation errors in total field magnetic data. The parallel alternating highs and lows in the data indicate the direction of survey lines over the grid and are the response of uneven sensor levels from line to line.

For the UXO problem, heading errors in static magnetic data can manifest in the form of false positives by subsequent target picking algorithms. This is found to occur where the alternating highs and lows in the data mimic a series of apparent dipole anomalies, thus misleading the current detection algorithm (presented in the next section) which seeks these magnetic dipole sources as potential UXO targets.

To level the magnetic data while preserving the high frequency content associated with UXO, we implement a 3 step approach for filtering the data. The original data demonstrating the corrugation errors is first presented in Figure 5.12(a).

1. Extract the high-frequency content of the data, which contains the response of UXO and scrap metal. For this step, we apply a high-pass Butterworth filter to each line of the magnetic data. The resulting high frequency information, referred to as residual data (Figure 5.12(b)), is then set aside temporarily.
2. Apply secondary filter perpendicular to survey lines for removing the leveling errors. The cut-off wavelength depends on the average line spacing during data acquisition, and the dominant wavelength typically approximates twice the line spacing. The resulting data, referred to as the regional field in Figure 5.12(c), is a smooth representation of the original data, less the high frequency component subtracted from Step 1, and reduced corrugation errors.
3. Add the high frequency data from Step 1 back to the regional field generated from Step 2 during leveling. The resulting data, Figure 5.12(d), has significantly reduced leveling errors, which occur in the across-line direction, while preserving the higher frequency response of UXO.

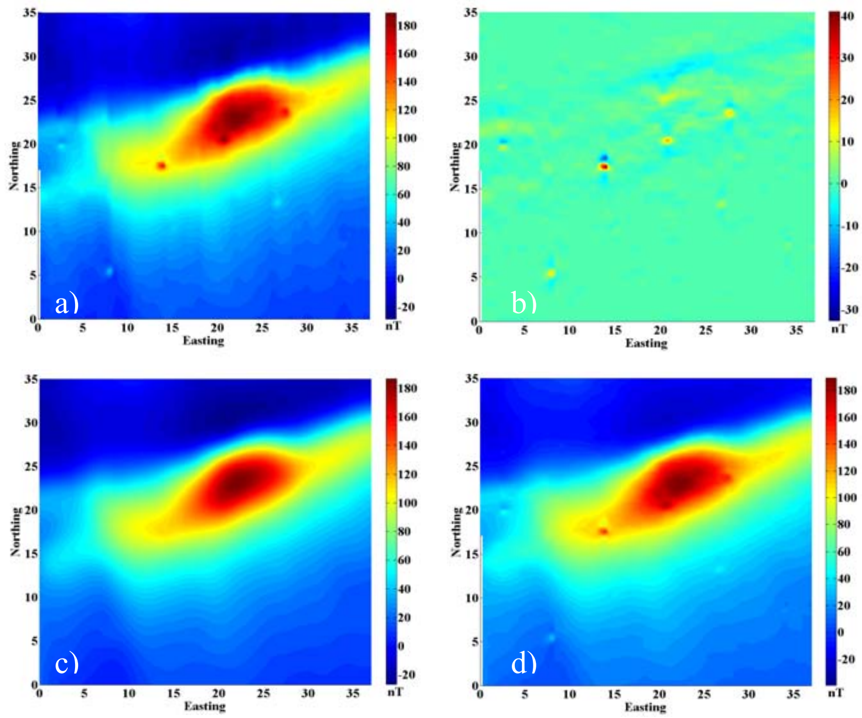

Figure 5.12: Application of decorrugation / leveling filter to magnetic data for the Dyke site at Chevalier Ranch, MT. (a) Original total-field magnetic data; (b) residual high frequency component from high-pass Butterworth filter; (c) regional field from magnetic geology after applying high-pass Butterworth filter for preserving response of UXO and leveling the data; and (d) final decorrugated magnetic data.

Separation of Magnetic Geology

An integral component of SERDP MM-1414 is the identification and development of processing techniques, both new and old, for separating the geologic response from UXO and scrap metal in strongly magnetic environments. Decorrugation of the magnetic data collected at Chevalier Ranch, MT, has demonstrated that, in addition to removing the effects of unleveled sensors during data acquisition, the multi-step process can provide an additional set of tools for improved UXO detection in magnetic environments.

In contrast to the discrete wavelet filter and iterative Wiener filter, which have been exploited thus far to mimic the magnetic response of the geology, the multi-step implementation of the decorrugation filter has demonstrated an alternative approach. Rather than designing filter parameters to mimic the broader response of magnetic geology for later separation, the decorrugation filter starts by directly stripping, line by line, the high frequency component of the magnetic data, including the responses of UXO-like anomalies. This portion of the data is then added back to the regional data after leveling. The final regional field after leveling is a good representation of the magnetic response of the geology, and the initially extracted high frequency content is a good representation of the data which we seek to recover for the next level of interpretation – selecting potential UXO targets within the separated magnetic data. We may therefore treat the residual data, Figure 5.12(b) from the set of decorrugation procedures at Chevalier Ranch, as data similar to that extracted by the iterative Wiener and wavelet filters for target selection at UXO remediation sites. We have thus concluded that separating geology from UXO response in certain magnetic environments may be achieved through either an iterative Wiener filter, discrete wavelet filter, or high-pass Butterworth filter, depending on the site.

5.3 Target selection

In order to validate the above approaches for separating geology, and to improve current state of practice for UXO detection based on magnetic method, a reliable technique for identifying these desired anomalies must be implemented – both before and after pre-processing. For this, we have modified and implemented an approach, originally discussed under a separate project funded by ERDC, for automatic detection of UXO anomalies in total-field magnetic data. The method is based on the concept of structural index (SI). We further the method by implementing it in combination with pre-processed data using the iterative Wiener and wavelet filters discussed in the previous sections for removing strong geologic responses in the magnetic data. The goal of this component is to better understand and develop practical procedures, appropriate to a geologic setting, for integrating new filtering technologies with newly evolving methodologies for detecting UXO in magnetic environments. In this section, we briefly describe the Hilbert transform-based extended Euler deconvolution technique (Nabighian and Hansen, 2001), outline a workflow for applying the method to detection of potential UXO targets (Davis *et al*., 2005), and present results of the method applied to three magnetic datasets, filtered and unfiltered, collected at Chevalier Ranch, MT.

5.3.1. Extended Euler method

The magnetic field produced by a dipole-like source, such as UXO, decays with inverse distance cubed, and therefore has a structural index (SI) of 3. Identifying magnetic anomalies having structural indices of 3, or close to 3, therefore enables the possibility of directly detecting potential UXO targets. This is the key concept of the recently developed Hilbert based extended Euler deconvolution method of Nabighian and Hansen (2001), modified by Davis *et al.* (2005) for automated target picking of UXO like targets. We have found that the method provides an efficient means for calculating the SI, and enables automatic anomaly detection based on computed SI. We next outline the basic method of extended Euler deconvolution method for computing the SI and location of potential UXO targets.

For a magnetic source body such as UXO, a given component of the anomalous magnetic field satisfies the following:

$$B_a(tx, ty, tz) = t^n B_a(x, y, z) \tag{5.5}$$

where n is the degree of homogeneity. For a dipole like source, such as a potential UXO target, the field decays with inverse distance cubed, and the corresponding degree of homogeneity in equation 5.5 is therefore n = -3. Differentiation of equation 5.5 yields Euler's homogeneity equation (or simply Euler's equation):

$$x\frac{\partial B_a}{\partial x} + y\frac{\partial B_a}{\partial y} + z\frac{\partial B_a}{\partial z} = nB_a \tag{5.6}$$

where *x, y, & z* are the field coordinates of the measured data for the source body, and the anomalous body itself is at the origin. If one assumes a compact source body, such as UXO or scrap metal at (x_o, y_o, z_o), and the data are observed above the surface at location *(x, y, z),* the above equation becomes:

$$(x - x_0)\frac{\partial B_a}{\partial x} + (y - y_0)\frac{\partial B_a}{\partial y} + (z - z_0)\frac{\partial B_a}{\partial z} = -NB_a \tag{5.7}$$

We note, that at this stage we have four unknowns: x_o, y_o, z_o, and the structural index N. For convenience, the structural index is defined as $N=-n$.

For standard Euler method, one assumes an *a priori* value for N, and therefore directly seeks the location of the anomalous source body (x_o, y_o, z_o). While this assumption may be appropriate for many problems, the severity of the UXO problem requires a more robust method for also calculating the structural index under varying site conditions, where the anomalous field does not behave as a perfect dipole. If a UXO's anomalous field does not behave as a perfect dipole, standard Euler method fails to detect the buried munition, and the item remains a hidden threat. This leads us to the Hilbert transform based extended Euler method of Nabighian and Hansen (2001).

For extended Euler method, the same Euler equation also holds true for the two components of 3D Hilbert transforms of the field:

$$\begin{aligned}
(x-x_0)\frac{\partial H_x(B_a)}{\partial x}+(y-y_0)\frac{\partial H_x(B_a)}{\partial y}+(z-z_0)\frac{\partial H_x(B_a)}{\partial z} &= -NH_x(B_a), \\
(x-x_0)\frac{\partial H_y(B_a)}{\partial x}+(y-y_0)\frac{\partial H_y(B_a)}{\partial y}+(z-z_0)\frac{\partial H_y(B_a)}{\partial z} &= -NH_y(B_a),
\end{aligned} \tag{5.8}$$

where H_x and H_y denote respectively the x- and y- component of the 3D Hilbert transform. With this added information, we can now solve directly for N, and it serves as the improved criterion for detecting UXO anomalies.

5.3.2. Workflow details for automatic anomaly detection

The method for automatic anomaly detection using the Hilbert transform based extended Euler deconvolution may be implemented through the following workflow. The method is described in greater details in Davis *et al.* (2005). We note that the workflow presented is only a component of the procedure we are developing here, which also incorporates pre-processing of magnetic data (when appropriate) using the iterative Wiener and wavelet filters described in the earlier parts of this chapter. The approach assumes one starts with a gridded magnetic data set

ΔT, which may or may not have undergone preprocessing to separate geology from the UXO data. This step is problem dependent, as we will present in the results to follow.

Step-1: Compute the two horizontal derivatives using stabilized numerical differentiation operators in order to reduce noise.

Step-2: Compute the vertical derivative in the Fourier domain through the use of 3D Hilbert transform relations (Nabighian, 1984),

$$\begin{aligned}\Delta\tilde{T}_z &= \tilde{H}_x\Delta\tilde{T}_x + \tilde{H}_y\Delta\tilde{T}_y \\ &\equiv -\frac{i\omega_x}{\sqrt{\omega_x^2+\omega_y^2}}\Delta\tilde{T}_x - \frac{i\omega_y}{\sqrt{\omega_x^2+\omega_y^2}}\Delta\tilde{T}_y\end{aligned} \tag{5.9}$$

where ω_x and ω_y are the wavenumbers of the 2D Fourier transform in the x- and y-direction, and $\Delta\tilde{T}_x$, $\Delta\tilde{T}_y$ and $\Delta\tilde{T}_z$ are respectively the Fourier transforms of the X, Y and Z derivatives of the total-field anomaly.

Step-3: Compute the two components of the 3D Hilbert transform of the original total-field anomaly and their three spatial derivatives to obtain the eight quantities related to the magnetic field.

Step-4: Using the eight quantities calculated in Step-3, solve equation (5.8) in each window using least squares. A range of window sizes is used. This step yields the *x, y, z* source location estimates and the structural index value *N* for that source.

Step-5: For the set of windows centered at the same location, find one solution whose structural index *N* is closest to 3. This solution is taken as the best solution associated with the set of windows with located on a common center.

Step-6: If a solution exists and the structural index is greater than a threshold value, we assume that the algorithm has detected a possible UXO-like anomaly. The corresponding location provides a first order estimate for the dipole position.

5.3.3. Results

We have applied the approach to three magnetic datasets collected at the three Montana locations presented in section 5.2 of this chapter. The three datasets collected at Chevalier Ranch, MT, are: Drainage; Anomaly; and Dyke. At the first two sites, applying the method directly to field magnetic data without pre-processing yields good results. The third site, Dyke, demonstrates the need for preprocessing to remove the strong geologic response in order to adequately resolve target locations. For that site, we will demonstrate the methods improved ability for target detection after that dataset has undergone pre-processing using the iterative Wiener filter and wavelet filter approaches presented at the start of this chapter.

We first present results for application of the automated target picking approach to the Drainage site. The site was selected for this study because of the presence of linearly extensive weak magnetic anomalies associated with a drainage feature (< 20nT). Greater detail on site's geology/mineralogy is available in the 2006 Annual Report. For this example, the data have not undergone preprocessing to separate magnetic geology from UXO. The magnetic dataset is presented in Figure 5.13. Superimposed over the magnetic data are the locations of the true UXO targets (surrounded by black circles), and the target picks through extended Euler deconvolution (white plus marks). The method has performed well for this site, identifying the true buried rounds as potential UXO targets based on their structural indices. The method has also identified additional dipole-like anomalies associated with geology as potential targets, i.e. false picks. Preprocessing of the data at this site using the currently formulated iterative Wiener filter and wavelet filter did not reduce the number of false targets greatly. Therefore, preprocessing of magnetic data under such site conditions, before applying this target picking approach, requires future research and modification to significantly reduce the number of false positives while still identifying UXO.

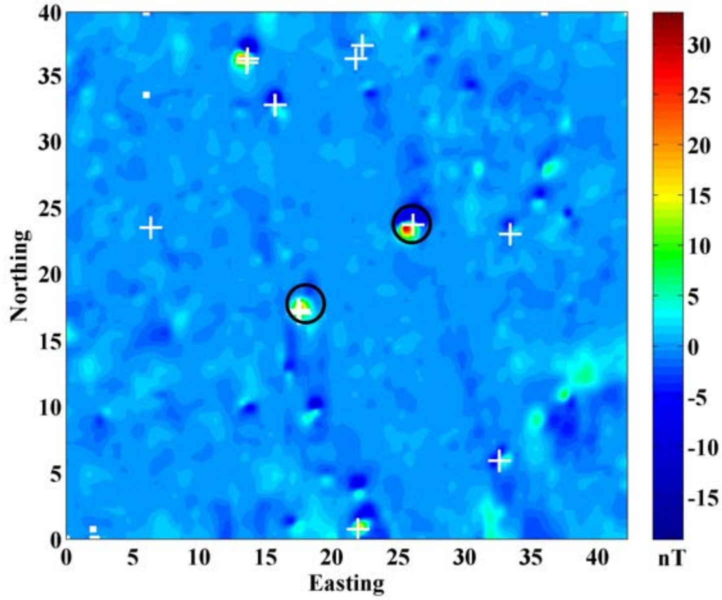

Figure 5.13: Total field magnetic data collected at Drainage site from Chevalier Ranch, MT. Within the data are outlined the locations of the two buried UXO (dark circles) and the potential UXO targets picked by the automated extended Euler deconvolution method. The approach successfully identified the two buried UXO. Additional false targets were predicted because of the dipole shape of the magnetic field at those locations.

The second test site we apply the automated picking algorithm to is at the location of Anomaly. The background response is characterized by a set of linear, dipolar anomalies that are spatially compact with a character that could be interpreted as UXO response. At this location, as with the previous site, data are run through our automated target picking approach before preprocessing. The magnetic data and target picking results are presented in Figure 5.14. Two of the three target locations are adequately resolved and the third target pick is shifted, likely due to overlap of UXO and strong geologic dipole response. A second result of the dipolar nature of the geology is that the method also identifies numerous false targets throughout the data region. Preprocessing with both iterative Wiener and wavelet filters, as with the Drainage data, did not improve the target picking ability of the extended Euler method. In particular, current implementation of the preprocessing methods reduced the detection of true targets due to the dipolar nature of the geologic magnetic anomalies. Reducing the number of false targets, while maintaining the ability to accurately detect UXO in such magnetic terrain with dipolar-type structure, is another important topic for future research.

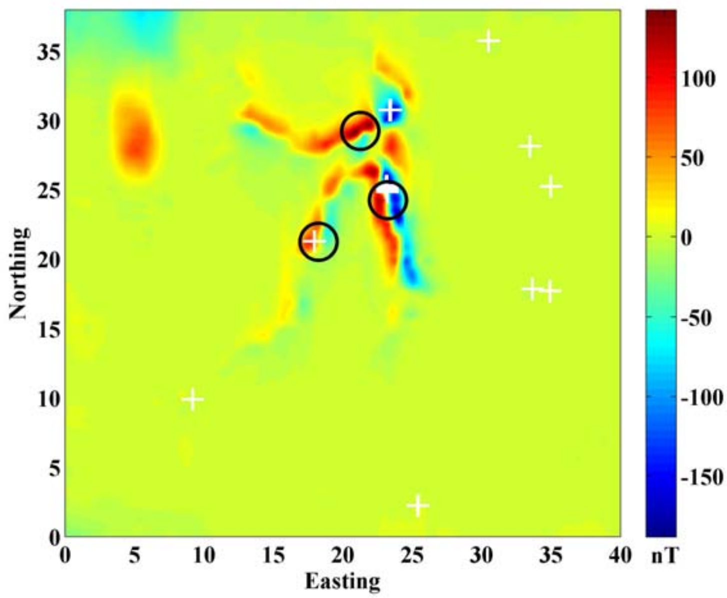

Figure 5.14: Total field magnetic data collected at Anomaly site from Chevalier Ranch, MT. Within the data are outlined the locations of the three buried UXO (dark circles) and the potential UXO targets picked by the automated extended Euler deconvolution method. The approach has identified two of the three UXO satisfactorily; however the third pick is shifted significantly to the north and east. The decreased performance of the method over the previous example, Figure 5.13, is due to the compact dipolar anomalies associated with strong magnetic geology.

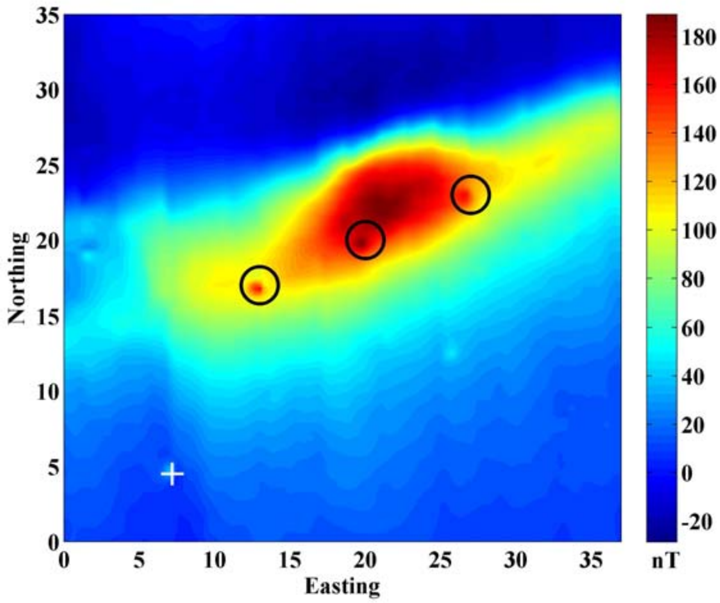

Figure 5.15: Total field magnetic data collected at Dyke site from Chevalier Ranch, MT. Within the data are outlined the locations of the three buried UXO (dark circles) and the potential UXO target (white plus-mark) picked by the automated extended Euler deconvolution method. The method failed to pick any of the true UXO targets, selecting only one false location at the lower left of the grid.

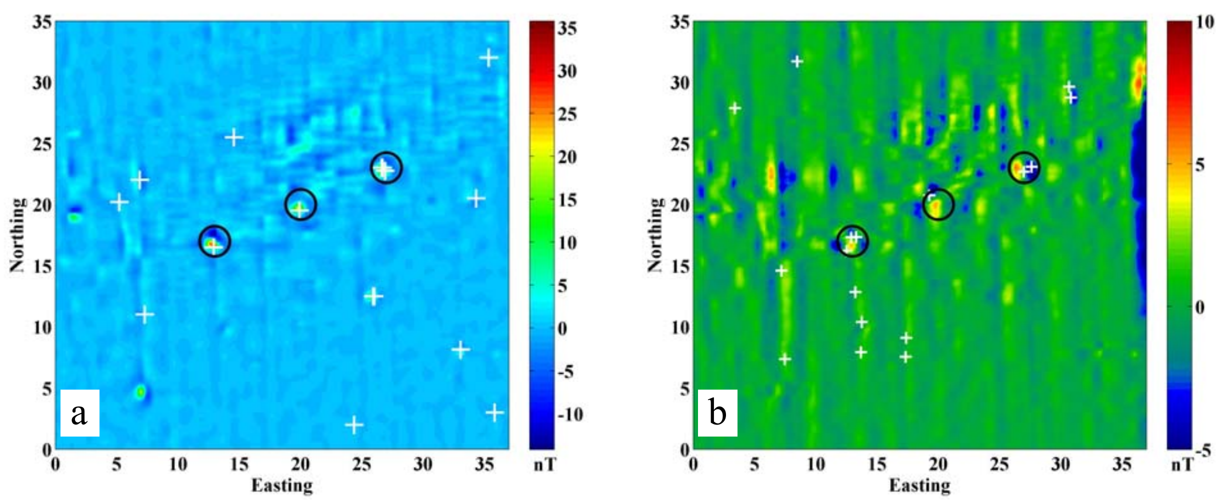

Figure 5.16: Preprocessed magnetic data from Dyke site at Chevalier Ranch, MT. (a) after applying the 3rd iteration Wiener filter to separate out geology, and (b) after applying the wavelet filter for the same purpose. True UXO targets are outlined with black circles, and targets predicted by extended Euler deconvolution applied to the datasets are represented by white '+'-marks. The method produced similar results for the two preprocessed data sets.

The final dataset which we apply the automated target picking algorithm to is Dyke (Figure 5.15). Within this dataset, the large magnetic anomaly is the magnetic response of a subsurface volcanic dyke with high magnetic susceptibility. Three UXO items were emplaced along the south flank of this geologic anomaly and are detectable through visible inspection. Orientation and depths of each ordnance item are located in Table 5.2. This site was selected for the target picking algorithm, however, because the response of the magnetic dyke has the undesired effect of preventing the current automated approach from successfully detecting the buried UXO. The poor target picking result is presented in Figure 5.15 by the single white '+'-mark at the lower left corner, demonstrating that none of the UXO targets are identified for this site. Such a result is not surprising, as Davis *et al.* (2005) describes difficulties of the approach in identifying potential UXO targets in the presence of large regional magnetic anomalies. We have therefore modified the approach by applying the extended Euler deconvolution method to data which have undergone preprocessing, using both iterative Wiener and wavelet filters, to remove the geologic component of the data. Details on the two preprocessing methods are available in the earlier parts of this chapter. Results of the automated picking algorithm after preprocessing are presented in Figure 5.16, (a) for the iterative Wiener filter, and (b) for the wavelet filtered data. The new approach has successfully identified each of the buried targets in both preprocessed datasets. This site has demonstrated the need to separate geology from UXO data when the background behaves similar to a large regional magnetic field. Additional false picks, as with the other sites, are still present in the final solution. We observe that most to all of the false picks result from the ridges associated with the heading errors in the data and are not jointly shared by the two approaches.

Target equivalence

The iterative Wiener and discrete wavelet filters have performed similarly in allowing for successful identification of previously masked UXO, but have also allowed for an increase in the number of false targets through subsequent detection algorithms. While false positives are generally undesirable at UXO remediation sites, results between the two processing techniques have shown to provide complementary information which may be exploited for the appraisal of automated target picks in magnetic environments.

As a means of improving target selection accuracy, we next apply a target equivalence methodology which seeks magnetic dipole parameters associated with UXO which are jointly preserved by independent pre-processing filters. Given that the response from magnetic geology is successfully removed from magnetic data, and that small dipole-like artifacts may remain – or even be generated – through processing algorithms, the dipole parameters associated with UXO-type sources will have the highest likelihood of achieving consistent detection by detection algorithms. Appraisal of target results is therefore achievable by jointly analyzing detection results after separate pre-processing is applied, and identifying the strong dipole parameters (potential UXO) consistent between them. Weaker dipole artifacts preserved or generated by either filtering technique alone will be naturally eliminated as potential UXO targets.

In Figure 5.16(a & b), we present automated target picks based on the magnetic dipole parameters which remain – or are generated – through independent filtering during separation of magnetic geology at Chevalier Ranch, MT. Panel (a) is the filtered data and target picks after application of the 3rd iteration Wiener filter. Panel (b) illustrates results after the discrete wavelet filter is applied. To identify target equivalence between the selected dipole anomalies, a distance threshold of 2 meters is applied such that solutions clustered within this radius are classified as equivalent solutions, or potential UXO targets. This clustering threshold is necessary to ensure that target positions, shifted slightly in space but associated with the same magnetic dipole, are properly identified for remediation.

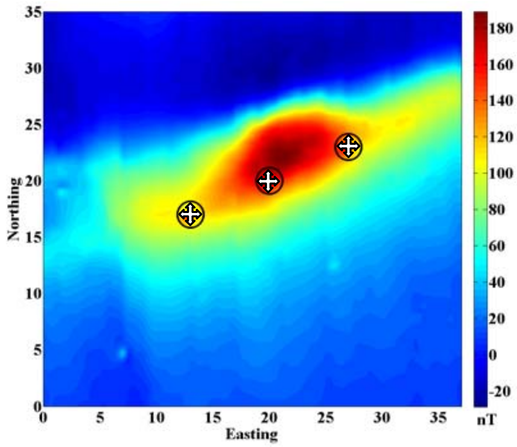

Figure 5.17: Target equivalence results for field data in strong magnetic environment. Targets common to both approaches illustrated in Figure 5.16 (a & b) within a specified clustering radius yield the three desired targets and no false picks.

Figure 5.17 illustrates results of the target equivalence approach applied to the same UXO site at Chevalier Ranch, MT. The two panels in Figure 5.16 demonstrate the dipole anomalies identified as potential UXO following pre-processing with the wavelet and iterative Wiener filters. There are a significant number of false positives throughout each of the sets of pre-processed magnetic data. However, in Figure 5.17, only the emplaced UXO targets are identified as strong magnetic dipoles and, therefore, reliable targets.

The equivalence approach for appraising the set of UXO target solutions has demonstrated a valuable addition to the set of procedures for properly identifying potential targets in strongly magnetic environments. The expanded methodology has allowed for successful identification of all emplaced UXOs at this site, while eliminating all false positives remaining from previous filtering approaches.

5.3.4. Discussion

The automated approach of UXO target picking using the Hilbert transform based extended Euler deconvolution method has demonstrated successful results in settings with high and varying magnetic geology. While the method identifies additional false targets, often associated with heading errors acquired during data collection, it has successfully identified most of the emplaced ordnance items. We have demonstrated, however, that preprocessing to separate the geologic response from UXO data may be required, depending on the nature of the geologic noise. The iterative Wiener and wavelet filter have both shown value for such separation. As commented by Davis *et al*. (2005) and observed within our field datasets, the presence of overlapping anomalies, either between UXO responses or between UXO and some geologic response, tend to degrade the Euler solutions and create false target picks. We add that dipole-like features in the magnetic data associated with geology likewise generate such false positives. This is expected, as the method seeks to identify these dipolar responses.

5.4. Summary

Results for interpretation of magnetic field data in strong magnetic environments demonstrate the need for a multi step processing approach, designed for separation of the response of magnetic geology from that of UXO-like anomalies, in conjunction with a robust target detection algorithm. The difficulties observed during this project have been twofold. First, the response from the environment will distort or completely mask the dipolar response of UXO-like anomalies, thus rendering current detection algorithms based on these dipole parameters ineffective. The second difficulty is that most processing approaches have been unable to properly filter the geologic response while preserving the sought dipolar response for effective UXO detection. The iterative Wiener filter and 1D discrete wavelet filter demonstrate improved results for separating the response of magnetic geology from that of UXO. However, the methods may also preserve or generate secondary dipolar anomalies due to corrugation effects from sensor level during data acquisition, or as artifacts generated by the filters themselves. The end result, which we conclude the chapter with, is that application of SI based target detection to both pre-processed data sets, followed by analysis of target equivalence items, may prove the most reliable detection approach in highly magnetic environments.

6. Electromagnetic Data Analysis

The final major technical objective of SERDP project MM-1414 focuses on the practical aspects of working with electromagnetic data in difficult magnetic environments.

> Develop methods and procedures for removing the effects of soil response from electromagnetic measurements for improved UXO detection and discrimination in magnetic environments.

In this chapter, we first demonstrate the effects on EM sensors of background geology, sensor height, and viscous remnant magnetization. We then outline a series of practical procedures for processing EM data in noisy geologic environments, picking targets by simulating soil response with correlated random numbers, and understanding the effects of VRM noise on recovered model parameters.

6.1 Introduction

Detection and identification of UXO at sites with large geologic background signals can be very difficult. The large frequency dependent component of susceptibility of Kaho‘olawe soils produce background responses of the same order of magnitude of UXO.

Consider a target buried in a halfspace. The measured sensor data can be written as:

$$\mathbf{d}^{obs} = F\left[target, host\right] + \text{noise}, \tag{6.1}$$

where $\mathbf{d}^{obs}$ is the observed sensor data and $F\left[target, host\right]$ represent the forward model that is function of the target and host. If the response of the target and host are approximately additive, we can write:

$$
\begin{aligned}
\mathbf{d}^{obs} &= F^{bg}\left[host\right] + F^{t}\left[target\right] + \text{noise} \\
&= \mathbf{d}^{bg} + \mathbf{d}^{target} + \text{noise}
\end{aligned}
\tag{6.2}
$$

where $\mathbf{d}^{bg} = F^{bg}\left[host\right]$ is the response due to the background host, $\mathbf{d}^{target} = F^{t}\left[target\right]$ is the response due to the target, $F^{int}\left[target, host\right]$ represents the interaction between target and host. In most cases $F^{t}\left[target\right]$ is chosen to be a dipole model representation of the target.

The most common approach to processing is to develop filtering techniques such that the background response $\mathbf{d}^{bg}$ can be estimated, and subsequently subtracted from the data. These filtering methods assume that the geologic, and therefore electromagnetic, properties of the host material are spatially slowly varying, while the anomalies of compact targets have a relatively smaller spatial wavelength. The filtered data is then inverted with the physical model $F^{T}\left[target\right]$ for the UXO response in free space. One of the major difficulties with this approach is the accuracy with which the background response $\mathbf{d}^{bg} = F^{bg}\left[host\right]$ can be estimated. In particular, movement of the transmitter and receiver relative to magnetic ground can produce significant small wavelength anomalies in the data (Walker *et al*. 2005; Foley *et al.*, 2005). High pass filters will have limited success in these cases. Our preferred approach to processing these data is to estimate a smoothly varying background geology, that is subsequently removed from the data. This approach requires accurate sensor positioning and orientation information to model the small wavelength variations.

Techniques for processing data collected at remediation sites with large geologic background signals are considered here. A number of synthetic data will be used to demonstrate filtering, target picking, and parameter estimation of data collected in a magnetic geology setting. The objective is to determine what type of information can be recovered from electromagnetic data collected in regions with highly magnetic geology.

6.2 Electromagnetic response of a viscous remnant magnetic halfspace

Let us consider a circular transmitter loop of radius a, carrying a current I, and at a height h above a 1-D layered earth. At an observation point at the center of the transmitter loop, the vertical component H_z and the radial component H_ρ of the $\mathbf{H}$-field are:

$$H_\rho(\omega) = 0 \tag{6.3}$$

$$H_z(\omega) = \frac{Ia}{2}\int_0^\infty \left[1 + \frac{P_{21}}{P_{11}} e^{-2u_o h}\right] \frac{\lambda^2}{u_o} J_1(\lambda a)\, d\lambda \tag{6.4}$$

where $u_o = \sqrt{\lambda^2 - k_o^2}$, k_o is the wave number of the air, and J_1 is the first order Bessel function. P_{21} and P_{11} are elements of the propagation matrix $\mathbf{P}$.

For a non conductive half-space and using quasi-static assumption, we can write the secondary field as

$$H_z^s(\omega) = \frac{Ia}{2}\left(\frac{\chi}{2+\chi}\right)\frac{a}{\left[a^2 + (2h)^2\right]^{3/2}} \tag{6.5}$$

In cases where $\chi << 2$,

$$H_z^s(\omega) \approx \frac{I}{4}\frac{a^2}{\left[a^2 + (2h)^2\right]^{3/2}}\chi(\omega) \tag{6.6}$$

Therefore the resistive limit response is approximately proportional to the susceptibility. If we represent the magnetic susceptibility with log uniform distribution of time constants and assume that $\tau_2 >> \tau_1$, then the field can be written as

$$H_z^s(\omega) \approx \frac{I}{4} \frac{a^2}{\left[a^2 + (2h)^2\right]^{3/2}} \frac{\chi_o}{\ln(\tau_2 / \tau_1)} \left(1 - \ln(\omega\tau_2) - i\frac{\pi}{2}\right) \tag{6.7}$$

The step-off response can be obtained via Fourier Transform:

$$\frac{\partial H}{\partial t} = -\frac{I}{4} \frac{a^2}{\left[a^2 + (2h)^2\right]^{3/2}} \frac{\chi_o}{\ln(\tau_2 / \tau_1)} \frac{1}{t} \left(e^{-t/\tau_2} - e^{-t/\tau_1}\right) \tag{6.8}$$

For $t << \tau_2$ and $t >> \tau_1$,

$$\frac{\partial H}{\partial t} \approx -\frac{I}{4} \frac{a^2}{\left[a^2 + (2h)^2\right]^{3/2}} \frac{\chi_o}{\ln(\tau_2 / \tau_1)} \frac{1}{t} \tag{6.9}$$

Equations 6.7 and 6.9 will be used as soil models.

For constant sensor height and orientation, the measured time domain response and frequency domain response are proportional to $G(\chi) = \chi_o / \log(\tau_2 / \tau_1)$. Therefore, in areas of low conductivity soil, electromagnetic sensors act as viscous remnant susceptibility meters. To demonstrate this, we can compare susceptibility measurements with sensor data collected on Kahoʻolawe. As part of this project surface soil samples were collected from Grid 2E and their susceptibility measured with a Bartington MS2B susceptibility meter. Comparisons of the susceptibility measurements and sensor data are shown in Figure 6.1.

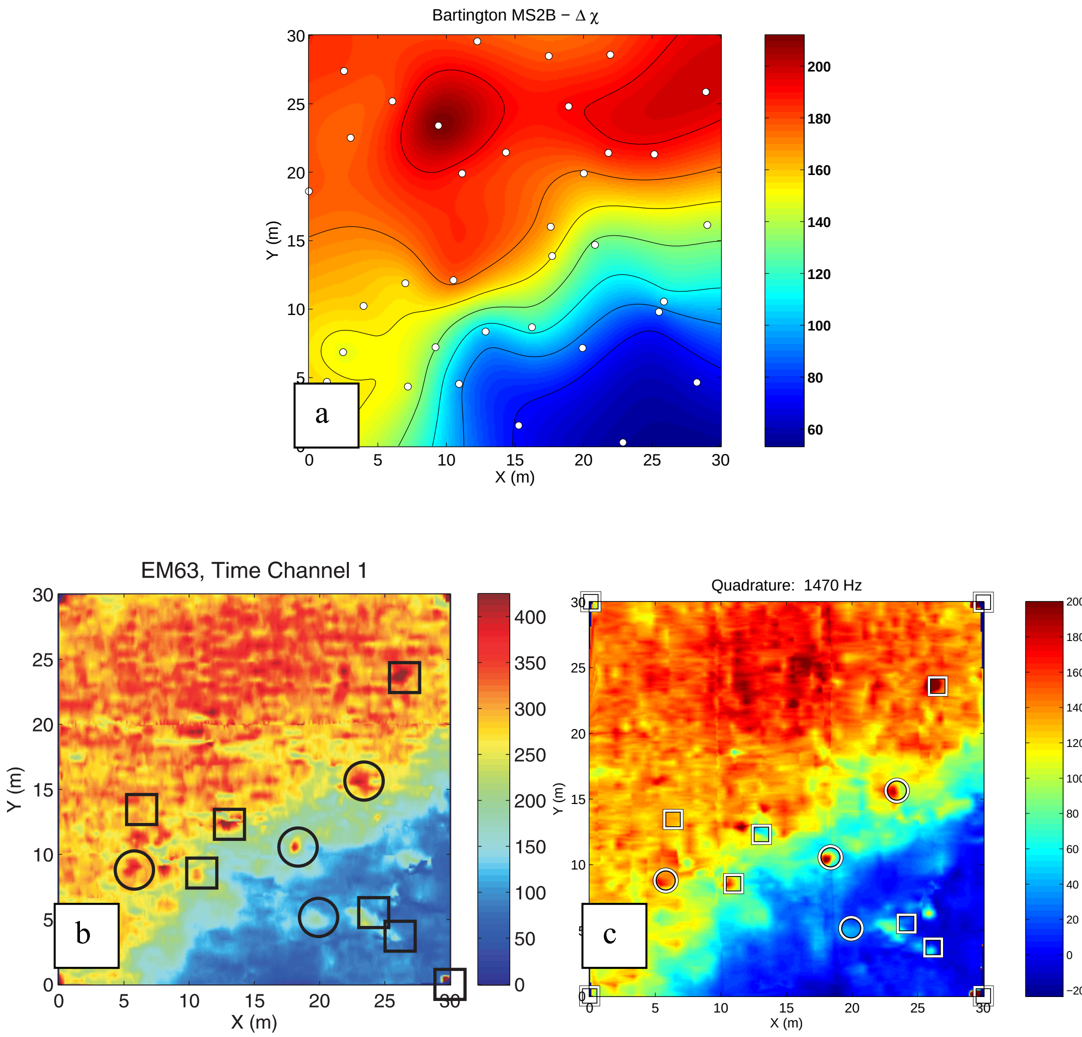

Figure 6.1: Comparison of Bartington MS2B susceptibility measurements with electromagnetic sensor data. (a) Bartington MS2B susceptibility measurements ($\Delta\chi$). White circles indicate sampling points. (b) First channel of Geonics EM63 data. (c) Geophex GEM3 quadrature data ($f = 1470$ kHz). Data collected on the Kaho'olawe Grid 2E are presented.

Figure 6.1(a) is a gridded image of the difference in the susceptibility $\Delta\chi$ measured by the Bartington MS2B susceptibility meter at frequencies of 4.7 kHz and 0.47 kHz. If we assume the log uniform distribution of time constants and the same assumptions made in deriving equation (6.9), we can show that

$$\Delta\chi \approx \frac{\chi_o}{\log(\tau_2/\tau_1)}\log(0.47kHz/4.7kHz). \tag{6.10}$$

EM63 and quadrature component GEM3 data are plotted in Figure 6.1(b) and (c), respectively. Clearly the three images of Figure 6.1 are similar to within a scaling factor.

In the frequency domain, the response is proportional to the susceptibility (Equation 6.6) and not the susceptibility difference. Bartington MS2D measurements were taken on Grid 2E. The Bartington MS2D is a portable susceptibility meter that measures the modulus of the complex susceptibility at frequency $f = 0.98$ kHz. Figure 6.2 compares measurements from Kaho'olawe Grid 2E made by the Bartington MS2D sensor with the amplitude of the GEM3 data at 1470 Hz. Both the GEM3 and Bartington measurements identify an increase in signal in the lower right portion of the grid that was not evident in Figure 6.1. This increase in signal is not seen in the susceptibility and sensor data of Figure 6.1 since the increase is likely due to an increase in the static susceptibility.

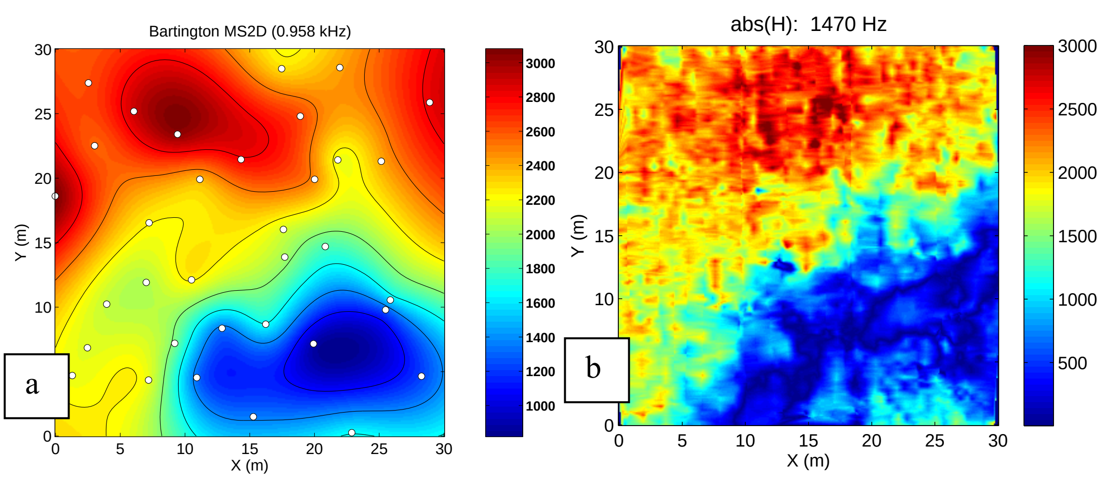

Figure 6.2: Comparison of Bartington MS2D susceptibility measurements with the inphase component of GEM3 data. (a) Bartington MS2D measurements. (b) Geophex GEM3 magnitude FEM data The MS2D measures the phase or sum of the complex susceptibility at $f = 0.98$ kHz.

6.3 Effect of height variations on sensor response

We can use equations 6 and 9 to demonstrate the importance of sensor height accuracy. In both the frequency and time domain, the magnitude of the background response is scaled by the function

$$\text{Scale Factor}\left(SF\right)=\frac{a^2}{\left[a^2+\left(2h\right)^2\right]^{3/2}} \tag{6.11}$$

Figure 6.3 plots this function for a loop with radius a=0.5m, normalized by the value at h = 0.3 m. Changes in height of only a few centimeters can change the signal by tens of percent. This formula can be used to study the effect of sensor height on the measured data.

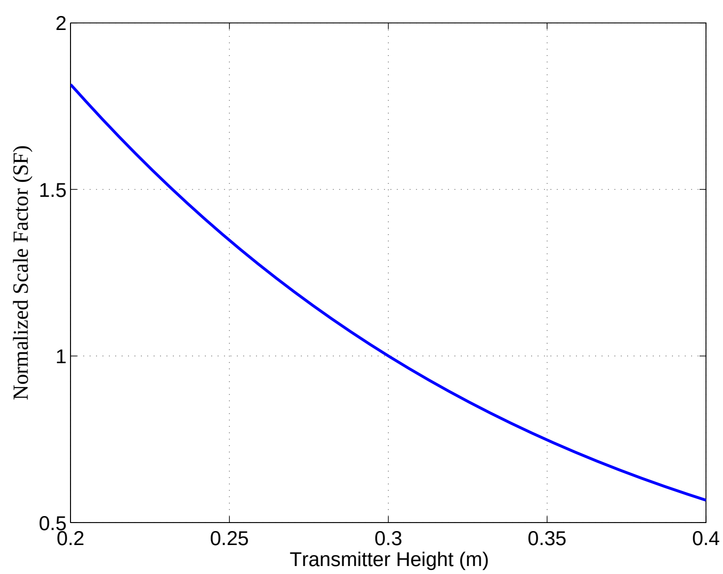

Figure 6.3: Scale factor normalized so the response is unity for a loop of radius a = 0.5 m and height h = 0.3 m.

6.3.1 Simulation of VRM geologic background response due to height variations

To demonstrate the importance of measuring the height of the sensor accurately, we forward model simulated height measurements. For this example we simulate heights based on the measurements made during a Geonics EM63 survey carried out on the FLBGR. Figure 6.4 has photographs of the GPO site. The site is relatively flat, but there are small "clumps" of dirt and grass that causes height and orientation variations in the EM63 cart.

Figure 6.4: On the top is a photograph of the FLBGR GPO looking southeast. The elevation of the grid decreases as we move from the Northwest corner to the Southeast corner. The photo on the bottom shows the small scale topography

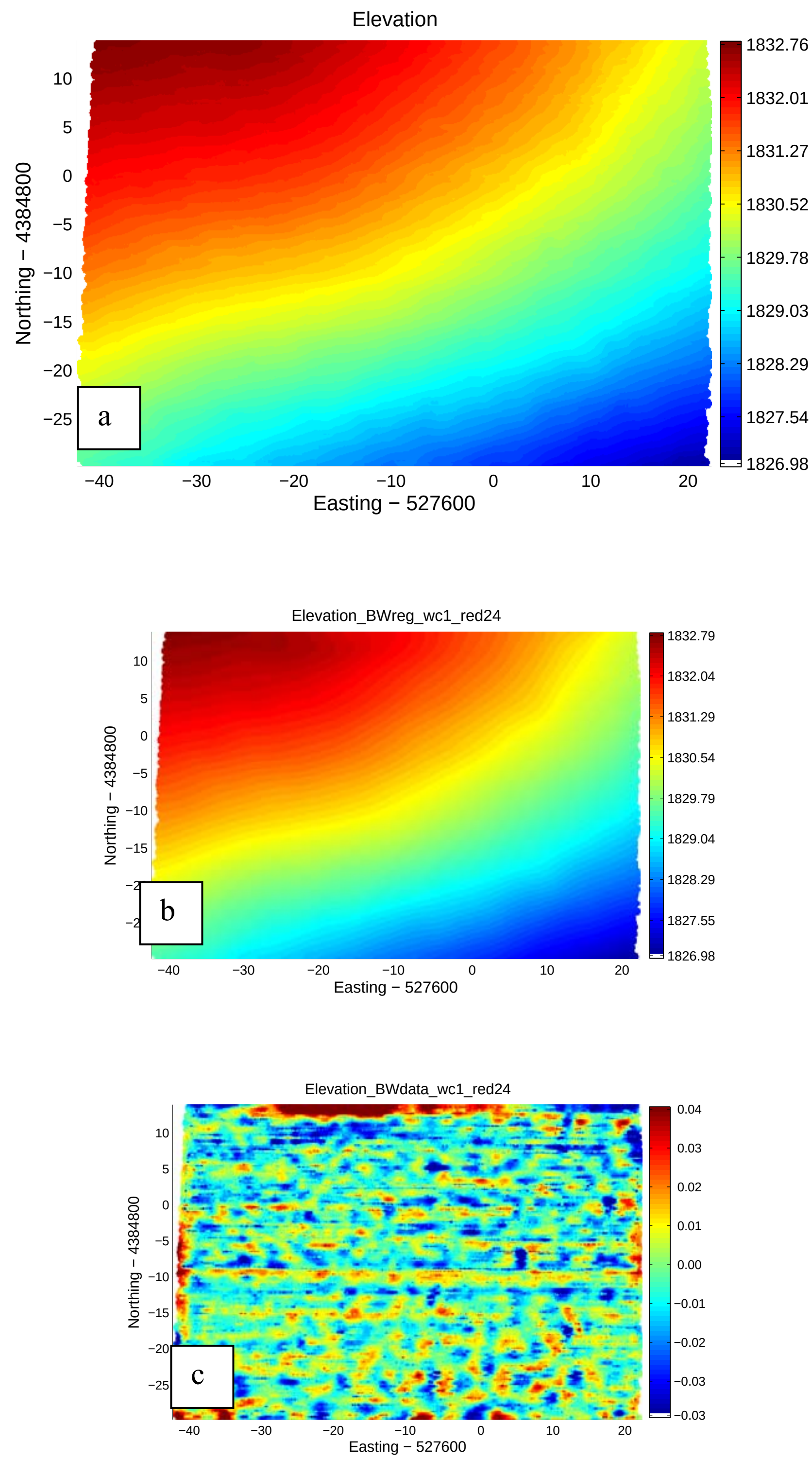

Figure 6.5: Elevation data measured using an RTS at the FLBGR. (a) Low-pass filtered elevation values. (b) Measured elevation. (c) Detrended elevation. The bottom plot portrays small scale height variations that will be used for simulating height variations in our synthetic modeling.4 All elevations are in meters.

The height of the sensor was measured using a Trimble RTS laser positioning system. Figure 6.5(a) shows the elevation measured during the survey, indicating the slight decease in elevation from the Northwest to Southeast corner (as is seen in Figure 6.4). The long wavelength elevation information is obtained through the application of a Butterworth filter (Figure 6.5(b)), and the short wavelength variations are obtained by subtracting the long wavelength component from the raw data.

A new elevation dataset is constructed by estimating the power spectra of the detrended elevation, and adding a random phase to the FFT. An inverse FFT produces elevation data with the same power spectrum as the measured elevation data. Figure 6.6 shows an example of the correlated random number procedure. We assumed that the error had a standard deviation of 2 cm. The bottom image of Figure 6.6 contains the corresponding response expressed as a percentage of the uniform VRM background. The bottom image was constructed by assuming a mean cart height of 30 cm.

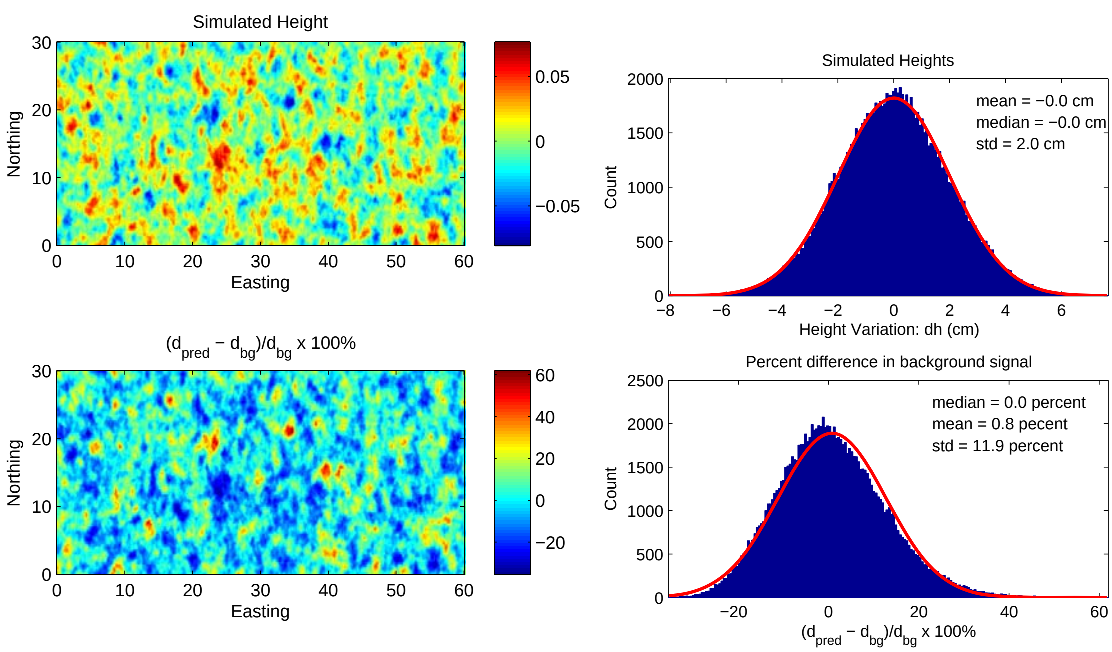

Figure 6.6: Simulated height values (left-top) and the corresponding response expressed as a percent of the uniform VRM background response (left-bottom). Heights are simulated using correlated random numbers generated from the power spectra estimated from Geonics EM63 height data. The distribution of simulated heights and corresponding response are plotted in the right column.

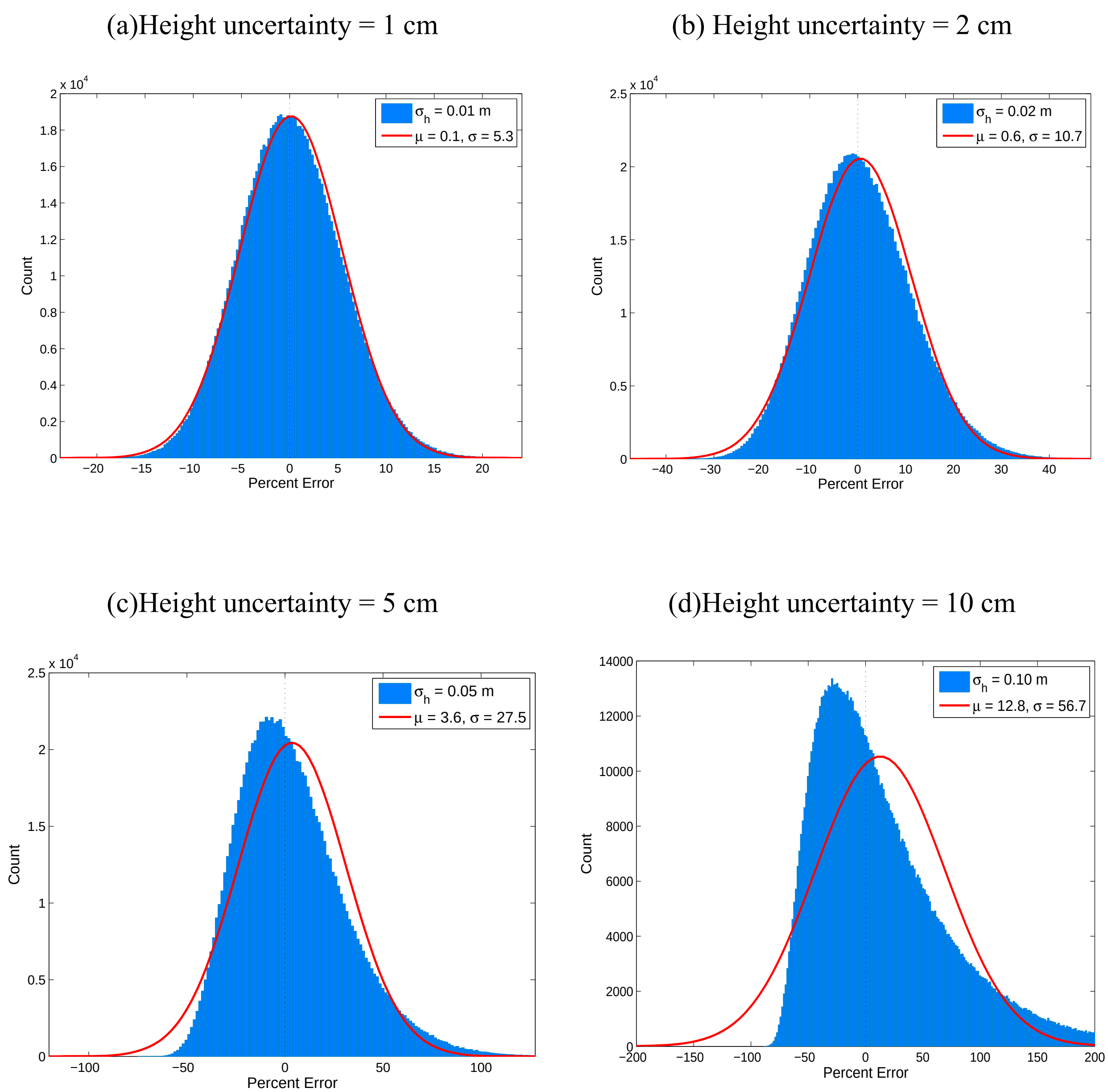

Figure 6.7: Effect of height errors on sensor data acquired over VRM soils. The red line indicates a best fit Gaussian. For large height errors the histogram for data errors is asymmetric and even a biased Gaussian is a poor representation.

6.3.2 Height errors and data variances

Figure 6.7 shows how different height errors translate to uncertainties in a channel of the measured sounding. For small changes in height the relationship between data error and height variation is approximately linear. A random height uncertainty of 2 cm (which will be assumed in these initial tests) produces a data uncertainty of 10 percent. However, the relationship becomes non-linear as height variations increase. This is a reflection that the value measured by the sensor increases rapidly as the sensor gets closer to the ground. As the standard deviation of the height error increases, the uncertainty in the measured data is no longer adequately described by a Gaussian. The associated probability density for the errors will be non-symmetric. This example highlights the importance of filtering the measured height to help reduce the random uncertainty in height. However, filtering may not be possible in cases where cart data are acquired where there is significant small wavelength topography, such as small holes and bumps. In such cases, there will be small wavelength features in the data that reflect the height variations of the sensor.

6.3.3 Sensor height and orientation on VRM response

A series of tests were carried out to investigate the effect of micro-topography and coil orientation on TEM data collected on Kaho'olawe island. These tests were a part of this project and UX-1355 "UXO Target Detection and Discrimination with Electromagnetic Differential Illumination", funded by the Strategic Environmental Research and Development Program (SERDP). Both a coil tilt test and a coil height test were performed with a Geonics EM61 MK2 sensor in a highly magnetic area of Kaho'olawe. During the tilt test, data were collected with the coil at seven tilt angles (Figure 6.8).

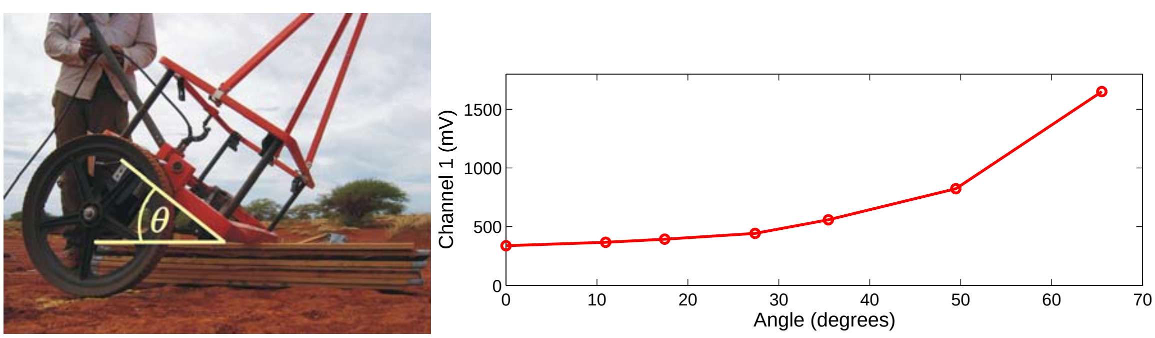

Figure 6.8: Tilt test carried out on Kaho'olawe Island using a Geonics EM61 Mark 2. The left photo is of Geonics EM61 Mark2 tilt test. The tilt angle is indicated by θ. The measured data is presented to the right.

At the largest angle, the edge of the EM61 transmitter coil was in contact with the ground. Tilting the coil 10 degrees forward results in an amplitude increase of approximately 30 mV. The height test varied the height of a horizontal Geonics EM61 with the ground (Figure 6.9). This was repeated for eleven heights ranging from 0 (EM61 coils resting on the ground) to 64 cm. As an example of how dramatic the effect of coil height can be, a coil positioned at 36 cm instead of the normal survey height of 40 cm, will have an amplitude increase of approximately 80 mV. The height test measurements were modelled using viscous remnant magnetic halfspace. The modelled behaviour of the signal with height (the blue curve in Figure 6.9) diverges from the measured response as the coil is closer to the ground. This may be due to the response of the coil being approximated using the field at the center of the receiver loop rather than explicitly integrating the flux over the loop. The effect of loop height is much more dramatic than sensor orientation differences.

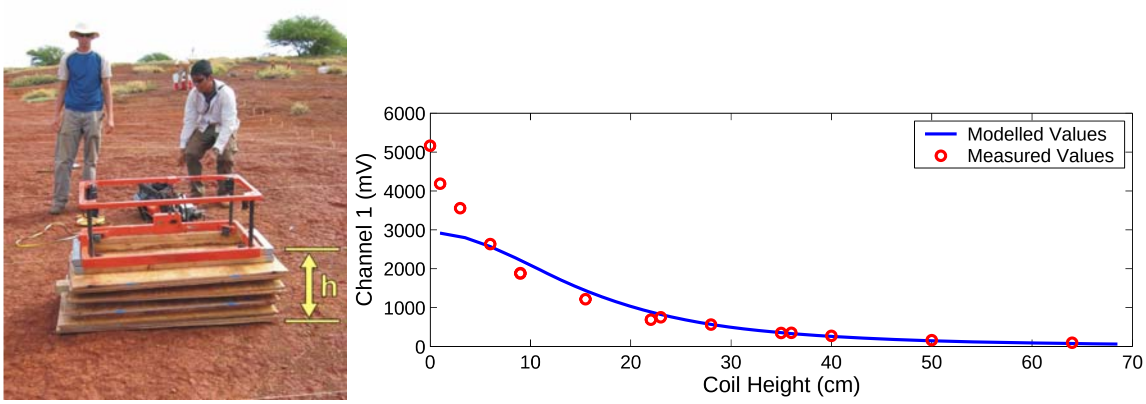

Figure 6.9: Height test carried out on Kaho'olawe Island using a Geonics EM61 Mark 2. The left photo is of Geonics EM61 Mark2 tilt test. The height of the coil is indicated by h. The measured (red dots) and modelled (blue line) height test data are presented to the right.

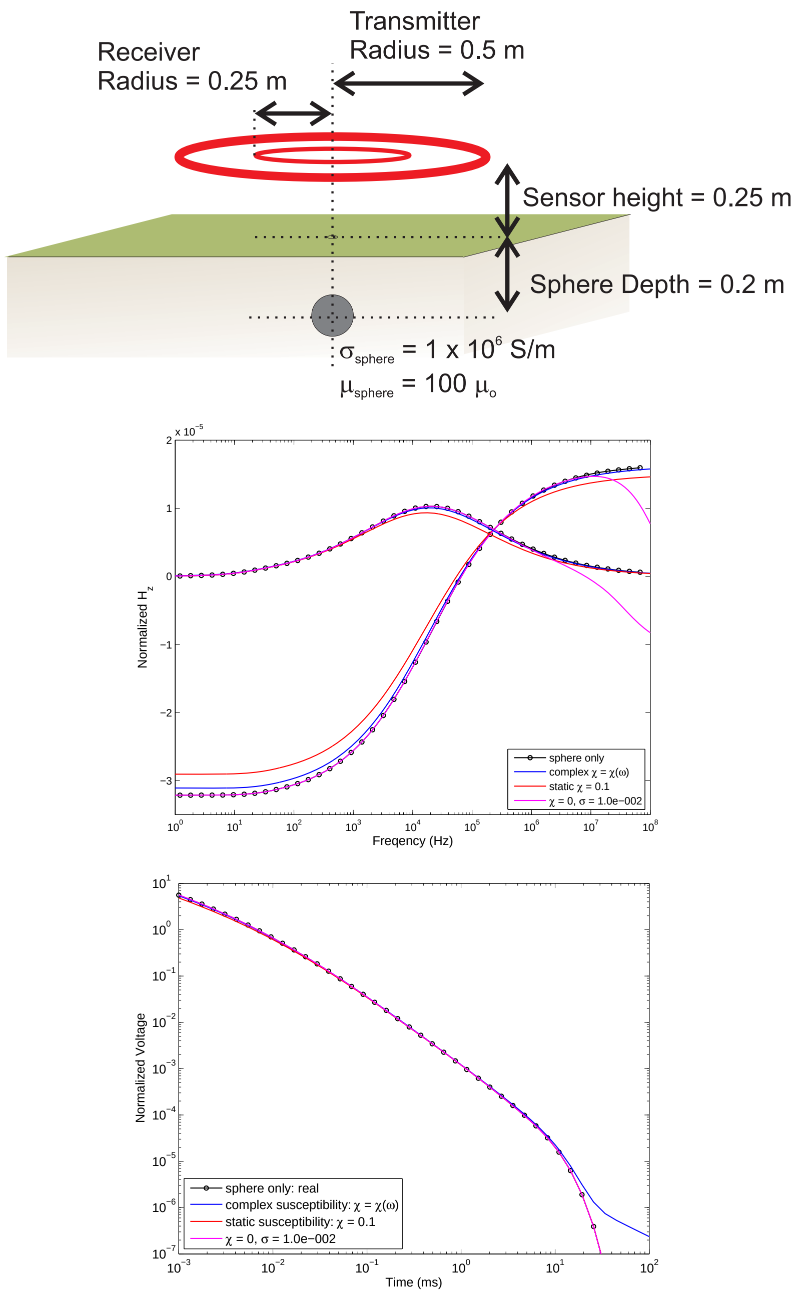

Figure 6.10: Studying the effect of a conductive or magnetic background halfspace on the dipole polarization tensor of a sphere using the formulation of Das (2006). Deviations from the sphere in free space polarization indicate non-additive interactions with the background host. Although there are some differences in the spectral (frequency domain) response, the time domain response is not significantly altered. Top - geometry of the test. The diameter of the sphere is assumed to be 5 cm, with a conductivity of 1×10^{6} S/m, and a magnetic permeability of $\mu = 100\mu_o$. Middle - frequency domain response of the sphere's polarization tensor. Bottom - time domain response of the sphere's polarization tensor, obtained through a Fourier transform of the spectral response in the middle image.

6.4 Additivity of background and target responses

Here we assume that the response of a target in a halfspace can be approximated well by adding the response of the target in free space and the response of the halfspace. The extent to which the additive assumption is appropriate can only be rigorously tested through the numerical modelling of Maxwell's equations. We can use the methodology of Das (2006) to estimate the first order effects of the background host on the target response. Das (2006) studies the effect of the background host material on the response function of a sphere, by (1) taking into account how the host material alters the primary field that illuminates the sphere and (2) taking into account how the host material alters the secondary field generated by the sphere that is measured at the receiver coil.

Figure 6.10 demonstrates how the polarization tensor for a sphere would change for 3 different scenarios: (1) A non conductive background host with a magnetic susceptibility model based on Kaho'olawe sample 7468-2734BP-12" ($\chi\left(f=0.46\text{kHz}\right)=0.02807, \chi\left(f=4.6\text{kHz}\right)=0.02634$), (2) A non conductive background host with a static susceptibility of $\chi=0.1$, and (3) A non-magnetic host with a halfspace conductivity of 0.01 S/m. For these results a sphere with a radius of 5 cm is placed at a depth of 0.2 m. The height of the co-axial transmitter and receiver loops is 0.25, and the radius of the transmitter and receiver loops are 0.5 m and 0.25 m, respectively.

Frequency domain response of the sphere's polarization tensor in free space and in the three different background geologies are plotted in Figure 6.10(b). The curves for the complex susceptible magnetic, static susceptible magnetic and conductive background cases represent the response of the sphere in the background host with the response of the halfspace subtracted. If the background response and sphere response were truly additive, each of the four different lines in Figure 6.10(b) would be equal. At lower frequencies the polarization tensor for the sphere is affected by the presence of magnetic materials, while at higher frequencies, the response is altered more by the presence of a conductive background. These spectral responses are transformed to the time domain via a Fourier transform. Although there are some changes in the spectral (frequency domain) response, the time domain response is not significantly altered.

6.5 Estimating response of background geology

Our general approach to processing electromagnetic data is to invert data for model parameters $\mathbf{m}$ that are representative of the physical characteristics of the target. Since our forward modeling function $F(\mathbf{m})$ is for a dipole in free space, we must estimate and remove the response due to geology. We assume that the response of the background geology and target response is additive

$$\mathbf{d}^{obs} = \mathbf{d}^{bg} + \mathbf{d}^{target} + noise \tag{6.12}$$

The background response $\mathbf{d}_{bg}$ is estimated by fitting a soil model at each station to obtain $G(\chi)$. A low pass filter is applied to $G(\chi)$, and the predicted soil response $\mathbf{d}_{bg}$ is subtracted from $\mathbf{d}_{obs}$ to obtain the target data $\mathbf{d}_{target}$.

This approach relies on the assumption that the small wavelength components in the data are due to compact targets, and not the geology. However, even if the magnetic properties of the soil are slowly varying, variations in cart height can add a significant high frequency component to the data. Therefore, our preferred approach is to estimate a soil model from the data.

$$V_{soil}(t) = R(orientation, height)\,G(\chi)\,f(t) \tag{6.13}$$

where $G(\chi) = \chi_o / \ln(\tau_2 / \tau_1)$ for a half-space, and $f(t) = 1/t$ for a step-off response. The function $G(\chi)$ is assumed to be spatially smooth, while the function R can have high frequency spatial variations due to sensor position and orientation variations. If we assume a half-space model for the soil, then a single parameter that is a function of the low frequency magnetic susceptibility and upper and lower limits of the soil decay time constants characterizes the response at each station location. We estimate this parameter such that it is laterally smooth. This is achieved by fitting each sounding independently, then applying a low pass filter to the $G(\chi)$, i.e. the susceptibility spatial distribution, rather than to the data directly.

The tilt and height tests illustrate that even small changes in coil orientation and the distance between the coil and a highly magnetic sub-surface can produce significant amplitude variations. Therefore, the amount of processing carried out on data is dependent on the accuracy of the sensor positioning and orientation. If the positioning and orientation of the sensor is sufficient to model the high spatial frequency components of the background response, then the approach of subtracting a background signal followed by parameter estimation can be considered. Otherwise, the background noise that can be encountered would likely limit the amount of target information that could be extracted from the data. In such a case, the data processing should focus on improving target detection and reducing false negatives due to soil, rather than determining shape and size characteristics through inversion.

Figure 6.11 summarizes a procedure for processing data that incorporates background subtraction. Once data have been collected, the data are then pre-processed to remove sensor related data artifacts (e.g. sensor drift), and to integrate positioning information. These data can then be used to estimate a soil susceptibility model. Estimation of soil susceptibility is complicated by the presence of dipole signals due to compact metallic objects and the quality of sensor position and orientation information. The data predicted by the soil susceptibility can then be subtracted from the pre-processed data:

- **Good Sensor Position Orientation Information:** In this case, the small spatial wavelength signal due to sensor motion can be predicted. The anomalies in the background-subtracted data are then inverted for dipole parameters. The resulting dipole parameters can then be incorporated into a feature vector for statistical classification.

- **Poor Sensor Position and Orientation Information:** In this case we would likely have to assume a constant elevation and orientation for the transmitter and receiver coils. The anomalies in the background-subtracted data may have a large amount of high spatial frequency (short wavelength) noise due to the unmodelled sensor motion. For this case, the objective should be simply to minimize the number of targets due to soil.

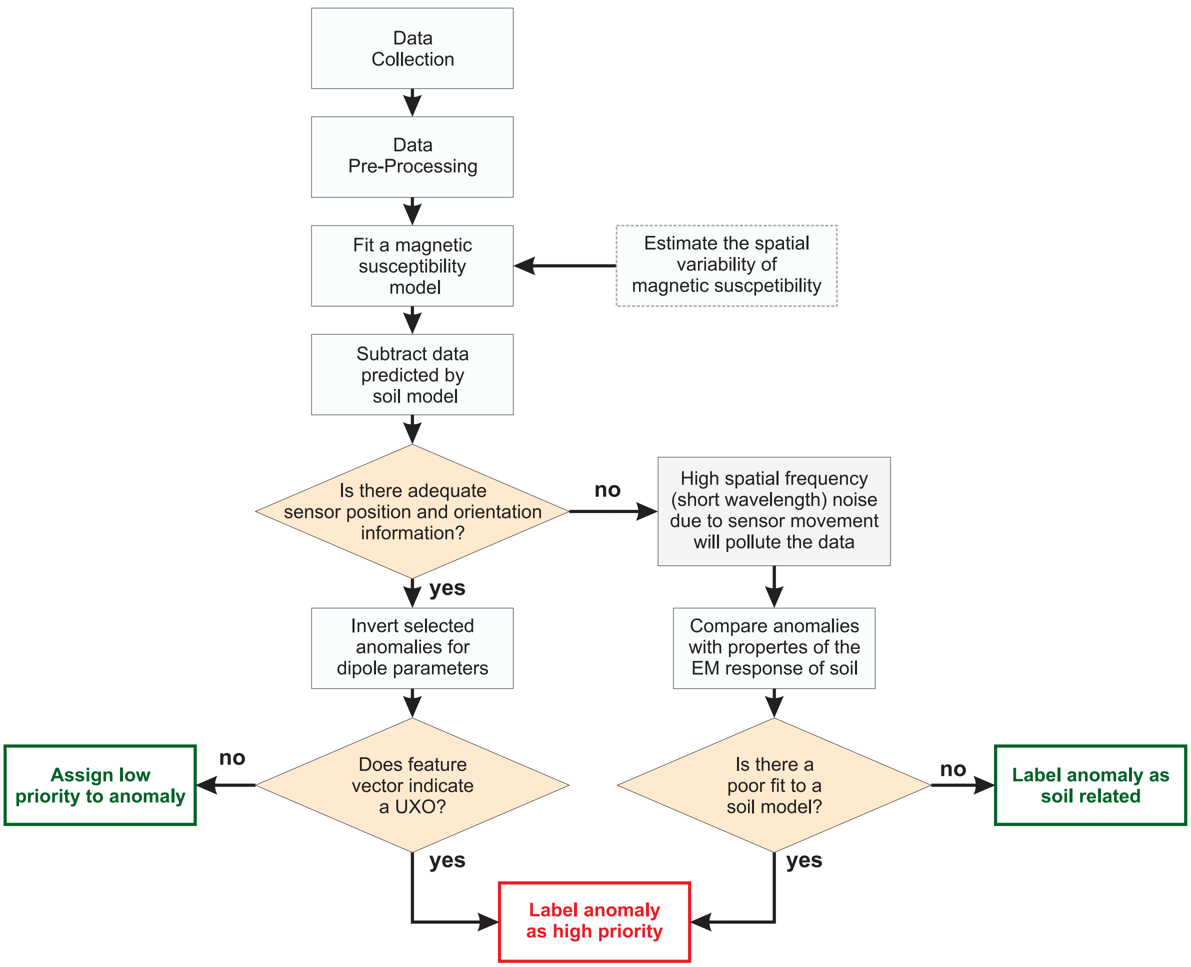

Figure 6.11: Processing EMI data in a magnetic setting.

6.6 Testing EMI processing methods using simulated TEM data

In this section we outline the generation of simulated data sets that is later used to investigate different processing techniques applied to electromagnetic data. Objectives for these simulations include:

1. Assessing our ability of spatial filtering, used in conjunction with soil models, to estimate background geologic response, and

2. Determining how the variance of class clusters in feature space is affected by filtering techniques, target geometries, and magnetic susceptibility characteristics.

These simulations will help us optimize the processing methods for data sets with significant geologic noise.

Due to the different possible survey modes, target types and geometries, and geologic signal variation characteristics, there are numerous data set types that can be modeled. A number of different survey parameters will be varied:

- **Target type:** Targets from the ATC standardized test set will be modeled. Dipole models will be used to approximate the EM response, with polarization parameters being derived from data acquired on the ERDC UXO test stand. Figure 6.12 has pictures of some of the different ordnance that will be studied. These are overlaid on a feature space plot containing parameters that describe the polarization tensor magnitude. Within each grid, targets are placed at depths of 0.25 and 0.5 m. The targets are randomly oriented.
- **Background Geology:** For all the simulated data sets, we will assume that the response of a UXO in a magnetic soil is the sum of the individual responses.
- **Sensor Type:** We are simulating data from multi-channel EMI sensors, since we want to exploit the time and frequency domain characteristics of soils to improve detection. In particular we are focusing on the Geophex GEM3 and Geonics EM63 sensor.

- **Survey Geometry:** Data will be modeled on 70 m square grids. For our initial simulations we focus on single sensors acquiring data along survey lines. We assume the commonly adopted survey acquisition parameters of 50 cm for line spacing and 10 cm along line for the station spacing. A sensor height of 30 cm is assumed.

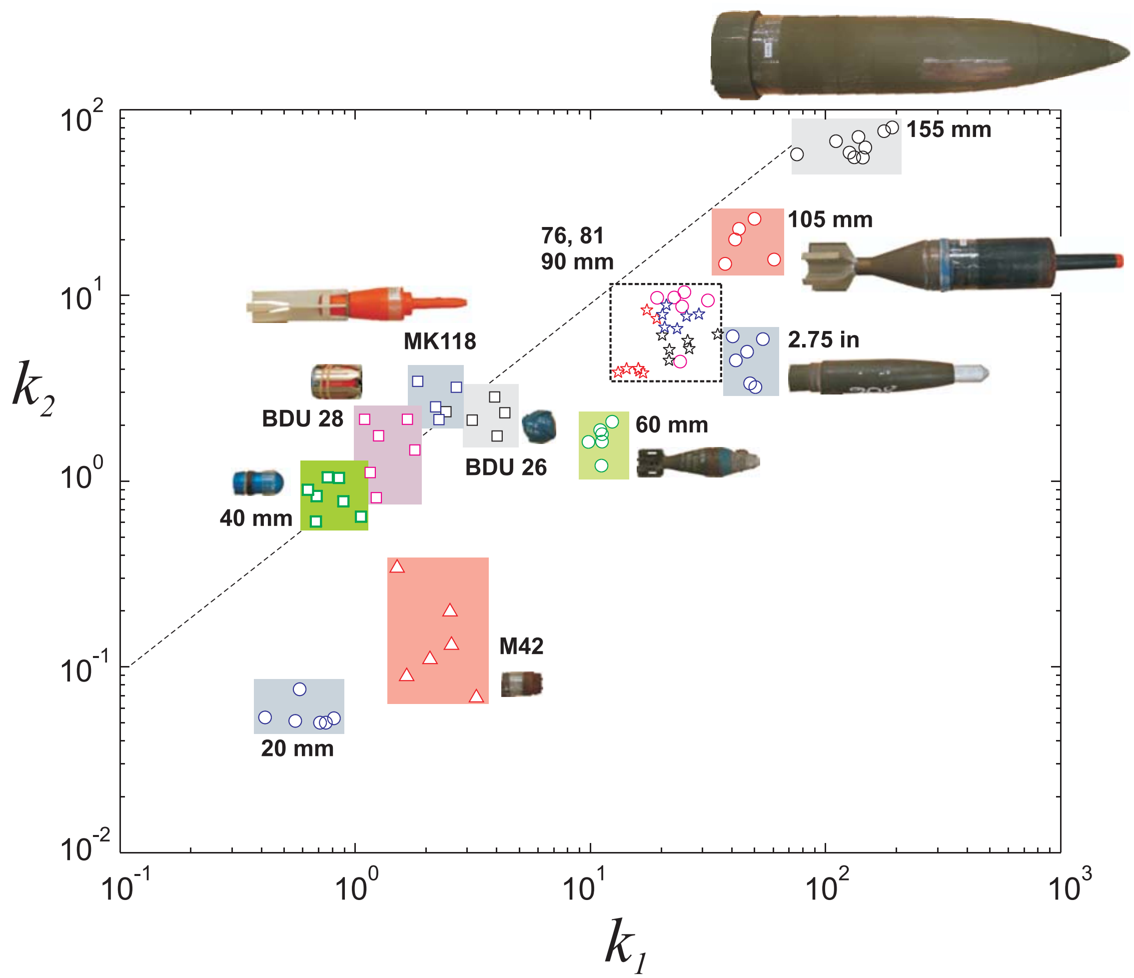

Figure 6.12: Example of recovered values for different targets. Parameters were estimated through inversions of Geonics EM63 data that were acquired on the USACE ERDC test stand in Vicksburg, MS.

In this section, processing is applied to data simulated Geonics EM63 data for a 40 mm projectile and 60 mm mortar (see Figure 6.12 for photos). The 40 mm projectile is buried at a depth of 25 cm and the 60 mm mortar is buried at a depth of 50 cm.

6.6.1 Simulated noise

The inverse problem for estimating dipole parameters can be cast as an optimization problem. Here we briefly present some essential points. For the data of this study we only consider uniform priors such that our problem is to minimize a data misfit function subject to box constraints:

$$\begin{aligned} &\min \varphi(\mathbf{m}) = \frac{1}{2}\left\| V_d^{-1/2}\left(\mathbf{d}^{obs} - F(\mathbf{m})\right)\right\|^2 \\ &\text{subject to } m_i^L \le m_i \le m_i^U \end{aligned} \tag{6.14}$$

where i represents model parameters which have upper and lower bounds. Finding a model that minimizes the above equation involves defining a data covariance vector V_d, the data vector $\mathbf{d}^{obs}$, the forward modeling function $F(\mathbf{m})$, the constraints m_i^L and m_i^U, and a numerical optimization procedure. The data vector $\mathbf{d}^{obs}$ is typically contaminated with noise:

$$d_i^{obs} = d_{dipole} + e_i \tag{6.15}$$

where e_i is the noise on the i^{th} datum.

The source of data errors can generally be categorized as being components of the data that can not be modeled with the dipole forward modeling function F(m). The components of e_i include modeling errors, sensor noise from natural and cultural sources, and processing artifacts. As e_i increases, the variance of the recovered parameters $\mathbf{m}$ increases. For example, for deeper targets the relative value of the data error compared to the target signal increases, and the ability to constrain the model parameters decreases. The choice of the least squares objective function is optimal when the errors e_i are Gaussian. Biased components of e_i will reduce the quality of the estimates of $\mathbf{m}$. The relationship between the data error bias and estimated values of $\mathbf{m}$ requires numerical simulations. A couple of examples of where biased components could be introduced include using a dipole model where the target response contains significant multipole components, and when background removal filtering produces data artifacts. In this section we describe how the noise is included in the simulated data.

6.6.2 Baseline noise

We define baseline noise to be the random signal produced in the sensor in the absence of nearby conductive bodies. There are numerous sources of EMI noise (for example Nabighian and Macnae (1991)). Efferso et al. (1999) examined the effect of AM and very low frequency (VLF) electromagnetic transmitters on TEM measurements. They observed for their particular TEM instrument that the standard deviation voltage signal exhibits a $1/t$ proportionality when AM transmitter noise is log-gated and stacked. Munkholm and Auken (1996) showed that log-gated and stacked white noise maps onto the TEM response as errors with a standard deviation exhibiting a $1/\sqrt{t}$ decay. Figure 6.13 shows a calculated noise floor (in green) for a grid of Geonics EM63 data acquired at FLBGR and the theoretical $1/\sqrt{t}$ decay due to Gaussian input noise.

The magnitude of the noise was estimated by calculating data statistics from regions on the grid where there were no UXO anomalies. For these simulations, we assume that the baseline error can be characterized by a single standard deviation for the entire grid (although past experience has shown that the magnitude of the baseline noise can vary as a function of Geonics EM63 survey event). Figure 6.13 plots realizations of the synthetic noise as a function of time channel.

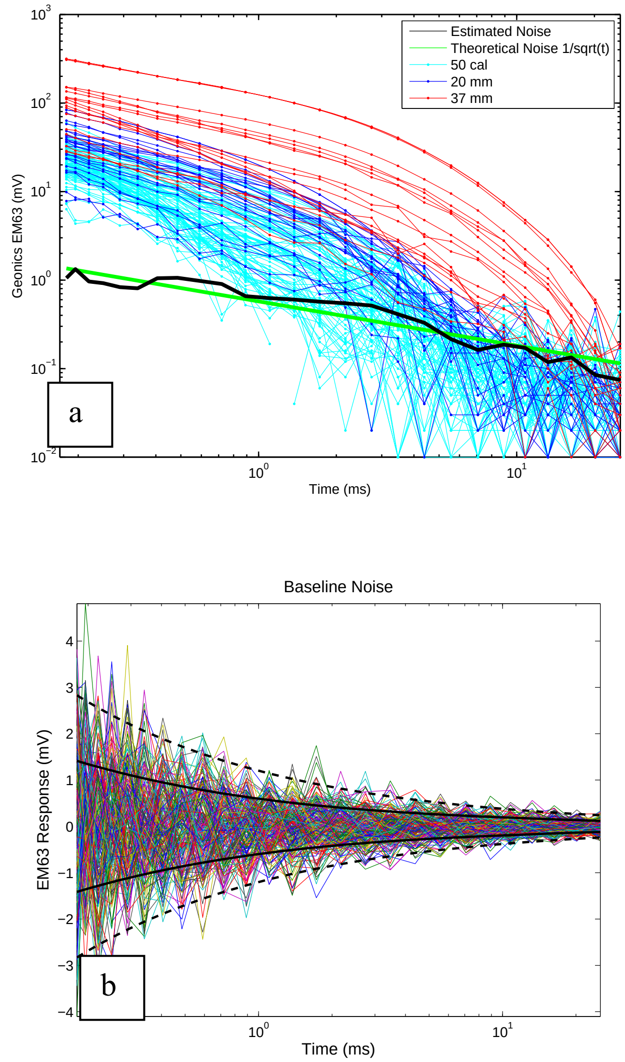

Figure 6.13: Baseline noise for magnetic soil simulations. (a) Calculated and theoretical noise floor for Grid 1914 at FLBGR. The calculated noise floor was based on Geonics EM63 data collected over areas where there were no UXO anomalies. Data over validated 50 caliber bullets, and 20 mm and 37 mm projectiles are also plotted. (b) Simulated baseline noise for the Geonics EM63. The standard deviation of the noise for each time channel is the same as the noise from data acquired at FLBGR. At each time channel the realizations shown in the Figure are represented by a Gaussian probability. The dark and dashed lines respectively correspond to 1 and 2 standard deviations.

6.6.3 Sensor position uncertainty

Sensor position and orientation are generally recorded with some combination of GPS, robotic total station, and IMU sensor. Inaccurate position and orientation information are sources of modeling error. For these simulations we assume that the pitch, roll and yaw can be measured to within an accuracy of 2 degrees. We assume the position errors are normally distributed with 2 cm standard deviation in northing, easting, and height. Our past tests have shown that the sensor data are more sensitive to sensor height variations than to position and orientation errors.

6.6.4 Simulating the magnetic background signal

We assume that there are two components of the background geologic response: (1) A long wavelength variation due to changes in magnetic susceptibility associated with geologic and/or weathering features, and (2) Short wavelength variations due to topography and sensor motion relative to the surface.

For the long wavelength variation, we assume that susceptibility decreases smoothly from a maximum at the South (y = 0 m) end of the grid to a minimum at the North (y = 70 m) end of the grid (Figure 6.14). There are three different magnitudes of background response considered. Background responses of 100 mV, 50 mV, and 20 mV in the first time channel are constructed. The response at the North end of the grid is one-half the value of the response at the South end of the grid. The time decay of the background response has a $1/t$ magnitude.

Smaller wavelength variations in the background response are assumed to be from either cart positioning (i.e., height and orientation) or from small topographic features, such as surface depressions (e.g. potholes) or small mounds of soil. For this first set of simulations, the recorded height has a 2 cm standard deviation noise added to the nominal height 30 cm. A shorter wavelength background response is simulated by using correlated random numbers. The smaller wavelength variations in the background response are simulated from the estimated power spectra of Kaho'olawe test plot data. The standard deviation of the small wavelength background response is set to be 15 percent of the background response.

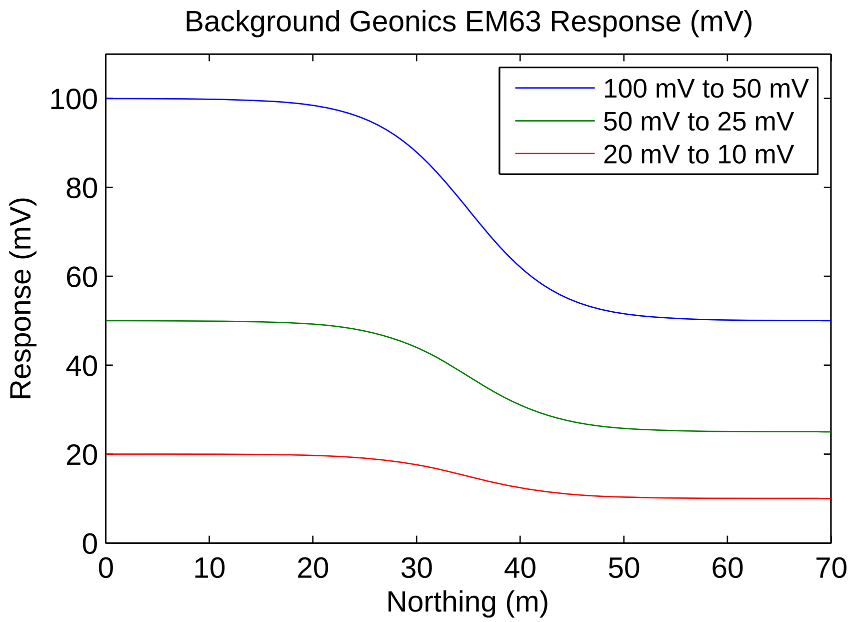

Figure 6.14: Variation of geologic background responses along a North/South line. The background response with a maximum of 50 mV and minimum of 25 mV is used for the examples of this chapter.

6.6.5 Examples of simulated data sets

Simulated data from a 40 mm M385 projectile and a 60 mm mortar are used to demonstrate filtering and inversion. Figure 6.15(a) shows the first channel of modeled data from a 40 mm projectile buried at a depth of 25 cm and randomly oriented at 36 locations in a rectangular grid. The free-space response of the 40 mm projectiles has a maximum first time channel value of 15 mV (Figure 6.15, upper left). The long wavelength background response decreases from a maximum of 50 mV at the South end of the grid, to a minimum of 25 mV at the North end of the grid. The standard deviation of the correlated noise is defined to be 15 percent of the long wavelength regional response. Fifteen percent corresponds to a height variation of approximately

3 cm. The spatial characteristics of the modeled response are based on Geonics EM63 data acquired on Kaho'olawe. A radial power spectra was estimated for a region within a Kaho'olawe grid with a background of approximately 50 mV. The total soil (i.e., non-target) response is plotted in the upper right of Figure 6.15. The total signal is plotted in the bottom image of Figure 6.15. The responses of the 40 mm projectiles are not easily identified in the total signal. The 40 mm projectile has a weak small amplitude signal due to its small size, aluminum construction and, of course, its distance from the sensor. The different components of simulated data for a 60 mm mortar buried at 50 cm in a background that has a maximum response of 50 mV in the first time channel is shown in Figure 6.15(b).

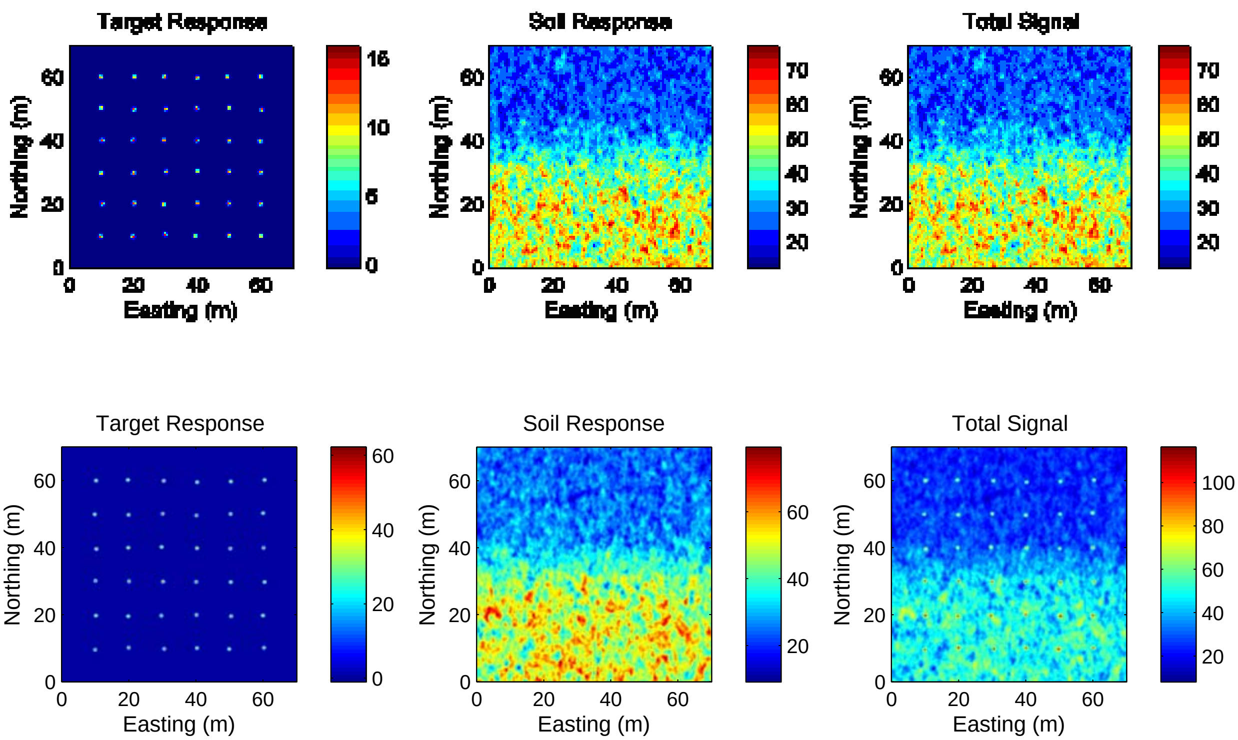

Figure 6.15: Data simulated for a 40 mm M385 (**top**) buried at a depth of 50 cm, and an ATC 60 mm mortar (**bottom**). The simulated target response is plotted for each in the left column. UXO are placed at all points on the grid. The simulated soil response is shown in the middle column, and the simulated survey data are shown on the right.

6.7 Picking targets in highly magnetic soils

The goal of target picking is to generate a list of survey locations at which there is a high probability that a target is present. The data can be written as

$$\mathbf{d}^{obs} = \mathbf{d}^{target} + \text{noise}. \tag{6.16}$$

In this case, we define the noise to be the random baseline noise of the instrument and the spatially correlated signal from topography and sensor movement. Since we are not fitting the data with a model, modeling error is not considered a noise source. Fundamentally, target picking labels a survey location as a potential target when the sensor data $\mathbf{d}^{obs}$ exceeds some threshold level. The choice of threshold depends on the characteristics of the noise and the target signal.

Target picking is an example of signal detection theory and hypothesis testing. The null hypothesis H_0 is that the signal is due to noise. The alternative hypothesis H_1 is that the signal is from a buried target. Let $p(x \mid H_0)$ be the pdf of x under H_0, i.e., the pdf of the noise. The variable x is some test statistic of the data (which can be the data itself). Let $p(x \mid H_1)$ be the pdf of x under H_1, i.e. the pdf of the target. For a threshold level τ, the probability of false alarm P_{FA} and the probability of detection P_D is defined as

$$P_{FA} = P\left[x > \tau; H_0\right] \tag{6.17}$$

$$P_D = P\left[x > \tau; H_1\right], \tag{6.18}$$

where the test statistic is x. The definitions of P_D and P_{FA} are expressed graphically for the example of a 40 mm projectile buried at a depth of 25 cm in a background geology whose mean response in the first time channel is 20 mV in Figure 6.16(a).

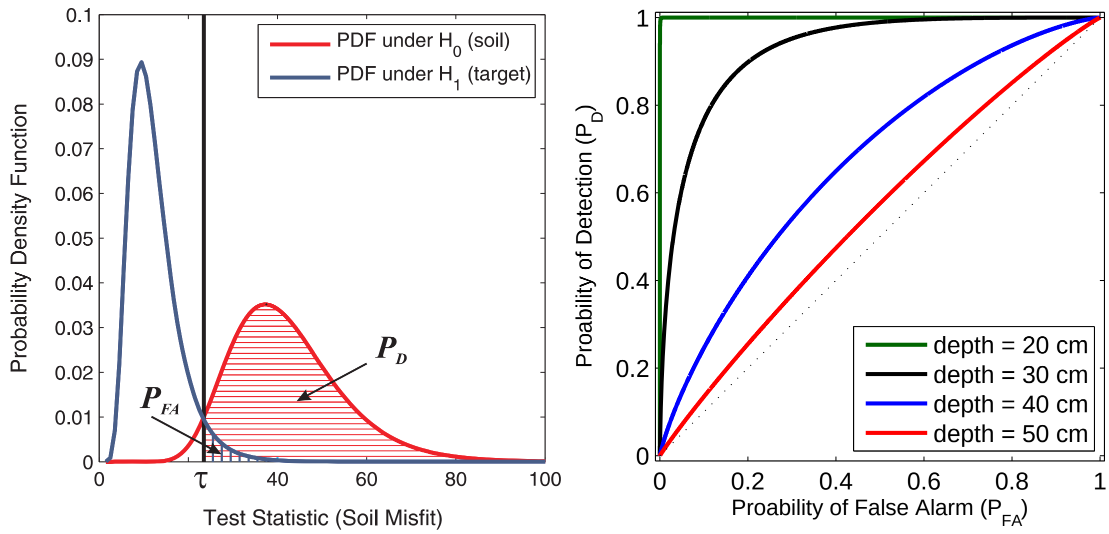

Figure 6.16: Soil fitting results for data simulated for a 40 mm projectile in a background geology whose mean response in the first time channel is 20 mV. (a) The pdf for a depth of 25 cm. (b) ROC curve for different target depths

The curves in Figure 6.16 were generated through simulations and fitting the experimental histograms with log-normal distributions. The ability to detect the 40 mm projectile is characterized by the width and separation of the two pdfs. As the depth of the target decreases, the signal-to-noise ratio of the anomaly will increase. The anomalies for these shallower targets will have a poorer fit to the soil model and the soil and target distributions will have greater separation. The ability to discriminate is summarized with a receiver operator characteristic (ROC) curve (Figure 6.16(b)). An ROC curve is constructed by plotting the P_{FA} against the P_D as a function of the test statistic. As we vary the soil misfit test statistic, a smooth curve is traced. It is clear that as depth decreases, the ability to discriminate improves. For a depth of 20 cm, it is possible to define an operating point such that all the 40 mm projectiles can be identified without detecting soil.

In general, types of targets to be found in a survey are not known ahead of time and, thus, $p(x \mid H_1)$ is generally unknown. In this case, the natural approach is to simply sort prospective targets by their probability of false alarm. For the single time channel case, this means picking points on a map where the measured data exceeds some threshold and sorting those values by the amplitude.

6.7.1 Single channel of data

To study target picking using a single time channel case, let us use the first time channel of the synthetic data sets (Figures 6.15(a) and (b)). We assume that the sensor height is 30 cm and the transmitter is horizontal, such that R is constant. Due to the spatially varying long wavelength background response we must either (1) define a spatially varying threshold must be defined, or (2) remove the background response through filtering. We choose to remove the background response for these example.

Figure 6.17 demonstrates the application of a simple low pass Butterworth filter to the image of gridded raw first time channel data image, and the subsequent picking based on the filtered image. Each image contain 10 cm square pixels. The gridded raw data are shown in each of the aforementioned figures upper left panel, with the low pass image plotted in the top right panel. Targets are picked using the image of high passed data, and the results are plotted in the bottom right corner. The criteria for labelling an anomaly are: (1) the pixel value is greater than a threshold of 10 mV and (2) there are at least 3 connected pixels that exceed the threshold. The small wavelength variations due to cart motion and topography are often picked. The number of non-UXO target picks increases in the South end of the grid, where the magnitude of the VRM is the highest.

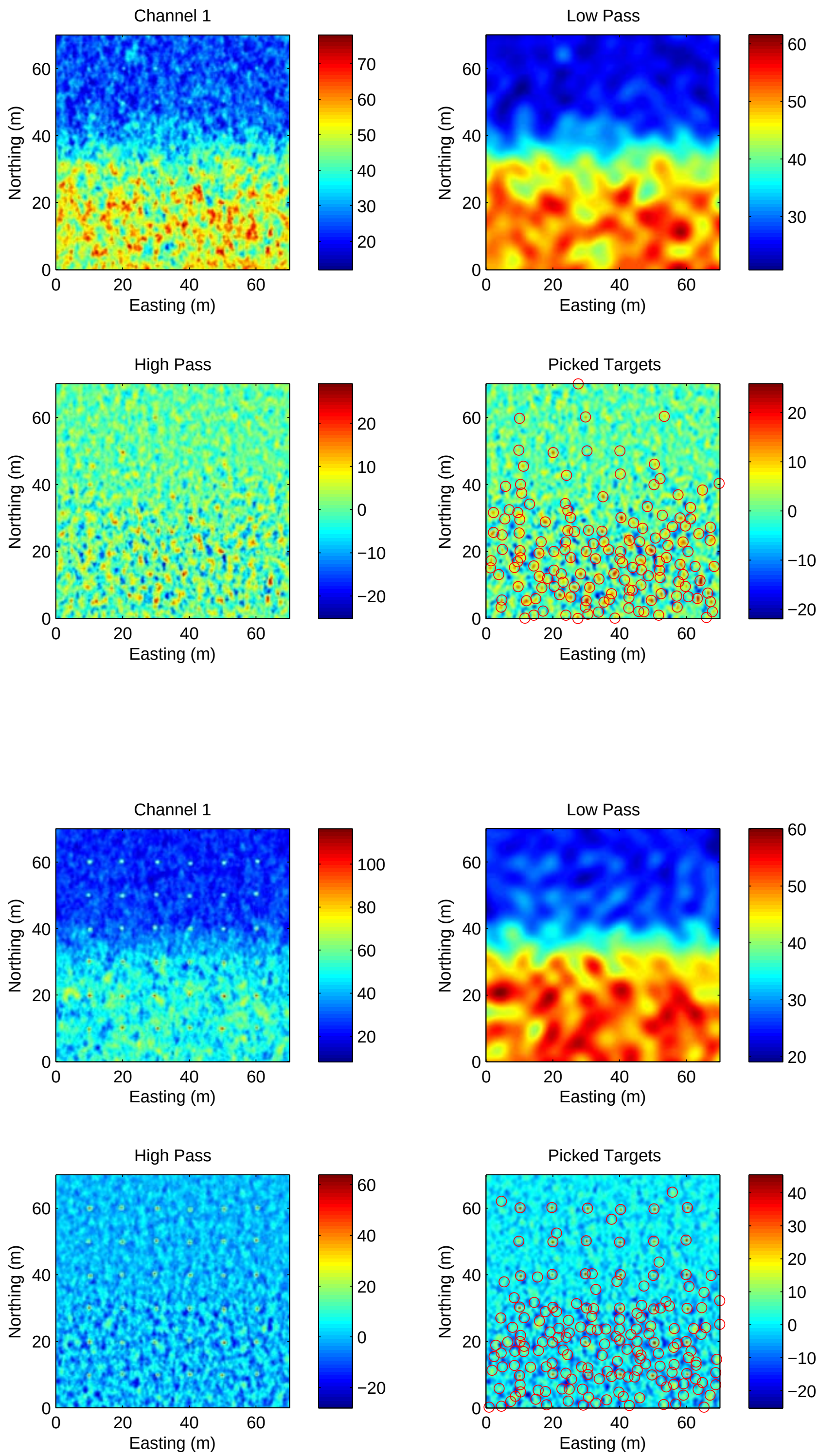

Figure 6.17: Target Picking results for a 40 mm projectile (top two rows) and 60 mm mortar (bottom two rows) buried in a magnetic background. For both data sets a 3 pixels must exceed the picking threshold of 10 mV to be picked. Target picking using the high pass filter results in many false positives due to large magnitude of the spatially correlated background response.

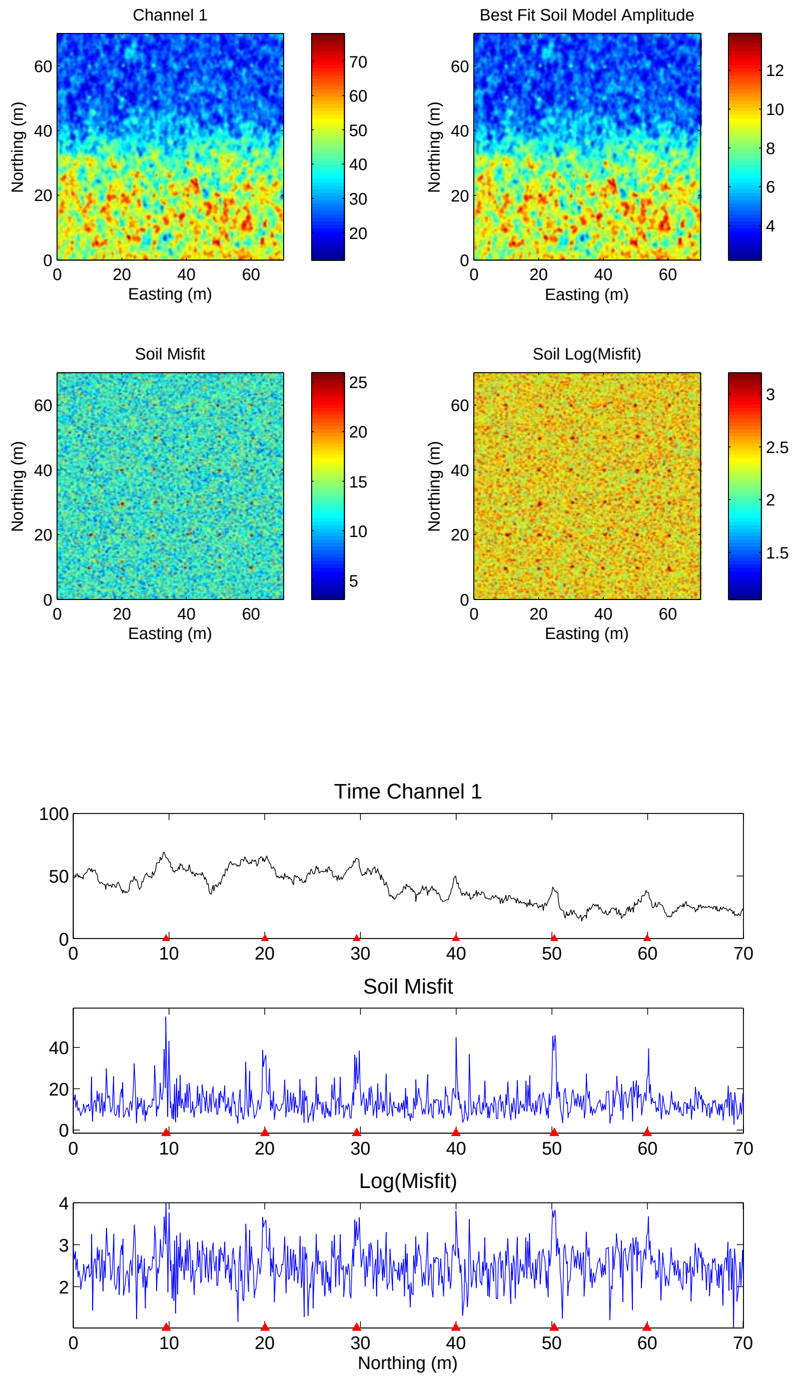

Figure 6.18: Soil fitting results for the 40 mm projectile data. (Top two rows) the amplitude of the soil response is plotted in the top right image, with the misfit and log-misfit to the soil response plotted in the bottom two plots (Bottom three plots) comparison of the first time channel raw data with the soil misfit along the line Easting = 10 m. The red triangles indicate the location of targets. At each location, the sounding data from the EM63 is inverted to find a best fitting soil model. It is clear the magnitude of the 40 mm response is similar to the soil response, and that the fitting of a soil model provides limited advantages for target picking purposes.

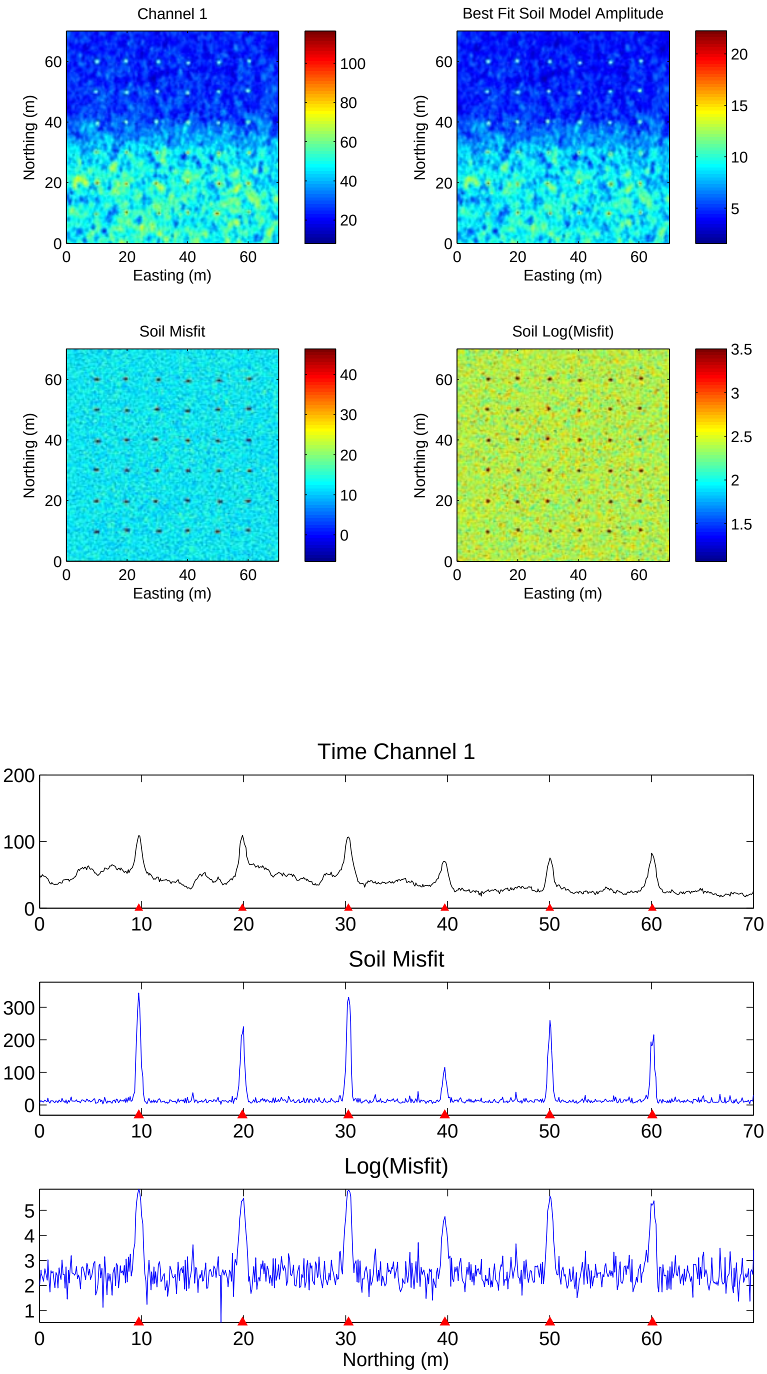

Figure 6.19: Soil fitting results for the 60 mm mortar data. (a) top two rows - the amplitude of the soil response is plotted in the top right image, with the misfit and log-misfit to the soil response plotted in the bottom two plots. (b) bottom three plots - comparison of the first time channel raw data with the soil misfit along the line Easting = 10 m. The red triangles indicate the location of targets. At each location, the sounding data from the EM63 is inverted to find a best fitting soil model. The 60 mm mortar is a much larger target than the 40 mm projectile, and therefore is much easier to detect in the raw data. The soil misfit has very distinct anomalies over each of the buried 60 mm.

6.7.2 Misfit to a soil model

With only a single time channel of data, we cannot use the characteristic temporal or frequency response of soil to reduce the number of geologic related peaks. Here we use the Geonics EM63 with potentially 26 time channels of data. If we fit a soil model to the data picks, we would expect that the misfit would be larger when the anomalies are due to UXO. The fitting procedure involves solving for a soil model that minimizes the least squares misfit between the measured sounding and soil response. The soil response is given by a characteristic soil decay multiplied by an amplitude A, i.e., $F^{soil} = Af(t)$. Figures 6.18 and 6.19 shows the misfit of the 40 mm and 60 mm data sets to the soil response. The soil misfit image is much more useful for target picking than using simply a single time channel of data.

From these results, we can conclude that target picking can be improved by using the soil misfit as a test statistic. Simulations can be used to study the effectiveness of this strategy for a given target and background response. Let us consider data simulated for a 40 mm projectile buried at a depth of 25 cm and in a background geology whose mean response is 20 mV, and has a short wavelength background noise with the same correlation lengths of Kaho'olawe data. The standard deviation of the short wavelength noise is 15 percent of the long wavelength response (i.e., 3 mV). Soundings with and without a target present are fit with a soil model, and are then used to estimate the pdf for soundings from soil ($p(\varphi;H_0)$) and pdf for soundings from the 40 mm projectile ($p(\varphi;H_1)$). Figure 6.20 compares both soil and 40 mm misfit distributions as a function of the misfit (Figure 6.20(a)) and the log of the misfit (Figure 6.20(b)).

The log normal distribution is a good representation of the pdf of the soil misfit. The experimental cumulative distribution function (i.e. the cdf obtained by binning and summing the soil misfit) and the theoretical log normal cdf are compared in Figure 6.21.

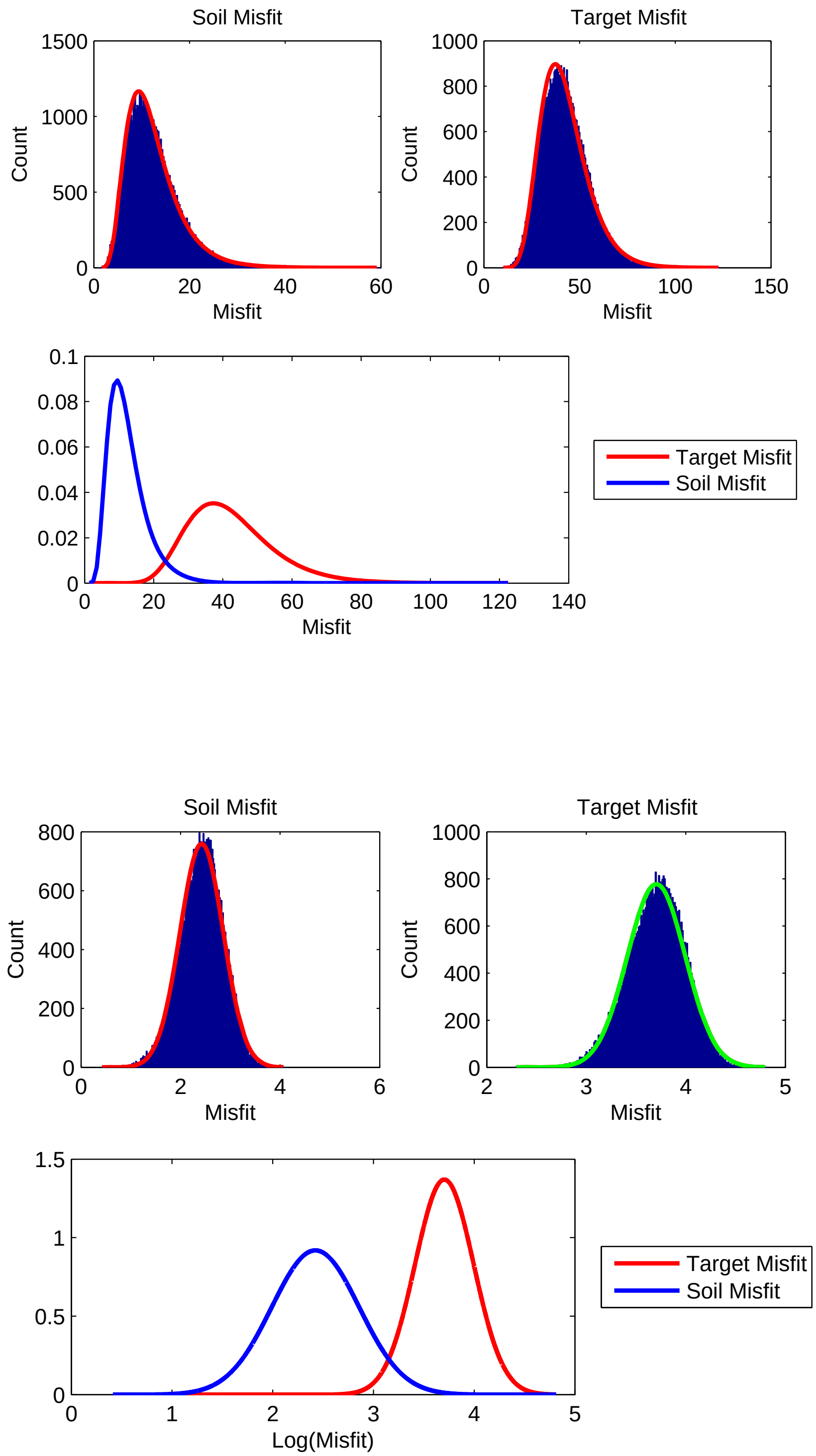

Figure 6.20: Soil target histograms for a ATC 40 mm projectile buried at a depth of 25 cm. (a) top two rows - Soil misfit φ. (b) bottom two rows - log of the soil misfit $\log(\varphi)$. The long wavelength background response is 20 mV.

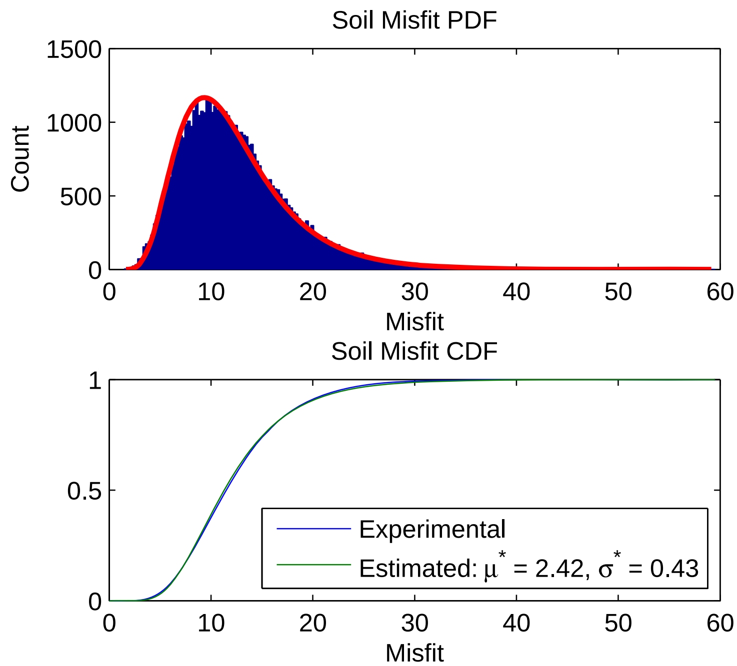

Figure 6.21: The pdf and cumulative distribution for a 40 mm buried at a depth of 25 cm in a magnetic background that has a response of 20 mV in the first time channel. The quantities μ^* and σ^* are the mean and standard deviation of $log(\varphi)$.

The ability to accurately pick targets depends on the separation and widths of the soil and 40 mm pdfs. As the overlap of the pdfs for soil and target misfits decreases, so does the probability of false negatives and misses. For a given geologic setting (and therefore soil pdf) the effectiveness of target picking relies on (1) the similarity of the target response to the soil model and (2) the signal strength. The main influence on signal strength is the depth of the target. Figure 6.22 compares the pdfs for a 40 mm at depths of 25 cm and 50 cm.

The pdf for the 40 mm at 50 cm is very similar to the pdf of the soil, thereby indicating that using the soil misfit for detecting this target will not be successful. The ROC curve for a number of different 40 mm depths are plotted in Figure 6.16(b). The ROC curve is diagnostic of the performance of a classifier as a tradeoff between the probability of false alarm and probability of detection. The ROC curve shows that a 40 mm at 50 cm has a ROC curve that nearly follows the line $P_{FA} = P_D$, which indicates that when the 40 mm is at 50 cm deciding whether a anomaly is due to soil or a target with soil misfit will not perform much better than simply flipping a coin. In contrast, a 40 mm at 20 cm has the perfect rock curve, with no false alarms prior to picking every all the targets.

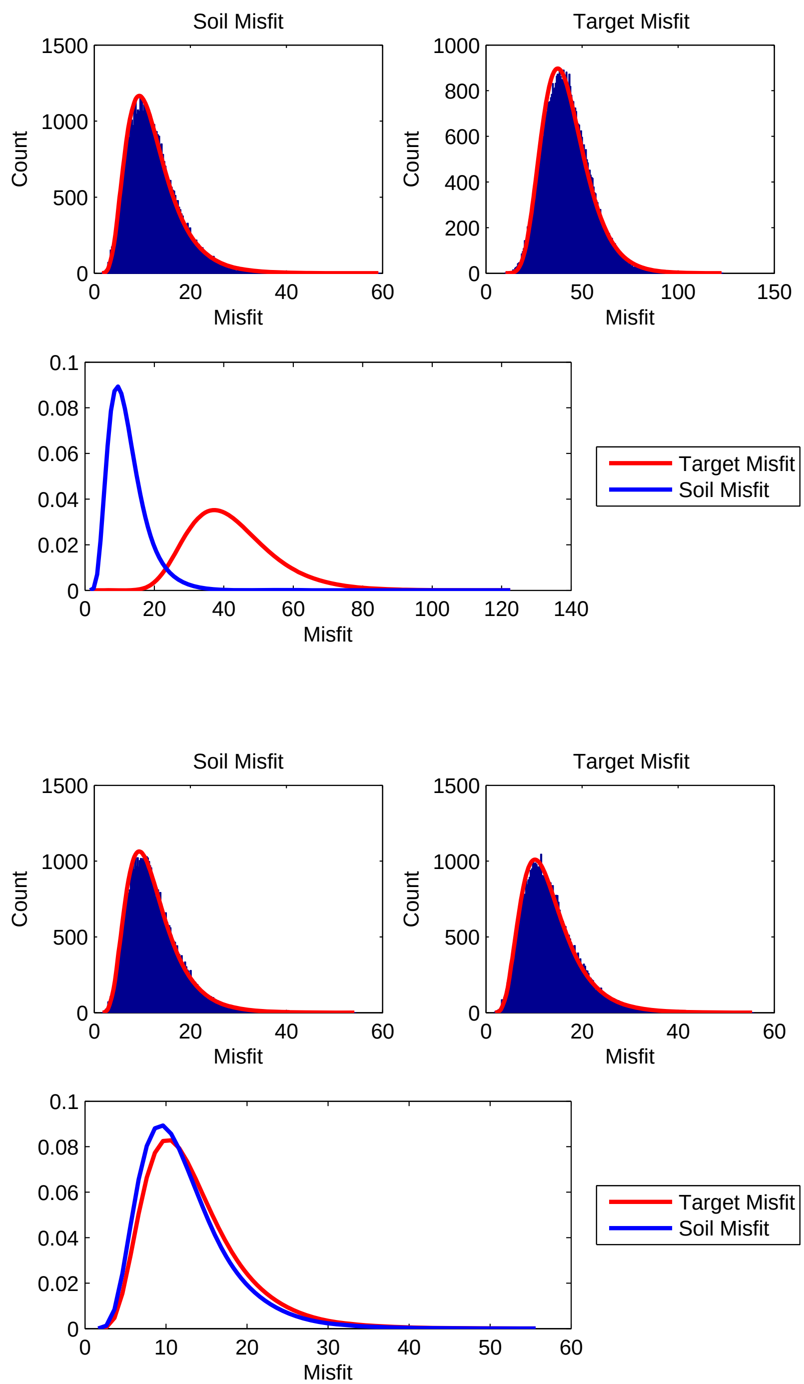

Figure 6.22: Soil target histograms for a ATC 40 mm projectile buried at a depth of (a) 25 cm for the top three figures, and (b) 50 cm for the lower three figures. The long wavelength background response is 20 mV. The pdf for the soil and target nearly overlap when the 40 mm is 50 cm deep.

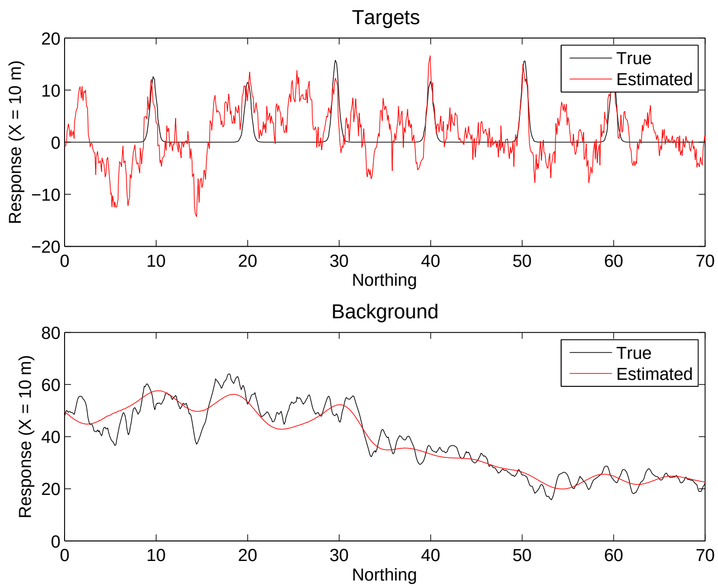

(a) 40 mm projectiles

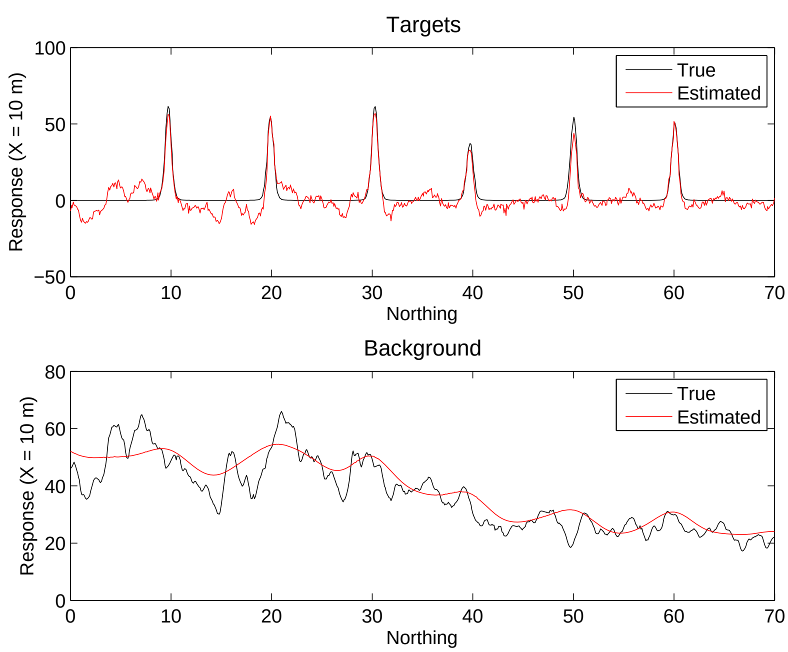

(b) 60 mm projectiles

Figure 6.23: Estimation of target signals through high-pass filtering of the data. Filtering results along the line Easting = 10 m are plotted.

6.8 Accuracy of filtering when estimating background response

Since our forward modeling function $F(\mathbf{m})$ is for a dipole in free space, we must estimate and remove the response due to geology. We assume that the response of the background geology and target response is additive

$$\mathbf{d}^{obs} = \mathbf{d}^{bg} + \mathbf{d}^{target} + noise \tag{6.19}$$

The background response $\mathbf{d}^{bg}$ is estimated by fitting the soil model of equation 6.9 at each station to obtain $G(\chi)$. A low pass filter is applied to $G(\chi)$, and the predicted soil response $\mathbf{d}^{bg}$ is subtracted from $\mathbf{d}^{obs}$ to obtain the target data $\mathbf{d}^{target}$. The inverse problem is then to minimize the data misfit

$$\begin{aligned} \varphi &= \frac{1}{2}\left\| V_d^{-1/2}\left(\mathbf{d}^{t\arg et} - F(\mathbf{m})\right)\right\|^2 \\ &= \frac{1}{2}\left\| V_d^{-1/2}\left(\left(\mathbf{d}^{obs} - \mathbf{d}^{bg}\right) - F(\mathbf{m})\right)\right\|^2 \end{aligned} \tag{6.20}$$

In this section we filter the data sets of Figure 6.15. Results are shown in Figure 6.23.

A simple Butterworth filter is used to estimate the background response. The low amplitude signal from the 40 mm projectile, and the similarity between the spatial wavelength of the background response and target anomaly result in a very poor recovery of the target anomalies. Filtering the 60 mm projectile data produces better results.

We quantify the ability to recover the true target data by calculating the difference between the estimated and true target data (Figure 6.24). We call this value the "absolute error" (as opposed to a relative, or percent error). The "absolute error" for the first time channel of data is shown in Figure 6.24. Data from a 5 m square region about each target is used for the calculation. The three histograms of Figure 6.24 show: (a) the distribution of the error for targets in the region when the average background response is 25 mV ($y > 45$), (b) the error distribution for targets in the region where the average background response is 50 mV ($y < 25m$), and (c) the error for all the targets within the 70 m grid.

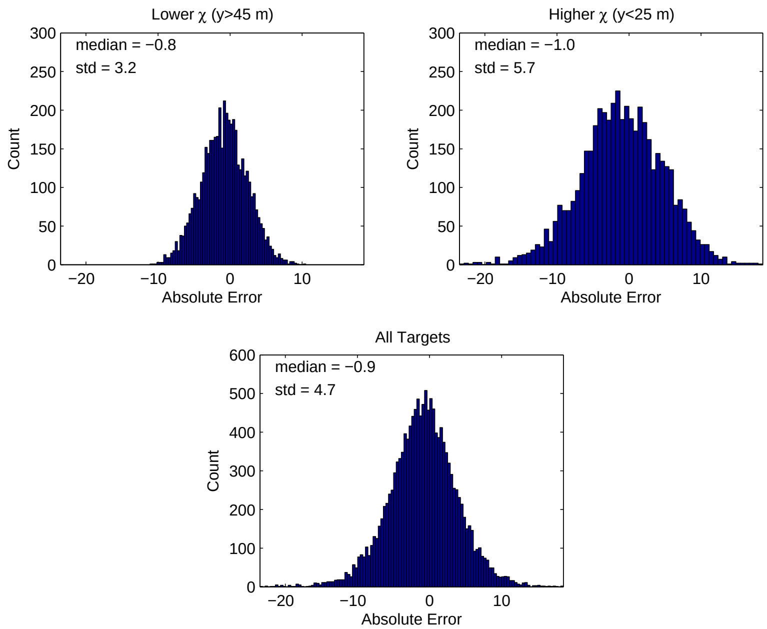

(a) A 40 mm projectile buried at a depth of 25 cm.

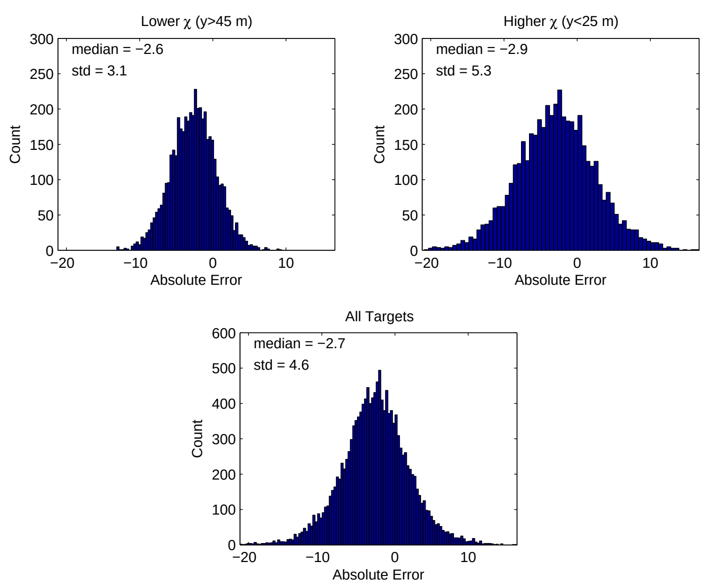

(b) A 60 mm mortar buried at a depth of 50 cm.

Figure 6.24: Accuracy of estimating target anomalies by subtracting a smoothly varying background response. Absolute error is defined as the estimated background minus the true target data. Data are within a 5 m square centered on the target.

The histograms confirm that the error is greater in areas where the magnetic background response is larger. In addition, there is a slight negative bias in the "absolute error" distribution, suggesting that we are underestimating the contribution of the background response.

6.9 Effect of VRM noise on recovered model parameters

The success of dipole model based discrimination algorithms depends on the ability of the data to constrain the inversion for the dipole parameters. To demonstrate this process we process synthetic data collected over a 60 mm mortar. We compare results from inverting: (a) synthetically generated data for 60 mm mortars buried in a non-magnetic background and (b) data with a background geology. The synthetic data set is 70 m square, with a long wavelength background geologic response that decreases smoothly from 50 mV at the south end of the grid, and 25 mV at the north end of the grid. Correlated noise is added in the same manner as the examples presented earlier. The 60 mm mortars are buried at a depth of 50 cm.

The background geology was estimated by using a low pass Butterworth filter. The background response is subsequently subtracted from the observations (Figure 6.25). Data within a 1.5 m circle radius centered about the picked targets were inverted for the dipole polarization tensor. The axial and transverse components are parameterized with the function $L(t) = kt^{-\beta}\exp(-t/\gamma)$. Figures 6.26(a) and (b) shows the data fit for a 60 mm mortar in a non-magnetic background and magnetic background, respectively. In the non-magnetic background case, the residual appears random. The magnetic background case was taken in a part of the grid where the mean background response is 50 mV. When inverting this anomaly, the residual shows background noise that appears spatially correlated.

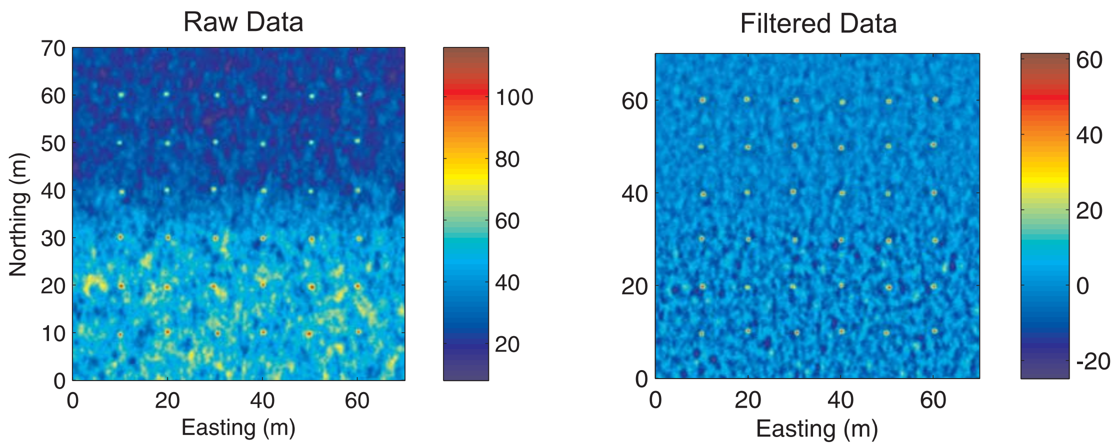

Figure 6.25: Data set with magnetic geology (left) and with the magnetic geology filtered and subtracted (right).

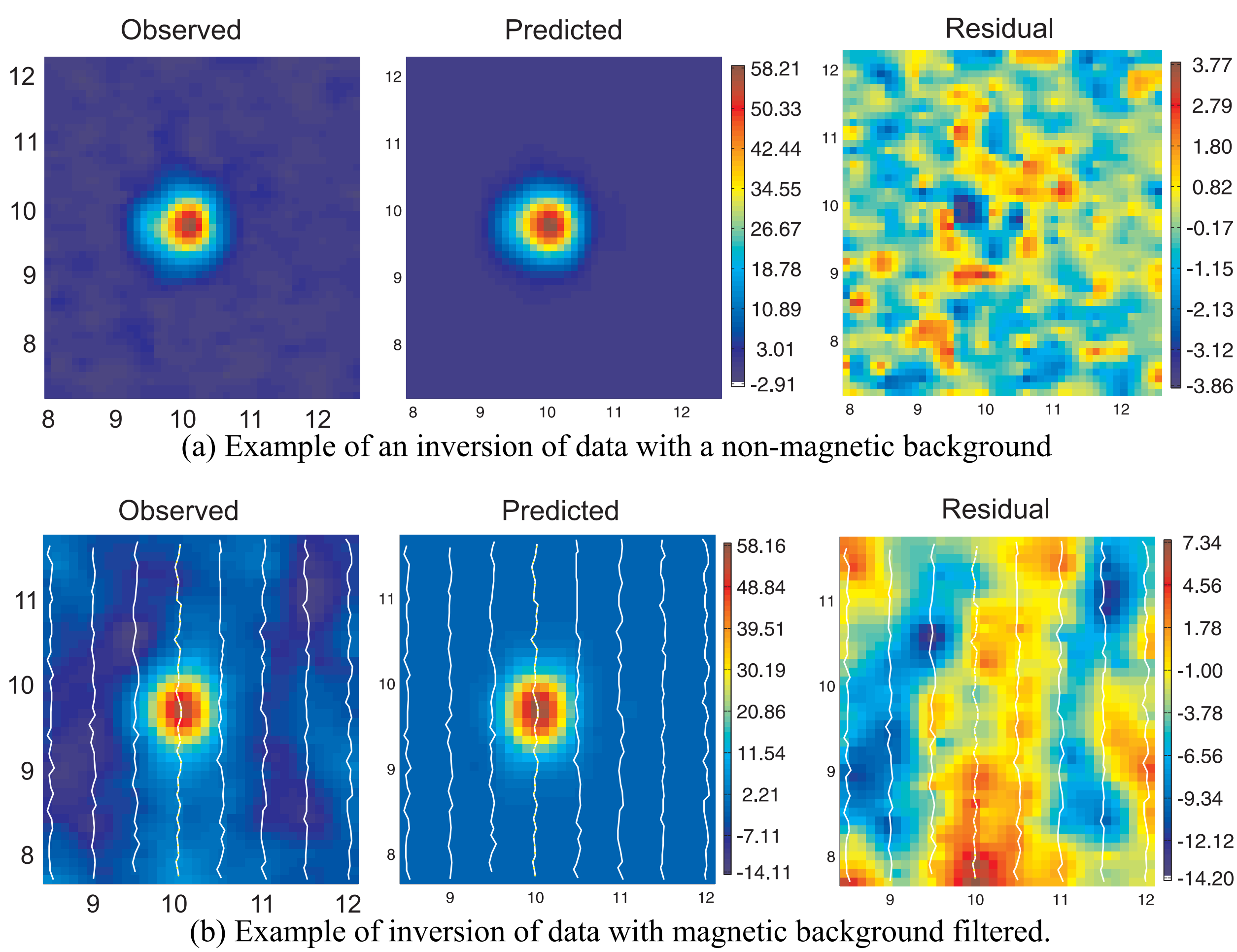

Figure 6.26: Inversion of synthetically generated 60 mm mortar data. The white lines in (b) indicate the synthetically generated cart locations.

Table 6.1. Comparing recovered parameters for data in Figure 6.26.

Parameter	Known values	Non-Magnetic Background Recovered Parameters	Non-Magnetic Background Standard Deviation	Magnetic Background Filtered Recovered Parameters	Magnetic Background Filtered Standard Deviation
Northing x (m)	9.96	9.93	0.02	10.02	0.01
Easting y(m)	9.73	9.77	0.02	9.73	0.02
Depth z (m)	0.50	0.51	0.03	0.05	0.02
φ (degrees)	-	-1.0	65.2	6.3	4.2
θ (degrees)	-	4.9	3.4	127.6	2.5
k_1	11.17	11.28	2.23	0.40	0.41
β_1	0.58	0.61	0.02	0.30	0.70
γ_1	3.21	3.44	0.33	1.24	1.25
k_2	1.83	1.26	0.24	0.37	0.03
β_2	1.08	1.24	0.12	0.78	0.03
γ_2	2.89	16.33	44.76	12.65	4.34
CorrCoeff		0.945		0.873	
Φ / N		0.857		0.888	

Table 6.1 lists the recovered parameters for the data fits in Figure 6.26. The inversion of data without a magnetic background host clearly recovers the 60 mm parameters more accurately than the inversion of data where a magnetic background response was removed via filtering. In particular the depth derived from the filtered data is shallow, resulting in low estimates of the polarization magnitudes k_1 and k_2. Inversion results for all the targets are plotted in Figures 6.27 to 6.29. Parameters derived from the non-magnetic background data are plotted using blue circles and parameters derived from the filtered magnetic background are data plotted using red triangles. The true values are indicated by a green box. Some observations:

- The SNR for both data sets was not high enough to constrain the estimated depth. Figure 6.27 plots the estimated depth vs. k_1, i.e., the magnitude of the axial polarization. It is clear that there is a trade-off between the depth and the magnitude of the axial polarization.

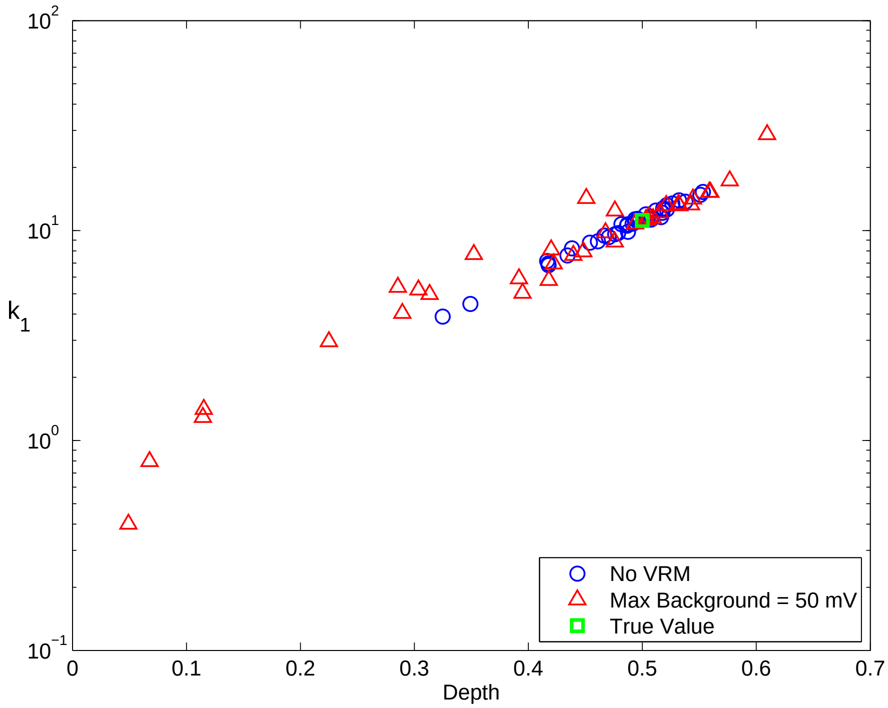

Figure 6.27: Magnitude of the axial polarization (k_1) and depth.

- The non-magnetic background data produces a cluster near the true polarization amplitudes k_1 and k_2 values (Figure 6.28(a)). Accurate estimation of the polarization amplitudes are not possible with the filtered data.

- Although the amplitude of the axial polarization is not well constrained by the filtered magnetic data, the decay parameters γ_1 and β_1 are relatively well constrained (Figure 6.28(b)), will likely be the best derived parameters for identification.

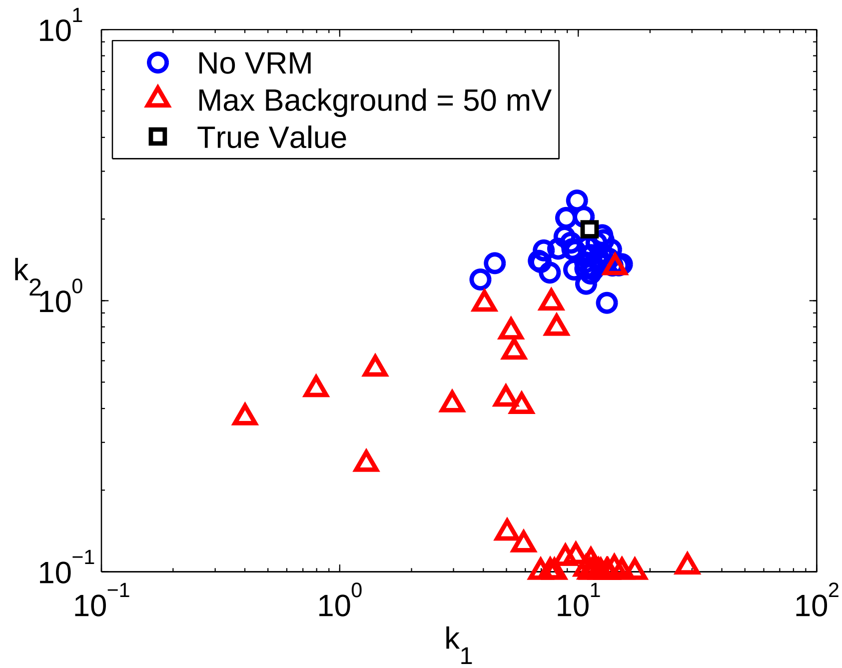

(a) Magnitude of the axial (k_1) and transverse (k_2) polarizations.

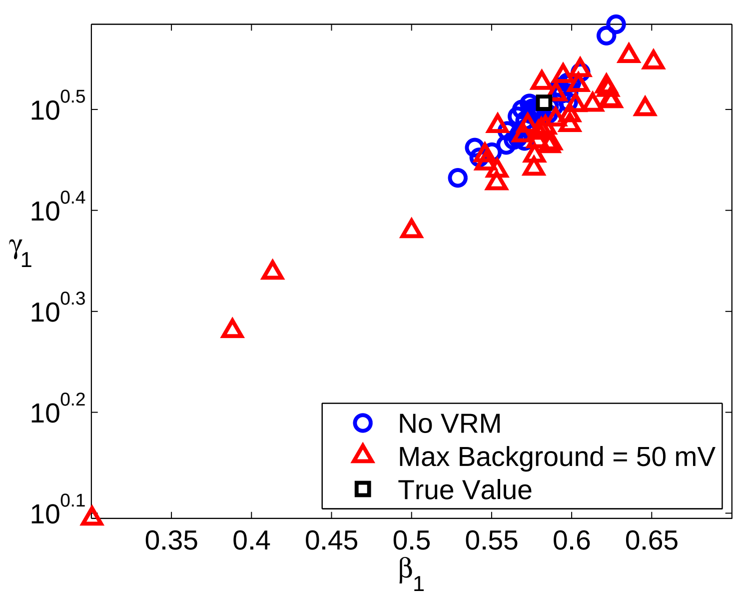

(b) Example of inversion of data with magnetic background filtered.

Figure 6.28: Inversion of synthetically generated 60 mm mortar data.

- Figure 6.29 shows the recovered polarization curves, confirming that the filtered magnetic background data are unable to estimate the amplitude of the axial components while correctly estimating its decay characteristics, and the transverse components of the data are poorly constrained.

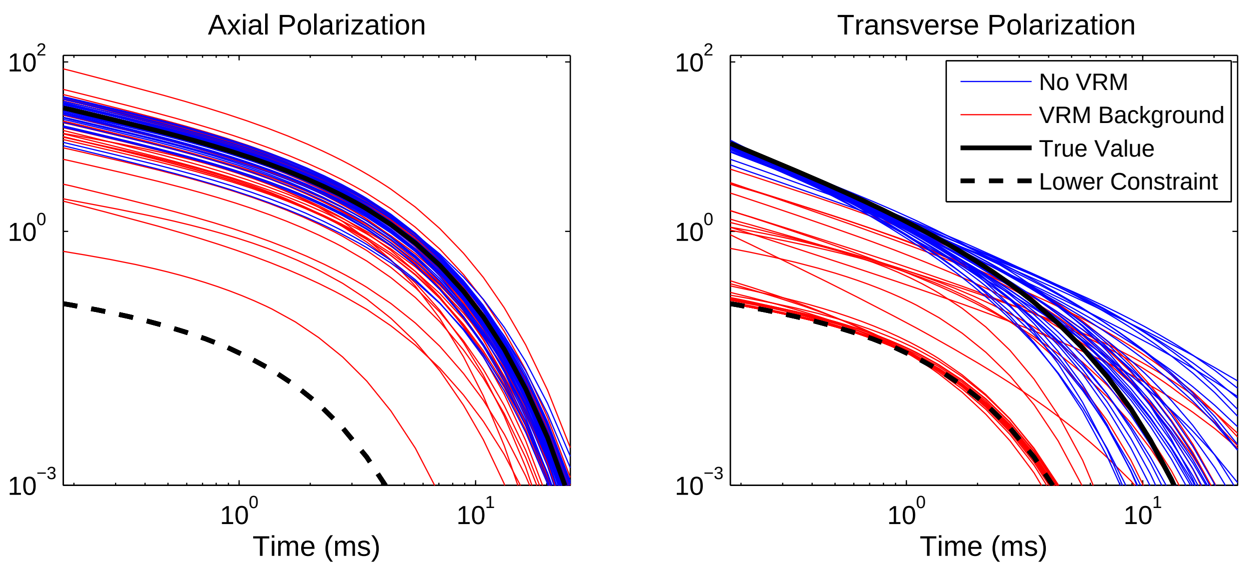

Figure 6.29: Recovered polarizations when inverting the 60 mm mortar data. The amplitude of the axial polarization is poorly constrained by the filtered data. Neither the amplitude nor decay behavior of the transverse polarization is well constrained by the filtered data.

6.10 Processing of data collected on Kaho'olawe Island, Hawaii

Geophysical data were collected on the island of Kaho'olawe, Hawaii as part of an Environmental Security Technology Certification Program (ESTCP) project to determine the effectiveness of EMI sensors fielded in areas with a large background geologic response (Cargile et al., 2004). Ordnance and ordnance related scrap were emplaced in a number of test plots. In this section we will apply target picking techniques on Geonics EM63 time domain and Geophex GEM3 frequency domain electromagnetic data collected over ESTCP Grid 2D and 2E (Table 6.2).

Table 6.2: Ground truth for Grids 2D and 2E.

Label	Target Name	X (m)	Y (m)	Depth (m)
1	Grid stake	0.00	0.00	0.00
2	Small Frag	29.04	1.36	0.15
3	2.75 ROCKET WARHEAD	56.17	3.70	0.38
4	MK-82 P. B. W/CON FINS	9.72	4.32	1.22
5	Large Frag	49.92	5.15	0.65
6	LAAW	54.15	5.52	0.13
7	Small Frag	4.58	5.70	0.10
8	Small Frag	22.31	5.82	0.10
9	81 mm Mortar	40.96	8.56	0.35
10	Med Frag	35.79	8.79	0.35
11	Large Frag	13.69	9.20	0.90
12	MK 76 P.B. (BDU 33)	23.32	10.20	0.71
13	Med Frag	48.35	10.56	0.20
14	5" HE PRACTICE	43.08	12.31	0.91
15	MK-3 PRACTICE BOMB	15.96	12.75	0.23
16	MK-81 P. B. W/S.E. FINS	7.92	12.77	1.02
17	20 MM	36.36	13.45	0.15
18	Large Frag	53.41	15.64	0.55
19	2.75" ILLUM	20.96	16.04	0.15
20	60 MM	12.63	16.21	0.20
21	SMAW ROCKET	4.40	20.86	0.76
22	Large Frag	10.15	20.94	0.70
23	MK 76 P.B. (BDU 33-(NOSE)	56.52	23.60	0.23
24	60 MM	28.32	26.63	0.15
25	Grid stake	60.07	30.02	0.00
26	Grid stake	30.09	30.03	0.00
27	Grid stake	0.08	30.04	0.00
28	Grid stake	30.00	0.00	0.00
29	Grid stake	60.00	0.00	0.00

6.10.1 Geonics EM63 TEM data

Naeva Geophysics, Inc. collected Geonics EM63 data at the ESTCP test site. Data on Grids 2D and 2E were collected on 60 m long, east-west lines with a linespacing of 50 cm. Data were collected in three 10 m wide sections. Before and after each section data were collected with the EM63 sensor elevated such that an in air measurement could be recorded, and sensor drift could be estimated and removed.

Sensor positioning was recorded with a GPS unit. Sensor orientation and height information were not provided with the data we received. For this analysis, we assume that the transmitter loop is at a height of 40 cm, and we assume that the loop is perfectly horizontal. Since we do not have accurate height and orientation information will not attempt to estimate the background response through the use of a low pass filter.

Figure 6.30 contains a plot of the sensor response for the first and tenth time gates, centered at t=0.18 ms and t=0.72 ms respectively. The weathering characteristics of the area results in a zone of high susceptibility that runs diagonally from the lower left to the upper right corners of the gridded data images. The high susceptibility causes background responses of greater than 300 mV in the first time channel of the EM63 data. The lowest level of background responses are approximately 50 mV in the lower right corner of the grid.

A soil model is fit to each of the soundings recorded within the grids. The fitting procedure involves solving for a soil model that minimizes the least squares misfit between the measured sounding and soil response. The soil response is given by a characteristic soil decay multiplied by an amplitude A, i.e. $F^{soil} = Af(t)$. Therefore, the fitting involves solving for a single amplitude parameter A. Figure 6.31 contains gridded images of the best fit amplitude A and misfit φ. The different sections of data being joined at $y = 10$ m and $y = 20$ m produce overlapping lines which result in some gridding artifacts. Several of the anomalies in the soil misfit image correspond to buried items (see Figure 6.34 for locations of known buried items). Anomalies not corresponding to emplaced items may be due to a buried metallic target, since it is possible that the site was not completely cleared of metal prior to preparing the test site.

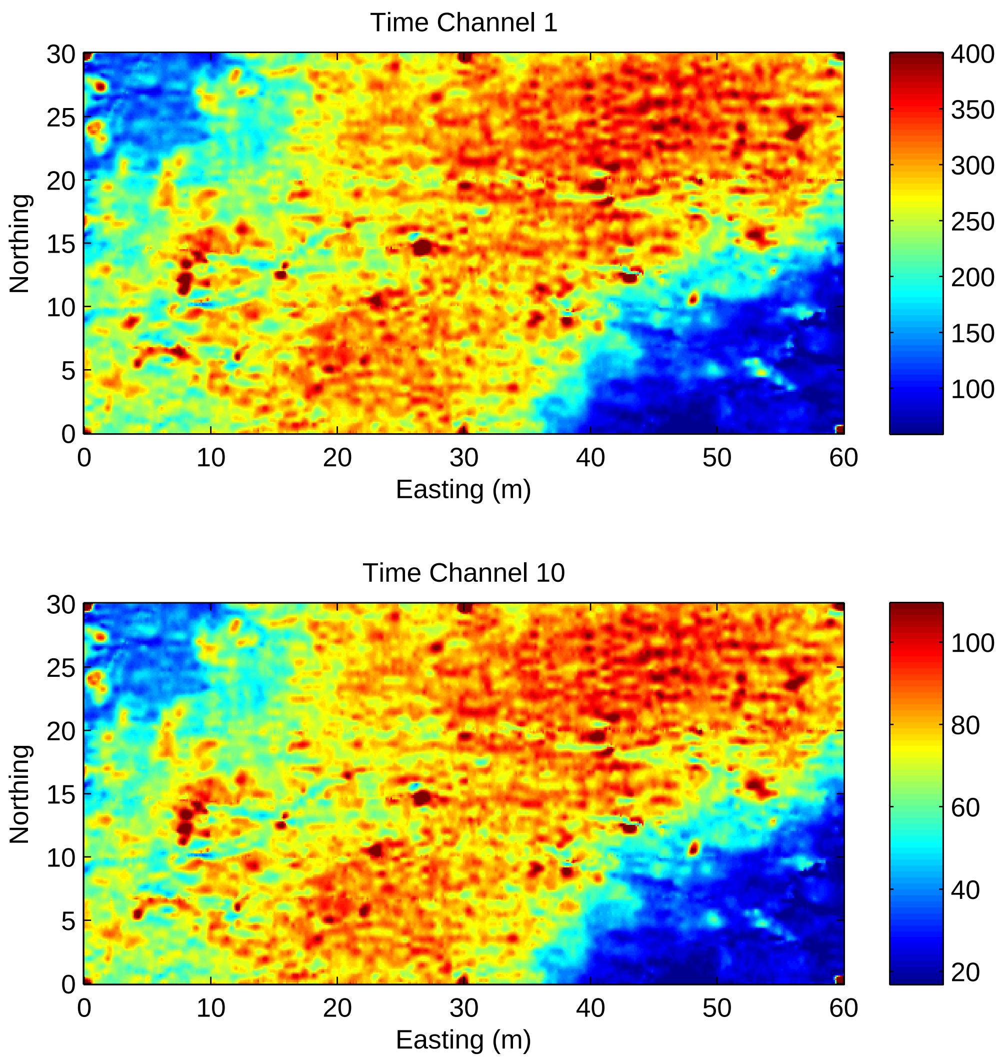

Figure 6.30: The first and tenth time channel of Geonics EM63 data collected over Grid 2D and 2E on Kaho'olawe Island, Hawaii.

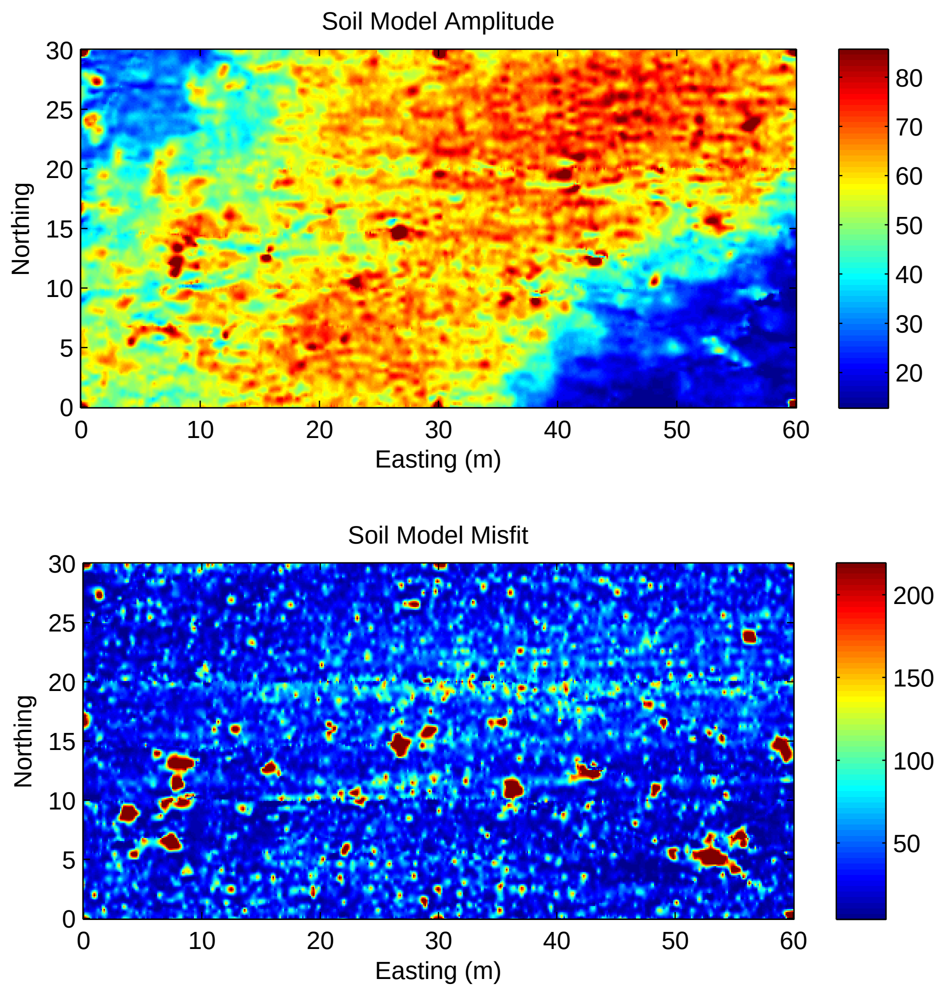

Figure 6.31: The soil model amplitude A and misfit φ for Geonics EM63 data collected on Kahoʻolawe.

Although it appears that several of the anomalies in Figure 6.31 correspond to emplaced items, we will not use the image for target picking purposes. Instead, our approach is to determine, for each sounding within the grid, the probability that the signal is due to soil (i.e. the null hypothesis). Since we do not have prior knowledge of the target types in the grid, we do not have an estimate of the pdf for the target misfits. Therefore we base our picks on the probability of false alarm P_{FA}. Calculating P_{FA} requires an estimate of the statistics of the soil misfit for the data set. The estimated probability density function and corresponding cumulative distribution function allows us to estimate the probability of false alarm P_{FA} for each sounding. That is, if a sounding has a soil misfit that is unlikely to belong to the distribution of soil misfits, then it will be classified as a target.

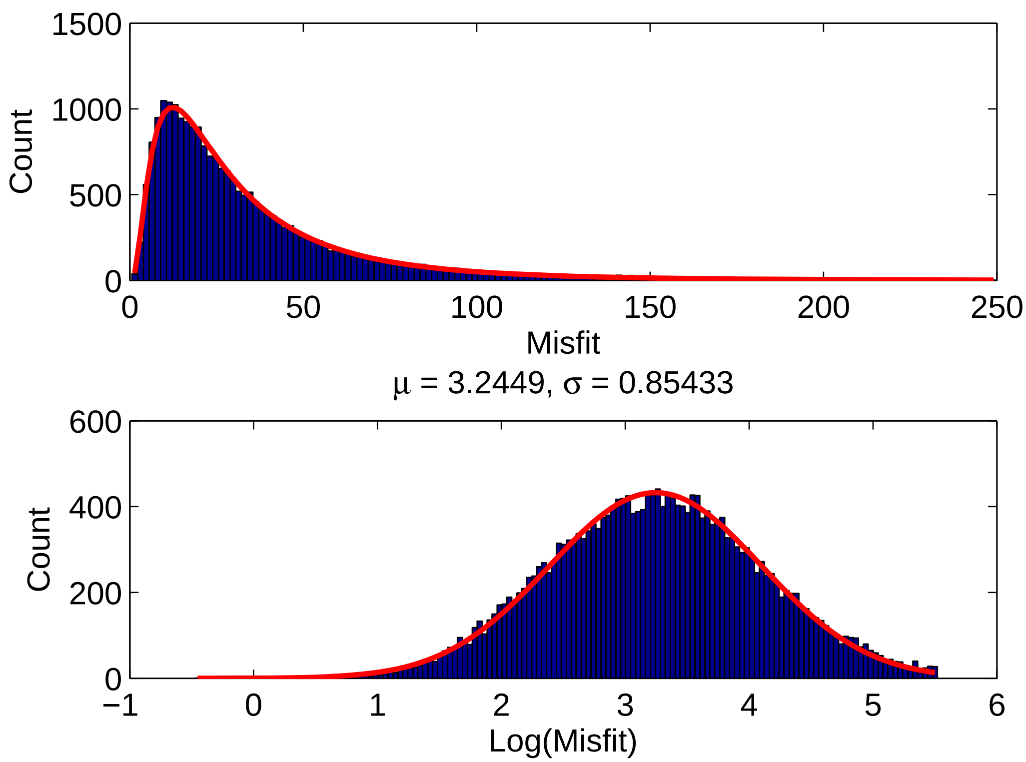

Figure 6.32: Values of misfits when fitting Geonics EM63 soundings in Grids 2D and 2E with a soil model.

Figure 6.32 contains plots of the misfit distributions. The upper plot shows a histogram of the raw misfit values and the lower plot shows a histogram of the log of the misfit values. Values of misfit greater than 250 are considered to be non-soil and are therefore not included when calculating the distribution statistics. Similar to the synthetic data results, the distribution of misfit values are well modelled with a log normal distribution. The mean of $\log(\varphi)$ is 3.24 and its standard deviation is 0.85. The red lines plotted on the histograms are distributions with this mean and standard deviation. The estimated cumulative distribution function is plotted in Figure 6.33. For each sounding a best fit soil model is calculated, and the misfit of the soil model is used to calculate probability of false alarm

$$P_{FA} = \int_{\varphi}^{\infty} p(x)\, dx = 1 - cdf(\varphi) \tag{6.21}$$

Figure 6.34(a) plots results of target picking according to P_{FA}. Grey dots mark locations of each sounding and the emplaced items, listed in Table 6.2, are indicated by circles (fragments and scrap items) and squares (ordnance items or corner grid stakes). Two thresholds for P_{FA} are plotted; soundings with $P_{FA} < 0.005$ are identified by blue circles, and soundings with $P_{FA} < 0.001$ are identified by red stars. A good target picking algorithm would be able to identify all the known targets (i.e. minimizing false negatives), with a minimal number of picked targets resulting from non-metallic items (i.e. false positives). It is difficult to determine the number of false positives in this example, since there are possibly targets present that were not cleared prior to preparing the test site. Indeed, when we visited Kaho‘olawe, we found that there were pieces of metal present in areas that were classified as cleared.

In any case, let us compare the picked targets with the locations of the known emplaced items. Setting a threshold of $P_{FA} < 0.005$ results in correctly locating all but 3 items: Targets 4, 17, and 21. Target 21 is a Shoulder launched Multi-purpose Assault Weapon (SMAW) Rocket. A SMAW rocket has a diameter of 84 mm. This particular rocket was reported to be buried at 76 cm which, due to its size, would be difficult to detect. Target 17 is a 20 mm projectile at a depth of 15 cm. Missing the 20 mm projectile is not unexpected, as the spatial size of the anomaly and the anomaly magnitude would be quite small. Target 4 is listed as a MK-82 at a depth of 1.22 m. Although 1.22 m is considered to be at the limit of detection depth for a Geonics EM63 sensor, the MK-82 is a type of 500 lb bomb that is 2.21 m long and 10.75 inches (221 mm) in diameter. There are a few reasons why the target picking might not of been able to identify the MK-82. It is possible that the anomaly within a couple of meters to the northwest of the groundtruth location is due to the buried MK-82. In addition, the MK-82 buried may be corroded, and thus have a weak signal. A final possibility is that the measured decays of the MK-82 may be similar to the characteristic soil decay. As the EM63 moves above a non-spherically symmetric target, the axial and transverse components will be "illuminated" at different angles by the primary field. This results in the observed decay (which is a linear combination of the target's axial and transverse polarizations) varying with position. However, if the signal-to-noise ratio of an anomaly is too low to allow for the collection of data at a number of locations, then the response might not change appreciably. If this response happens to be similar to the soil, the target will not be identified using a soil model misfit. This mechanism for false negatives is unavoidable. Responsible application of this method requires modeling the soil misfit for targets that may be encountered in a survey, and then generating receiver operator characteristic curves to quantify the success of the method.

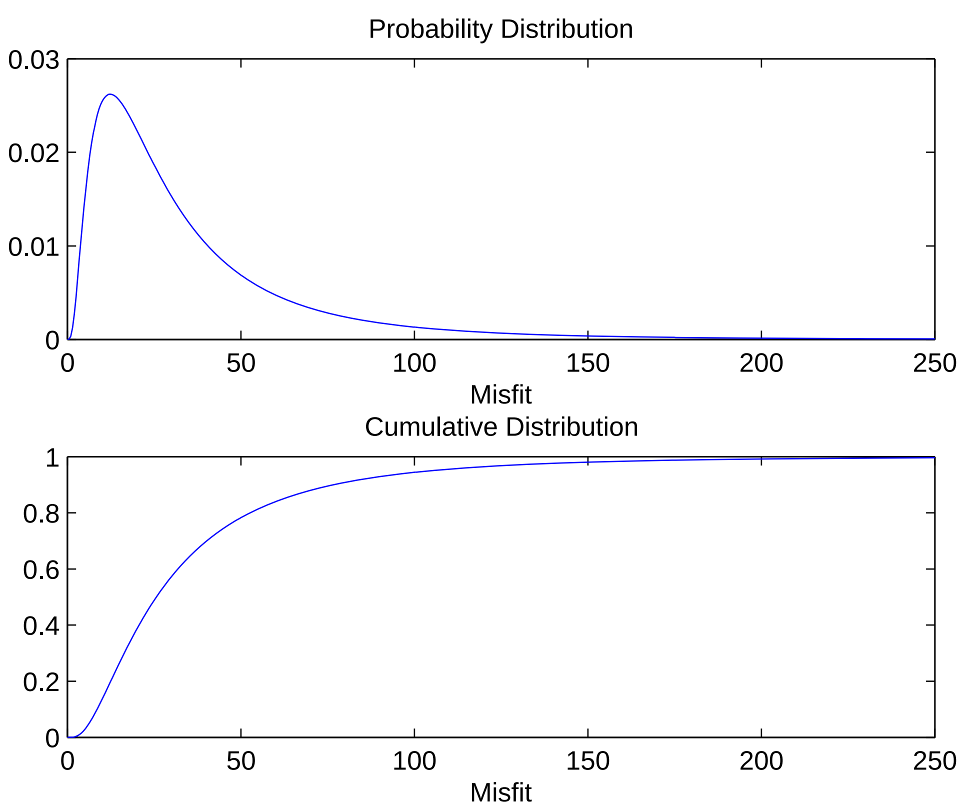

Figure 6.33: Estimated probability density function and cumulative density function for the soil misfit of the Kaho'olawe EM63 data.

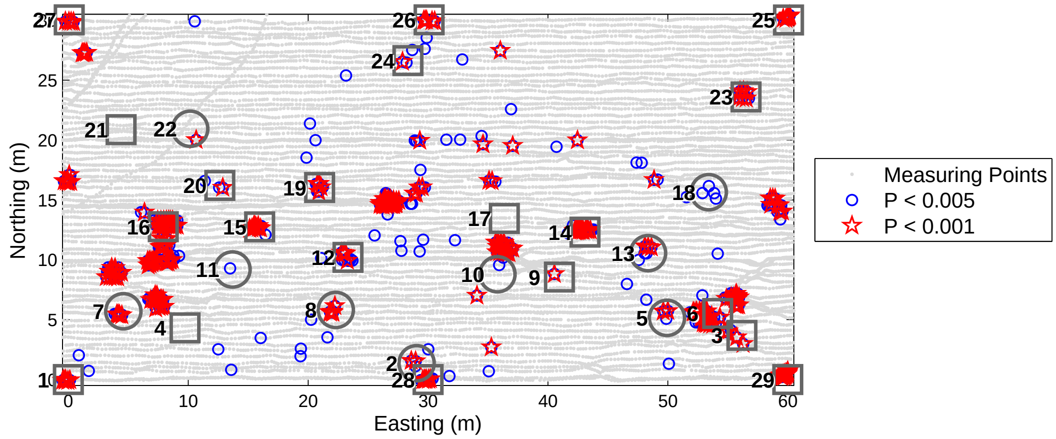

Figure 6.34: Target picking results when using the P_{FA}. Sounding locations are indicated by gray dots. Gray circles indicate emplaced non-UXO items such as frag, while gray squares indicate emplaced UXO items.

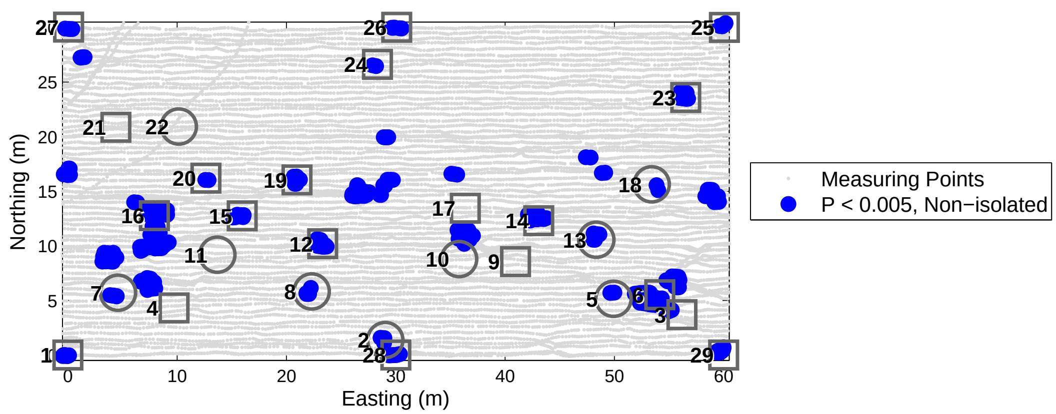

Figure 6.35: Target picking results when choosing anomalies whose $P_{FA} < 0.005$. Target picks where there is only a single sounding has a misfit falling below the threshold are removed from the list.

When using $P_{FA} < 0.005$ as a threshold, we see that there are a number of false positives. Decreasing the threshold to 0.001 (red stars) reduces the number of false positives to 7, but also increases the number of misses. In particular, targets 11 and 18 are no longer picked when the threshold is decreased. For these data, rather than decreasing the threshold to reduce false positives, it would be a better idea to recognize that targets generally have more than one sounding in which the soil misfit is large. If we look at the false positives for the $P_{FA} < 0.005$ target list, we see that majority of them are isolated soundings. Removing target picks associated with isolated soundings having a poor misfit reduces the number of false positives (Figure 6.35). However, requiring more than one sounding to define a target results in Targets 9, 11, and 22 no longer being picked as targets. Targets 11 and 22 are deep fragments (90 and 70 cm depth, respectively). Target 9 is an 81 mm mortar buried at a depth of 35 cm. Target 9 has a single sounding with a misfit that falls below both the $P_{FA} < 0.005$ and $P_{FA} < 0.001$ thresholds.

Comparing our target picking results to the known emplaced items have shown that using the misfit of a soil model can be effective in improving detection when processing multiple time channel TEM data.

6.10.2 Geophex GEM3 FEM data

Frequency domain electromagnetic data were collected at Kahoʻolawe using the Geophex GEM-3 sensor (Figure 6.36). The GEM-3 consists of a co-axial transmitter and receiver loops that simultaneously collects the frequency domain response at frequencies determined by the operator (Won et al., 1997).

For the ESTCP demonstration the GEM-3 was mounted on a wheeled cart, and configured to collect data at 10 frequencies located at 90, 150, 390, 750, 1470, 2970, 5910, 11910, 23850 and 47940 Hz. A 1 m circular transmitter loop was used. Data were collected by Geophex Ltd. and they provided us with sensor drift collected data from grid 2E. Grid 2E was surveyed in 3 parts. Each section was 10 m wide, with lines running in a north-south direction with a line spacing of 0.5 m.

Figure 6.36: A photo of Alex Oren from Geophex Ltd. collecting data at the Kaho‘olawe UXO test site. Data were collected with cart mounted version of the GEM-3. A 1 m circular transmitter loop was used for the demonstration.

Gridded images of the inphase (real) and quadrature (imaginary) components of the fifth frequency (1470 Hz) data are plotted in Figures 6.37(a) and (b), respectively. Compact anomalies due to several of the emplaced ordnance items can be observed in the quadrature component of the data. However, the high susceptibility zone that runs diagonally from the lower left to the upper right corners of the grid dominate the sensor response. Figures 6.37(c) and (d) show the long wavelength component of the data estimated using a 2D median filter. Subtraction of this background response produces the detrended versions of the data (Figures 6.37(e) and (f)). As was the case with the time domain case, the detrended data contain numerous soil related small wavelength anomalies due to sensor movement and topography.

(a) In Phase (Real) data for $f = 1470$ Hz

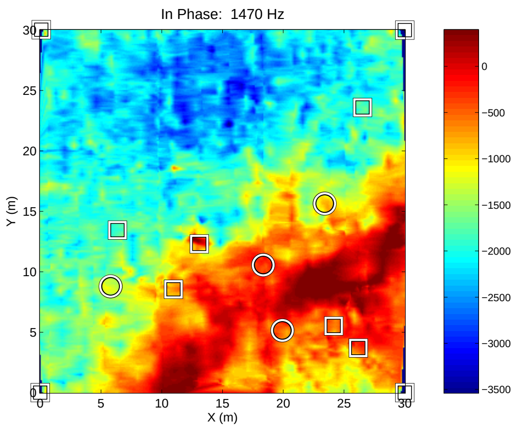

(b) Quadrature (Imaginary) data for $f = 1470$ Hz

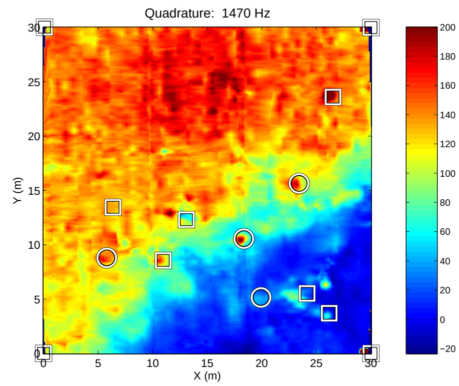

(c) Median filter estimate of the in phase data for $f = 1470$ Hz

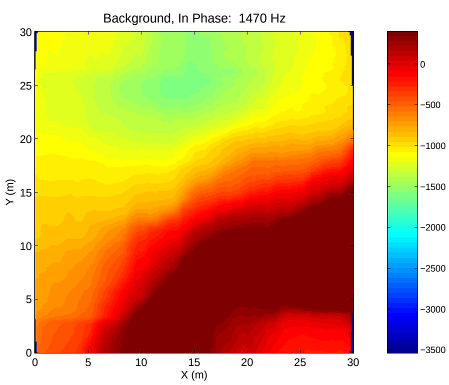

(d) Median filter estimate of the quadrature data for $f = 1470$ Hz

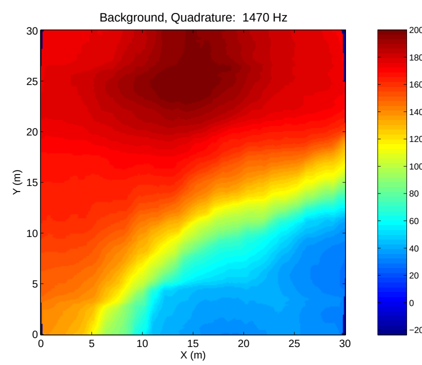

(e) Detrended in phase data

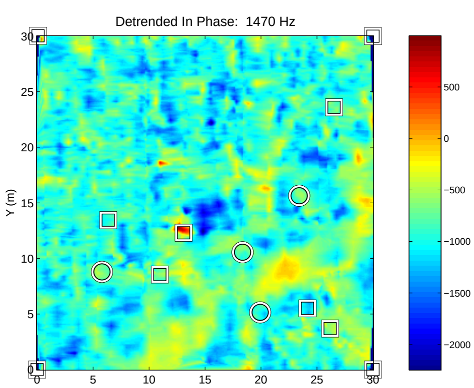

(f) Detrended quadrature data

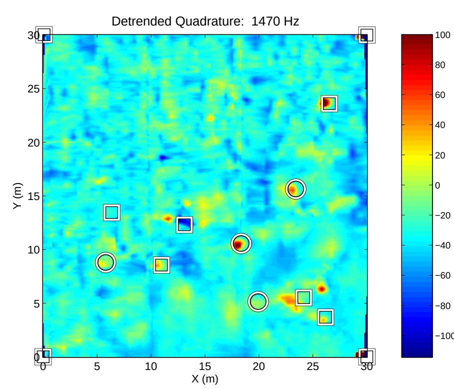

Figure 6.37: Geophex GEM3 data collected over grid 2E at Kaho‘olawe.

We process the GEM3 data by fitting a soil model. We fit the inphase and quadrature components of each FEM sounding with the following soil model:

$$H^{real} = m_1 \ln(\omega) + m_2 \tag{6.22}$$

$$H^{imag} = m_1 \tag{6.23}$$

Therefore, we have a two element model vector $\mathbf{m} = [m_1, m_2]^T$ which we estimate through minimizing a least squares objective function

$$\varphi = \frac{1}{2}\left\| F[m_1, m_2] - d^{obs} \right\|^2 \tag{6.24}$$

where $\mathbf{d}^{obs} = [H^{real}, H^{imag}]^T$. The lowest two frequencies ($f = 90$ and 150 Hz) and the highest frequency ($f = 47940$ Hz) are not included in the data vector due to the noise in these data. The gridded image of the log of the soil misfit ($\log(\varphi)$) is plotted in Figure 6.38. Figure 6.38 clearly shows the three separate surveys that make up the Grid 2E data. The noise characteristics of the instrument is clearly different for each survey. The middle section of data is clearly distinguished by its relatively lower misfit. The rightmost section of data ($x > 20$ m), has a misfit that is correlated with the amplitude of the soil response.

We will use the soil misfit results of Figure 6.38 in two ways: (1) Estimate the probability of false alarm for each sounding (as we did with the time domain data), and (2) Remove the long wavelength components of the soil misfit, and pick from the gridded image of the detrended data.

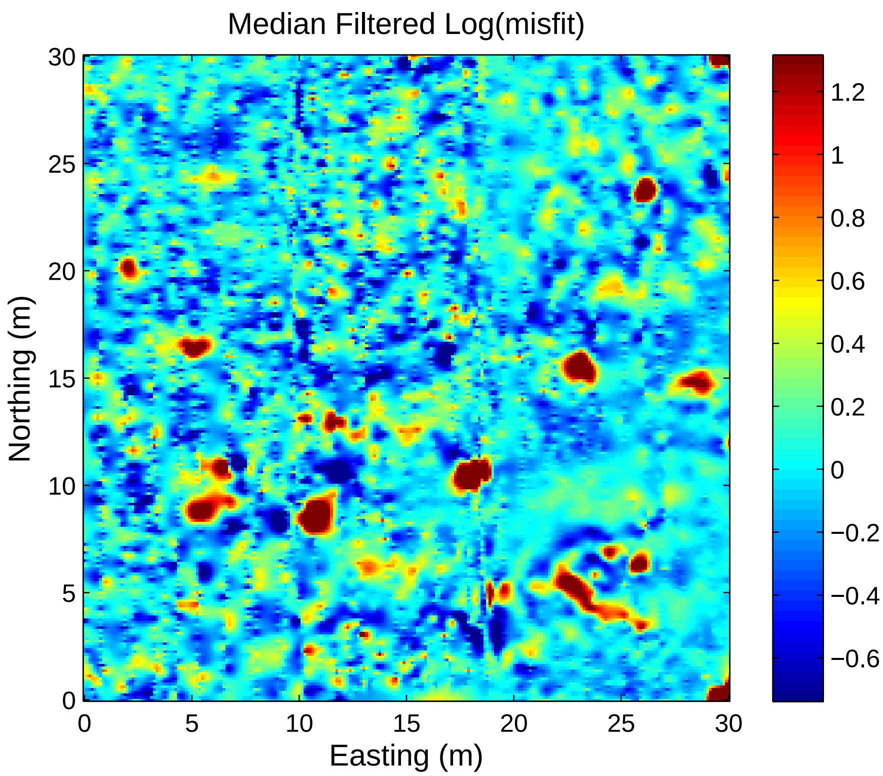

Figure 6.38: The calculated log of the misfit from fitting the model of equation 6.23 to the GEM3 data. The three separate survey events are clearly seen.

6.10.3 Target picking by calculating probability of false alarm

Since the soil misfit distributions for the GEM data are different for each of the three sections (Figure 6.39), we calculate a unique soil misfit distribution for each section. Figure 6.39 contains the histograms for the soil misfit in each of the three surveys. The histograms are fit with log normal distributions, and their respective cumulative distributions are computed (Figure 6.40). Figure 6.41 shows target picking results with two threshold values: $P_{FA} < 0.001$ and $P_{FA} < 0.005$. The picked targets correspond well with the ground truth. Target 17, a 20 mm projectile buried at a depth of 15 cm, was the only non-scrap emplaced item undetected by this method. Due to its small size, Target 17 was also missed when the target picking technique was applied to the Geonics EM63 data. Target 5 was undetected, but, after taking a closer look at the GEM3 sounding positions in the vicinity of the target, the miss may be due to inadequate spatial coverage. Target 9 (81 mm) is clearly identified by the picking method, although it was missed when processing the EM63 data.

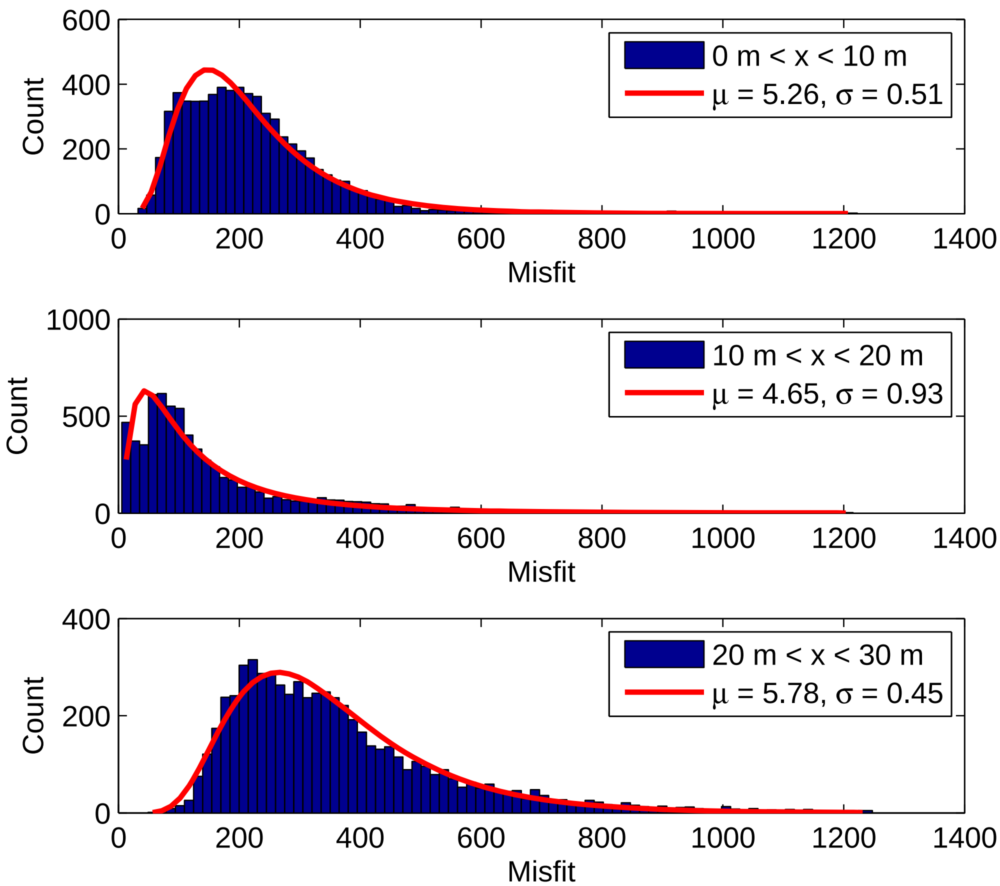

Figure 6.39: Histograms of the 3 surveys that make up the Grid 2E dataset.

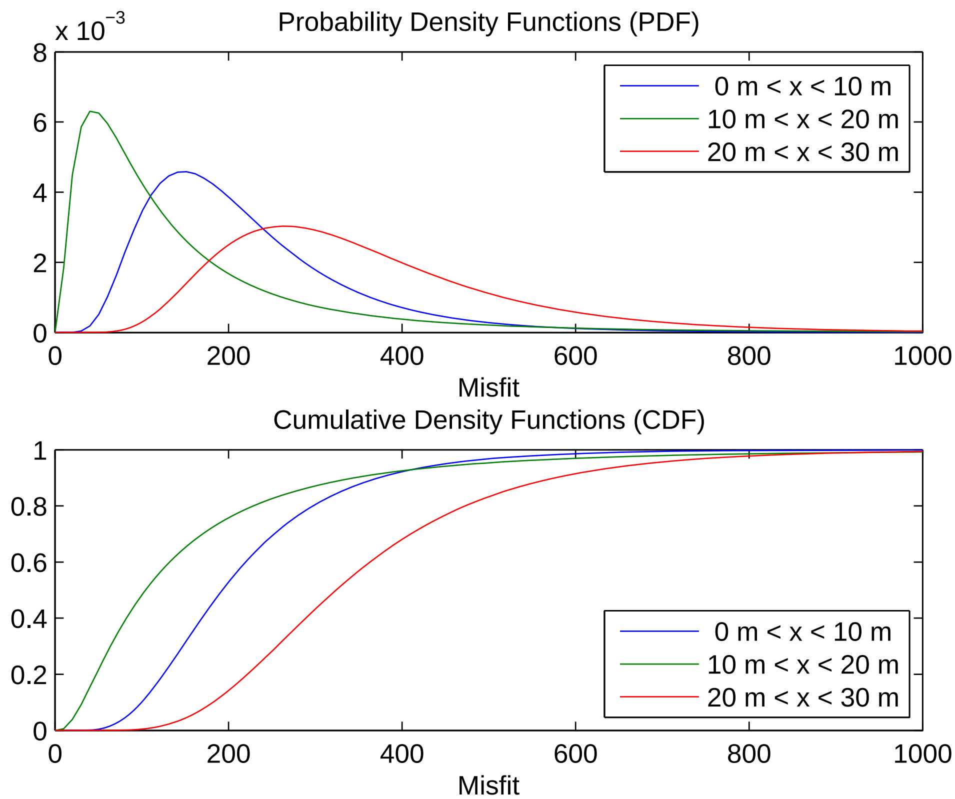

Figure 6.40: Probability density functions and cumulative density functions for the soil misfit of the three surveys of Grid 2E.

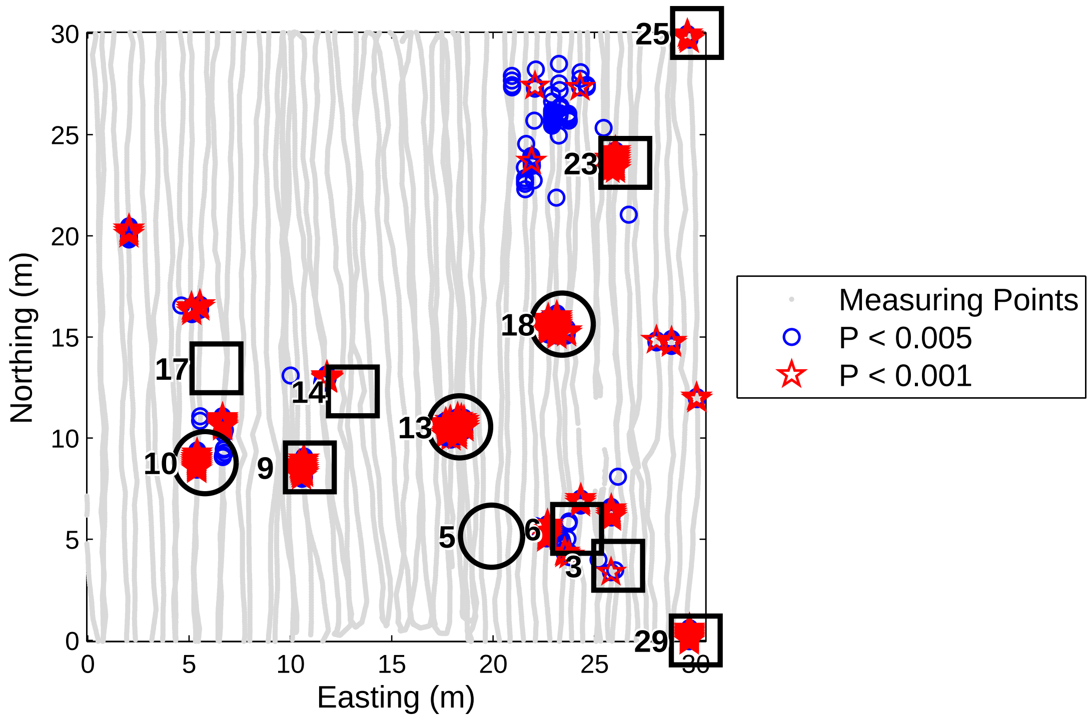

Figure 6.41: Target picking results when using P_{FA} for detection. The positions of the GEM3 sensor are indicated by grey points.

6.10.4 Target picking from log-misfit image

An alternative to examining the soil misfit for each sounding is to work with the gridded image of the soil misfit. We will work with the log of the misfit. Due to the different dc offsets of the soil misfit for the three survey sections making up Grid 2E, we apply an along line median filter for each survey sections. A 2D filter was not used due to the relatively narrow width of the data swath. Gridding the high-passed results produces the image in Figure 6.42(a). A pixel size of 0.125 m was chosen for the gridding. In order to determine a reasonable threshold for $\log(\varphi)$, we histogram the log of the misfits (Figure 6.42(b)).

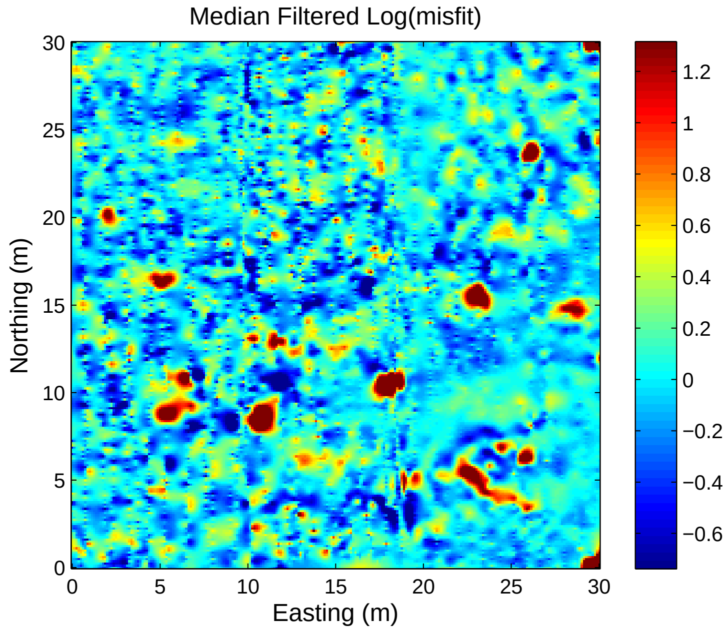

(a) Gridded image of median filtered log of the soil misfit.

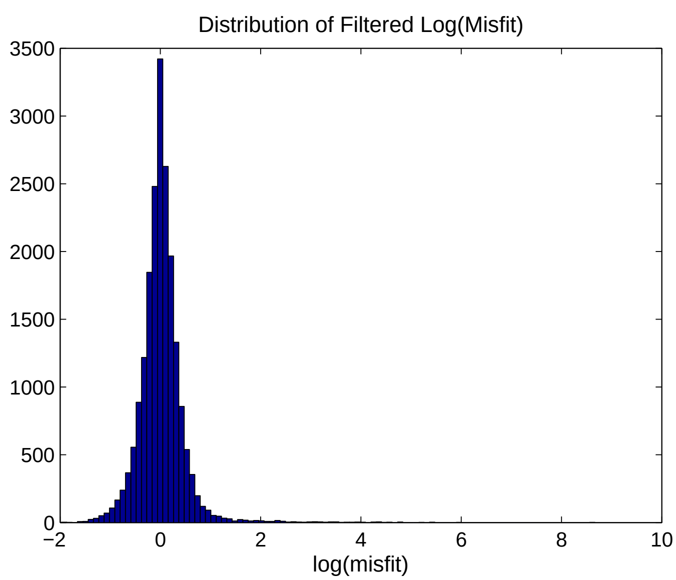

(b) Histogram of the filtered log of the soil misfit

Figure 6.42: Results from median filtering data from Figure 6.38.

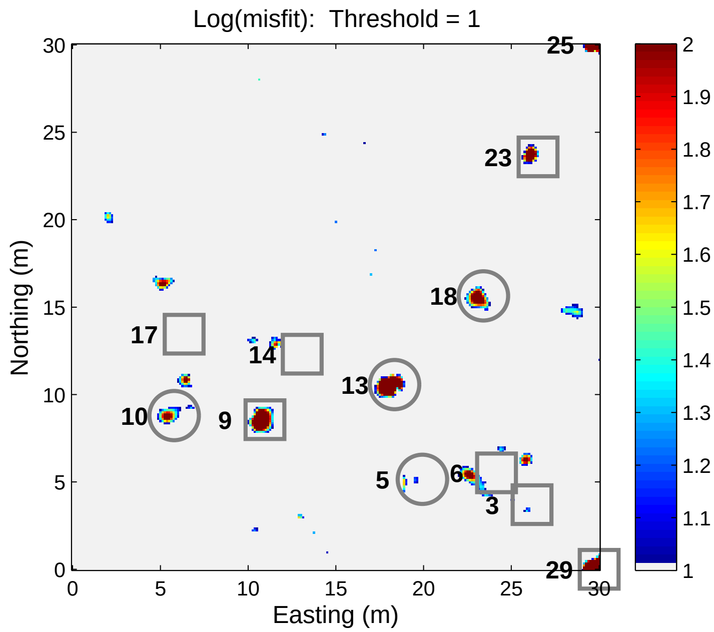

(a) Anomalies in the image of Figure 6.42 that are greater than unity, i.e. $\ln(\varphi) > 1$.

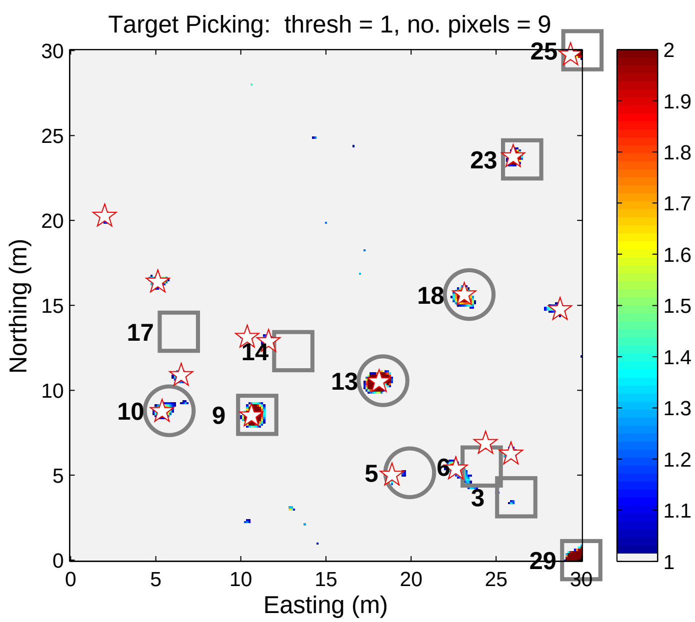

(b) Anomalies that have more than nine pixels greater than unity.

Figure 6.43: Target picking using the median filtered version of the log of the soil misfit φ. A target is defined when a $\log(\varphi)$ anomaly has three pixels greater than one.

Figure 6.43(a) contains gridded images where pixels with values less than or equal to unity are colored gray. Targets are chosen to be those anomalies that have at least 9 connected pixels that exceed the threshold $\log(\varphi) > 1$ (Figure 6.43(b)). The performance of target picking from the soil misfit image is, in this example, approximately equivalent to using P_{FA} of each sounding.

6.11 Simulating data response using correlated random numbers

Correlated random numbers (CRN) refers to a process of generating random spatially correlated numbers, where each random realization has a common prescribed power spectrum and probability distribution function (PDF). For our purposes the prescribed power spectrum generally decays with increasing wave number. The resulting distributions are approximately Gaussian. A careful prescription of a power spectrum can result in numbers that may be used to simulate the geologic response from several types of geophysical instruments.

Let $D(\omega_x,\omega_y)$ be the Fourier transform of correlated random data on the observation surface to be modeled, and $P(\omega_x,\omega_y)$ be its power spectrum, where (ω_x,ω_y) are wavenumbers in the x and y directions, respectively. Then the 2D Fourier transform of the data is given by

$$\widetilde{D}(\omega_x,\omega_y) = \sqrt{P(\omega_x,\omega_y)}\, e^{-i\phi(\omega_x,\omega_y)} \tag{6.25}$$

where $\phi(\omega_x,\omega_y)$ is the phase term. Given a prescribed power spectrum, different realizations of the random process may be simulated by assigning a different random phase, where values are uniformly distributed between 0 and 2π. All realizations have the same power spectra, and thus have more or less the same variability in the space domain. However, the locations of features seen in each realization will be different.

Using this procedure the response of a magnetic background may be simulated by windowing a region of data that is representative of the response. From the windowed data a parameterized surface may be fit to the spectrum, thus allowing the creation of simulations of the original windowed surface on an arbitrarily size grid. The following sections describe several parameterizations that have been used and briefly describe their advantages and disadvantages, followed by some examples of fitting the parameters to power spectra of windowed data.

6.11.1 Radial power spectra

This is the simplest parameterization and is useful when the most elementary of investigations into the effect of correlated noise is sought. It is also useful for parameterizing 3-D distributions of physical properties in the subsurface (Sinex, 2006). Assume a simple radial power spectrum of the form

$$P(\omega_r) = \frac{1}{\left[1 + (\omega_r / \omega_o)^2\right]^\beta} \tag{6.26}$$

where $\omega_r = \sqrt{\omega_x^2 + \omega_y^2}$ and ω_0 is a cutoff frequency and it is inversely proportional to the correlation length of the random process. The parameter β determines how fast the spectrum decays with wave number toward infinity, thus how correlated the process is. A value of $\beta = 0$ produces a flat power spectrum and corresponds to an uncorrelated random process or white noise, while ω_0 prevents the power from decaying at values less than its value. A desired variance of the resulting distribution may be obtained by scaling the values of the power spectrum greater than the DC component, while a mean can be assigned to the DC value. Figure 6.44 shows two realizations of a power spectrum parameterized with $\omega_0 = 1$ and $\beta = 2.5$. The scale is linear and can have values based on any prescribed mean and variance.

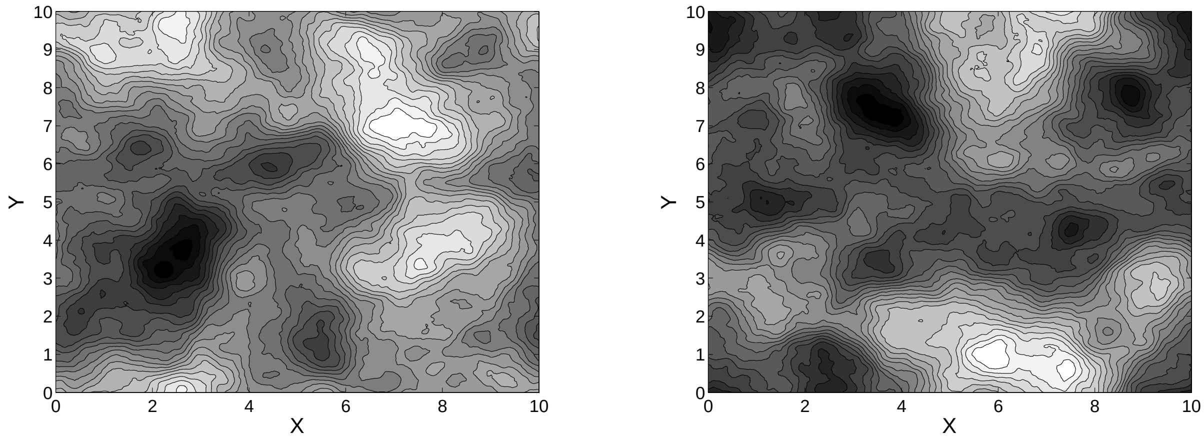

(a) Realization 1 (b) Realization 2

Figure 6.44: Two realizations of CRN with $\omega_o = 1$ and $\beta = 2.5$

6.11.2 2D power spectra

The following parameterizations or power spectrum models are natural extensions of the simple radial power spectrum parameterizations, where they exhibit an identical behavior along each of their principal axes. Let the principal axes be defined in terms of the wave number coordinates by,

$$\begin{aligned}\omega_x' &= \cos(\theta) * \omega_x - \sin(\theta) * \omega_y \\ \omega_y' &= \sin(\theta) * \omega_x + \cos(\theta) * \omega_y\end{aligned}$$

then two new parameterizations can be defined as,

$$P_1(\omega_x, \omega_y) = \frac{1}{\left[\left(\frac{\omega_x'}{\omega_{ox}'}\right)^2 + \left(\frac{\omega_y'}{\omega_{oy}'}\right)^2 + 1\right]^{\beta_x}} \tag{6.27}$$

$$P_2(\omega_x, \omega_y) = \frac{1}{\left[\left(\frac{\omega_x'}{\omega_{ox}'}\right)^2 + 1\right]^{\beta_x} * \left[\left(\frac{\omega_y'}{\omega_{oy}'}\right)^2 + 1\right]^{\beta_x}} \tag{6.28}$$

$$P_3 = P_1 + \alpha * P_2 \tag{6.29}$$

Plotting Equations 6.27 and 6.28 reveal very different decay patterns (see Figure 6.45) While Equation 6.28 is a natural extension to two dimensions of Equation 6.27, Equation 6.29 provides a very different decay pattern. With the power decaying slowest along the principal axis directions, this parameterization lends itself well to random noises that are oriented along line and across survey lines. Equation 6.29 takes a linear combination of Equations 6.27 and 6.28, thus giving a set of parameters that are robust to the advantages of both models.

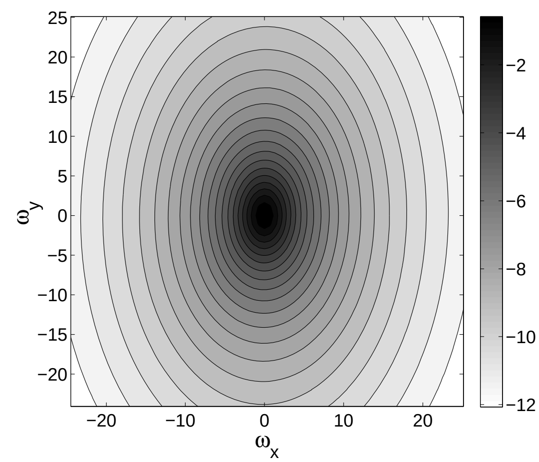

(a) Equation 6.27: Power spectrum

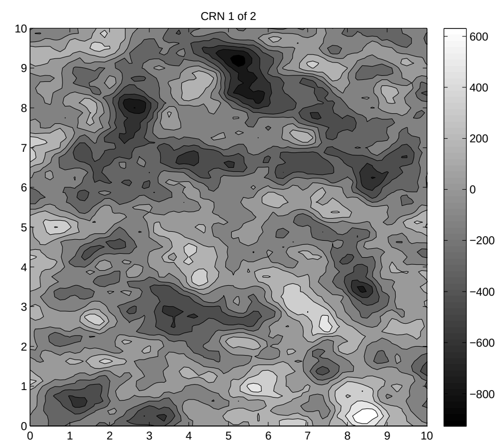

(b) Equation 6.27: CRNs

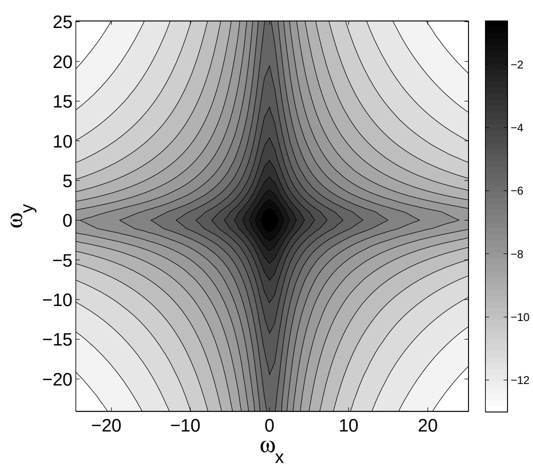

(c) Equation 6.28: Power spectrum

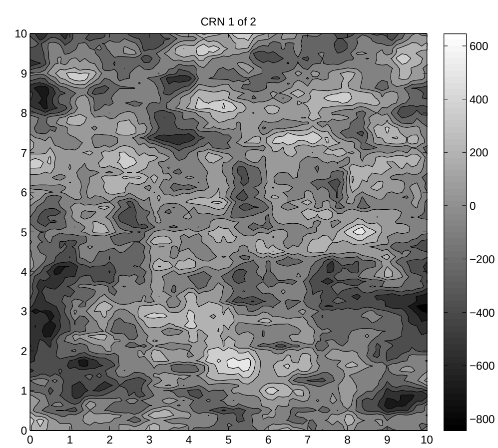

(d) Equation 6.28: CRNs

Figure 6.45: Plots of the power spectra and CRNs that result from equations 6.27 and 6.28.

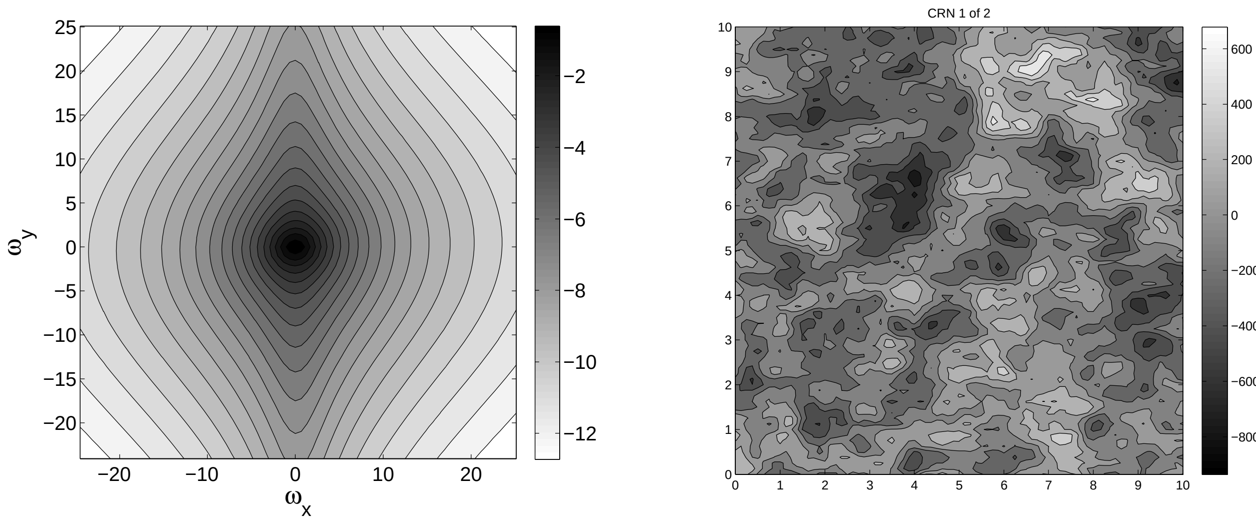

(a) Equation 6.29: Power Spectrum (b) Equation 6.29: CRNs

Figure 6.46: Plot of the power spectrum and CRNs resulting from equation 6.29.

6.11.3 Recovery of power spectrum models

The previous parameterizations represent three of many possible models for characterizing correlated random noise in geophysical data. The following presents the results of fitting each of the models to a single in-phase channel of GEM3 data taken over a large gradient at Kaho'lawe, Hawaii. The model parameters are recovered using a non-linear least squares minimization algorithm. Let each model describe a normalized power spectrum (i.e σ^2=1 and μ = 0) and be parameterized by the following model vectors,

$$
\begin{aligned}
m_1 &= [\theta, \omega_x, \omega_y, \beta] \\
m_2 &= [\theta, \omega_x, \omega_y, \beta_x, \beta_y] \\
m_3 &= [\theta', \omega'_x, \omega'_y, \beta', \theta, \omega_x, \omega_y, \beta_x, \beta_y, \alpha]
\end{aligned}
$$

Figure 6.47 gives results of fitting the m_1 model above to the GEM3 data, where the recovered model was m_1 ~ [0.7,2.1,3.1, 2.3]. Both the variance and mean of the data are estimated separately in order to reduce the complexity of the inverse problem. The result of this procedure is the ability to generate random realizations of noise that are spectrally and statistically similar to the measured data. The last final challenge is extrapolate the noise realizations to all of the multi-channel data. This problem will be addressed in a subsequent section, while the following section discusses extending the use of CRN to produce non-stationary noise realizations.

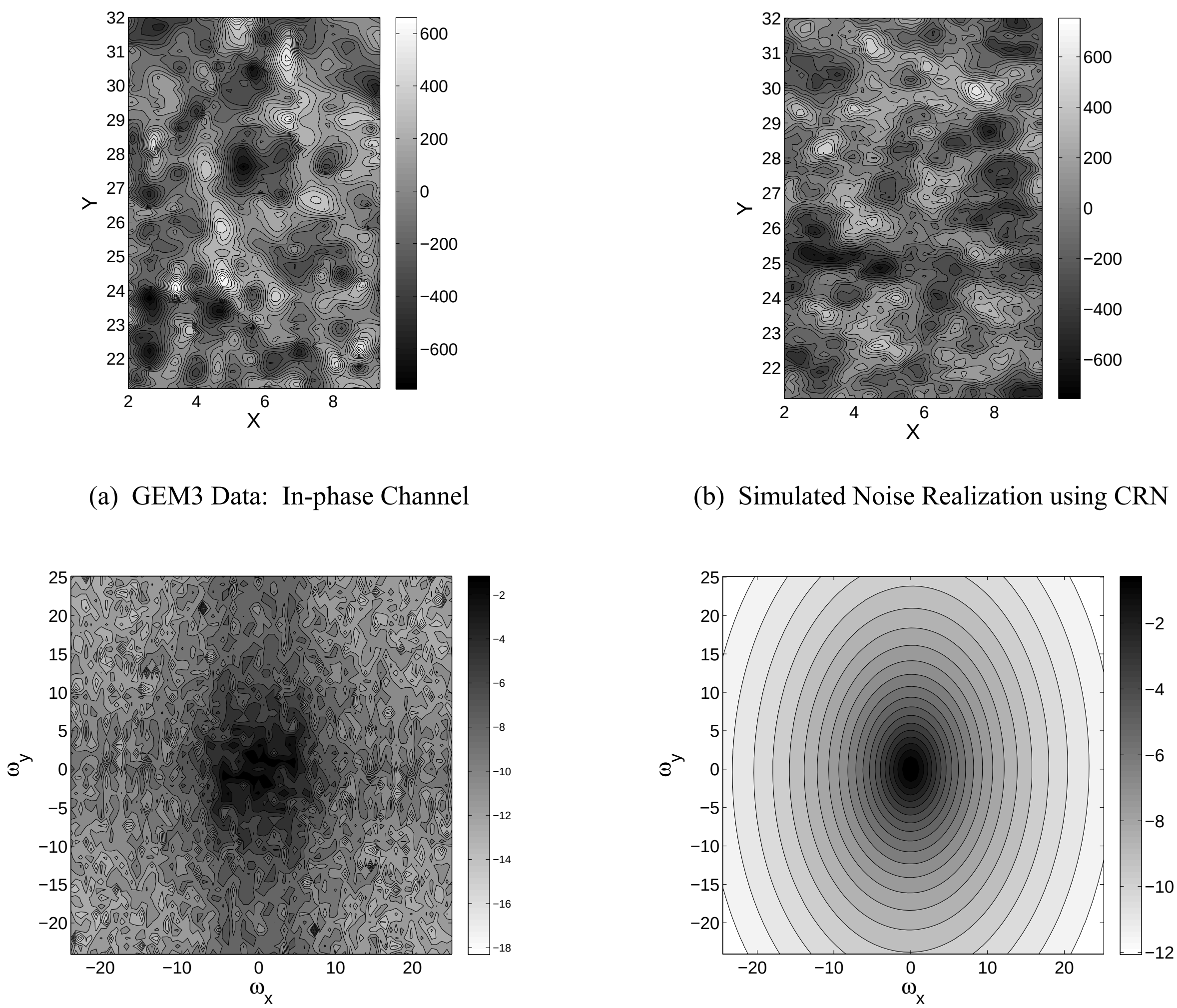

(a) GEM3 Data: In-phase Channel

(b) Simulated Noise Realization using CRN

(c) GEM3 Data: Power Spectrum

(d) Estimated Power Spectrum

Figure 6.47: Example of data simulation using CRNs

6.11.4 Multiple correlated random numbers

Non-stationary CRNs or noise realizations where the statistical properties of the noise gradually vary from one location to another can be pieced together by the use of multiple concurrent sets of CRN with different prescribed power spectra and an identical phase. The combining is done by averaging all the concurrent realizations (i.e. differing in their prescribed power spectra) into a single set of CRNs, by the use of a spatial weighting function. The result is an average of multiple correlated random numbers or MCRNs.

Using MCRN is desirable when statistical properties such as the variance or dominant wavelength of the noise varies smoothly from one spatial location to another. A practical procedure for simulating a single data channel of geophysical data would be,

1. Select windows of multiple image regions that represent regions where the statistical properties are assumed to be approximately constant.
2. Determine the best fit model, m_i for each individual window.
3. Forward model each CRN realization (with identical phase) at concurrent locations.
4. Choose an average weighting function that averages all the CRNs in such a way that the statistical properties of each window are honored.

6.11.5 Averaging functions

The choice of an averaging function should be chosen based on a case by case basis, but in general it must obey the following. Let an individual weighting function be expressed as, $w_i(x,y)$, where x and y are the spatial coordinates and i is an index that refers to a particular CRN, then we must satisfy,

$$\sum_{i=1}^{N} w_i = 1$$

With the above condition satisfied, then any choice may be used for assigning weights to the spatial locations.

An easily implemented choice is to calculate weights based on the distance that a particular averaging location is away from an estimation location. Then by satisfying the relationship above the contribution of a CRN at an estimation location will decay to zero for all but the CRN that is anchored at the location. Let a distance function be computed for each estimation location,

$$d_i(x,y) = \sqrt{(x-\tilde{x}_i)^2 + (y-\tilde{y}_i)^2} \tag{6.30}$$

where $(\tilde{x},\tilde{y})$ indicates the i^{th} estimation location or center of a windowed region. The weighting function is then,

$$w_i(x,y) = \frac{\dfrac{1}{d_i(x,y)}}{\sum_{i=1}^{N} \dfrac{1}{d_i(x,y)}}$$

The above distance value, d_i computes distances based on spatial locations on a horizontal observation surface. Note that the distance function may be computed for any function of the spatial coordinates, (x,y). With the weights, $w_i(x,y)$, and several CRN simulations, $CRN_i(x,y)$, a MCRN realization may be computed by

$$MCRN = \sum_{i=1}^{N} w_i(x,y) CRN_i(x,y)$$

6.11.6 Example using MCRN

This section demonstrates using MCRN to simulate a non-stationary background response. The data simulated is in-phase GEM3 data from Kaho'olawe, Hawaii. Figure 6.48(a) shows a plot of the GEM data. The simulation of the noise in this image is best done using the relatively shorter wavelength components, therefore the long wavelength component or regional field may be removed by subtracting from the data a low-pass filtered component. Filtering has been done using a low-pass Butterworth filter. The filtered result is shown in Figure 6.48(b). Subtracting the filtered data from the original data gives the data seen in Figure 6.50(b). A careful observation of the data in Figure 6.50(b) reveals that both the amplitude and correlation lengths of the data vary as a function of the regional low-pass filtered data. Long-wavelength noise occurs where the regional is large and short wavelength noise occurs where the regional is small.

It is known that a majority of this noise is caused by random changes in sensor orientation, where the response due to sensor orientation changes as a function of the background regional field strength.

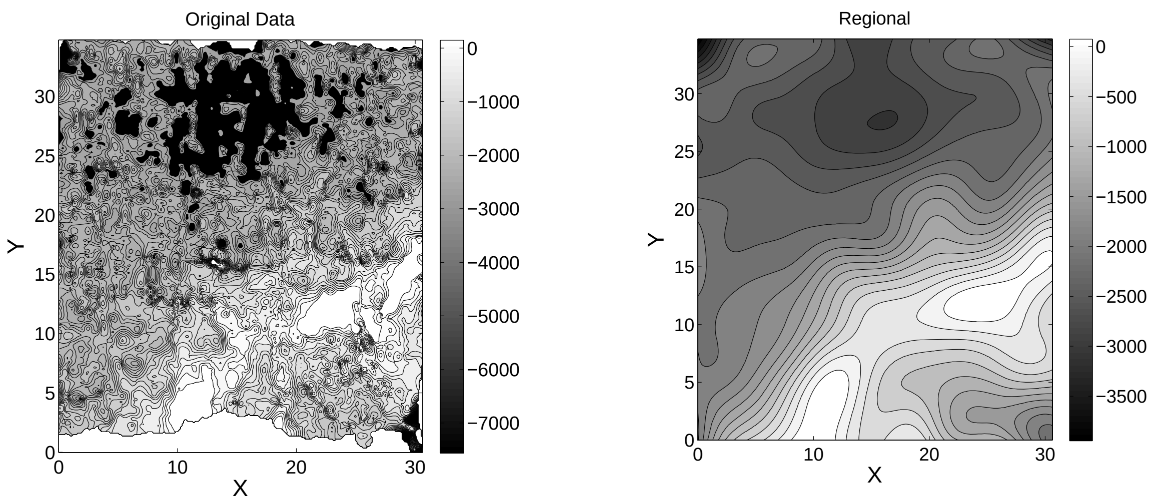

(a) GEM3 Data: In-phase Channel (b) Estimated regional trend

Figure 6.48: Results of applying a Butterworth filter to Kaho'olawe Gem3 data

Due to the relationship between the noise characteristics and the regional field, for this particular noise simulation, it is useful to compute the averaging weights for MCRN using the regional surface values. Lets call the regional surface, $R(x,y)$, then the distance function, d_i, in Equation 6.30 becomes,

$$R(x,y) = \left| R(x,y) - R(\tilde{x},\tilde{y}) \right|$$

where $R(\tilde{x},\tilde{y})$ is the value of the regional at the i^{th} estimation location.

A comparison of weighting functions for two estimation locations based on the spatial distance and regional distance weights are given in Figure 6.49. The differences here are very noticeable. Using a spatial weighting function, the weights vary from 0 to 1 radially and anchor at 0 or 1 at the estimation locations. Using a regional weighting function the weights anchor to 0 or 1 along contour lines of the original regional surface. This means that a particular estimation location will translate to an estimation contour of the original regional surface.

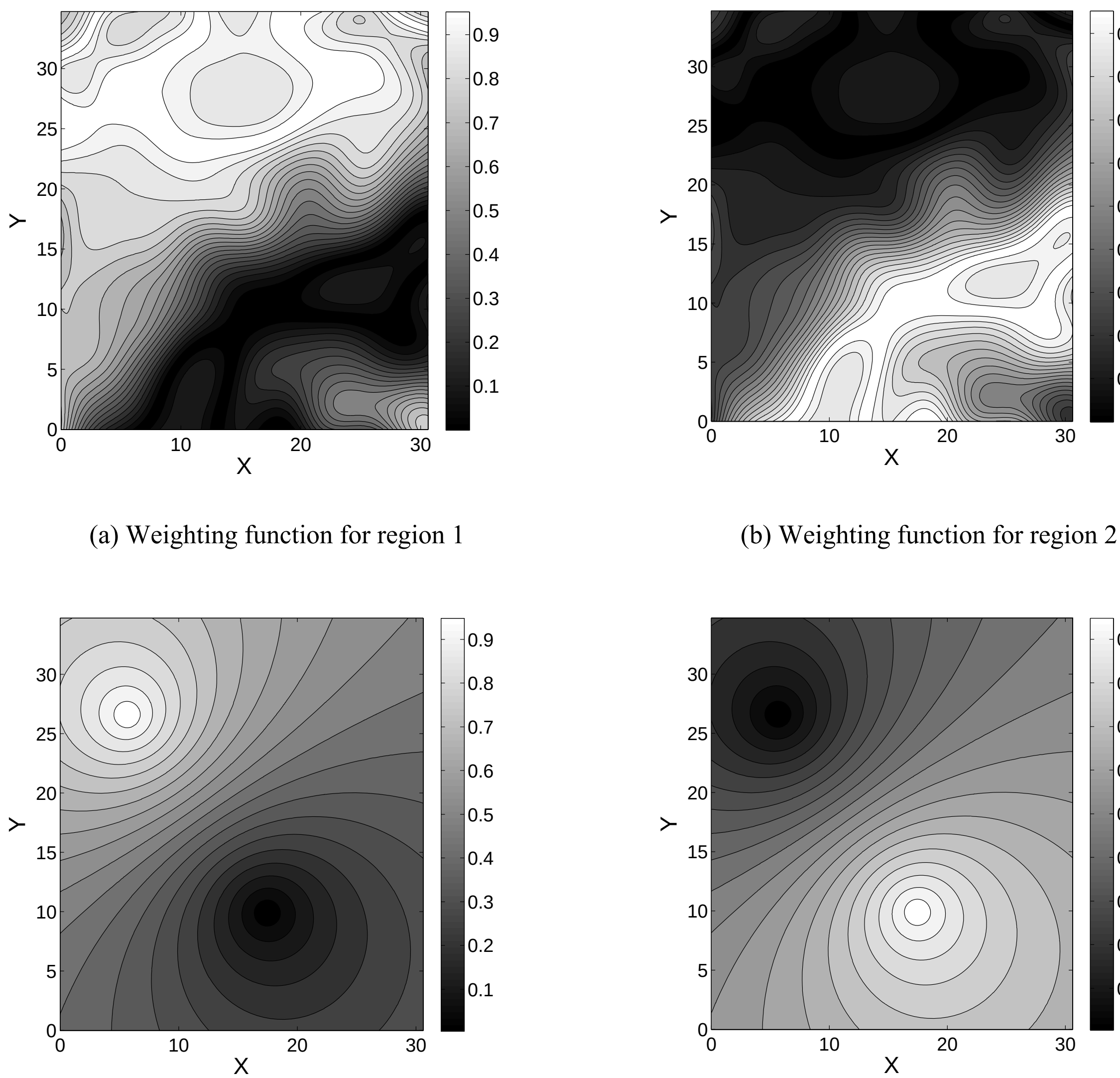

(a) Weighting function for region 1

(b) Weighting function for region 2

(c) Weighting function for region 1

(d) Weighting function for region 2

Figure 6.49: Example of data simulation using MCRNs

For this data it is appropriate to use the regional distance weights. Figure 6.50 shows the results of a single realization using MCRN in two regions in a single data set. Figure 6.51 shows the variograms derived from actual data in the two regions from which we define the statistical properties used in the simulation. The x and y curves refer to the semivariance in the Northing and Easting directions respectively.

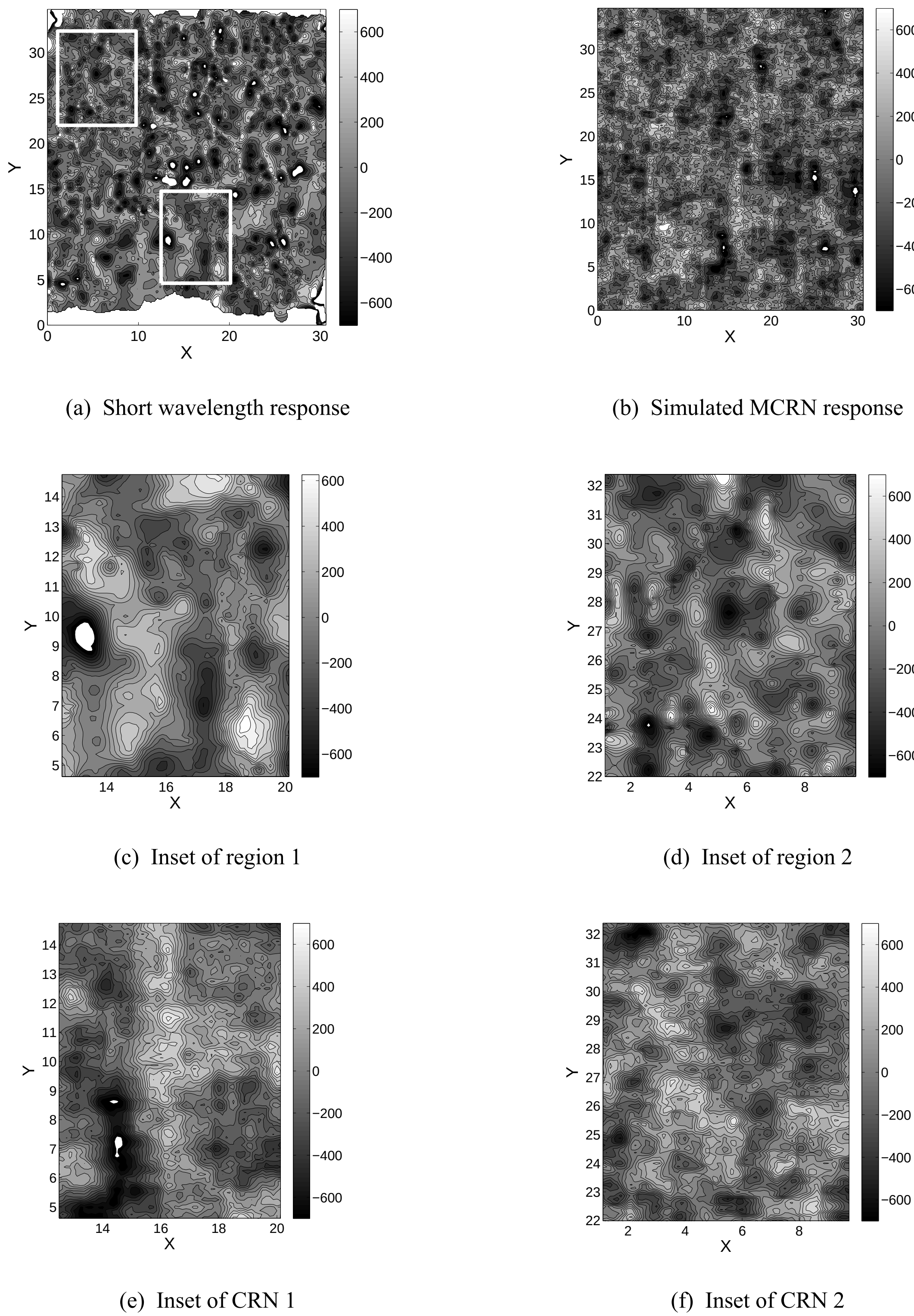

(a) Short wavelength response
(b) Simulated MCRN response
(c) Inset of region 1
(d) Inset of region 2
(e) Inset of CRN 1
(f) Inset of CRN 2

Figure 6.50: Example of data simulation using MCRNs.

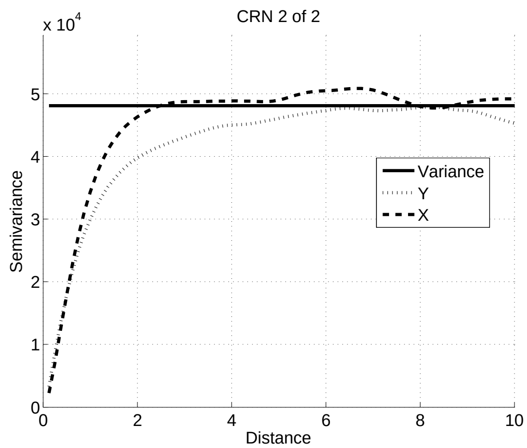

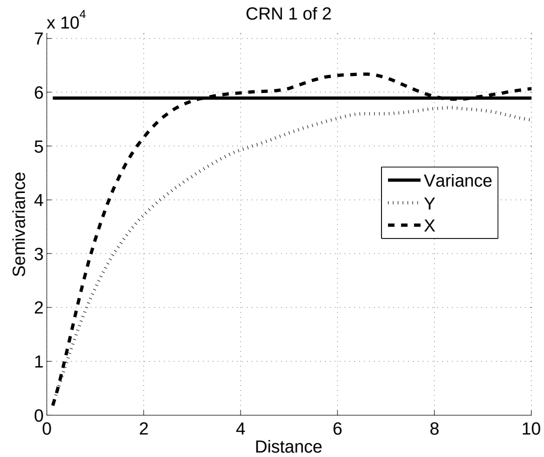

(a) Variogram of region 1 (b) Variogram of region 2

Figure 6.51: Variograms derived from actual data in the two regions from which we define the statistical properties used in the simulation. The x and y curves refer to the semivariance in the Northing and Easting directions respectively.

6.11.7 Discrimination using MCRN at field site

In this section we present a simple example of how MCRN can be used to investigate the discrimination potential at a UXO remediation site on the Former Camp Sibert, Alabama. At this particular site, the discrimination objective is to identify 4.2-inch mortars. A geophysical prove-out (GPO) site containing thirty intact 4.2-inch mortars and eight partial mortars was prepared. Geonics EM63 time domain electromagnetic data were acquired on the GPO site. The Geonics EM63 sensor is a pulse induction type metal detector that measures the time decay of the secondary field at 26 time gates whose centers range from 0.18 ms to 25 ms. The sensor is mounted on a cart, and the data are collected in a dynamic mode with a line separation of approximately 0.5 m and an along track station spacing of approximately 0.1 m.

Figure 6.52(a) contains a gridded image of the first time channel of Geonics EM63 data. The seeded targets are indicated by the squares. The scale is chosen to show that there is a background signal that decreases in strength from approximately 25 mV in the Northern section of the grid to 10 mV in the southern part of the grid. Figure 6.52(b) plots examples of measured decays in the area of the grid a weaker background (indicated by the letter A) and the stronger background response (indicated by B). The black lines that overlay the measured data is the expected VRM response for a Geonics EM63 sensor. Clearly, the background signal at this site is due to the presence of VRM.

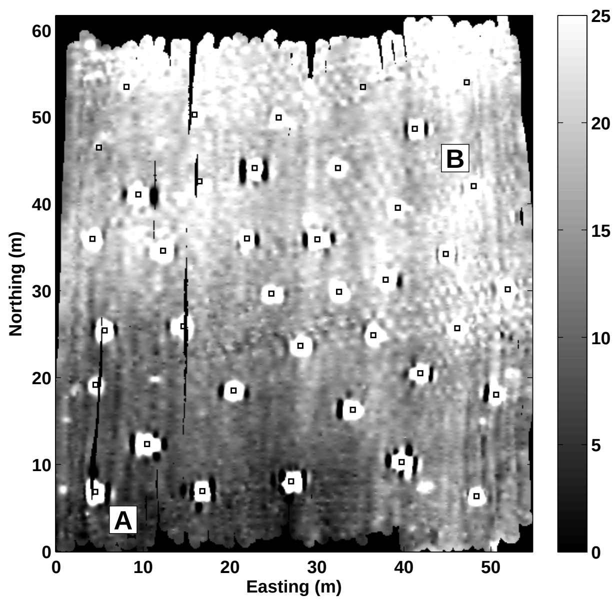

(a) Image of gridded first time channel of data. Location of seeded targets are indicated by black squares.

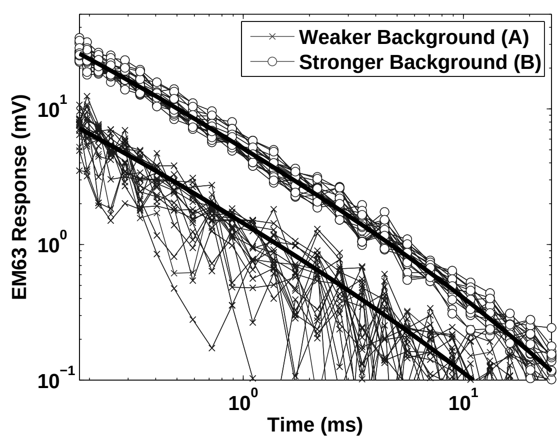

(b) Time decays measured at two different locations in the grid.

Figure 6.52: Geonics EM63 data acquired at the Camp Sibert Geophysical Proveout grid.

The GPO data were inverted for the best fit dipole model, and the corresponding diagonalized dipole polarization tensor. The response measured by the Geonics EM63 sensor can be written as

$$V(t) = \frac{\mu_o}{4\pi r^3} \mathbf{m}(t) \cdot (3\hat{\mathbf{r}}\hat{\mathbf{r}} - \mathbf{I}) \tag{6.31}$$

The induced dipole moment is

$$\mathbf{m}(t)=\frac{1}{\mu_o}\mathbf{A}^T\mathbf{F}(t)\mathbf{A}\cdot\mathbf{b}^P \tag{6.32}$$

where **A** is the Euler rotation tensor, $\mathbf{b}^P$ is the primary field generated by the transmitter at the ordnance location, and **F** is the electromagnetic polarization tensor. The target's shape, size, and material properties (i.e., conductivity and magnetic susceptibility) are contained in **F**. The primary field in the TEM case ($\mathbf{b}^P$) will vary with transmitter/receiver location. The polarization tensor **F**(t) for has the form

$$\mathbf{F}(t)=\begin{bmatrix} L_3(t) & 0 & 0 \\ 0 & L_2(t) & 0 \\ 0 & 0 & L_1(t) \end{bmatrix} \tag{6.33}$$

If L_1 (t)= L_2 (t)= L_3 (t), then the target has spherical symmetry, and if $L_1(t)> L_2(t)= L_3(t)$, then the target is rod-like with axial symmetry. Several parametric forms for $L(t)$ have been considered (Bell, 2001; Smith, 2004; Pasion, 1999). In this paper we use a parameterization suggested by J.D. McNeill (personal communication)

$$L_i(t)=k_i t^{-\beta_i}\exp(-t/\gamma_i) \tag{6.34}$$

where k_i controls the magnitude of the polarization, β_i defines the power law decay and γ_i is the fundamental time constant, and i = 1,2,3. Pasion *et al.* (2001) successfully modeled Geonics EM63 data using Equation 6.34.

The forward model can be summarized as $\mathbf{d} = F[\mathbf{p}]$, where F is the forward modeling operator and **p** is the model (or parameter) vector defined as

$$\mathbf{p}=[X,Y,Z,\phi,\theta,\psi,k_1,\beta_1,\gamma_1,k_2,\beta_2,\gamma_2,k_3,\beta_3,\gamma_3] \tag{6.35}$$

The objective of data inversion to determine the model vector **p** which predicts a response that best matches the observed data. For a description of the inversion procedure (and a more detailed discussion of dipole modeling techniques), we direct the user to Pasion (2007).

The GPO data were detrended using a 200 point median filter then inverted. This particular filter was chosen for this example since line filtering is commonly used in the geophysical community for eliminating long wavelength background responses. Figure 6.53 contains feature plots when inverting the GPO data.

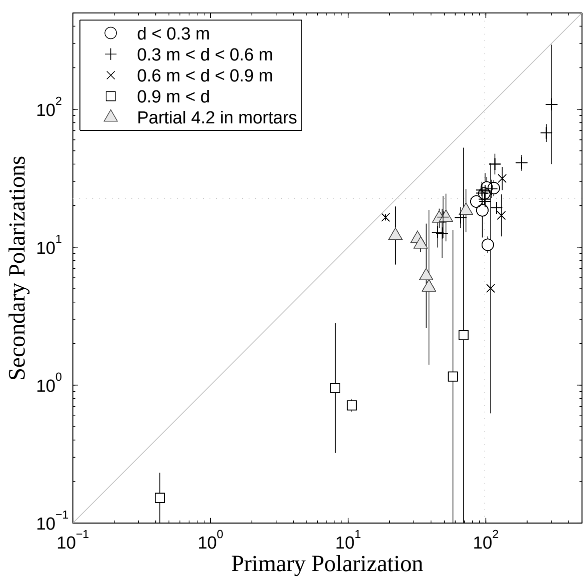

(a) Size parameters: k_1 vs. k_2, k_3

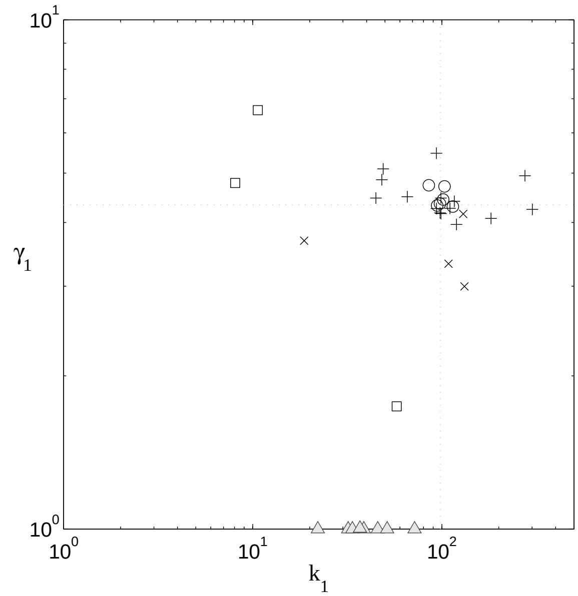

(b) Amplitude and time constant parameters for the primary polarization: k_1 vs. γ_1.

Figure 6.53: Feature plots when inverting Geonics EM63 data acquired on the Geophysical Prove-out grid.

In the ideal case of $F[\mathbf{p}]$ being exact, with the model vector $\mathbf{p}$ is a function of the target only, and not position and orientation, then there should be no scatter in parameter plots of a specific target type. Due to sensor noise (i.e. the noise in the sensor that would be measured in the absence of conductive material) and the spatially correlated noise due to the VRM background, the parameters generally plot as a cluster. Discrimination relies on targets of interest having well separated clusters. Figure 6.53(a) plots the size parameter k for the primary polarization and the secondary polarizations. The vertical line for each point extends between the secondary polarization k values. Ideally, an axially symmetric target would plot as a single point. The amount of spread in the k values corresponding to the 4.2-inch mortar is correlated to the depth of the targets. For deeper targets, the signal becomes more dominated by sensor and geologic noise and the spread increases. For deep targets (depth greater than 0.9 m) discrimination is not possible. Figure 6.53 (b) plots the strength k_1 and time constant γ_1 of the primary polarization. Clearly, the combination of primary polarization strength and time constant provides a more robust discrimination feature than size alone.

The GPO inversion results provided limited insight into the potential for discrimination at the Sibert site due to the relatively few number of targets and target types. Simulations can be used to investigate some simple concerns regarding discrimination at this site:

(1) How is our ability to discriminate 4.2-inch mortars from partial mortars using a dynamic mode Geonics EM63 survey at Camp Sibert dependent on the depth of the target?

(2) Can a smaller target than a 4.2-inch mortar be discriminated using the same survey parameters?

To address these questions, we carry out the MCRN procedure of the previous section using the GPO data. Anomalies for 4.2-inch mortars, partial 4.2-inch mortars, and 60 mm mortars were added to the data by using the forward modeling of Equation 2.31 and using dipole parameter model vector.

Figure 6.54 contains a sample data fit for one of the simulated 4.2-inch mortar anomalies. The observed and predicted data match quite well. However the data are unable to correctly constrain the recovered parameters. The expected and recovered polarization parameters and their estimated variances are listed in 2.54(d). The decay characteristics of the primary polarization (i.e. β_1 and γ_1) are the only parameters that are well constrained.

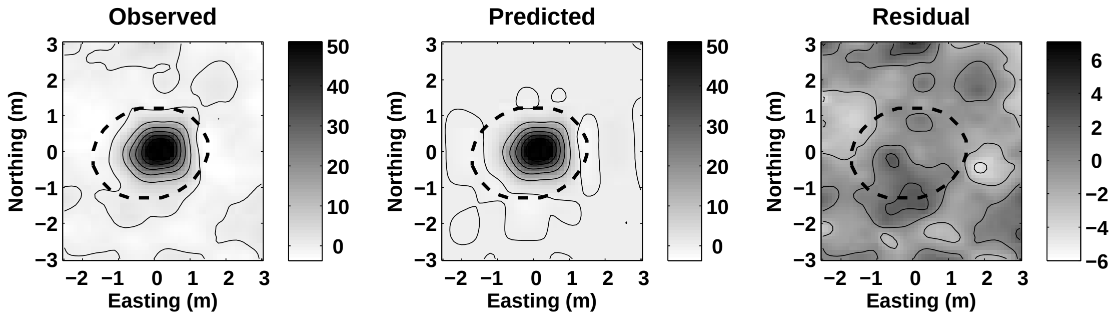

(a) Time Channel 1

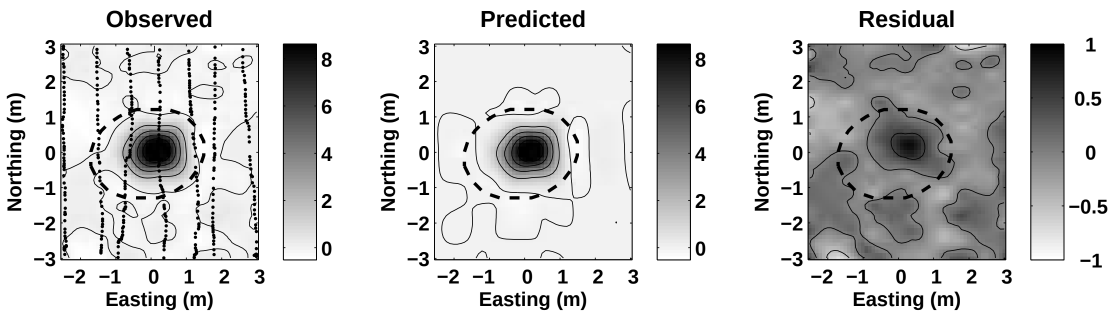

(b) Time Channel 10

Parameter	Expected	Recovered
Northing	578239.55	578239.58 ± 0.02
Easting	3751319.40	3751319.53 ± 0.04
Depth	0.81	0.88 ± 0.02
k_1	98.3	140.8± 6.9
β_1	0.53	0.55 ± 0.39
γ_1	4.33	4.15 ± 1.19
k_2	22.6	11.3 ± 12.5
β_2	0.95	0.91 ± 0.02
γ_2	3.8	1.68 ± 0.17
k_3	22.6	0.10 ± na (constraint)
β_3	0.95	0.30 ± 0.35
γ_3	3.8	1.02 ± 0.37

(c) Table of Recovered Parameters

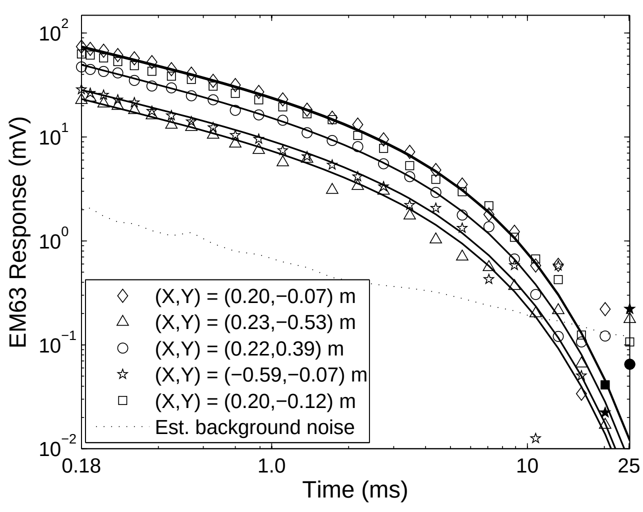

(d) Comparison of predicted and observed decays

Figure 6.54: Sample fit of one of the simulated 4.2-inch mortar anomalies.

Figure 6.55 contains results from inverting intact and partial 4.2 inch anomalies from the simulated data. Although the separation of clusters in the size based parameters space degrades with depth, some level of discrimination is possible. For depths up to 90 cm, it appears that the k_1 vs. γ_1 parameters would allow for good discrimination between the partial and intact 4.2 inch anomalies. Figure 6.55(f) shows that for the deeper (and thus lower signal-to-noise) 4.2 inch mortars, the discrimination ability using the k_1 vs. γ_1 plot begins to degrade.

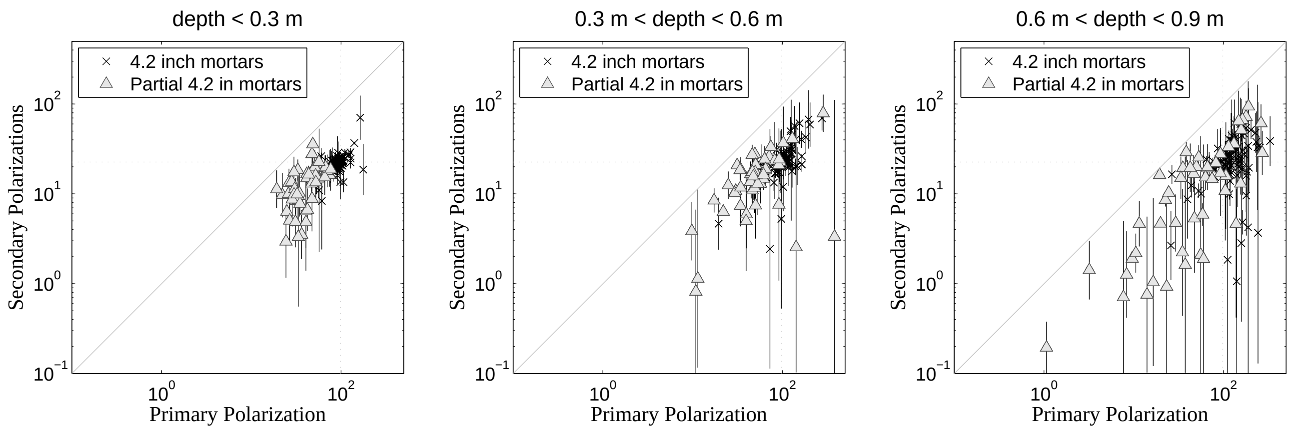

k_1 vs. k_2, k_3. Depth less than 0.3 m.

k_1 vs. k_2, k_3. Depth greater than 0.3 m and less than 0.6 m.

k_1 vs. k_2, k_3. Depth greater than 0.6 m and less than 0.9 m

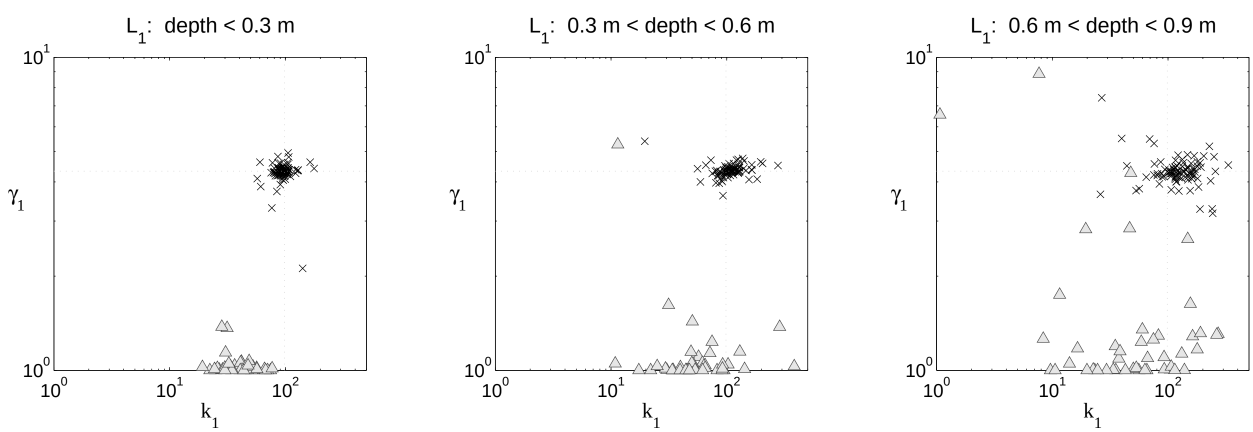

Amplitude and time constant parameters for the primary polarization: k_1 vs. γ_1. Depth less than 0.3 m.]{

Amplitude and time constant parameters for the primary polarization: k_1 vs. γ_1. Depth greater than 0.3 m and less than 0.6 m.

Amplitude and time constant parameters for the primary polarization: k_1 vs. γ_1. Depth greater than 0.6 m and less than 0.9 m.

Figure 6.55: Feature plots when inverting simulated data over intact and partial 4.2 inch mortars.

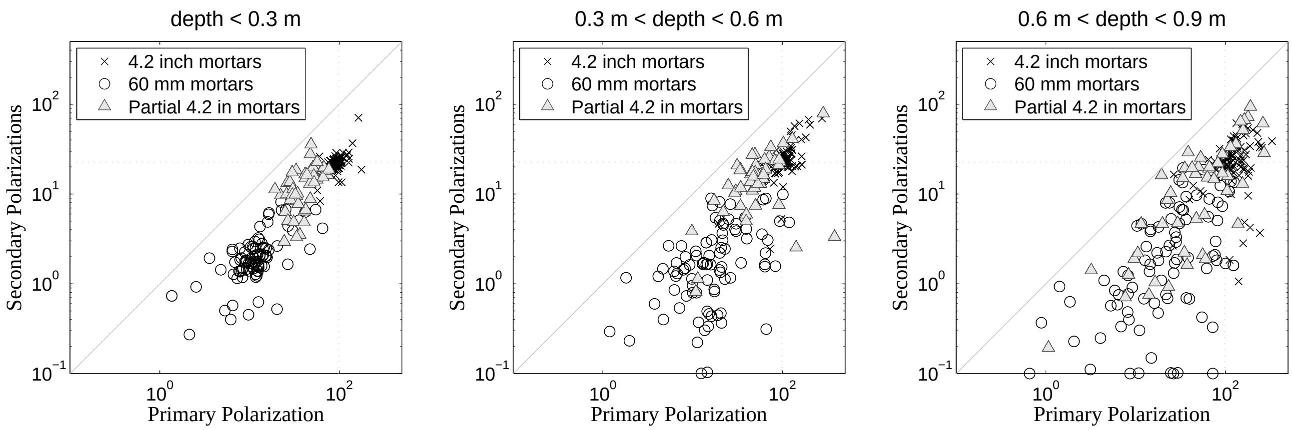

k_1 vs. mean(k_2., k_3). depth less than 0.3 m.

k_1 vs. mean(k_2., k_3). depth less than 0.6 m and greater than 0.3 m.

k_1 vs. mean(k_2., k_3). Depth less than 0.9 m and greater than 0.6 m.

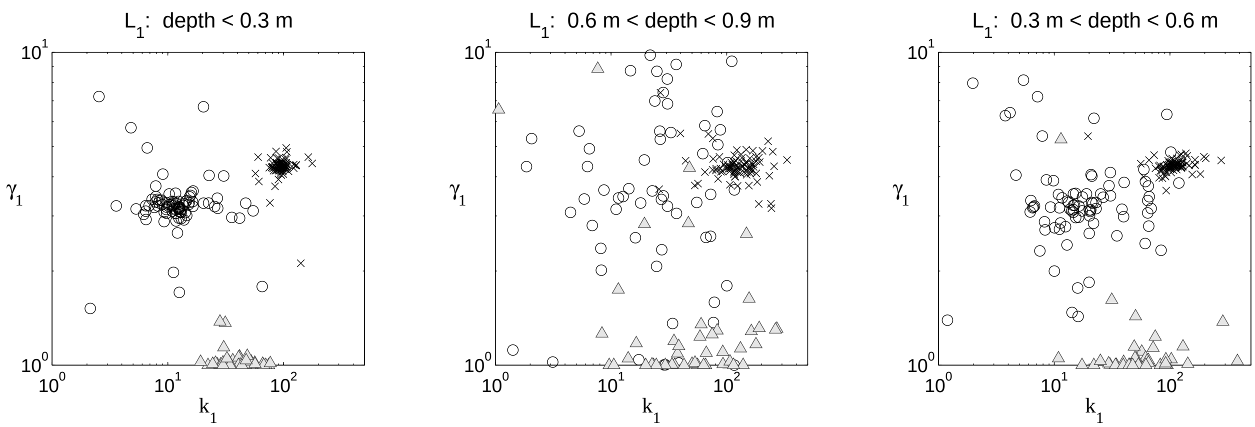

k_1 vs. γ_1. depth less than 0.3 m.

k_1 vs. γ_1. depth less than 0.6 m and greater than 0.3 m.

k_1 vs. γ_1. depth less than 0.9 m and greater than 0.6 m

Figure 6.56: Comparison of parameter fitting results for the intact and partial 4.2 inch mortars and 60 mm mortars

We would expect that discrimination of smaller targets with the spatial sampling and background noise of the dynamic mode survey of the GPO would be limited. Figure 6.56 compares the parameter cluster plots for the intact and partial 4.2-inch mortars and 60 mm mortars. For clarity, we plot the secondary *k* values as a single point representing the average of the two values. When the targets are shallow, there is separation in both the size based features and the characteristics of the primary polarization (Figures 6.55 (a) and (d), respectively), suggesting discrimination of 60 mm is possible when target depths are less than 0.3 m. However, as targets are deeper, the variance in target clusters increase. For depths between 30 and 60 cm, the size based parameters begin to noticeably lose discrimination potential (Figure 6.56 (b)), but some level of discrimination success could be achieved by using the properties of the primary polarization (Figure 6.56 (e)). For targets greater than 60 cm (Figures 6.55(c) and (f), we see that discrimination would not be likely. In order to better constrain the parameters for the 60 mm mortar, changes would have to be made to the survey parameters such as line spacing and acquisition speed.

6.11.8. Summary

To develop a set of effective processing techniques for EM data at sites with a strong background signal, one must carry out data simulations with realistic spatial and spectral representations of geologic noise. We have presented the use of correlated random numbers (CRNs) for simulating the two dimensional spatial characteristics for the background response due to geologic material. We then demonstrate the validity of the approach for simulating the response of frequency domain data collected over soils exhibiting strong viscous remanent magnetization (VRM) at Kaho'olawe, Hawaii. Finally, we demonstrate the potential of multiple correlated random numbers as a means of discriminating UXO at the Former Camp Sibert, Alabama.

6.12 Discussion

The most common approach to EM processing is to: (1) develop a target list based on a property of the data, (2) develop filtering techniques such that the background response can be estimated, and subsequently subtracted from the data, and (3) the spatially filtered data is then inverted with the physical model for the UXO response in free space. In this section, we looked at different aspects of processing electromagnetic data collected in regions with highly magnetic geology. Synthetic data sets were generated to help study the effectiveness of filtering, target picking, and inversion.

We showed that sensor height changes of only a few centimeters can change the measured soil signal by tens of percent. Therefore, in regions where there is a significant VRM response, accurate sensor positioning and orientation information are required to model the measured data. The standard high pass filter approach will have limited success due to the high spatial frequency components of the data introduced by the sensor movement and small scale topography. Instead of filtering the data directly, an improved approach would be to include sensor position information in estimates of the soil properties. These soil properties can then be filtered if the assumption that the soil properties of the host medium is smooth is valid.

In general, TEM data is not collected with accurate sensor position and orientation information. Sensor movement then leads to the numerous anomalies that are similar to those from UXO. When the number of soil anomalies make the target picking directly from the data ineffective, the misfit of the measured time or frequency sounding to a soil model is a potential diagnostic for determining if a sounding is from soil or metal. The use of the soil model misfit was shown to be effective for picking targets in Geonics EM63 and Geophex GEM3 data acquired on Kaho'olawe.

An analysis of how noise due to the background response affects dipole inversion parameters was carried out. Data collected at magnetic sites with very accurate sensor motion information was not available during this research. Therefore our analysis focused on the effects of not including the sensor motion information into the processing. Inversion of synthetic data showed that not including this information leads to inaccurate recovery of the polarization tensor magnitude. The decay characteristics of the axial polarization tensor appears to be better constrained than the amplitude. The transverse component is not recovered well.

The final example of this section showed that an estimate of the background response could be improved with the use of horizontal component data. Target picking on the horizontal component can be an effective in highly magnetic soil since no spatial filtering is required. The effectiveness of using the horizontal component is limited by the smaller signal to noise ratio of the horizontal component.

7. Discussion

This is the final report for the SERDP project MM-1414 and it covers the research results accomplished since the projects inception in 2005. The basic premise of the project is the theoretical understanding achieved through SERDP SEED project UX-1285, which predicted that spatially variable frequency-dependent susceptibility in soils hosting UXO can produce strong background response in both electromagnetic and magnetic data. Such responses can mask UXO signatures or produce false alarms. Improving UXO detection and discrimination in such strongly magnetic environments requires the characterization and removal of these responses. The overall objective of the current project has therefore been to understand and characterize the spatial variation and frequency dependence of soil magnetic susceptibility so that effective means can be developed for characterizing and removing soil responses.

This study therefore focused on four primary research tasks that were completed over the life-span of the project. These objectives included:

1. Understanding the geologic origins and physics of soil magnetization.
2. Characterizing the spatial variation of magnetic susceptibilities at UXO remediation sites.
3. Developing methods and procedures for removing the effects of magnetic soils from magnetic data.
4. Developing methods and procedures for preprocessing of electromagnetic data in highly magnetic environments.

The research performed over the life span of this project progressed satisfactorily with all major research tasks completed according to the project plan. To start, five major field sessions were conducted at four sites:

1. Kaho’olawe Island, HI
2. Big Island, HI (two sites – Waimea and Waikoloa)
3. Chevalier Ranch in Helena Valley, MT
4. Sentinel Plains, AZ

Through laboratory analyses of soil samples and interpretation of geophysical data collected at these sites, we have developed a significant improvement in understanding the origins, composition and spatial distribution of magnetic soils in varying magnetic environments. For example, we have confirmed observationally the frequency-dependent magnetic susceptibility of soils originating from well-weathered volcanics and volcanic ashes. Strong correlation between the strength of frequency-dependent susceptibility and measured time-domain and frequency-domain EMI responses of background soil confirms the effect of such soil on magnetic and electromagnetic sensor data. Thus, we have observed the viscous remanent magnetization in the field. Through our laboratory and field observations, we have also developed a 3D soil distribution model and 3D geostatistical model of frequency dependent magnetic susceptibility for improved modeling of geophysical data in these environments. Lastly, through our field work we have discovered that sites previously thought to be benign may exhibit weak viscous remanent magnetization. Thus the field activities from this project have broad implications for ongoing and future remediation efforts in similar environments within the continental US.

Understanding the geologic origins and physics of soil magnetization

The first phase of MM-1414 focused heavily on field work and associated sample and data analyses to address the first two research questions. The work was carried out at five field sites during the first two years of the project. A total of 377 soil samples were collected from these sites. Magnetic and EMI data sets were likewise acquired to supplement existing data sets. Geologic information and maps were also compiled for the sites, supplemented by direct observation during the field work.

Laboratory analyses indicated that the complex susceptibilities exhibit frequency dependence consistent with the presence of a broad range of relaxation times, such that the real part of the complex susceptibility is a linearly decreasing function with logarithmic frequency, and the imaginary part is proportional to the slope of the real part. Corresponding to such susceptibilities, direct observations show the inverse time decay of measured voltage in time-domain EM responses. Thus we have observed VRM in the field, which is the basic premise of the project. Furthermore, the strengths of soil magnetic susceptibility and its frequency dependence are directly related to the degree or maturity of soil development. Well developed soil has a much higher susceptibility and stronger frequency dependence. At sites with well developed soil horizons, both increase towards the ground surface, and the difference is correlated with the increased degree of weathering near the surface.

Mineralogically, the well developed soils have more fine particles that contain single magnetic domains. These single-domain particles are responsible for the broad distribution of relaxation times and the corresponding complex susceptibility. It is therefore logical to expect that other sites can potentially have similar magnetic soils if well developed soils, with magnetic minerals or volcanic ashes, are present.

This project has identified that, at Waikoloa and Waimea on the Big Island, the soil is comparable to many locations in the southwest continental U.S., where relatively unweathered volcanic basalt material is found. These sites and their magnetic signatures have been poorly characterized. The presence of strong complex susceptibility at Waikoloa and Waimea lead us to believe that VRM with comparable strength may be present at these uninvestigated sites in southwest US. We also note that soils formed in volcanic ash (Andisols) are widespread in the west and northwest U.S. Most Hawaii soils have a component of ash. Andisols may be magnetic. Therefore, we also expect a similar VRM effect at these sites. Currently, we have very limited knowledge of the magnetic properties and mineralogy of these soils. The understanding and approaches obtained from current research should have broad implications at these sites too.

<u>Characterizing the spatial variation of magnetic susceptibilities at UXO remediation sites</u>

A major accomplishment through MM-1414 has been the development of a method for generating full 3D soil distribution models which incorporate all soil (surface and pit)-sample measurements of frequency dependent magnetic susceptibilities. We have demonstrate the method applied to the most magnetically complex site, Kaho'olawe HI, utilizing 36 surface soil samples and 28 samples collected at varying depths throughout soil pits A-B-C-& D. The 3-D soil-distribution models were an essential component of the project, which allowed us to better understand the geophysical responses of highly magnetic soils in a fully 3-D geologic setting. To generate the model, we calculated the Cole-Cole model parameter α, distributed over a 3D volume from soil samples collected and cataloged at Kaho'olawe, to generate a 3D soil distribution model characterizing VRM. From this model, we likewise developed a methodology to performed 3D geostatistical simulations. The simulations are conditioned with the frequency-dependent magnetic susceptibility data measured from the soil samples and incorporate the autocorrelation properties derived from the spatial power spectra of high-resolution EMI data. In essence, the soil measurements characterize the overall magnitude of the frequency dependence of the soil susceptibility and its long wavelength variation, whereas the EMI data constrain the short wavelength variation. These procedures may allow future SERDP research projects to reproduce the modeling approach for developing new filter technologies based on the 3D spatial distribution of VRM.

Given the high variability of soil susceptibility, it is recommended that future instrument developments take this environment-specific effect into consideration. The characterized spatial variation and magnitude of soil susceptibility provides the basis for carrying out numerical simulation to optimize the design parameters of future EMI instruments and to possibly adjust acquisition parameters during deployment. The established soil susceptibility parameters and 3D model can be used directly for such studies; and the procedure we established can be used to assess the soil susceptibility and its variation at different sites for this purpose.

Developing methods and procedures for removing the effects of magnetic soils from magnetic data

We have modified and implemented two filtering approaches for UXO magnetic data in order to separate the response of strong magnetic geology from UXO anomalies. The two methods are an iterative Wiener filter approach, and a wavelet filter approach. The iterative Wiener filter directly separates UXO-like anomalies from geology by estimating a transfer function using the power spectra of the data and geology. Current implementation requires only estimation of the background geologic response while future versions may incorporate estimations of the desired signal (approximation of the dipole moment of the UXO). At present an iterative approach to the filtering has produced the best results but future processing algorithms may include both an iterative and multi-faceted approach using the power spectra of all three quantities (field data, desired signal, and background response). The development of the processing algorithm has been tested on the data collected at Chevalier Ranch. Results show promise in being able to successfully remove the influence of the background geology in many magnetic environments.

In addition to the iterative Wiener filter for separating the response of magnetic geology from UXO, we have also implemented an automated wavelet transform-based de-noising method for the same purpose. We apply the method to extract background geologic responses that are typically longer wavelength or exhibit lineation. Wavelet transforms have two potential advantages over Fourier transforms for separating the magnetic response of UXO from magnetic soils. The first is multiresolution decomposition, and the second is time/space localization. The wavelet-based approach uses compactly supported orthonormal wavelets and the process has the capability of selectively extracting localized high-frequency anomalies, such as those associated with UXO for the proposed approach, while recognizing and avoiding sharp features that are present in the signal but associated with geology. These properties have the potential to allow for a fast and accurate means of separating geology from UXO-like anomalies in magnetic datasets. The method has been applied to two sets of UXO magnetic datasets from Chevalier Ranch. At the field sites, the magnetic susceptibilities associated with geology are found to either reduce or completely mask the magnetic response of our buried targets. The method, as implemented, produces similar results to the iterative Wiener filter for separating the geologic anomalies from UXO in total-field magnetic data. The two filtering methods combined have helped us understand (1) the advantages and disadvantages of the two fundamentally different filtering approaches, and (2) the geologic conditions under which each method may prove valuable, or ineffective.

Finally, we have modified an approach, originally developed under a separate project funded by ERDC, for automatic detection of UXO anomalies in total-field magnetic data. The method is based on the concept of structural index (SI). We further developed the method by implementing it in combination with pre-processed data using the iterative Wiener and wavelet filters for removing strong geologic responses in the magnetic data. The goal of this component has been to better understand and develop practical procedures, appropriate to a geologic setting, for integrating new filtering technologies with recently developed methodologies for detecting UXO in magnetic environments. The automated approach of UXO target picking using the Hilbert transform-based extended Euler deconvolution method has demonstrated successful results in settings with high and varying magnetic geology. The method has repeatedly identified several false targets within the data regions tested; however, it has also successfully identified all hazardous munitions. We have demonstrated, however, that preprocessing to separate the geologic response from UXO data may be required, depending on the nature of the geologic noise. Iterative Wiener filter and wavelet filter have both shown promise for such separation. We have observed that the presence of overlapping anomalies, either between UXO responses or between UXO and some geologic response, tend to degrade the Euler solutions and create false target picks. We have also concluded that dipole-like features in the magnetic data associated with geology likewise generate such false positives. The three test sites have demonstrated the need for further development of the extended Euler deconvolution target picking approach in terrains with strong magnetic geology, such that it may successfully detect all harmful munitions, while significantly reducing the number of false picks.

Developing methods and procedures for preprocessing of electromagnetic data in highly magnetic environments

In parallel to development and implementation of filters for UXO magnetic data sets, MM-1414 utilized data inversion simulations to quantify the effectiveness of different processing techniques applied to frequency domain and time domain electromagnetic data contaminated by magnetic geologic noise. We have focused on time-domain EMI data for its wider utility in practice, but also carried out substantial work with frequency-domain data.

The predominant effect of frequency-dependent magnetic soil is its *1/t* response in the time-domain EMI measurements. This response persists spatially and over the decay time of the measurements. The strength of the soil response overpowers the UXO signal and masks the UXO anomaly, and therefore causes difficulties in both detection and discrimination. Numerical simulations based on realistic susceptibility and soil thicknesses show that even a thin layer of such soil could have a profound influence on the EMI data with the corresponding *1/t* decay.

Furthermore, if the soil layer is sufficiently extended laterally around the sensor and appears to be a 1D medium locally, the sensor data do not contain enough information to resolve the depth variation of the susceptibility.

Beyond this rather straightforward notation of the magnetic soil effect, MM-1414 has identified two other types of effect that can adversely affect EMI data in a major way. The first is the spatial variability of the soil magnetic susceptibility, whose EMI response can often be on the same wavelength as those of UXO. The second is noise produced by the variation in height and orientation of the EMI sensor induced by the micro-topography over such soils. The strong soil response manifests itself in the EMI data as random variations through the inaccuracy in sensor positioning. Therefore, the accurate tracking of sensor positioning and orientation in such magnetic environment is crucial in practical applications.

Expanding upon the statistical simulation of the magnetic soil based on sample and EMI data, we have also investigated the use of mixed correlated random noise (CRN) in simulating spatial variability of the soil property. The mixed CRN allows us to capture the location-dependent statistical properties of the magnetic soil. We examined some of the properties of EMI data collected in magnetic settings and demonstrate the use of CRNs on EMI data acquired at Kaho'olawe, Hawaii.

Based on the understanding achieved through these efforts, we have investigated the two ultimate goals in EMI data processing in magnetic environments, namely, UXO detection and discrimination, and developed a set of theoretically sound and practically useful tools.

For detections, we investigated several different target-picking approaches: (1) filtering of the EMI data to remove underlying geologic response and picking potential UXO targets based on the residual anomaly; (2) fitting soil response with *1/t* decay and using the misfit portion of the data as the residual UXO anomaly for target picking; and (3) using an information theoretical approach to pick anomalies based on hypothesis testing in which a null-hypothesis assumes the presence of only soil responses. All three approaches have been found effective to different degrees and they all can serve as potential tools in active clearance efforts.

To improve the UXO discrimination, we have focused on the parametric inversion for recovering polarization tensors from EMI data. Our work has shown that it is imperative to incorporate a *1/t* in the inversion as part of the parameterization in TEM data inversion. This added component accounts for the presence of magnetic soil and alleviates the bias of recovered UXO parameters used in the subsequent discrimination analysis. We have illustrated the feasibility of the approach for UXO discrimination in magnetic environments using data from geophysical prove-out grids and different field sites.

In summary, the MM-1414 project has been successful in all aspects of the planned research and we have accomplished much more. The research results constitute a consistent and self-contained body of knowledge on the subject of magnetic soil with frequency-dependent susceptibility, or viscous remanent magnetization (VRM), and its effect on EMI sensor data in UXO geophysics. We have developed a set of methods for processing and separating such geologic responses from both TMI and EMI data to improve the detection and discrimination UXOs. The results have already been applied in more recent research projects funded by SERDP and in actual clearance work.

8. References

Bell, T., Barrow, B., and J.T. Miller, 2001b, Subsurface discrimination using electromagnetic induction sensors: *IEEE Transactions Geoscience & Remote Sensing*, 39:1286–1293

Bell, T., Barrow, B., Miller, J., and D. Keiswetter, 2001a, Time and frequency domain electromagnetic induction signatures of unexploded ordnance: *Subsurface Sensing Technologies and Applications*, 2(3):153 – 175

Beran, L., 2005, Classification of unexploded ordnance: Master's thesis, University of British Columbia

Billings, S., and C. Youmans, 2006, Experiences with unexploded ordnance discrimination using magnetometry at a live-site in Montana: Journal of Applied Geophysics Special Issue

Billings, S.D., 2004, Discrimination and classification of buried unexploded ordnance using magnetometry: *IEEE Transactions Geoscience & Remote Sensing*, 42:1241 – 1251

Billings, S.D., Pasion, L.R., Oldenburg, D.W. and J. Foley, 2003, The influence of magnetic viscosity on electromagnetic sensors: in *EUDEM-SCOT2, International Conference on Requirements and Technologies for the Detection, Removal and Neutralization of Landmines and UXO*, H. Sahli, A. Bottoms and J. Cornelis (Editors), Brussels

Billings, S.D., Pasion, L.R., Oldenburg, D.W., and J. Foley, 2003, The influence of magnetic viscosity on electromagnetic sensors: in *Proceedings of EUDEM-SCOT2, International Conference on Requirements and Technologies for the Detection, Removal and Neutralization of Landmines and UXO*

Blazek, A., 1973, Thermal analysis: Series in Analytical Chemistry, Van Nostrand Reinhold Company, London, 281 pp

Buselli, G, 1982, The effect of near surface superparamagnetic material on electromagnetic measurements: *Geophysics*, 47(9):1315–1324

Buynevich, I.V., Bitinas, A. and D. Pupienis, 2007, Lithological anomalies in a relict coastal dune: Geophysical and paleoenvironmental markers: Geophysical Research Letters, 34: L09707, doi:10.1029/2007GL029767

Cargile, D.M., Bennett, H.H., Goodson, R.A., DeMoss, T.A., and E.R. Cespedes, 2004, Advanced UXO detection/discrimination technology demonstration – Kaho'olawe, Hawaii: Technical report, U.S. Army Research and Development Center, Vicksburg, MS, ERDC/EL TR-04-1

Chao, T.T. and L. Zhou, 1983, Extraction techniques for selective dissolution of amorphous iron oxides from soils and sediments: Soil Science Society of America Journal, 47: 225-232

Chao, T.T., and L. Zhou, 1983, Extraction techniques for selective dissolution of amorphous iron oxides from soils and sediments: Soil Science Society of America Journal, v. 47, p. 225-232

Clague, D.A. and G.B. Dalrymple, 1987, The Hawaiian-Emperor volcanic chain Part II, in Volcanism in Hawaii, R.W. Decker, T.L. Wright, and P.H. Stauffer, Editors. U.S. Geological Survey Professional Paper 1350. p. 5-54

Clague, D.A. and G.B. Dalrymple, 1989, Tectonics, geochronology, and origin of the Hawaiian-Emperor Chain, in The Eastern Pacific Ocean and Hawaii, E.L. Winterer, D.M. Hussong, and R.W. Decker, Editors. Geological Society of America: Boulder, CO. p. 188-217

Colani, C., and M. J. Aitken, 1966, Utilization of magnetic viscosity effects in soils for archaeological prospection: *Nature*

Cole, K.S., and R.H. Cole, 1941, Dispersion and adsorption in dielectrics: J. Chem. Phys., v. 9, p. 341

Collins, L.M., Zhang, Y., Li, J., Wang, H., Carin, L., Hart, S.J., Rose-Pehrsson, S.L., Nelson, H.H., and J.R. McDonald, 2001, A comparison of the performance of statistical and fuzzy algorithms for unexploded ordnance detection: *IEEE Transactions on Fuzzy Systems*, 9(1):17–30

Cornell, R.M. and U. Schwertmann, 2003, The iron oxides: structure, properties, reactions, occurrences and uses. Second ed. Weinheim: Wiley-VCH. 664

Das, Y, 2006, Effects of soil electromagnetic properties on metal detectors: *IEEE Transactions on Geoscience and Remote Sensing*, 44(6):1444–1453

Das, Y., McFee, J.E. and G. Cross, 2002, Soil properties database for humanitarian demining: a proposed initiative: 17th World Congress of Soil Science, The International Union of Soil Science, Bankok, Thailand

Davis, K., Li, Y., and M.N. Nabighian, 2005, Automatic detection of UXO magnetic anomalies using extended Euler deconvolution: 75th Ann. Internat. Mtg., Soc. Expl. Geophys., Expanded Abstracts, p. 1133-1137

Dearing, J.A., 1994, Environmental magnetic susceptibility: using the Bartington MS2 system, Chi Publishing

Donoho, D.L., 1993, Nonlinear wavelet methods for recovery of signals, densities, and spectra from indirect and noisy data, Different perspectives on wavelets: Proceeding of Symposia in Applied Mathematics, V. 47, I. Daubechies ed., Amer. Math. Soc., Providence, RI, p. 173-205

Donoho, D.L., and I.M. Johnstone, 1994, Ideal spatial adaptation via wavelet shrinkage: Biometrika, v. 81, p. 425-455

Donoho, D.L., and I.M. Johnstone, 1995, Adapting to unknown smoothness via wavelet shrinkage: Journal of the American Statistical Association, v. 90, p. 1200-1224

F. Efferso, E. Auken, and K. I. Sorensen, 1999, Inversion of band-limited TEM responses: Geophysical Prospecting, 47:551–564

Fabian, K., 2003. Some additional parameters to estimate domain state from isothermal magnetization measurements: Earth and Planetary Science Letters, 213: 337-345

Fabris, D., Coey, J.M.D. and W.D.N. Mussel, 1998, Magnetic soils from mafic lithodomains in Brazil. Hyperfine Interactions: 113: 249-258

Fannin, P.C., and S.W. Charles, 1995, On the influence of distribution functions on the after-effect function of ferrofluids: *Journal of Physics D*, 28:239–242

Farquharson, C.G., Oldenburg, D.W., and P. S. Routh, 2003, Simultaneous 1D inversion of loop-loop electromagnetic data for magnetic susceptibility and electrical conductivity: Geophysics, v. 68, p. 1857-1869.

Földvari, M., 1991, Measurement of different water species in minerals by means of thermal derivatography: in *Thermal analysis in geosciences: Lecture Notes in Earth Sciences*, W. Smykatz-Kloss and S.S.J. Warne (Editors), Springer-Verlag, Berlin, pp. 84-101

Foley, J., Billings, S., Pasion, L., Walker, S., and C. Pasion, 2005, UXO target detection and discrimination with electromagnetic differential illumination: Technical report, Strategic Environmental Research and Development Program (SERDP)

Freeman, V.L., Ruppel, E.T., and M.R. Klepper, 1958, Geology of part of the Townsend valley - Broadwater and Jefferson Counties, Montana. United States Government Printing Office: Washington. p. 481-556

Hamilton, Warren B., 2003, An alternative earth, GSA Today, V.13, No. 11, pp. 4–12

Hansen, R.O., and R.S. Pawlowski, 1989, Reduction to the pole at low latitudes by Wiener filtering: Geophysics, v. 54, p. 1607-1613.

Hawaii Statewide GIS Program website, last viewed April 2006: http://www.state.hi.us/dbedt/gis/download.htm

Hendrickx, J.M.H., Harrison, J.B.J, Van Dam, R.L., Borchers, B., Norman, D.I., Dedzoe, C.D., Antwi, B.O., Asiamah, R.D., Rodgers, C., Vlek, P., and J. Friesen, 2005, Magnetic soil properties in Ghana, in: *Detection and Remediation Technologies for Mines and Minelike Targets X,* R.S. Harmon, J.T. Broach and J. Holloway, J.H. (Editors): SPIE, Orlando, pp. 165-176

Holmgren, G.G. S., 1967, A rapid citrate-dithionite extractable iron procedure: Soil Science Society of America Proceedings, v. 31, p. 210-211.

Hunt, C.P., Moskowitz, B.M., and S.K. Banerjee, 1995, Magnetic properties of rocks and minerals: in Rock Physics and Phase Relations, T.J. Ahrens, ed., AGU, Washington DC, p. 189-204

I.J.Won, Keiswetter, D., Hanson, D.R., Novikova, E., and T.M. Hall, 1997, GEM-3: A monostatic broadband electromagnetic induction sensor: Journal of Environmental and Engineering Geophysics, 2(1):53–56

Lee, T., 1983, The effect of a superparamgnetic layer on the transient electromagnetic response of a ground: *Geophysical Prospecting*, 32:480–496

Leeman, W.P., Gerlach, D.C., Garcia, M.O., and H.B. West, 1994, Geochemical Variations in Lavas from Kahoolawe Volcano, Hawaii: Evidence for Open System Evolution of Plume-Derived Magmas. Contributions to Mineralogy and Petrology. 116: p. 62-77

Li, Y., Meglich, T., Krahenbuhl, R., Pasion, L., Walker, S., Oldenburg, D., Billings, S., van Dam, R., and B. Harrison, 2005, SERDP MM-1414 2005 Annual Report.

Lindsley, D.H. (Editor), 1991, Oxide minerals: petrologic and magnetic significance: Reviews in mineralogy, 25, Mineralogical Society of America, Chelsea, 506 pp

Lyrio, J., Tenorio, L., and Y. Li, 2004, Efficient automatic denoising of gravity gradiometry data: Geophysics, v. 69, p. 772-782

Macdonald, G.A., Abbott, A.T., and F.L. Peterson, 1983, Volcanoes in the sea. Honolulu, HI: University of Hawaii Press

Mallat, S., 1998, A wavelet tour of signal processing: Academic Press Inc

Meglich, T., Li, Y., Pasion, L., Oldenburg, D., Van Dam, R.L., and S. Billings, 2008, Characterization of frequency-dependent magnetic susceptibility in UXO electromagnetic geophysics: SEG Annual Meeting, Las Vegas, Nevada

Mullins, C.E., 1977, Magnetic susceptibility of the soil and its significance in soil science - a review: Journal of Soil Science, 28: 223-246

Munkholm, M.S., and E. Auken., 1996, Electromagnetic noise contamination on transient electromagnetic soundings in culturally disturbed environments: Journal of Engineering and Environmental Geophysics, 1(2): 119–127

Nabighian M.N. and J.C. Macnae, 1991, Time Domain Electromagnetic Prospecting Methods, in *Electromagnetic Methods In Applied Geophysics*: Volume 2, pp 427–520, Society of Exploration Geophysicists

Nabighian, M.N., and R.O. Hansen, 2001, Unification of Euler and Werner deconvolution in three dimensions via the generalized Hilbert transform: Geophysics, v. 66, p. 1805-1810

Nakamura, S. and C.W. Smith, 1995, Soil survey of Island of Kahoolawe, Hawaii. USDA, NRCS: Washington, D.C. p. 73

Naughton, J.J., MacDonald, G.A., and V.A. Greenberg, 1980, Some additional potassium-argon ages of hawaiian rocks: The Maui volcanic complex of Molokai, Maui, Lanai and Kahoolawe. Journal of Volcanology and Geothermal Research. 7(3-4): p. 339-355

Olhoeft, G.R. and D.W. Strangway, 1974, Magnetic relaxation and the electromagnetic response parameter: Geophysics, v. 39, p. 302-311

Oxford, R.B., and G.L. Bender, 1973, Proposed natural areas Sentinel Plain Lava Flow. Report No. 37: Arizona Academy of Science for Planning Division, Department of Economic Planning and Development, Office of the Governor, State of Arizona, Phoenix, Arizona

Pasion, L.R., 1999, Detecting unexploded ordnance with time domain electromagnetic induction: Master's thesis, University of British Columbia

Pasion, L.R., 2007, *The Inversion of Time Domain Electromagnetic Data for the Detection of Unexploded Ordnance*: PhD thesis, University of British Columbia

Pasion, L.R., and D.W. Oldenburg, 2001, A discrimination algorithm for UXO using time domain electromagnetics: *Journal of Engineering and Environmental Geophysics*, 6(2):91–102

Pasion, L.R., Billings, S.D., Oldenburg, D.W., and S.E. Walker, 2006, Application of a library based method to TEM data for the identification of UXO: *Journal of Applied Geophysics*, 61(3):279–291

Pasion, L.R., Billings, S.D., Oldenburg, D.W., Sinex, D., and Y. Li, 2003, Evaluating the effects of magnetic susceptibility in UXO discrimination problems: SERDP SEED Project UX-1285

Percival, D.B., and A.T. Walden, 2000, Wavelet methods for time series analysis: Cambridge University Press

Piper, J.D.A., 1987, Paleomagnetism and the continental crust: Wiley, New York, 434 pp

Sanchez, V., Li, Y., Nabighian, M., and D. Wright, 2006, Numerical modeling of magnetic moments for UXO applications: Proceedings of SPIE—Targets and Backgrounds XII: Characterization and Representation, Watkins, W. R., and D. Clemend, ed., v. 6239

Sinex, D., and Y. Li, 2004, Effects of magnetic soils on magnetometry in UXO discrimination problems: Proceedings of SAGEEP 2004

Singer, M.J. and P. Fine, 1989, Pedogenic factors affecting magnetic susceptibility of Northern California soils: Soil Science Society of America Journal, 53: 1119-1127

Singer, M.J., Fine, P., Verosub, K.L. and O.A. Chadwick, 1992, Time dependence of magnetic susceptibility of soil chronosequences on the California coast: Quaternary Research, 37: 322-332

Singer, M.J., Verosub, K.L., Fine, P. and J. TenPas, 1996, A conceptual model for the enhancement of magnetic susceptibility in soils: Quaternary international, 34-36: 243-248

Sky Research, 2006, Geophysical workplan; geophysical technology study at Sentinel Plain

Smith, J.T., Morrison, H. F., and A. Becker, 2004, Parametric forms and the inductive response of a permeable conducting sphere: *Journal of Environmental and Engineering Geophysics*, 9:213–216

Speyer, R.F., 1994, Thermal analysis of materials: Marcel Dekker, New York

Stucki, J.W., Goodman, B.A. and U. Schwertmann (Editors), 1988, Iron in soils and clay minerals: Reidel, Dordrecht, 893 pp

Thompson, R. and F. Oldfield, 1986, Environmental magnetism: Allen & Unwin, London, 227 pp

Tite, M.S. and R.E. Linington, 1975, Effect of climate on the magnetic susceptibility of soils: Nature, 256: 565-566

USGS Hawaiian Volcano Observatory website, last viewed April 2006: http://hvo.wr.usgs.gov/products

Van Dam, R.L., Harrison, J.B.J., and J.M.H. Hendrickx, In Preparation, Magnetic behavior in a soil climosequence on a young volcanic island

Van Dam, R.L., Harrison, J.B.J., Hirschfeld, D., Meglich, T., Li, Y., and R. North, Accepted, Mineralogy and magnetic properties of basaltic substrate soils: Kaho'olawe and Big Island, Hawaii: Soil Science Society of America Journal

Van Dam, R.L., Harrison, J.B.J., Hirschfeld, D., Meglich, T., Li, Y., and R. North, 2008, Mineralogy and magnetic properties of basaltic substrate soils: Kaho'olawe and Big Island, Hawaii: Soil Science Society of America Journal, 72(1): 244-257

Van Dam, R.L., Harrison, J.B.J., Rittel, C.L., Hendrickx, J.M.H. and B. Borchers, 2006, Magnetic soil properties at two arid to semi-arid sites in the western United States, in *Detection and remediation technologies for mines and minelike targets XI*, T. Broach, R.S. Harmon and J.H. Holloway Jr (Editors): The International Society for Optical Engineering, SPIE, Orlando, Fl, pp. 0O1-0O11

Van Dam, R.L., Hendrickx, J.M.H., Harrison, B., Borchers, B., Norman, D.I., Ndur, S., Jasper, C., Niemeyer, P., Nartey, R., Vega, D., Calvo, L., and J.E. Simms, 2004, Spatial variability of magnetic soil properties, in *Detection and Remediation Technologies for*

Mines and Minelike Targets IX, R.S. Harmon, J.T. Broach and J.H. Holloway (Editors): SPIE, Orlando, pp. 665-676

Van Dam, R.L., Hendrickx, J.M.H., Harrison, J.B.J. and B. Borchers, 2005, Conceptual model for prediction of magnetic properties in tropical soils, in *Detection and Remediation Technologies for Mines and Minelike Targets X*, R.S. Harmon, J.T. Broach and J. Holloway, J.H. (Editors): SPIE, Orlando, pp. 177-187

Van Dam, R.L., Schlager, W., Dekkers, M.J. and J.A. Huisman, 2002, Iron oxides as a cause of GPR reflections: Geophysics, 67(2): 536-545

Van Devender, T.R., and M.A. Dimmitt, 2006, Conservation of Arizona upland Sonoran desert habitat. Status and threats of Buffelgrass (Pennisetum ciliare) in Arizona and Sonora: Project #2004-0013-003)

Walker, S.E., Pasion, L.R., Billings, S.D., Li, Y. and D.W. Oldenburg, 2005, Examples of the effect of magnetic soil environments on time domain electromagnetic data: SAGEEP, EEGS, Atlanta, GA

Walker, S.E., Pasion, L.R., Billings, S.D., Oldenburg, D.W., and Y. Li, 2005, Examples of the effect of magnetic soil environments on time domain electromagnetic data: in *Proceedings from SAGEEP 05*

Ward, S.H. (Editor), 1990, Geotechnical and environmental geophysics: Investigations in Geophysics, 5., Society of Exploration Geophysicists, Tulsa, 1032 pp

Ware, G. H., 2001, EM-63 decay curve analysis for ordnance discrimination: in *Proceedings of Partners in Environmental Technology Techinical Symposium and Workshop*

Wedepohl, K.H., 1969, Composition and abundance of common igneous rocks, in Handbook of Geochemistry, K.H. Wedepohl, Editor. Springer-Verlag: Berlin

Wiener, N., 1949, Extrapolation, interpolation, and smoothing of stationary time series: Cambridge, MIT

Wolfe, E.W. and J. Morris, 1996, Geologic map of the island of Hawaii. U.S. Department of the Interior

Wood, C.A. and J. Kienle, J. (Editors), 1990, Volcanoes of North America: United States and Canada: Cambridge University Press New York, 354 pp

Wright, T.L. and D.A. Clague, 1989, Petrology of Hawaiian lava, in The Eastern Pacific Ocean and Hawaii, E.L. Winterer, D.M. Hussong, and R.W. Decker, Editors. Geological Society of America: Boulder, CO. p. 218-237

Zhang, Y., Collins, L., Yu, H., Baum, C. E., and L. Carin. 2003, Sensing of unexploded ordnance with magnetometer and induction data: Theory and signal processing: *IEEE Transactions on Geoscience and Remote Sensing*, 41(5):1005–1015

9. Appendices

9.1 Articles or papers published in peer-reviewed journals

Van Dam, R.L., Harrison, J.B.J., Hirschfeld, D.A., Meglich, T.M., Li, Y., and North, R.E. 2008. Mineralogy and magnetic properties of basaltic substrate soils: Kaho'olawe and Big Island, Hawaii. Soil Science Society of America Journal, 10.2136/sssaj2006.0281, 72(1), 244–257. Published online 11 January 2008.

9.2 Technical reports

Li, Y., Krahenbuhl, R., Meglich, T., Oldenburg, D., Pasion, L., Billings, S., Van Dam, R.L., Harrison, J.B.J.

- 2006. Improving UXO Detection and Discrimination in Magnetic Environments, SERDP Project MM-1414, Annual Report, April 2006.

- 2007. Improving UXO Detection and Discrimination in Magnetic Environments, SERDP Project MM-1414, Annual Report, January 2007.

- 2008. Improving UXO Detection and Discrimination in Magnetic Environments, SERDP Project MM-1414, Annual Report, February 2008.

9.3. Conference/symposium proceedings and/or papers scientifically recognized and referenced

Van Dam, R.L., Harrison, J.B.J., Hendrickx, J.M.H., North, R.E., Simms, J.E., and Li, Y. 2005. Mineralogy of magnetic soils at uxo remediation sites in Hawaii. 18th Symposium on the Application of Geophysics to Engineering and Environmental Problems, Atlanta. Environmental and Engineering Geophysical Society.

Van Dam, R.L., Harrison, J.B.J., Hendrickx, J.M.H., Borchers, B., North, R.E., Simms, J.E., Jasper, C., Smith, C.W. and Li, Y. 2005. Variability of magnetic soil properties in Hawaii. In: Detection and Remediation Technologies for Mines and Minelike Targets X (Eds R.S. Harmon, J.T. Broach and J. Holloway, J.H.), 5794, pp. 157-164. SPIE, Orlando.

Van Dam, R.L., Harrison, J.B.J., Hendrickx, J.M.H., Borchers, B., North, R.E., Simms, J.E., Smith, C., and Li, Y. 2005. Variability of magnetic soil properties in Hawaii. The international Society for Optical Engineering, SPIE, Detection and remediation technologies for mines and minelike targets X, 5794, 157-164.

Van Dam, R.L., Harrison, J.B.J., Rittel, C.L., Hendrickx, J.M.H., and Borchers, B. 2006. Magnetic soil properties at two arid to semi-arid sites in the Western United States. The international Society for Optical Engineering, SPIE. Detection and remediation technologies for mines and minelike targets XI, 6217, 0O1-0O11.

Van Dam, R.L., Hendrickx, J.M.H., Harrison, J.B.J., and Harmon, R.S. 2008, Towards a model for predicting magnetic susceptibility of bedrock regolith and soils. The international Society for Optical Engineering, SPIE. Detection and remediation technologies for mines and minelike targets XIII.

Hannam, J.A., Van Dam, R.L., and Harmon, R.S. 2009. A synthesis of current knowledge and future directions for soil magnetism research. The international Society for Optical Engineering, SPIE. Detection and remediation technologies for mines and minelike targets IV.

Hannam, J.A., Van Dam, R.L., and Harmon, R.S. 2009. Soil magnetism research: State of the art and future directions. 22nd Symposium on the Application of Geophysics to Engineering and Environmental Problems, Forth Worth. Environmental and Engineering Geophysical Society.

9.4 Published technical abstracts

Krahenbuhl, R., Li, Y., Davis, K., Nabighian, M., 2007, Separation of geologic noise in UXO magnetic data using discrete wavelet transform. The UXO/Countermine/Range Forum, Orlando, FL, USA, August 27-30 2007.

Meglich, T., Li, Y., Pasion, L.R., Walker, S., Van Dam, R.L., Oldenburg, D.W., Billings, S., and Harrison, J.B.J., 2006, Characterization of frequency dependent complex magnetic susceptibilities on electromagnetic induction methods. The UXO/Countermine/Range Forum, Las Vegas, Nevada, USA, July 10-13, 2006.

Meglich, T., Li, Y., Pasion, L.R., Oldenburg, D.W., Van Dam, R.L., and Billings, S., 2008, Characterization of Frequency-Dependent Magnetic Susceptibility in UXO Electromagnetic Geophysics. SEG Annual Meeting. Las Vegasa, Nevada, USA, November 9-14 2008.

Van Dam, R.L., Hendrickx, J.M.H., and Harrison, J.B.J. 2006. Magnetic susceptibility to characterize soil development on basaltic substrate, Hawaii. 18th World Congress of Soil Science. Philadelphia, Pennsylvania, USA, July 9-15, 2006.

Van Dam, R.L., 2008, From rock to soil: changes in magnetic properties during weathering of basalt. Workshop on Soil Magnetism: Multi-disciplinary Perspectives, Emerging Applications and New Frontiers. 18-20 August 2008, Cranfield University, UK.